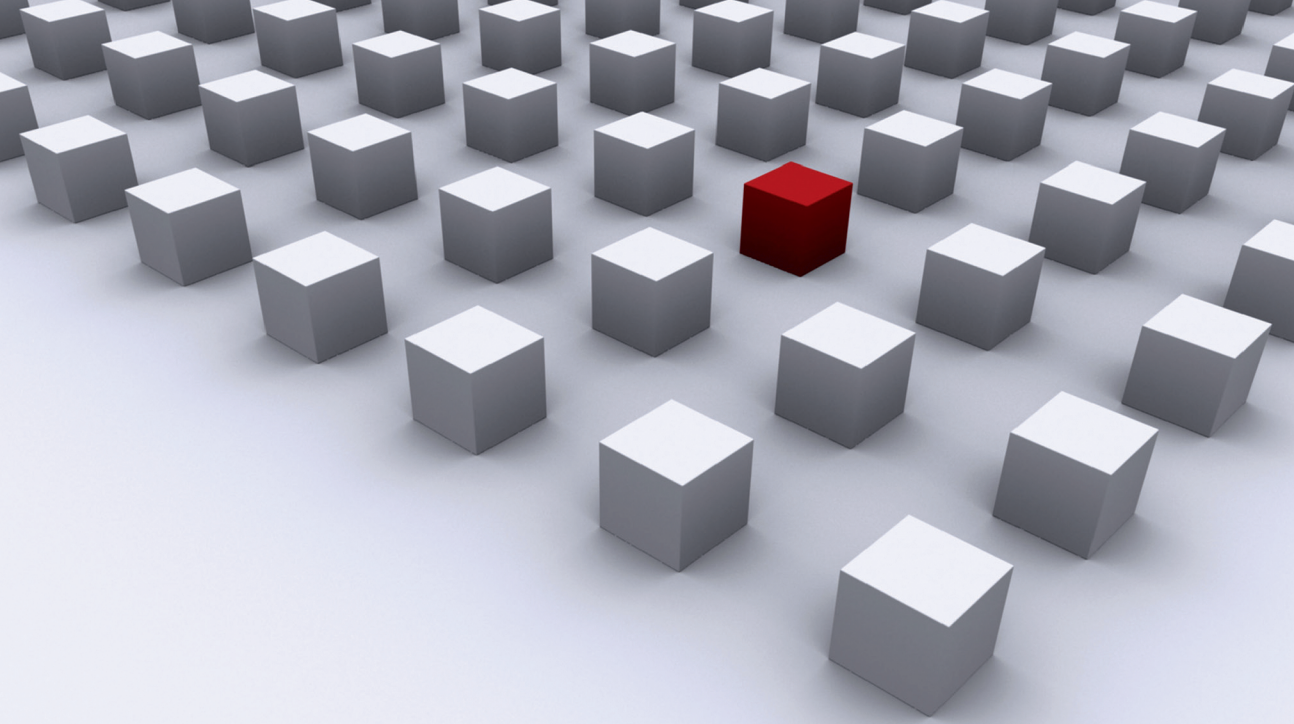

Phillipp Reck

Quantum echoes and revivals in two-band systems and Bose-Einstein condensates

Universitätsverlag Regensburg

52 Dissertationsreihe Physik

Phillipp Reck

Quantum echoes and revivals in two-band systems and Bose-Einstein condensates

Quantum echoes and revivals in two-band systems and Bose-Einstein condensates

Dissertation zur Erlangung des Doktorgrades der Naturwissenschaften (Dr. rer. nat.)
der Fakultät für Physik der Universität Regensburg
vorgelegt von

Phillipp Reck

aus Erlangen
im Jahr 2017

Die Arbeit wurde von Prof. Dr. Klaus Richter angeleitet.
Das Promotionsgesuch wurde am 30.10.2017 eingereicht.

Prüfungsausschuss:	Vorsitzender:	Prof. Dr. Franz Gießibl
	1. Gutachter:	Prof. Dr. Klaus Richter
	2. Gutachter:	Prof. Dr. John Schliemann
	weiterer Prüfer:	Prof. Dr. Tilo Wettig

Dissertationsreihe der Fakultät für Physik der Universität Regensburg, Band 52

Herausgegeben vom Präsidium des Alumnivereins der Physikalischen Fakultät:
Klaus Richter, Andreas Schäfer, Werner Wegscheider

Phillipp Reck

Quantum echoes and revivals in two-band systems and Bose-Einstein condensates

Universitätsverlag Regensburg

Bibliografische Informationen der Deutschen Bibliothek.
Die Deutsche Bibliothek verzeichnet diese Publikation
in der Deutschen Nationalbibliografie. Detailierte bibliografische Daten
sind im Internet über http://dnb.ddb.de abrufbar.

1. Auflage 2018

Leibnizstraße 13, 93055 Regensburg

Konzeption: Thomas Geiger
Umschlagentwurf: Franz Stadler, Designcooperative Nittenau eG
Layout: Phillipp Reck
Druck: Docupoint, Magdeburg
ISBN: 978-3-86845-154-2

Weitere Informationen zum Verlagsprogramm erhalten Sie unter:
www.univerlag-regensburg.de

Contents

1 Introduction – a tiny story of time, including demons **1**

2 Basic concepts **7**
2.1 Graphene . . . 7
2.1.1 Low energy Hamiltonian . . . 7
2.1.2 Graphene in a magnetic field . . . 12
2.2 TQT: A library for simulating the time evolution of quantum wave packets . . . 13

3 Dirac Quantum Time Mirror **17**
3.1 Echo mechanism and transition amplitude . . . 17
3.2 Simulations with Gaussian wave packets . . . 24
3.3 Change of the echo wave packet in real space . . . 28
3.4 Long pulse durations . . . 30
3.5 Wave packets with more complicated shapes . . . 36
3.6 Discussion of the experimental realization and outlook . . . 38

4 Dirac quantum time mirrors under perturbations **41**
4.1 Disorder . . . 41
4.1.1 Implementation of the disorder potential . . . 41
4.1.2 Scattering time . . . 43
4.1.3 Loschmidt Echoes . . . 45
4.1.4 Discussion . . . 50
4.2 General discussion of perturbations . . . 52
4.3 Static magnetic field . . . 56
4.4 Static, in-plane electric field . . . 60
4.5 Conclusion and outlook . . . 63

5 Quantum time mirror for general two-band systems **65**
5.1 General theory of the QTM for two-band systems . . . 65
5.1.1 Transition amplitude . . . 65
5.1.2 Effective time reversal and wave packet echo . . . 69
5.2 Linear band structure with different slopes . . . 72
5.3 Hyperbolic bands . . . 75
5.3.1 Mass gap . . . 75
5.3.2 Other homogeneous pulses . . . 78
5.4 Asymmetric parabolic bands . . . 81

5.5 Conclusion for the two-band QTM 86

6 Effective time-inversion for Bose-Einstein condensates 87
6.1 Introduction to Bose-Einstein condensates and the nonlinear Schrödinger equation 87
6.2 Towards quantum time mirrors for BEC 88
6.2.1 Action of the nonlinear kick 88
6.2.2 Simulations to quantify the echo 93
6.3 Quantum time lens 95
6.3.1 Single pulse 95
6.3.2 Multiple pulses – self-regulation due to the nonlinearity 99
6.4 Solitons in the pulsed NLSE 101
6.4.1 1d solitons in the limit of weak pulses with high repetition rate 101
6.4.2 Simulating pulsed solitons 103
6.5 Summary - BEC mirrors, lenses and solitons 105

7 Zitterbewegung 107
7.1 From theoretical predictions of relativistic particles to experimental realizations in BEC and semiconductors 107
7.2 Frequency, amplitude and decay of the zitterbewegung in general two-band systems 108
7.3 Time-independent zitterbewegung in graphene 114
7.3.1 Pristine graphene 114
7.3.2 Gapped graphene - parallel and modified perpendicular zitterbewegung 117
7.4 Time-dependent zitterbewegung in graphene 121
7.4.1 First order time-dependent perturbation theory 122
7.4.2 Rotating wave approximation 128
7.4.3 High driving frequency 133
7.4.4 Numerical results for the zitterbewegung frequencies 135
7.4.5 Long-time behavior of the zitterbewegung 140
7.4.6 Summary and discussion of the driven zitterbewegung 143
7.5 Echoes of the zitterbewegung using the QTM-protocol 143
7.5.1 Analytical prediction of the echo strength 143
7.5.2 Numerical confirmation of the echo of the zitterbewegung . . . 146
7.5.3 Disorder 148
7.6 Summary, discussion and outlook 150

8 Summary 151

A Calculating overlaps for the transition amplitude in graphene 157

B Matrix elements of the Pauli matrices in the basis of (gapped) graphene eigenstates 159

C Normalization factor in the disorder potential 161

D Time-dependent perturbation theory and the interaction picture 164

Chapter 1

Introduction – a tiny story of time, including demons

Philosophically, the flow of time has probably always been a mystery for mankind. Although is seems not to be as fundamental as the question about the sense of life, which practically everyone wondered about for a longer or shorter time before turning one's attention to more pragmatic issues, many great thinkers dedicated themselves to the affairs of time.

Already in ancient Greece in the pro-Socratic philosophy [1], there were two words for time (which of course had their godly personification): Chronos and Kairos. While the first stands for the steady flow of time which can be measured quantitatively, the other describes the time felt individually and the time for the right moment.

Also in the literature, time is a reoccurring subject, most of all in modern science fiction. The possibility of time travels is played out in uncountable stories with all of its implications and paradoxes like meeting oneself and influencing the past. The consequences are visualized by the trousers of time: one starts in one leg (present), going up to the waistband (past) and changing the conditions there such that one goes done the other leg leading to a different present. Related to this metaphor is the multiverse theory that "everything happens somewhere", where somewhere might mean a hypothetical parallel universe.

From a physical point of view, the flow of time in only one direction (future) has been coined as the arrow of time by Arthur Eddington [2]. With the formulation of the laws of thermodynamic in the 19th century at the latest, the arrow of time was considered in modern physics, e.g. by Boltzmann [3] and Loschmidt [4]. The important corresponding thermodynamic theorem is the second, which says that the entropy of a closed system increases over time. Although the arrow of time poses some fundamental questions ("Why is there an arrow of time; that is, why is the future so much different from the past?" [5]), the entropy seems to be the classical observable by which one can tell the chronological order. As an easy example, think of two photos of a flower vase: in one picture, it is intact, in the other one, hundreds of shards are visible. Which photo has been taken before the other one? In other words, which picture shows the higher ordering of the involved particles?

There have been many gedankenexperiments trying to violate the second law of thermodynamics often involving some kinds of demons [6]. A famous example is

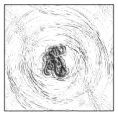

the Maxwell demon, which sits on a gate between two closed boxes filled with air of the same temperature allows the passage of particles from left to right only if their kinetic energy is below average and from right to left if above average. Another less famous demon, which is more closely related to our work, is the Loschmidt demon. Consider two adjacent boxes, one filled with air, the other one with vacuum. Upon connecting the two boxes, the air particles will flow out of the filled box and distribute uniformly in the enlarged volume. This state has a higher entropy, since there are again more micro states for the uniform distribution in the larger box than in the smaller one. Now, the demon comes into play. By perfectly inverting the motion ($\mathbf{v} \to -\mathbf{v}$) of any gas particle in the system (and considering perfect elastic collisions between particles), every particle would propagate back exactly the time-reversed way, bouncing off of the same particle as it did before the inversion and finally going back to the initial box. Although the boxes are still connected, every particle is now again in the initial volume, which means that the entropy recovers its initial value, thus violating the second law. The problem of the realization of this demon is obviously the difficulty of reversing the motion of all the particles individually. The possibility of an experimental realization is worsened by the fact that the velocity-inversion has to be strictly perfect due to the chaotic behavior of the many-body systems – even if only one particle is not perfectly reverted, but moves let's say in a slightly different direction, all of its prior collisions will not take place the way they did before. Therefore, all the particles it collided with are not going back to their initial position. But equally in the next step, all those particle will not collide with the particles they did before the process. This exponentially growing deviation from perfect time-inversion will lead in the end not to the recovery of the particles in the smaller volume, but again to a uniform distribution in the larger volume.

Despite the non-realizability of the initial Loschmidt demon, time-inversion protocols have been invented for all kinds of systems in the 20th century. Maybe the first and certainly one with the highest applicability is the spin echo developed by Hahn in the 1950's [7]. The echo makes use of the nuclear magnetic resonance (NMR) discovered by Bloch [8, 9] and Purcell [10], for which they were awarded the Nobel prize for physics in 1952. The idea behind the NMR is that magnetic moments, here the nuclear spins, rotate around a static, perpendicular magnetic field of strength B with the Larmor frequency $\omega_L = \gamma B$, where γ is the gyromagnetic ratio. However, due to inelastic interaction with its environment, a nuclear spin will align along the direction of the magnetic field on the time scale T_1 of the order of some 100 ms to a few seconds [11]. An additional radio frequency pulse close to resonance with the Larmor frequency rotates the direction of the spin an arbitrary amount away from its aligned position, e.g. perpendicular to the magnetic field ($\pi/2$-pulse).

In general, not a single nuclear spin is manipulated but a macroscopic ensemble, e.g. all the nuclei of the hydrogen atoms in water molecules. There, the Larmor frequency of the nuclear spins is given by $\omega_L \simeq 42.6\,\mathrm{MHz}\times B[\mathrm{T}]$. After a $\pi/2$-pulse, all spins are perpendicular to the static magnetic field and therefore rotate (in phase). Since rotating magnetic moments emit electromagnetic radiation, this rotation can be measured. However, due to slightly different environments and thus different local magnetic fields of close magnetic moments, every spin rotates with

a slightly different Larmor frequency. The more the rotation of the spins is out of phase, the more the emitted radiation interferes destructively until no signal is measured. The related decay time is called T_2^* and is in general much smaller than T_1.

The spin echo, also called Hahn echo, effectively time-inverts the dephasing process related to T_2^*. Thereto, an additional π-pulse is needed. The spins, which are in a plane perpendicular to the static field, are therefore rotated by 180°, so that they are still in the same plane, but inverted, meaning that the faster rotating spins find themselves "behind" the slower ones, catching up over time, and the ensemble rephases again, which leads to a measurable echo.

This "catching up" process works of course only as long faster rotating spins stay faster, i.e. as long as the environment does not change. In an experiment, this environmental change will happen and its effect can be measured in an exponential decay with the time scale denoted T_2, which cannot be reverted by the spin echo.

For technical application of the spin echo, like non-invasive imaging of biological tissue, all kinds of modifications and extensions are applied, such as making the external magnetic field (and therefore ω_L) position dependent, to get spatially resolved pictures [12, 13], for which Lauterbur and Mansfield got the Nobel prize in medicine in 2003. The technical enhancements are such that although early NMR needed up to an hour for making a single picture, it is nowadays even possible to make real-time videos, i.e. more than 24 pictures per second, that can be watched immediately [14, 15].

Note that in this setup, there are quite some differences to an (effective) time-inversion, e.g. the precession direction of the spins does not change as it would for a time-inversion, but instead the trick is to bring the fast spins behind the slow ones. Nevertheless, since the spins rephase and therefore the emitted signal can be measured as an echo, it seems as if the time has been inverted. Therefore, the spin echo as an effective time-inversion protocol can be seen as the first time mirror protocol for a macroscopic, classical ensemble of individual quantum system, however for a discrete Hilbert space (spin 1/2).

Our goal is a time mirror protocol for the wave function of a quantum system, e.g. an electron in a solid, thus for a continuous Hilbert space. Therefore, let us consider what is known of time-reversal mirrors for classical systems with continuous degrees of freedom, i.e. classical waves, and whether the techniques are transferable to quantum wave functions.

Since the late 20th century, time-reversal mirrors have been of practical importance in many fields like medicine, telecommunication, material analysis, and generally in wave control [16–19]. They have been realized with all kind of classical waves like sound [20,21], elastic [16], electromagnetic [22] and recently water waves [23,24]. The basic concept is the following. An initially localized wave propagates through some locally confined random medium in which it is scattered. Outside of the scattering region, an array of receiver-emitter antennas measures and records the incident wave amplitude as function of time at many positions. After some time the signal is rebroadcast from each position, however in time-inverted manner, i.e. which came in last is emitted first. Thus, similar to the case of the Loschmidt demon, any scattering process takes place the same way (but backwards), such that the wave

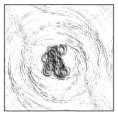

is finally refocused to its initial position, as long as the random medium does not change over time [25–27].

The great advantage compared to the chaotic behavior of the gas particles discussed above, which mainly scattered among each other, is that the scattering process for the wave is not chaotic. The reason for this can be heuristically motivated by the following argument: changing the initial condition of a discrete particle (e.g. a ball) going through a random scattering might lead to missing the first obstacle, for instance, which will lead to a completely different trajectory. An extended wave (or at least parts of it) on the other hand, will always hit the obstacle, such that a slight change of initial conditions only leads to a slight change of the trajectory. Therefore, even if the rebroadcast of the individual emitters is not perfect, an echo of the initial wave is achieved. For visible light, this time-inversion mirror is difficult to implement due to missing controllable antennas [19]. Nevertheless, time-reversed waves can also be generated for monochromatic light, using three- or four-wave mixing [28, 29].

The problem of the measuring-rebroadcasting protocol for a quantum wave function is apparent: a measurement at one position will heavily influence the outcome of all other measurements due to the projection axiom in quantum mechanics. Thus, for the quantum time mirror in a continuous Hilbert space, other methods have to be applied. An alternative to control the wave via the spatial boundaries is a manipulation via time boundaries [30–36]. Similar protocols were considered, using time- and space-modulated one-dimensional photonic [37–39] and magnonic crystals [40, 41]. For a specific, one-dimensional propagation, time-reversal protocols have been proposed [42, 43] and realized in a kicked rotor model of atomic matter waves [44], but only in a narrow momentum range.

The new development of the so-called instantaneous time mirror (ITM) [45] has been the initiator of the idea for the proposed quantum time mirror (QTM) protocol in this thesis. In their work, Bacot et al. show the effective time-inversion of the motion of water waves by applying a short disruption to the system, after which each wave peak splits and parts of it propagate back in the opposite direction to the initial position. The sudden modification they use is a short change of the gravitational potential by accelerating the bottom of the box filled with water, which generates effective source terms in the wave equation, called "Cauchy sources", which define new initial conditions that lead to a partial reversion of the waves propagation, in agreement with the Huygens-Fresnel principle. Although the time-inversion is not perfect (actually, the "reflected" wave is proportional to the time-derivative $\partial\phi/\partial t$ instead of ϕ), distinct echoes are not only seen for radially spreading waves generated by a point source, but also for more complicated initial wave structures, like a smiley of the Eiffel tower.

The important feature of the ITM is the fact that no knowledge of the wave structure and thus no measurement is needed at the time of the homogeneous pulse. Therefore, this basic scheme is in principle transferable to quantum systems. However, a direct transfer is not possible because of the very fact that the differential equations governing the time-evolution deviate in the case of water waves and quantum systems. Nevertheless, we want to generate similarly an echo of quantum wave packets by applying a short time-dependent perturbation (e.g. a potential $V(t)$),

which is homogeneous in space. Since no measurement is involved, the system will continue to propagate according to the Schrödinger equation, without being projected to the respective eigenstates of the measured observable. The important point is to make sure that the velocity of parts of the wave packet change sign, such that they move back to the initial position.

The thesis is organized as follows.

In **chapter 2**, the basic principles and tools used in the thesis are presented. First, we give a short overview of graphene and derive its low energy band structure, since it is the physical system mainly considered in the thesis. As we are interested in the propagation dynamics, the unusual constant magnitude of the velocity of electrons in graphene is stressed. Moreover, the main numerical tool used to propagate wave packets is briefly presented, which is the time-dependent quantum transport (TQT) library developed by Viktor Krueckl [46].

In **chapter 3**, the first proposed quantum time mirror setup is investigated in graphene, as representative of any two-band system that is effectively described by the massless Dirac equation. The time-dependent potential briefly opens a gap such that the initial eigenstates undergo some kind of Rabi-oscillation and partly end up in the other band which has an opposite propagation direction. Therefore, one could speak of the "population inversion quantum time mirror". The mechanism is verified both analytically and numerically and the effects of shape changing of the wave packet, the behavior for long pulses, as well as its mode of action for more complex wave structures is studied. The chapter ends with a discussion about problems and possibilities for an experimental realizability of this Dirac QTM, as well as an overlook of the areas of research which might profit from the effective time-inversion.

In **chapter 4**, the Dirac QTM discussed in the previous chapter is revisited and investigated for static perturbations to the Dirac Hamiltonian in regard of the question of whether the effective time-inversion is destroyed or unaffected. Therefore, the QTM with specific kinds of perturbations – disorder, electric and magnetic fields – is investigated both, analytically and numerically. Moreover, in a general section, any kind of static perturbation is discussed to be able to anticipate its qualitative action on the QTM. An outlook is given in which the possibility of using time-dependent electromagnetic fields as alternative way to induce the needed transition from one band to the other, is discussed.

In **chapter 5**, the population inversion QTM mechanism is generalized for any effective two-band system, where on the one hand requirements are derived for the effective time-inversion to happen at all, and on the other hand, the quantitative echo strengths are derived if these requirements are fulfilled. The general, analytical findings are numerically verified in three example band structures, linear bands with different slopes, the gapped Dirac equation, i.e. hyperbolic bands, and parabolic bands with different curvatures.

In **chapter 6**, a different echo mechanism is studied for the nonlinear Schrödinger equation, which describes for instance the propagation of the ground state of a Bose-Einstein condensate (BEC). Here, the nonlinear part is used to effectively accelerate the wave function so that parts of it reverse their direction of motion. Moreover, with the same principle the broadening of the wave function, related to Heisenberg's

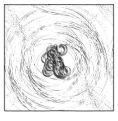

uncertainty principle, can be inverted and the wave function refocuses again. Instead of a time mirror, we denote this refocusing setup by a "time lens" due to its optical analogy. Using the lens pulse over and over again, the broadening of the wave function can be prevented over long times and even approximate solitonic solutions, i.e. waves that don't change their shape, can be achieved.

In **chapter 7**, the zitterbewegung of electrons in graphene is discussed. After an extensive introduction about the well-known decay of zitterbewegung for wave packets in the static case, we explore its behavior in a driving potential with the hope of getting long-time surviving modes. Although this chapter seems to be completely independent of the rest of the work, the relation to the population inversion QTM becomes visible when a mass pulse is used to invert the afore-mentioned decay of the zitterbewegung, leading to an echo, similar to the Hahn-echo. In a disordered setup, we show exemplarily that the echo strength, i.e. the ratio between revived and initial amplitude, behaves similarly to the echo fidelity, which means that it decays exponentially with the elastic scattering time, but unlike the echo fidelity, the zitterbewegung is in principle a measurable quantity. Due to its similarity to the Hahn echo, one could now think of using the well-known techniques, e.g. to get an spatial resolution of the elastic scattering time, and thus disorder strength, in a sample.

In **chapter 8**, the findings of this thesis are summarized and an outlook is given on possible future research directions of the QTM.

Chapter 2
Basic concepts

2.1 Graphene

2.1.1 Low energy Hamiltonian

The first theoretical appearance of graphene was already 65 years ago, when P. Wallace [47] used a two-dimensional, hexagonal lattice of carbon atoms (graphene) as a first approach to graphite, which consists of many such layers that are stacked one above the other and coupled by van der Waals forces. In the following decades, graphene was used as a model system to understand more complicated carbon allotropes, e.g. carbon nanotubes, and it was theoretically investigated due to the surprising analogy to relativistic quantum mechanics for small energies [48–52], although it was predicted that as a strictly two-dimensional structure, it is thermodynamically unstable [53, 54]. Therefore, it was very surprising when in 2004, K. Novoselov and A. Geim [55] were able to produce single layers of graphite: graphene. The unexpected existence of free-standing graphene can be explained by the stabilizing effect of slight crumbling [56]. The discovery was honored 2010 by the Nobel prize for physics and lead to an enormous increase of research interests in the field of graphene, not only because of its high charge carrier mobility and mechanical stability due to the σ-bonding of neighboring atoms.

Although the original method, the mechanical exfoliation from highly ordered pyrolytic graphite, produces high quality graphene flakes, it is not suitable for mass production, as only a few of the exfoliated flakes are single layers which have to be picked out manually. Therefore, other methods have to be deployed like the epitaxial growth on SiC [57, 58] by making use of the effect that by rising temperature, the silicon atoms vaporize first, leaving behind only the carbon atoms which then form a graphene sheet on the surface of the SiC crystal. Another method is the chemical exfoliation, which again obtains graphene out of highly ordered graphite, but instead of pealing off individual layers mechanically, the van der Waals interactions are broken by ultrasonication. The resultant flakes are stabilized by a chemical detergent and can be put on a substrate of choice [59, 60]. Nowadays most promising for applications as electrical devices (e.g. transistors) is ultraclean graphene, i.e. graphene encapsulated in hexagonal Boron-Nitride (hBN), with has among others the advantaged that it is flat, it is relatively free of charge puddles and dangling bonds and it has a very similar lattice constant to graphite, such that almost no

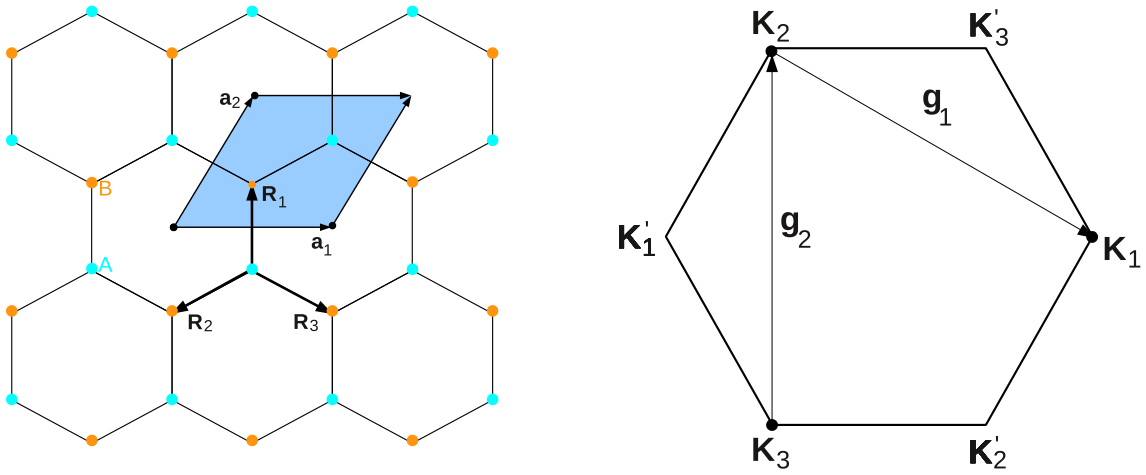

(a) (b)

Figure 2.1: (a) The graphene honeycomb lattice is shown with the lattice vectors $\mathbf{a}_1 = a(1,0)$ and $\mathbf{a}_2 = a(\frac{1}{2}, \frac{\sqrt{3}}{2})$ and the vectors between the nearest C atom neighbors $\mathbf{R}_1 = a_{\mathrm{CC}}\,(0,1)$, $\mathbf{R}_2 = a_{\mathrm{CC}}\left(-\frac{\sqrt{3}}{2}, -\frac{1}{2}\right)$ and $\mathbf{R}_3 = a_{\mathrm{CC}}\left(\frac{\sqrt{3}}{2}, -\frac{1}{2}\right)$. The surface that is marked blue is the unit cell. There are two nonequivalent C atoms in the unit cell called A(blue) and B(orange). Panel (b) illustrates the Brillouin zone in reciprocal space with the reciprocal lattice vectors $\mathbf{g}_1$ and $\mathbf{g}_2$. The corners of the Brillouin zones are the $\mathbf{K}$-points which are connected to each other by reciprocal lattice vectors and the $\mathbf{K}'$-points.

strain is induced [61]. The encapsulation protects the graphene from environmental influences and keeps it clean such that mean free paths of the order of 28μm [62] and more are possible.

In this subsection, we want to derive the low energy Hamiltonian of graphene in the tight-binding approach. There are numerous publications showing this derivation and we will follow notation-wise and conceptually Sasaki and Saito [63].

As already mentioned, graphene is a two-dimensional lattice of carbon atoms which are arranged in a hexagonal structure as shown in Fig. 2.1(a). The primitive translations are given by the two lattice vectors $\mathbf{a}_1 = a(1,0)$ and $\mathbf{a}_2 = a(\frac{1}{2}, \frac{\sqrt{3}}{2})$, where $a = \sqrt{3}a_{\mathrm{CC}} \approx 2.46$Å with $a_{\mathrm{CC}} \approx 1.42$Å being the bond length between the two neighboring carbon atoms. An important fact is that there are two carbon atoms (often called A and B sites) in the unit cell, which leads to several interesting consequences for the electronic structure as discussed below.

The Brillouin zone is a hexagon which is rotated with respect to the real space hexagon by 90°, see Fig. 2.1(b). The reciprocal lattice vectors are $\mathbf{g}_1 = \frac{2\pi}{a}\left(1, -\frac{1}{\sqrt{3}}\right)$ and $\mathbf{g}_2 = \frac{2\pi}{a}\left(0, \frac{2}{\sqrt{3}}\right)$. The adjacent corners of the Brillouin zone (the $\mathbf{K}$-points) are not equivalent as they are not separated by the reciprocal lattice vector. Thus there are two triplets of equivalent $\mathbf{K}$-points: $\mathbf{K}_1 = \frac{2\pi}{a}\left(\frac{2}{3}, 0\right)$, $\mathbf{K}_2 = \frac{2\pi}{a}\left(-\frac{1}{3}, \frac{1}{\sqrt{3}}\right)$ and $\mathbf{K}_3 = \frac{2\pi}{a}\left(-\frac{1}{3}, -\frac{1}{\sqrt{3}}\right)$, connected to each other by reciprocal lattice vectors and $\mathbf{K}'_1 = -\frac{2\pi}{a}\left(\frac{2}{3}, 0\right)$, $\mathbf{K}'_2 = -\frac{2\pi}{a}\left(-\frac{1}{3}, \frac{1}{\sqrt{3}}\right)$ and $\mathbf{K}'_3 = -\frac{2\pi}{a}\left(-\frac{1}{3}, -\frac{1}{\sqrt{3}}\right)$, which are also equivalent to each other. The time-reversal transformation converts $\mathbf{K}$ into $\mathbf{K}'$ and

vice versa.

Most important for electronic properties of graphene is its band structure near the $\mathbf{K}^{(\prime)}$-point. In the tight-binding model, we consider the electrons to be strongly bound to the atoms, such that only the nearest-neighbor hopping is essential and therefore, the Hamiltonian is given by [63]

$$H_0 = -\gamma_0 \sum_{i\in \mathrm{A}} \sum_{a=1,2,3} \left(\left(c_{i+a}^B\right)^\dagger c_i^A + \left(c_i^A\right)^\dagger c_{i+a}^B \right). \tag{2.1}$$

This Hamiltonian describes the hopping from an A atom to a B atom and vice versa. The operator c_i^A is the annihilation operator of an electron at the A atom at point $\mathbf{r}_i$ and accordingly, $\left(c_i^A\right)^\dagger$ is the creation operator. Analogously, c_{i+a}^B and $\left(c_{i+a}^B\right)^\dagger$ create or annihilate electrons at B atoms at $\mathbf{r}_{i+a} = \mathbf{r}_i + \mathbf{R}_a$. The index i runs over all A atoms of the lattice and $\gamma_0 \approx 2.7\,\mathrm{eV}$ is the nearest-neighbor hopping integral.

Since there are two atoms in the unit cell, we may choose the basis states as two Bloch sums over sites A and B respectively:

$$|\Psi_A^{\mathbf{k}}\rangle = \frac{1}{\sqrt{N_u}} \sum_{i\in A} e^{i\mathbf{k}\cdot\mathbf{r}_i} \left(c_i^A\right)^\dagger |0\rangle, \tag{2.2}$$

$$|\Psi_B^{\mathbf{k}}\rangle = \frac{1}{\sqrt{N_u}} \sum_{i\in B} e^{i\mathbf{k}\cdot\mathbf{r}_i} \left(c_i^B\right)^\dagger |0\rangle. \tag{2.3}$$

The normalization factor N_u is the number of hexagonal cells and $|0\rangle$ is the vacuum state.

To derive the Hamiltonian matrix in this basis, we have to calculate the overlaps $\langle\Psi_A^{\mathbf{k}}|H_0|\Psi_A^{\mathbf{k}}\rangle$, $\langle\Psi_B^{\mathbf{k}}|H_0|\Psi_A^{\mathbf{k}}\rangle = \langle\Psi_A^{\mathbf{k}}|H_0|\Psi_B^{\mathbf{k}}\rangle^*$ and $\langle\Psi_B^{\mathbf{k}}|H_0|\Psi_B^{\mathbf{k}}\rangle$. Acting with Eq. (2.1) on Eq. (2.2) we obtain

$$\begin{aligned} H_0|\Psi_A^{\mathbf{k}}\rangle &= -\frac{\gamma_0}{\sqrt{N_u}} \sum_{i\in A} \sum_{a=1,2,3} \sum_{j\in A} e^{i\mathbf{k}\cdot\mathbf{r}_j} \left(\left(c_{j+a}^B\right)^\dagger \underbrace{c_i^A \left(c_j^A\right)^\dagger |0\rangle}_{\delta_{ij}} + \underbrace{\left(c_i^A\right)^\dagger c_{i+a}^B \left(c_j^A\right)^\dagger |0\rangle}_{0} \right) \\ &= -\frac{\gamma_0}{\sqrt{N_u}} \sum_{i\in A} \sum_{a=1,2,3} e^{i\mathbf{k}\cdot\mathbf{r}_i} \left(c_{i+a}^B\right)^\dagger |0\rangle. \end{aligned} \tag{2.4}$$

Therefore, the following matrix element becomes

$$\begin{aligned} \langle\Psi_B^{\mathbf{k}}|H_0|\Psi_A^{\mathbf{k}}\rangle &= -\gamma_0 \frac{1}{N_u} \sum_{i\in A} \sum_{a=1,2,3} \sum_{j\in B} e^{i\mathbf{k}\cdot\mathbf{r}_i} e^{-i\mathbf{k}\mathbf{r}_j} \langle 0| \underbrace{c_j^B \left(c_{i+a}^B\right)^\dagger}_{\delta_{j,i+a}} |0\rangle \\ &= -\gamma_0 \sum_{a=1,2,3} e^{-i\mathbf{k}\cdot\mathbf{R}_a}, \end{aligned} \tag{2.5}$$

where we use in the last step that $e^{i\mathbf{k}\cdot\mathbf{r}_i} e^{-i\mathbf{k}\cdot\mathbf{r}_{i+a}} = e^{-i\mathbf{k}\cdot\mathbf{R}_a}$. The sum $\sum_{i\in A} 1 = N_u$ cancels with $1/N_u$. Furthermore, as $\langle\Psi_A^{\mathbf{k}}|H_0|\Psi_B^{\mathbf{k}}\rangle = \left(\langle\Psi_B^{\mathbf{k}}|H_0|\Psi_A^{\mathbf{k}}\rangle\right)^*$, we get

$$\langle\Psi_A^{\mathbf{k}}|H_0|\Psi_B^{\mathbf{k}}\rangle = -\gamma_0 \sum_{a=1,2,3} e^{i\mathbf{k}\cdot\mathbf{R}_a}. \tag{2.6}$$

On the other hand $\langle\Psi_A^{\mathbf{k}}|H_0|\Psi_A^{\mathbf{k}}\rangle = 0$, because of

$$\langle\Psi_A^{\mathbf{k}}|H_0|\Psi_A^{\mathbf{k}}\rangle = -\gamma_0\frac{1}{N_u}\sum_{i\in A}\sum_{a=1,2,3}\sum_{j\in A}e^{-i\mathbf{k}\cdot\mathbf{r}_j}e^{i\mathbf{k}\cdot\mathbf{r}_i}\langle 0|c_j^A\left(c_{i+a}^B\right)^\dagger|0\rangle, \tag{2.7}$$

where c_j^A and $\left(c_{i+a}^B\right)$ commute and $c_j^A|0\rangle = 0$. In the same manner, $\langle\Psi_B^{\mathbf{k}}|H_0|\Psi_B^{\mathbf{k}}\rangle = 0$ and we see that the Hamiltonian has the following form

$$H = -\gamma_0\begin{pmatrix} 0 & \sum\limits_{a=1,2,3}e^{i\mathbf{k}\cdot\mathbf{R}_a} \\ \sum\limits_{a=1,2,3}e^{-i\mathbf{k}\cdot\mathbf{R}_a} & 0 \end{pmatrix}. \tag{2.8}$$

We are interested in the Hamiltonian near the **K**-point. If we insert $\mathbf{K}_1 = \left(\frac{4\pi}{3a}, 0\right)$ (or, equivalently, $\mathbf{K}_2$ or $\mathbf{K}_3$), we find

$$\sum_{a=1,2,3}e^{i\mathbf{K}_1\cdot\mathbf{R}_a} = e^0 + e^{i\frac{4\pi}{3a}\frac{-1}{2}a} + e^{i\frac{4\pi}{3a}\frac{1}{2}a} = 1 + e^{-i\frac{2\pi}{3}} + e^{i\frac{2\pi}{3}} = 0. \tag{2.9}$$

However, if we are not exactly at $\mathbf{K}_1$ but at $\mathbf{K}_1 + \mathbf{k}$ where $\mathbf{k}$ is small compared to $\mathbf{K}_1$, we have to expand the exponential functions and the sum gives

$$\sum_{a=1,2,3}e^{i(\mathbf{K}_1+\mathbf{k})\cdot\mathbf{R}_a} \approx \sum_{a=1,2,3}e^{i\mathbf{K}_1\cdot\mathbf{R}_a}i\mathbf{k}\cdot\mathbf{R}_a + \underbrace{\sum_{a=1,2,3}e^{i\mathbf{K}_1\cdot\mathbf{R}_a}}_{0} \tag{2.10}$$

$$= ik_y a_{\mathrm{CC}} + i(-\frac{1}{2} - i\frac{\sqrt{3}}{2})(-\frac{\sqrt{3}}{2}k_x - \frac{1}{2}k_y)a_{\mathrm{CC}} + i(-\frac{1}{2} + i\frac{\sqrt{3}}{2})(\frac{\sqrt{3}}{2}k_x - \frac{1}{2}k_y)a_{\mathrm{CC}}$$
$$= -\frac{3}{2}a_{\mathrm{CC}}(k_x - ik_y). \tag{2.11}$$

Thus, Eq. (2.8) reduces to

$$H_0^{\mathbf{K}} = \gamma_0\frac{3}{2}a_{\mathrm{CC}}\begin{pmatrix} 0 & k_x - ik_y \\ k_x + ik_y & 0 \end{pmatrix} = \hbar v_F\mathbf{k}\cdot\boldsymbol{\sigma}, \tag{2.12}$$

where $\boldsymbol{\sigma}$ is the vector of Pauli matrices $\boldsymbol{\sigma} = \begin{pmatrix} \sigma_x \\ \sigma_y \end{pmatrix}$ with $\sigma_x = \begin{pmatrix} 0 & 1 \\ 1 & 0 \end{pmatrix}$, $\sigma_y = \begin{pmatrix} 0 & -i \\ i & 0 \end{pmatrix}$ and the Fermi velocity is

$$v_F = \gamma_0\frac{3a_{\mathrm{CC}}}{2\hbar} \approx \frac{c}{300}. \tag{2.13}$$

The matrix structure of the Hamiltonian arises from the two carbon atoms within the unit cell and this additional degree of freedom is called pseudospin.

The same strategy can be applied to the nonequivalent corners $\mathbf{K}'$ and we can see that the appropriate Hamiltonian is related to the Hamiltonian at the **K**-points by the time-reversal. The time-reversal operator is $\widehat{T} = \sigma_x\widehat{C}$, where $\widehat{C}$ is the complex conjugation operator. Thus, from Eq. (2.12) follows

$$H_0^{\mathbf{K}'} = \widehat{T}H_0^{\mathbf{K}}\widehat{T} = \gamma_0\frac{3}{2}a_{\mathrm{CC}}\begin{pmatrix} 0 & -k_x - ik_y \\ -k_x + ik_y & 0 \end{pmatrix} = \hbar v_F\mathbf{k}\cdot\boldsymbol{\sigma}', \tag{2.14}$$

where $\boldsymbol{\sigma}' = \begin{pmatrix} -\sigma_x \\ \sigma_y \end{pmatrix}$.

Combining the Hamiltonian for the two different corners of the Brillouin zone and assuming that they do not interact, we get

$$\mathcal{H} = \hbar v_F \begin{pmatrix} \mathbf{k}\cdot\boldsymbol{\sigma} & 0 \\ 0 & \mathbf{k}\cdot\boldsymbol{\sigma}' \end{pmatrix}, \tag{2.15}$$

which is Hamiltonian that describes massless, relativistic fermions. The only change is that these particle have in graphene a much smaller velocity v_F instead of the speed of light c, which is the parameter in the original Dirac-Weyl Hamiltonian.

The two decoupled corners of the Brillouin zone lead to independent parts of the Hamiltonian in Eq. (2.15), which are the same except for an overall sign and complex conjugation, thus the physics is the same for both corners. Therefore, in the rest of the thesis, we will only consider the **K**-points:

$$H = \hbar v_F \mathbf{k}\cdot\boldsymbol{\sigma}. \tag{2.16}$$

In this thesis, the degeneracy which comes in general from the **K**′-points is not important for the echoes and therefore omitted. The same holds for the spin degeneracy of the spin-independent Hamiltonian.

The eigenenergies of Eq. (2.12) can be found by diagonalization

$$E_\pm(\mathbf{k}) = \pm\hbar v_F \left|\mathbf{k}\right|, \tag{2.17}$$

and the corresponding eigenstates are in the basis of Eqs. (2.2) and (2.3)

$$\langle \mathbf{k} \mid \varphi_{\mathbf{k},s}\rangle = \frac{1}{\sqrt{2}} \begin{pmatrix} 1 \\ s e^{i\gamma_\mathbf{k}} \end{pmatrix}, \tag{2.18}$$

where $\gamma_\mathbf{k} = \arctan\frac{k_y}{k_x}$ is the polar angle in **k**-space. There is no gap between the conduction and the valence band which touch each other in the $\mathbf{K}^{(\prime)}$-point (which is at $\mathbf{k}$=0). Furthermore, as the dispersion relation is linear, the band structure close to the $\mathbf{K}^{(\prime)}$-point looks like a cone.

Graphene has very interesting effects because of this linear energy dispersion of the electrons near the corners of the Brillouin zone and its subsequent analogy to relativistic quantum mechanics [47, 50, 64, 65]. A special feature is for instance the Klein paradox [66, 67], which states that under certain circumstances, e.g. vertical incidence, particles can tunnel through a barrier with probability 1, thus always passing as if there was no barrier at all. Another effect is the anomalous integer quantum Hall effect that is in graphene observable at room temperature [68–70], where a strong magnetic field is applied perpendicular to the graphene sheet.

For our purposes, the linear band structure is interesting due to its implied constant speed, similar to photons. Since we want get an echo of electron wave packets with the quantum time mirror, we have to invert their motion and inverting their motion means changing their velocity. A normal mirror for light – let us call it space mirror – is a discontinuity in space, which is why the momentum changes sign and the velocity is inversed. In the case of the time mirror, we want to use accordingly a discontinuity in time, i.e. a time-dependent term in the Hamiltonian,

which changes the sign of the energy of the wave packet. Since the slope of negative energy branch in the band structure has the negative slope of the positive branch, which is due to the sub-lattice or chiral symmetry ($E_-(\mathbf{k}) = -E_+(\mathbf{k})$), also the velocity changes sign and the wave packet is supposed to come back.

2.1.2 Graphene in a magnetic field

In this subsection, we want to see what happens with graphene in a homogeneous magnetic field [50]. Here, we follow the review article by Goerbig [71].

Since we are not interested in the spin, we neglect the Zeeman term related to the magnetic field, but only concentrate on the orbital effects. Therefore, we have to substitute the canonical momentum in Eq. (2.16) by the kinetic momentum

$$\mathbf{p} \to \mathbf{\Pi} = \mathbf{p} + e\mathbf{A}(\mathbf{r}), \tag{2.19}$$

with the vector potential $\mathbf{A}(\mathbf{r})$, which yields in symmetric gauge $\mathbf{A}(\mathbf{r}) = \frac{B}{2}(x, -y, 0)$, where B is the magnetic field strength. Since the components of $\mathbf{\Pi}$ do not commute,

$$[\Pi_x, \Pi_y] = -i\hbar eB, \tag{2.20}$$

we can define ladder operators as in the harmonic oscillator

$$\hat{a} = \sqrt{\frac{1}{2\hbar eB}}\left(\Pi_x - i\Pi_y\right), \tag{2.21}$$

$$\hat{a}^\dagger = \sqrt{\frac{1}{2\hbar eB}}\left(\Pi_x + i\Pi_y\right), \tag{2.22}$$

which are chosen such that their commutator is normalized

$$[\hat{a}, \hat{a}^\dagger] = 1. \tag{2.23}$$

The graphene Hamiltonian then becomes

$$H_B = \hbar\omega' \begin{pmatrix} 0 & \hat{a} \\ \hat{a}^\dagger & 0 \end{pmatrix}, \tag{2.24}$$

with $\hbar\omega' = \sqrt{2\hbar eB}v_F$. To solve the eigenvalue equation

$$H_B\psi_n = E_n\psi_n, \tag{2.25}$$

we use the ansatz

$$\psi_n = \begin{pmatrix} u_n \\ v_n \end{pmatrix}, \tag{2.26}$$

which yields the coupled set of equations

$$\hbar\omega' v_F \hat{a} v_n = E_n u_n, \tag{2.27}$$

$$\hbar\omega' v_F \hat{a}^\dagger u_n = E_n v_n. \tag{2.28}$$

Decoupling the two equations by letting act $\hat{a}^\dagger$ on Eq. (2.27) and then inserting Eq. (2.28), we get for the second spinor component

$$\hat{a}^\dagger \hat{a} v_n = \left(\frac{E_n^2}{\hbar\omega'}\right)^2 v_n. \tag{2.29}$$

Therefore, v_n is proportional to the eigenstate $|n\rangle$ of the usual number operator $\hat{n} = \hat{a}^\dagger\hat{a}$, with $\hat{n}|n\rangle = n|n\rangle$, for $n > 0$. Due to the square in Eq. (2.29), the energy E_n has two solutions for a given n and yields

$$E_{n,\pm} = \pm\hbar\omega'\sqrt{n} = \pm\sqrt{2\hbar e B}v_F\sqrt{n}. \tag{2.30}$$

From the coupled Eqs. (2.27) and (2.28), we see that the relations $u_n \sim \hat{a}v_n \sim \hat{a}\,|n\rangle$ and $\hat{a}^\dagger u_n \sim v_n \sim |n\rangle$ imply that $u_n \sim |n-1\rangle$ and the eigenstates become

$$\psi_{n\neq 0,s} = \frac{1}{\sqrt{2}}\begin{pmatrix} |n-1\rangle \\ s\,|n\rangle \end{pmatrix}, \tag{2.31}$$

with $s = \pm 1$. For $n = 0$, there is a special case with $E_0 = 0$ and

$$\psi_{n=0} = \frac{1}{\sqrt{2}}\begin{pmatrix} 0 \\ |n=0\rangle \end{pmatrix}. \tag{2.32}$$

In the same way, the eigenstates can be obtained if there are additional terms in the Dirac Hamiltonian of Eq. (2.24) like a mass term:

$$H_B = \hbar\omega'\begin{pmatrix} 0 & \hat{a} \\ \hat{a}^\dagger & 0 \end{pmatrix} + M\sigma_z. \tag{2.33}$$

In that case, the eigenenergy becomes

$$\varepsilon_{n,\pm} = \pm\sqrt{M^2 + E_n^2}, \tag{2.34}$$

where $E_n = E_n^+$ is the energy of the case without mass gap. The eigenstates are

$$\chi_{n,s} = \frac{1}{\sqrt{2}\sqrt{\varepsilon_n^2 - \varepsilon_n^s M}}\begin{pmatrix} E_n|n-1\rangle \\ (\varepsilon_{n,s} - M)\,|n\rangle \end{pmatrix}. \tag{2.35}$$

2.2 TQT: A library for simulating the time evolution of quantum wave packets

In general, to propagate a quantum state $|\psi\rangle$, one has to solve the differential equation known as Schrödinger equation

$$i\hbar\frac{\partial}{\partial t}|\psi\rangle = \hat{H}|\psi\rangle, \tag{2.36}$$

with the Hamilton operator $\hat{H}$. Formally, it can be solved using the time-evolution operator

$$U(t_0, t) = \mathcal{T}\exp\left(-\frac{i}{\hbar}\int_{t_0}^{t}\hat{H}(t')\,\mathrm{d}t'\right), \tag{2.37}$$

where $\mathcal{T}$ is the time-ordered product, which means for the exponential

$$U(t_0,t) = 1 + \sum_{n=1}^{\infty} \left(\frac{-i}{\hbar}\right)^n \int_{t_0}^{t} \mathrm{d}t_1 \int_{t_0}^{t_1} \mathrm{d}t_2 \cdots \int_{t_0}^{t_{n-1}} \mathrm{d}t_n \; \hat{H}(t_1)\hat{H}(t_2)\cdots\hat{H}(t_n). \tag{2.38}$$

The time-evolution then yields

$$|\psi(t)\rangle = U(t_0,t)|\psi(t_0)\rangle. \tag{2.39}$$

A general property of the time-evolution operator is that a time evolution from t_0 to t is the same as an evolution first from t_0 to t' and then from t' to t, with $t_0 < t' < t$:

$$U(t_0,t) = U(t',t)U(t_0,t'). \tag{2.40}$$

Moreover, for time-independent Hamiltonians, the time-evolution operator simplifies to

$$U(t_0,t) = \exp\left(-i\frac{\hat{H}}{\hbar}\cdot(t-t_0)\right). \tag{2.41}$$

On the other hand, any function can be approximated by step-wise constant functions – the smaller the steps, the better the approximation. Thus, the time-ordered exponential of Eq. (2.37) can be estimated by

$$U(t_0, t_0+N\delta t) \approx \prod_{j=0}^{N-1} \exp\left(-i\frac{\hat{H}(t_0+j\delta t)}{\hbar}\cdot\delta t\right), \tag{2.42}$$

where the Hamiltonian is made step-wise constant for the time duration δt. The advantage is that instead of the nested integrals of Eq. (2.38), a rather easy multiplication can be performed. Of course, one has to make sure that the time step δt is small enough, such that the numerical result is converged.

However, this discrete slicing of the time is not enough. Instead of solving the differential equation in Eq. (2.36) for the time propagation, we have the problem of an operator in an exponential function, which is defined by its (infinite) series expansion. The c++ library "Time-dependent Quantum Transport" (TQT), which is publicly available, has been developed by Viktor Krueckl [46] as part of his PhD project to take care of this expansion as efficient as possible for 1d or 2d systems. The expanded time-evolution operator acts on a numerically defined initial state in real space. Since an sufficiently smooth function can be approximated by its values at discrete points, the space is discretized by a grid, in 2d with $N_x \times N_y$ points. Thus, the wave function becomes a complex valued $(N_x \times N_y)$-matrix, in our case usually 256×256 or 512×512 for 2d systems.

Here, we give a minimal, user-related overview of the TQT library. For more information, e.g. more details about the implementation we redirect to the publicly available PhD thesis of Viktor Krückl [46].

The Hamiltonian can be either given as tight-binding Hamiltonian or as mixed position and momentum space representation, i.e. a function of both, the position and momentum operator, the latter being the Hamiltonian used in most cases for analytical calculations. In the mixed representation, instead of using the spatial

derivative, the momentum operator acts in momentum space, i.e. the wave function is transformed by a fast Fourier transform, then the momentum operator acts as factor, and finally the inverse fast Fourier transformation is applied to get back to position space. The reason for using the Fourier transformation instead of the derivative is the numerical instability of the latter. Since the momentum operator acts several times (in higher orders k_i^n) in each small time step, the errors add up quickly. In this thesis, only the mixed representation of position and momentum operator is used.

Let us come back to the expansion of the operator exponential in the time-evolution operator. The first guess might be to use the standard Taylor expansion around 0, which has the problems of slow convergence for highly oscillating functions like the time evolution operator ($U \sim \mathrm{e}^{-i\omega t}$). Moreover, the error for non-zero arguments in the exponential increases exponentially in the Taylor expansion.

Instead other expansion methods have to be applied, depending on the exact system. For time-independent systems, an expansion in Chebyshev polynomials is better suited due to their faster convergence for oscillating functions [72, 73]. The recursion relation for the Chebyshev polynomials of first kind is

$$T_0(z) = 1, \qquad T_1(z) = z, \qquad T_n(z) = 2zT_{n-1}(z) - T_{n-2}(z), \tag{2.43}$$

and with the scalar product

$$\langle f|g\rangle = \int_{-1}^{1} \frac{f(z)g(z)}{\sqrt{1-z^2}}\,\mathrm{d}z, \tag{2.44}$$

they form an orthogonal basis set in the interval $(-1, 1)$. Not only do the Chebyshev polynomials converge faster, but also the deviation to the exponential with imaginary argument is almost constant in the (arbitrarily scalable) interval $(-1, 1)$. The order of the expansion, i.e. the number of polynomials, is automatically chosen such that the error by expansion are smaller than the numerical accuracy, for a reasonable energy rescaling ΔE, i.e. that all important energies of the physical system are smaller than ΔE such that the expansion effectively takes place in the interval $(-1, 1)$. The advantage for time-independent systems is that the expansion of the Hamiltonian, i.e. the coefficients for the Chebyshev polynomials is the same for all times, such that they have to be calculated only once. On the other hand, the action on the state changes of course with time, since also the state changes with time, which takes the major part of the calculation time.

For time-dependent Hamiltonians, a Lanczos method is used to expand the time-evolution operator [74, 75]. The difference here is that instead of expanding in a fixed set of polynomials, the time-evolution operator is expanded in terms of the wave function ψ itself and powers of the Hamiltonian acting on the wave function $\hat{H}^n\psi$. The thereby spanned subspace is an N-dimensional Krylov subspace $\mathcal{K} = \mathrm{span}\{\psi, \hat{H}\psi, \ldots, \hat{H}^{N-1}\psi\}$, which is orthonormalized to get the basis vectors u_n by a Gram-Schmidt procedure during the recursive creation for better numerical stability:

$$u_0 = \frac{\psi(t_0)}{|\psi(t_0)|}, \tag{2.45}$$

$$u_1 = \frac{\hat{H}u_0 - \alpha_0 u_0}{\beta_0}, \tag{2.46}$$

$$u_{n+1} = \frac{\hat{H}u_n - \alpha_n u_n - \beta_{n-1}u_{n-1}}{\beta_n}, \tag{2.47}$$

with the overlaps $\alpha_n = \langle u_n \mid \hat{H} \mid u_n \rangle$ and $\beta_{n-1} = \langle u_{n-1} \mid \hat{H} \mid u_n \rangle$. Note that u_n is a linear combination of powers of $\hat{H}$ acting on ψ, with highest order n.

The truncated Hamiltonian in this subspace becomes tridiagonal

$$H_{\mathcal{K}} = \begin{pmatrix} \alpha_0 & \beta_0 & 0 & \cdots & 0 \\ \beta_0 & \alpha_1 & \beta_1 & & 0 \\ 0 & \beta_1 & \alpha_2 & & 0 \\ \vdots & & & \ddots & \beta_{N-2} \\ 0 & \cdots & 0 & \beta_{N-2} & \alpha_{N-1} \end{pmatrix}, \tag{2.48}$$

which can be diagonalized by conventional algorithms and enables the calculation of approximate eigenvalues of the operator $\hat{H}$ [76]. With the matrix of eigenvectors $\mathbf{T}$ and eigenvalues $\mathbf{E}$ of the Hamiltonian in the reduced Krylov space $H_{\mathcal{K}}$, the time-evolution of one small time step is given by

$$\psi(t+\delta t) = \sum_{n=0}^{N-1} \left[\mathbf{T}^t \exp\left(-\frac{i}{\hbar} \mathbf{E} \delta t \right) \mathbf{T}\ \psi_{\mathcal{K}}(t) \right]_n \cdot u_n. \tag{2.49}$$

The expansion in the Krylov subspace is faster than a Taylor expansion [77] and for the Krylov space, a dimension N in the range 10–40 is usually enough. In this thesis, the Lanczos method is used for time-dependent Hamiltonians. It turned out that the dimension of the Krylov space of $N = 15$ suffices in our cases.

Since the state can now be calculated for any time on our discrete time line, an arbitrary (observable) quantity like expectation values can be obtained as a function of the time for the propagation. Due to storage reasons, only these functions are usually saved instead of the states at any time.

In general, an important application of the TQT library are transport calculations. Although not directly obvious, the propagation of wave packets can be used to obtain the energy-resolved scattering matrix of an arbitrary (but time-independent) scattering region, which can be for instance used to calculate the current in a given setup. However, since we do not calculate transport properties in this thesis, this rather involved theory is not presented here, but we redirect again to Viktor Krückl's PhD thesis [46], where it is thoroughly demonstrated.

As mentioned in the beginning, this section is supposed to give a minimally needed overview of the functionality of TQT. Since it is not the purpose of this thesis to go to the limits of TQT or extend its fundamental functionalities, we abstain from describing unnecessary details of the implementation of the library. Instead, the physics of quantum time mirrors is about to be investigated thoroughly. In that regard, TQT is used as a tool and verification mechanism to reinforce ideas and analytical results, as well as exploring regimes where analytical calculations are not possible. On the other hand, naturally the simulations have initiated ideas leading in new directions, which we studied in turn analytically using approximations understand the most fundamental issues. Therefore, almost any data obtained by simulation using TQT in this thesis is accompanied by analytical calculations, sometimes with as easy as possible approximations, sometimes as exact as possible where in the end only an integral is solved numerically.

Chapter 3
Dirac Quantum Time Mirror

3.1 Echo mechanism and transition amplitude

The linear band structure of graphene in vicinity of its **K**- and **K′**-points is beneficial for the sake of echoes due to two features. One feature is the constant magnitude of the phase velocity v_F and the other even more important one is its chiral symmetry implying negative velocity of the valence band ($E < 0$) as compared to the conduction band ($E > 0$). For this reason, our goal will be to revert the population of the two bands by a pulse. The velocity after the pulse has the same magnitude v_F, but points in the opposite direction as compared to before. Thus a perfect echo of the initial state is achieved – provided perfect population inversion.

The initial Hamiltonian we use is an effective low-energy Hamiltonian around the **K**-point given by the massless Dirac equation in 2d, compare Sec. 2.1.1,

$$H_0 = \hbar v_F \, \mathbf{k} \cdot \boldsymbol{\sigma} = \hbar v_F \begin{pmatrix} 0 & k_x - i k_y \\ k_x + i k_y & 0 \end{pmatrix} \tag{3.1}$$

Note that for graphene, the Pauli matrices σ_i are operators in the pseudospin space. The additional degeneracy of spins is not of importance for the basic principle of the echo and therefore not considered.

Since $\mathbf{k}$ is a good quantum number, the eigenenergies and eigenvectors can be labeled by $\mathbf{k}$ and a band index $s = \pm$:

$$E_{\mathbf{k},s} = s \, \hbar v_F k =: s \, E_k, \tag{3.2}$$

$$\langle \mathbf{k} \mid \varphi_{\mathbf{k},s} \rangle = \frac{1}{\sqrt{2}} \begin{pmatrix} 1 \\ s \, \mathrm{e}^{i\gamma_{\mathbf{k}}} \end{pmatrix}, \tag{3.3}$$

where $k = |\mathbf{k}|$ and $\gamma_{\mathbf{k}}$ is the polar angle in reciprocal space. An important feature is that for every $\mathbf{k}$, the eigenstates $|\varphi_{\mathbf{k},s}\rangle$ are complete in pseudospin space meaning that

$$\sum_s |\varphi_{\mathbf{k},s}\rangle\langle\varphi_{\mathbf{k},s}| = |\mathbf{k}\rangle\langle\mathbf{k}| \, \mathbb{1}_{\mathrm{ps}} \tag{3.4}$$

with $\mathbb{1}_{\mathrm{ps}}$ being the unit operator in pseudospin space.

Since the Hamiltonian in Eq. (3.3) is not only immanent to graphene, other systems whose time propagation is described by the same Hamiltonian can be used for this echo mechanism, like artificial graphene or Dirac plasmons. Moreover, the

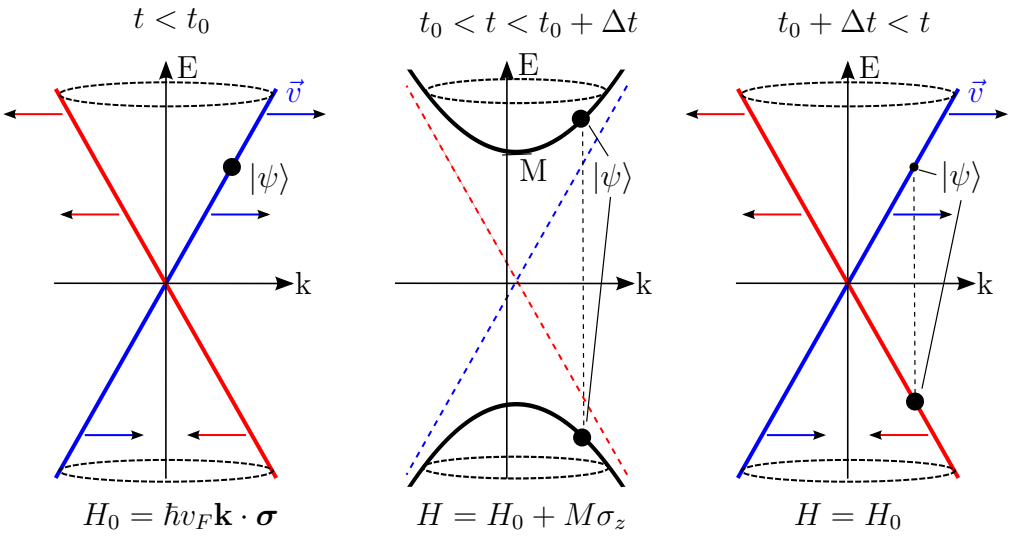

Figure 3.1: Transition mechanism in graphene for an exemplary initial state $|\psi\rangle$, induced by opening a band gap. The band structure before, during and after the pulse is shown. Due to the linear band structure, the magnitude of the group velocity is constant, but the direction is opposite in the blue band and in the red band, indicated by the colored arrows. Before the pulse, the initial state is in the blue band and moves therefore to the right. During the pulse, a band gap opens and the initial state is not in an eigenstate of the Hamiltonian anymore but in a superposition of the two new eigenstates, which oscillate with different frequencies. Depending on the pulse strength M and the pulse duration Δt, the state switches partly to the other band (red branch). Due to the opposite velocity, this part of the state goes after the pulse back to its initial position as an echo.

exact coupling between the (pseudospin) and momentum is not important. The same echo mechanism also works for 3D topological insulator surface states, which can be described by $H_{\mathrm{TI}} = \hbar v_F \mathbf{k} \cdot (\boldsymbol{\sigma} \times \hat{\mathbf{e}}_z)$ [78], whose band structure is also linear. The only difference is the pseudospin orientation of the energy-eigenstates, which is not relevant, since a unitary rotation of the spin-space maps one Hamiltonian in the other. Nevertheless, to avoid confusion, we will consider only graphene henceforth, but all results also apply to the afore mentioned systems.

Again, to stress the main mechanism of our proposed quantum time mirror (QTM), the echo is achieved by inverting the energy, but keeping the momentum $\mathbf{k}$ fixed, as can be seen in Fig. 3.1. In consequence, the direction of the velocity of every mode is also inverted ($\mathbf{v} \to -\mathbf{v}$) due to the peculiar band structure.

The transition is induced by a time-dependent Hamiltonian $H_1(t)$, which is chosen to be nonzero only for $t_0 < t < t_0 + \Delta t$ where t_0 is the time of the pulse and Δt is the pulse duration. The full Hamiltonian during the pulse is $H(t) = H_0 + H_1(t)$ and the time evolution operator U becomes

$$U(t_0, t_0 + \Delta t) = \mathcal{T} \exp\left(-i/\hbar \int_{t_0}^{t_0+\Delta t} H(t)\, \mathrm{d}t\right), \tag{3.5}$$

with $\mathcal{T}$ denoting the time-ordered product, resp. the time-ordered exponential. For

simplicity, we choose

$$H_1(t) = \begin{cases} \hat{M}, & t_0 < t < t_0 + \Delta t, \\ 0, & \text{otherwise}, \end{cases} \tag{3.6}$$

meaning that the pulse is switched on and off abruptly to a constant potential $\hat{M}$, which is homogeneous in space. This simplifies the time evolution operator during the pulse, getting rid of the time ordered exponential

$$U(t_0, t_0 + \Delta t) = \exp\left(-\frac{i}{\hbar}(H_0 + \hat{M})\Delta t\right). \tag{3.7}$$

Note that the restriction of abrupt switching of the pulse is not a necessary condition for the echo. Qualitatively the same results for other pulse shapes, as long as it is fast enough (diabatic) compared to the other energies in the system, e.g. the pulse strength or the energy of the wave packet. Moreover, since $H(t)$ is not space-dependent, $\mathbf{k}$ is still a good quantum number, i.e. the momentum operator $\hbar\hat{\mathbf{k}}$ commutes with H, but energy is not conserved due to the time-dependence.

A perfect occupation inversion of the bands is achieved if $U(t_0, t_0 + \Delta t)$ maps an eigenstate at $\mathbf{k}$ onto the eigenstate with negative energy and the same $\mathbf{k}$:

$$U(t_0, t_0 + \Delta t)\,|\varphi_{\mathbf{k},\pm}\rangle = \alpha\,|\varphi_{\mathbf{k},\mp}\rangle, \quad \alpha \in \mathbb{C},\ |\alpha|^2 = 1. \tag{3.8}$$

Because of this condition, it is reasonable to choose $\tilde{M} = M\sigma_z$. Due to the structure of the eigenstates in Eq. (3.3), we see that σ_z serves the purpose

$$\sigma_z\,|\varphi_{\mathbf{k},\pm}\rangle = |\varphi_{\mathbf{k},\mp}\rangle, \tag{3.9}$$

since σ_z only changes the sign of the second component of the spinor. Physically, $M\sigma_z$ is an effective mass term in the Dirac equation, which opens a gap. The full Hamiltonian reads:

$$H = H_0 + H_1 = \hbar v_F\,\mathbf{k}\cdot\boldsymbol{\sigma} + f(t)M\sigma_z, \quad \text{with } f(t) = \begin{cases} 1, & t_0 < t < t_0 + \Delta t, \\ 0, & \text{otherwise.} \end{cases} \tag{3.10}$$

The eigenvalues and eigenvectors of H during the pulse become

$$\varepsilon_{\mathbf{k},\pm} = \pm\sqrt{M^2 + \hbar^2 v_F^2 k^2} = \pm M\sqrt{1+\kappa^2}, \tag{3.11}$$

$$\begin{aligned} \langle \mathbf{k} \mid \chi_{\mathbf{k},\pm}\rangle &= \frac{1}{\sqrt{(M+\varepsilon_{\mathbf{k},\pm})^2 + \hbar^2 v_F^2 k^2}} \begin{pmatrix} M + \varepsilon_{\mathbf{k},\pm} \\ \hbar v_F k\, \mathrm{e}^{i\gamma_{\mathbf{k}}} \end{pmatrix} \\ &= \frac{1}{\sqrt{2}\sqrt{1+\kappa^2 \pm \sqrt{1+\kappa^2}}} \begin{pmatrix} 1 \pm \sqrt{1+\kappa^2} \\ \kappa\, \mathrm{e}^{i\gamma_{\mathbf{k}}} \end{pmatrix}. \end{aligned} \tag{3.12}$$

Here we introduced the dimensionless quantity

$$\kappa = \frac{\hbar v_F k}{M}, \tag{3.13}$$

which is the ratio between the energy of a mode without perturbation and the gap width and is therefore an inverse, relative measure for the pulse strength.

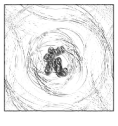

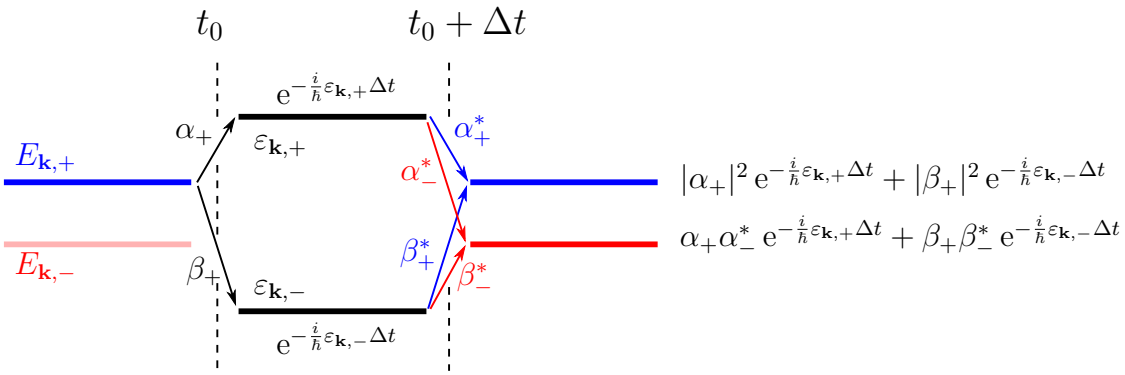

Figure 3.2: Visualizing the derivation of the transition amplitude $A(\mathbf{k})$ of Eq. (3.15), for a single $\mathbf{k}$-mode with initially positive energy. During the pulse it splits into the new eigenstates with the same $\mathbf{k}$, which have energy $\varepsilon_{\mathbf{k},\pm}$. Due to the different energies, these two parts acquire different phases $\mathrm{e}^{-\frac{i}{\hbar}\varepsilon_{\mathbf{k},\pm}\Delta t}$ and when the pulse is switched off at $t = t_0 + \Delta t$, both of them split into the initial eigenenergies again, and the individual terms interfere depending on different phases collected.

A small remark concerning the notation: Here and in the rest of the thesis, the eigenstates of the initial Hamiltonian are called $|\varphi_{\mathbf{k},s}\rangle$, whereas during the pulse, they are denoted by $|\chi_{\mathbf{k},s}\rangle$, independent of whether the initial Hamiltonian is already gapped or not.

Now that we have defined our system, we investigate analytically the time evolution of a wave packet from $t = 0$ to the pulse at $t = t_0$ and then until the (possible) echo. For this, we decompose the initial wave packet into eigenstates of H_0 to simplify the time evolution until the pulse,

$$|\phi\rangle = \sum_{\mathbf{k}} \sum_{s=\pm} \langle\varphi_{\mathbf{k},s}|\phi\rangle\, |\varphi_{\mathbf{k},s}\rangle = \sum_{\mathbf{k}} \sum_{s=\pm} \phi_{\mathbf{k},s} |\varphi_{\mathbf{k},s}\rangle. \tag{3.14}$$

Here we denote $\phi_{\mathbf{k},\pm} = \langle\varphi_{\mathbf{k},s}|\phi\rangle \in \mathbb{C}$, which is the projection of the initial wave packet to the eigenstates of graphene. Since $\mathbf{k}$ is a good quantum number at any point in time, the nontrivial part of the time evolution is only due to the pseudospin terms.

Before investigating the whole time evolution of the process, we consider the action of the time evolution operator *during* the pulse (compare Eq. (3.7)) to an arbitrary wave packet. It is enough to look only at the eigenstates of H_0 because any wave packet is a superposition of $|\varphi_{\mathbf{k},s}\rangle$.

The following derivation is illustrated in Fig. 3.2, where an initial eigenstate splits during the pulse in the two new eigenstates and acquires during the pulse different phases. After the pulse, every new eigenstate splits again and the different "paths" interfere.

$$\begin{aligned} \mathrm{e}^{-\frac{i}{\hbar}H(t_0+\Delta t-t_0)}|\varphi_{\mathbf{k},s}\rangle &= \sum_{s'=\pm} \mathrm{e}^{-\frac{i}{\hbar}H\Delta t}|\chi_{\mathbf{k},s'}\rangle\langle\chi_{\mathbf{k},s'}|\varphi_{\mathbf{k},s}\rangle \\ &= \sum_{s'=\pm} \mathrm{e}^{-\frac{i}{\hbar}\varepsilon_{\mathbf{k},s'}\Delta t}|\chi_{\mathbf{k},s'}\rangle\langle\chi_{\mathbf{k},s'}|\varphi_{\mathbf{k},s}\rangle \end{aligned}$$

$$= \sum_{s',s''=\pm} \mathrm{e}^{-\frac{i}{\hbar}\varepsilon_{\mathbf{k},s'}\Delta t} \langle \varphi_{\mathbf{k},s''}|\chi_{\mathbf{k},s'}\rangle\langle\chi_{\mathbf{k},s'}|\varphi_{\mathbf{k},s}\rangle \, |\varphi_{\mathbf{k},s''}\rangle. \tag{3.15}$$

We inserted the eigenstates of H during the pulse to make the time evolution trivial. Eq. (3.15) corresponds to the terms stated on the right hand side of the picture, with

$$\alpha_\pm = \langle \chi_{\mathbf{k},+} \mid \varphi_{\mathbf{k},\pm}\rangle, \tag{3.16}$$

$$\beta_\pm = \langle \chi_{\mathbf{k},-} \mid \varphi_{\mathbf{k},\pm}\rangle, \tag{3.17}$$

i.e. $\alpha_\pm$ corresponds to the new *positive* energy and $\beta_\pm$ to the new *negative* energy. To calculate the overlaps of the given eigenstates is straight forward but a bit tedious, which is why we moved it to App. A. Inserting the result of the product of overlaps calculated in Eq. (A.3) into Eq. (3.15), we obtain

$$\begin{aligned}
&\mathrm{e}^{-\frac{i}{\hbar}H\Delta t}|\varphi_{\mathbf{k},s}\rangle \\
&= \sum_{s',s''=\pm} \mathrm{e}^{-\frac{i}{\hbar}\varepsilon_{\mathbf{k},s'}\Delta t} \left(\frac{\delta_{ss''}}{2} + s' \cdot \frac{\delta_{ss''}}{2} \cdot \frac{s\kappa}{\sqrt{1+\kappa^2}} + s' \cdot \frac{1-\delta_{ss''}}{2\sqrt{1+\kappa^2}} \right) |\varphi_{\mathbf{k},s''}\rangle \\
&= \left(\cos\left(-\frac{\varepsilon_{\mathbf{k},+}\Delta t}{\hbar}\right) + \frac{is\kappa}{\sqrt{1+\kappa^2}} \sin\left(-\frac{\varepsilon_{\mathbf{k},+}\Delta t}{\hbar}\right)\right) |\varphi_{\mathbf{k},s}\rangle \\
&\quad + \frac{i}{\sqrt{1+\kappa^2}} \sin\left(-\frac{\varepsilon_{\mathbf{k},+}\Delta t}{\hbar}\right) |\varphi_{\mathbf{k},-s}\rangle.
\end{aligned} \tag{3.18}$$

As stated in Eq. (3.9), the population reversal operator is σ_z, therefore we can write

$$\begin{aligned}
\mathrm{e}^{-\frac{i}{\hbar}H\Delta t}|\varphi_{\mathbf{k},s}\rangle &= \left[\left(\cos\left(\frac{\varepsilon_{\mathbf{k},+}\Delta t}{\hbar}\right) - \frac{is\kappa}{\sqrt{1+\kappa^2}} \sin\left(\frac{\varepsilon_{\mathbf{k},+}\Delta t}{\hbar}\right)\right) \mathbb{1} \right. \\
&\quad \left. - \frac{i}{\sqrt{1+\kappa^2}} \sin\left(\frac{\varepsilon_{\mathbf{k},+}\Delta t}{\hbar}\right) \sigma_z \right] |\varphi_{\mathbf{k},s}\rangle \\
&=: \Big[B(k,s)\mathbb{1} + A(k)\sigma_z \Big] |\varphi_{\mathbf{k},s}\rangle.
\end{aligned} \tag{3.19}$$

$A(k)$ is the k-dependent *transition* amplitude from one band to another, whereas $B(k,s)$ is the part of the wave packet which is not changed by the pulse and is therefore lost for the echo. That is why we will often omit the term $B(k,s)$ in the rest of this chapter, in cases where we consider only the echo strength.

In general and for the rest of the thesis, we define the transition amplitude as

$$A(\mathbf{k}) = \langle \varphi_{\mathbf{k},-s} \mid U(t_0, t_0+\Delta t) \mid \varphi_{\mathbf{k},s}\rangle, \tag{3.20}$$

where $|\varphi_{\mathbf{k},s}\rangle$ are in general the eigenstates of the initial Hamiltonian. Since here, the transition amplitude in Eq. (3.19) does not depend on s, the initial band of the wave packet does not affect the echo strength. This means that the echo is the same for a wave packet with positive energy or a wave packet with negative energy or even a wave packet, which is built up from states in both bands. We see that the $\mathbf{k}$-dependent amplitude for the echo yields

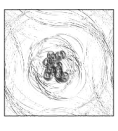

$$
\begin{aligned}
A(k) = \langle\varphi_{\mathbf{k},-s}|\mathrm{e}^{-\frac{i}{\hbar}H\Delta t}|\varphi_{\mathbf{k},s}\rangle &= -\frac{i}{\sqrt{1+\kappa^2}}\sin\left(\frac{\varepsilon_{\mathbf{k},+}\Delta t}{\hbar}\right) \\
&= -\frac{i}{\sqrt{1+\kappa^2}}\sin\left(\frac{M\Delta t}{\hbar}\sqrt{1+\kappa^2}\right) \\
\Rightarrow \quad \boxed{A(k) = -\frac{i}{\sqrt{1+\kappa^2}}\sin\left(\mu\sqrt{1+\kappa^2}\right)}&, \qquad (3.21)
\end{aligned}
$$

where we introduced the dimensionless quantity $\mu = \frac{M\Delta t}{\hbar}$ and $\kappa = E_k/M$ as above. The first thing to notice is that $|A(k)| \leq 1$ and the equality holds only for $\kappa = 0 = k$ and $\mu = \pi(2n+1)/2$ with $n \in \mathbb{N}_0$. Furthermore, for a large transition probability (close to 1), mostly the prefactor matters since by adjusting μ, via the pulse length Δt, the sine can be tuned to yield $\simeq 1$. The prefactor $\sqrt{1+\kappa^2}^{-1}$ becomes larger, the smaller κ, i.e. the condition $M \gg E_k$ is necessary for a good echo.

Now, we calculate the full time evolution of the initial, arbitrary wave packet $|\phi_0\rangle$ from $t = 0$ until the echo at $t_{\text{echo}} = t_0 + \Delta t + t_1$, $t_1 > 0$, when the wave packet arrives at its initial position. We are again only interested in the part of the wave packet which comes back, i.e. only the energy inverted part. Therefore, we calculate the overlap of the time-evolved wave packet $|\phi(t_{\text{echo}})\rangle$ with the energy inverted, initial wave packet $|\phi_0^-\rangle = \sigma_z \mid \phi_0\rangle$:

$$
\begin{aligned}
\langle\phi_0^- \mid \phi(t_{\text{echo}})\rangle &= \langle\phi_0 \mid \sigma_z U(0, t_{\text{echo}}) \mid \phi_0\rangle \\
&= \sum_{\substack{\mathbf{k}, \\ s=\pm}} \phi^*_{\mathbf{k},s}\phi_{\mathbf{k},s}\langle\varphi_{\mathbf{k},s} \mid \sigma_z(0, t_{\text{echo}}) \mid \varphi_{\mathbf{k},s}\rangle \\
&= \sum_{\substack{\mathbf{k}, \\ s=\pm}} |\phi_{\mathbf{k},s}|^2\langle\varphi_{\mathbf{k},s} \mid \sigma_z\mathrm{e}^{-\frac{i}{\hbar}H_0 t_1}\mathrm{e}^{-\frac{i}{\hbar}H\Delta t}\mathrm{e}^{-\frac{i}{\hbar}H_0 t_0} \mid \varphi_{\mathbf{k},s}\rangle \qquad (3.22)
\end{aligned}
$$

Here, the time evolution operator can be split up into stepwise time-independent Hamiltonians using the identity

$$
U(t_A, t_B) = U(t_C, t_B)U(t_A, t_C). \qquad (3.23)
$$

The evolution until the pulse as well as the evolution after the pulse are trivial because $|\varphi_{\mathbf{k},s}\rangle$ is an eigenstate of the acting Hamiltonian H_0.

$$
\langle\phi_0^- \mid \phi(t_{\text{echo}})\rangle = \sum_{\substack{\mathbf{k} \\ s=\pm}} |\phi_{\mathbf{k},s}|^2\mathrm{e}^{-\frac{i}{\hbar}(E_{\mathbf{k},-s}t_1 + E_{\mathbf{k},s}t_0)}\langle\varphi_{\mathbf{k},s} \mid \sigma_z\mathrm{e}^{-\frac{i}{\hbar}H\Delta t} \mid \varphi_{\mathbf{k},s}\rangle \qquad (3.24)
$$

Indeed, the two phases before and after pulse cancel if $t_1 = t_0$, i.e. that $t_{\text{echo}} = 2t_0 + \Delta t \simeq 2t_0$ for every eigenstate, because $E_{\mathbf{k},s} = -E_{\mathbf{k},-s}$. The last term, i.e. the overlap in Eq. (3.24) is just the transition amplitude, which is why the overlap of the flipped initial wave packet and time evolved wave packet at the echo becomes

$$
\langle\phi_0^- \mid \phi(t_{\text{echo}})\rangle = \sum_{\substack{\mathbf{k} \\ s=\pm}} A(k)\,|\phi_{\mathbf{k},s}|^2. \qquad (3.25)
$$

More conveniently, we want to know the part of $|\phi(t_{\text{echo}})\rangle$ which has traveled back to the initial position, which we call $|\phi_{\text{echo}}\rangle$. Therefore, for every eigenstate $|\varphi_{\mathbf{k},s}\rangle$, we have to subtract the part $B(k,s)\mathbb{1}$ in echo Eq. (3.19) for every initial eigenstate, which is not reflected:

$$|\phi_{\text{echo}}\rangle = |\phi(t_{\text{echo}})\rangle - \sum_{\substack{\mathbf{k}\\ s=\pm}} B(k,s)\,\phi_{\mathbf{k},s}\,|\varphi_{\mathbf{k},s}\rangle = \sum_{\substack{\mathbf{k}\\ s=\pm}} A(k)\,\phi_{\mathbf{k},s}\,|\varphi_{\mathbf{k},s}\rangle, \tag{3.26}$$

or in reciprocal space:

$$\begin{aligned}\langle \mathbf{k} \mid \phi_{\text{echo}}\rangle &= \sum_{\substack{\mathbf{k}'\\ s=\pm}} A(k')\,\phi_{\mathbf{k}',s}\,\underbrace{\langle \mathbf{k} \mid \varphi_{\mathbf{k}',s}\rangle}_{\propto\delta_{\mathbf{k}\mathbf{k}'}} = A(k)\sum_s \langle \mathbf{k} \mid \varphi_{\mathbf{k},s}\rangle\langle\varphi_{\mathbf{k},s} \mid \phi_0\rangle \\ &= A(k)\langle \mathbf{k} \mid \phi_0\rangle,\end{aligned} \tag{3.27}$$

where we used the completeness of the eigenstates in pseudospin space (Eq. (3.4)). Thus, in reciprocal space, every single $\mathbf{k}$-mode of the wave packet at the time of the echo is given solely by the initial wave packet multiplied by the transition amplitude. Since we the echo state is given in $\mathbf{k}$-space by Eq. (3.27), this means that also the state in real space and we can also calculate any physical property (expectation values, or measures of the echo strength, etc.) at the time of the echo.

Above, the transition amplitude and its importance for the echo state are derived by performing the time evolution explicitly (brute force), using the eigenstates of the Hamiltonian before, during and after the pulse. In the rest of this subsection, we want to show an alternative and more elegant way of deriving the transition amplitude $A(k)$, by making use of the following identity:

$$\mathrm{e}^{-i\mathbf{n}\cdot\boldsymbol{\sigma}} = \mathbb{1}\cos\left(|\mathbf{n}|\right) - i\frac{\mathbf{n}\cdot\boldsymbol{\sigma}}{|\mathbf{n}|}\sin\left(|\mathbf{n}|\right), \tag{3.28}$$

which follows from the fact that $\sigma_i^2 = \mathbb{1}$ and that the anticommutator of two Pauli matrices yields $\{\sigma_i, \sigma_j\} = 2\delta_{ij}\mathbb{1}$. However, this holds only as long as the components of $\mathbf{n}$ commute which is always the case if they are scalars, but not necessarily if they are operators.

As we have seen above, the propagation except for the pulse is trivial. Therefore, we only consider $t \in [t_0, t_0 + \Delta t]$. Writing $H = H_0 + H_1 = \mathbf{h}\cdot\boldsymbol{\sigma}$, the time evolution operator reads

$$U(t_0, t_0+\Delta t) = \mathrm{e}^{-\frac{i}{\hbar}\mathbf{h}\cdot\boldsymbol{\sigma}\,\Delta t} = \mathbb{1}\cos\left(\frac{|\mathbf{h}|\,\Delta t}{\hbar}\right) - i\frac{\mathbf{h}\cdot\boldsymbol{\sigma}}{|\mathbf{h}|}\sin\left(\frac{|\mathbf{h}|\,\Delta t}{\hbar}\right), \tag{3.29}$$

where, in this example, $\mathbf{h} = (\hbar v_F k_x, \hbar v_F k_y, M)^T$ is in principle an operator for the orbital degree of freedom, but since $\mathbf{k}$ is a good quantum number, the components of $\mathbf{h}$ commute wit each other. Thus, $|\mathbf{h}| = M\sqrt{1+\kappa^2}$ with $\kappa = \hbar v_F k/M$ as above.

The propagation of $|\varphi_{\mathbf{k},s}\rangle$ during the pulse yields

$$\begin{aligned}U(t_0, t_0+\Delta T)|\varphi_{\mathbf{k},s}\rangle &= \left[\cos\left(\frac{|\mathbf{h}|\,\Delta t}{\hbar}\right) - i\frac{\mathbf{h}\cdot\boldsymbol{\sigma}}{|\mathbf{h}|}\sin\left(\frac{|\mathbf{h}|\,\Delta t}{\hbar}\right)\right]|\varphi_{\mathbf{k},s}\rangle \\ &= \left[\cos\left(\frac{M\,\Delta t}{\hbar}\sqrt{1+\kappa^2}\right) - i\frac{H_0+H_1}{|\mathbf{h}|}\sin\left(\frac{M\,\Delta t}{\hbar}\sqrt{1+\kappa^2}\right)\right]|\varphi_{\mathbf{k},s}\rangle\end{aligned}$$

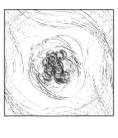

$$= \left[\cos\left(\mu\sqrt{1+\kappa^2}\right) - i\,\frac{s\kappa+\sigma_z}{\sqrt{1+\kappa^2}}\sin\left(\mu\sqrt{1+\kappa^2}\right)\right]|\varphi_{\mathbf{k},s}\rangle, \tag{3.30}$$

which is the same result as in Eq. (3.19). Again, only the terms $\propto \sigma_z$ matter for the echo and the transition amplitude becomes:

$$A(k) = \langle\varphi_{\mathbf{k},-s}|U(t_0, t_0+\Delta t)|\varphi_{\mathbf{k},s}\rangle = \frac{-i}{\sqrt{1+\kappa^2}}\sin\left(\mu\sqrt{1+\kappa^2}\right), \tag{3.31}$$

the same as Eq. (3.21).

This calculation is much shorter, but only valid as long as the components of $\mathbf{h}$ commute, which is the case for spatially homogeneous Hamiltonians. However, later in Chap. 4, when an additional perturbation is applied (e.g. disorder or external fields), this need not be true anymore. For instance for a magnetic field, the canonical momentum is then replaced by the kinetic momentum due to minimal coupling and thus, the components $h_x \propto p_x - eBy$ and $h_y \propto p_y + eBx$ do not commute. Therefore, special care has to be taken in more general systems.

To conclude the section, we want to stress that analytically, the time evolution can be obtained exactly and that we know the echo wave function (see Eq. (3.27)). In the next subsection, we want to see numerically, if our results can be verified, i.e. whether the proposed quantum time mirror setup works in simulation.

3.2 Simulations with Gaussian wave packets

For the numerical simulations, the Time-dependent Quantum Transport (TQT) library is used as described in Sec. 2.2. A wave packet, typically Gaussian, is propagated by H_0 until $t = t_0$, kicked by the time-dependent perturbation $M\sigma_z$ and then it evolves again freely in time (by H_0).

To quantify the echo strength, we use a correlator $\mathcal{C}$ between the initial state $|\phi_0\rangle$ and the state at a later time $|\phi(t)\rangle$ which is related to their (spatial) overlap. However, we can not use the fidelity $\langle\phi_0 \mid \phi(t)\rangle$, which is often to quantify echoes (see e.g. [79]), because the initial state $|\phi_0\rangle$ lives in a different band than the echo part of $|\phi(t)\rangle$ and therefore, they are orthogonal. Moreover, we are not interested in the exact pseudospin structure or some accumulated phases of the wave packet during the evolution, which is why we use in the correlator only the moduli of the spinors,

$$\mathcal{C}(t) = \int \mathrm{d}^2\mathbf{r}\,|\phi_0(\mathbf{r})|\,|\phi(\mathbf{r},t)|. \tag{3.32}$$

Alternatively, one could use the (altered) fidelity $\langle\phi_0 \mid \sigma_z \mid \phi(t)\rangle$, also called "echo fidelity", where we have to compensate for the energy inversion via the included σ_z. Both, the echo fidelity and the correlation in Eq. (3.32), yield qualitatively the same results. However, it is quite unlikely that in an experimental setup the full spinor including phases can be measured. Rather, only the position can be observed which is why we stick to the correlation defined in Eq. (3.32). Nevertheless, the echo fidelity will become important for the theory side when we include disorder in Sec. 4.1, because there, the theory of Loschmidt echoes is directly linked to the fidelity.

As seen in Subsec. 3.1, the reflected part of the wave packet can be calculated analytically (Eq. (3.25)) in reciprocal space. For a general wave packet, this leads to the following *echo strength*, i.e. the correlator at time $t_{\text{echo}} = 2t_0 + \Delta t$,

$$\mathcal{C}(t_{\text{echo}}) = \int \mathrm{d}^2\mathbf{r}\, |\phi_0(\mathbf{r})|\, |\phi(\mathbf{r}, t_{\text{echo}})| = \int \mathrm{d}^2\mathbf{r}\, \Big|\phi_0(\mathbf{r})\Big| \Big| \int \frac{\mathrm{d}^2\mathbf{k}}{2\pi}\, A(k)\phi_0(\mathbf{k}) e^{i\mathbf{k}\cdot\mathbf{r}}\Big|. \tag{3.33}$$

This somewhat inconvenient formula can be simplified, if the transition amplitude $A(k)$ is constant over the range of the wave packet in reciprocal space, e.g. if considering a plane wave. In that case, the transition amplitude can be approximatively taken out of the integral. Using the normalization condition of $|\phi_0\rangle$, the echo strength simplifies to

$$\begin{aligned} \mathcal{C}(t_{\text{echo}}) &= |A(k_0)| \int \mathrm{d}^2\mathbf{r}\, \Big|\phi_0(\mathbf{r})\Big| \Big| \int \frac{\mathrm{d}^2\mathbf{k}}{2\pi}\, \phi_0(\mathbf{k}) e^{i\mathbf{k}\cdot\mathbf{r}}\Big| \\ &= |A(k_0)| \int \mathrm{d}^2\mathbf{r}\, \Big|\phi_0(\mathbf{r})\Big|^2 \\ \Rightarrow \quad \mathcal{C}(t_{\text{echo}}) &= |A(k_0)|. \end{aligned} \tag{3.34}$$

Here the transition amplitude $A(k_0)$ is the same as the echo strength of our simulation.

For wave packets highly peaked around $\mathbf{k}_0$ with modulus $|\mathbf{k}_0| = k_0$, the simplification that $A(k)$ is constant for all $\mathbf{k}$-modes in the wave packet is still approximately valid as shown below. Assuming a Gaussian wave packet with mean wave vector $\mathbf{k}_0$ and width Δk in $\mathbf{k}$-space, a sufficient condition for the approximation used above is $|\Delta k| \ll |\mathbf{k}_0|$ (and μ small enough such that also $\mu|\Delta k| \ll |\mathbf{k}_0|$). Under this assumption, the transition amplitude becomes

$$\begin{aligned} A(k_0 + \Delta k) =& A(k_0) - i\frac{\Delta k}{k_0} \underbrace{\frac{1}{1+\kappa_0^2}}_{\leq 1} \Big(\mu \underbrace{\cos(\mu\sqrt{1+\kappa_0^2})}_{\leq 1} - \underbrace{\frac{1}{\sqrt{1+\kappa_0^2}} \sin(\mu\sqrt{1+\kappa_0^2})}_{\leq 1} \Big) \\ &+ \mathcal{O}(\frac{\Delta k^2}{k_0^2}), \end{aligned} \tag{3.35}$$

where $\kappa_0 = E_{k_0}/M$. The absolute value of the first order term is bounded from above and therefore, the first order correction in Eq. (3.35) is smaller than

$$(\mu + 1)\frac{\Delta k}{k_0} \approx \mu \frac{\Delta k}{k_0}. \tag{3.36}$$

This correction is negligible as long as μ is small compared to the large value $k_0/\Delta k$, and therefore the transition amplitude is fairly well approximated by $A(k_0 + \Delta k) \approx A(k_0)$. Thus, we can approximate the echo strength $\mathcal{C}(t_{\text{echo}})$ for a wave packet that is narrow in $\mathbf{k}$-space and centered around $\mathbf{k}_0$ by

$$\boxed{\mathcal{C}(t_{\text{echo}}) \approx |A(k_0)|}\,. \tag{3.37}$$

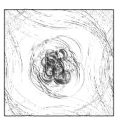

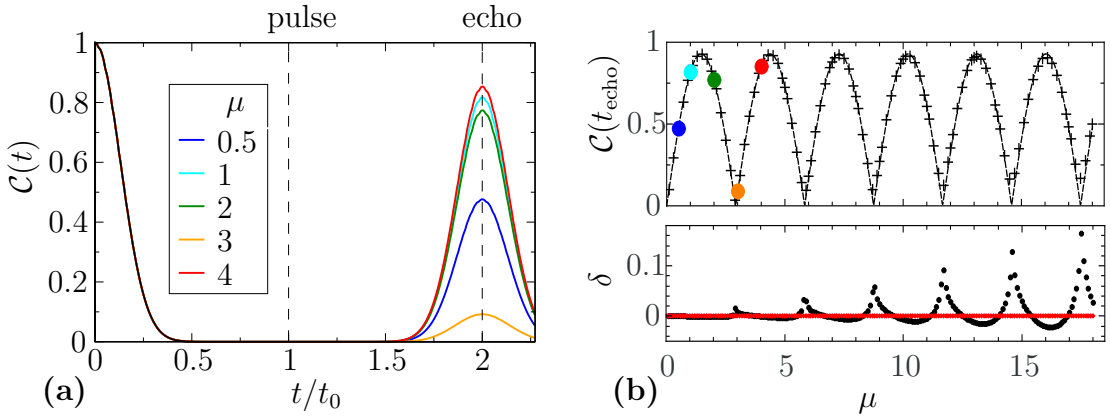

Figure 3.3: Simulation of the time evolution of Gaussian wave packets for typical sets of parameters $\kappa_0 = 0.4$ and varying $\mu = M\Delta t/\hbar$. (a) The correlation of Eq. (3.32) is shown as a function of time for simulations with different values for μ. The echo strength $\mathcal{C}(t_{\text{echo}})$ at $t_{\text{echo}} \simeq 2t_0$ depends strongly and non monotonically on μ. (b) In the upper panel, the echo strength $\mathcal{C}(t_{\text{echo}})$ is shown as a function of μ. The black crosses belong to simulation data, whereas the dashed line is the analytical approximation for plane waves of Eq. (3.37). The colored dots belong to the simulation of panel (a). The lower panel shows the difference δ between analytical calculations and simulation, again as a function of μ. The black dots are the difference for the approximation in Eq. (3.37) and the red diamonds for the exact solution of Eq. (3.33), showing good agreement.

To verify the echo strength of Eq. (3.33) and Eq. (3.37), the propagation of a Gaussian wave packet is simulated. The initial wave packet is

$$\langle \mathbf{r} \mid \phi_0 \rangle = \frac{1}{\sqrt{\pi}\sigma} \exp\left(-\frac{r^2}{2\sigma^2} + i\mathbf{k}_0 \cdot \mathbf{r} \right), \tag{3.38}$$

which yields in reciprocal space

$$\langle \mathbf{k} \mid \phi_0 \rangle = \frac{1}{\sqrt{\pi}\Delta k} \exp\left(-\frac{(\mathbf{k} - \mathbf{k}_0)^2}{2\Delta k^2} \right), \tag{3.39}$$

where the width in $\mathbf{k}$-space is reciprocal to the width in real space, $\Delta k = 1/\sigma$. To make use of the approximation for the echo strength in Eq. (3.37), we choose $\Delta k = 1/8\,|\mathbf{k}_0|$, such that the transition amplitude is nearly constant for the whole wave packet. As we have seen in Eq. (3.21), the transition amplitude only depends on the ratio of the initial energy and pulse strength $\kappa_0 = \hbar v_F k_0/M = E_{k_0}$, which is why the exact values k_0 and M do not matter.

In Fig. 3.3(a), the correlation $\mathcal{C}(t)$ defined in Eq. (3.32) is shown for simulations of the wave packet with fixed $\kappa_0 = 0.4$ and varying μ, i.e. changing the pulse length Δt. Since the initial wave packet is normalized, the correlation at $t = 0$ yields 1. The wave packet then moves away from its initial position which causes the correlation to decline because the overlap in real space decreases between initial wave packet and propagated wave packet. At $t = t_0$, the pulse potential H_1 is switched on for a short time, between $\Delta t \sim 0.002t_0$ and $\Delta t \sim 0.02t_0$, such that μ has the value indicated

in the legend of the plot. Due to the pulse, parts of the wave packet revert their motion (see Subsec. 3.1). The pulse does not affect the correlation immediately, but the echo takes place later at $t_{\text{echo}} = 2t_0 + \Delta t \simeq 2t_0$. The echo strength strongly depends on the value μ, as expected from Eq. (3.37).

In the upper panel of Fig. 3.3(b), the echo strength which is numerically found as the maximum of the correlation after the pulse, $\mathcal{C}_{\max} = \max_{t>t_0} \mathcal{C}(t)$, is plotted as a function of μ, with the same wave packet as before and again for fixed $\kappa_0 = 0.4$. Since the echo happens at the expected time t_{echo}, we find $\mathcal{C}_{\max} = \mathcal{C}(t_{\text{echo}})$ and will use it in the rest of the thesis equivalently. The black crosses are the data points from the simulation and the black dashed line is the approximated echo strength from Eq. (3.37). The colored dots are the simulation data points that correspond to the colored lines in 3.3(a). The results of simulation and analytical approximation match almost perfectly for this wave packet. The deviations of analytics and simulation are shown in the lower panel of Fig. 3.3(b). The black dots are the differences in echo strength between the simulation and the approximation Eq. (3.37). As expected in Eq. (3.36), the discrepancies increases with larger μ.

Furthermore, the deviations between simulation and approximation is the largest when the sine has a root in Eq. (3.21). This is due to the fact that at these points, no echo is expected at all. However, every $\mathbf{k}$-mode in the wave packet that has a different absolute value than k_0 does contribute to the echo. The main difference here, compared to other μ, is that the echo is stronger for both, larger and smaller k. Usually, there are some modes with higher transition amplitude than $\mathbf{k}_0$, but there are (almost) as many modes with a smaller transition amplitude, such that this effect is nearly canceled on average (respectively moved to higher order corrections in $\Delta k/k_0$). Additionally, the slope of the sine is the highest at its roots such that a deviation in the argument close to multiples of π changes the value of sine – and thus of $A(k)$ – the most.

A similar effect is visible at the maxima of $A(k)$. There, the deviation between simulation and approximation has also maxima, because the errors of the estimated echo strength do not cancel. The echo is overestimated since every $\mathbf{k}$-mode except for $\mathbf{k}_0$ has a smaller transition amplitude than expected. However, since the slope is 0 at these points, the deviations of the transition amplitude are not as large as at the roots of the sine.

The red data points in the lower panel of Fig. 3.3(b) show the difference between the exact analytical echo strength in Eq. (3.33) and the same simulations as before. The result of Eq. (3.33) is obtained numerically by a fast Fourier transform of the product of the initial wave packet times the analytical transition amplitude $A(k)$ to real space, and a subsequent numerical integration by a Riemann sum. The results of the simulation and of the expectation match almost perfectly. The deviations are for all examined values of μ smaller than $5 \cdot 10^{-5}$ with a mean absolute value of the difference of only $3.4 \cdot 10^{-7}$, which is probably due to some minor inaccuracies in the numerics.

In Fig. 3.4, the echo strength is plotted as a function of κ_0, in panel (a) for a fixed $\mu = 1.8$ and in (b) for $\mu = 0.5\pi/\sqrt{1+\kappa_0^2}$, such that the sine in $A(k_0)$ (Eq. (3.37)) equals 1. The echo strength strongly depends on $\kappa_0 = \hbar v_F k_0/M$. As expected from Eq. (3.37), it is necessary for a strong echo to open a large gap compared to the

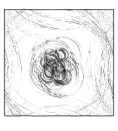

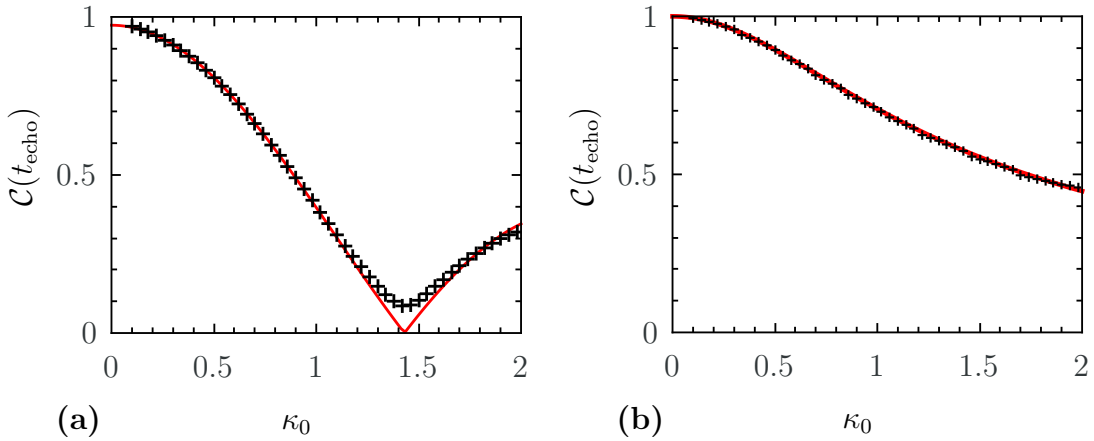

Figure 3.4: Echo strength as a function of κ_0.(a) The simulated echo strength (black crosses) for $\mu = 1.8$ is shown and matches the analytical approximation (red) in Eq. (3.37) very well with the limitations described in the main text. (b) The pulse length Δt is adjusted for every κ_0 such that the sine in Eq. (3.37) becomes 1 and therefore, only the prefactor $1/\sqrt{1+\kappa_0^2}$ (red curve) determines the echo strength. Again, the approximation matches the simulated data (black crosses) very well. The small subtle, step-like structure in the simulation data is due to a limited resolution in the timeline meaning that μ can only have discrete values.

initial energy of the wave packet ($\kappa_0 \ll 1$). In that case, the wave packet during the pulse lives symmetrically on both energy bands, so that the transition after the pulse can occur with a high probability.

For the sake of completeness, the joined dependence of the echo on both, μ and κ_0 is shown in Fig. 3.5(a). Since simulation and approximation are again in very good agreement, only the analytical version is shown because there more data points are available.

Above, we have shown that the QTM protocol works in principle as expected for Gaussian wave packets that are highly peaked in **k**-space. Now, we want to go to more subtle effects, such as deformations of the wave packet in real space and long Δt behavior, as well as what is its effect to more complex wave packets and whether something changes if both bands are occupied.

3.3 Change of the echo wave packet in real space

Due to the fact that in general, the transition amplitude depends on k, different **k**-modes of the wave packet are reflected with different probabilities and thus, the echo wave packet has a different structure in **k**-space compared to the initial one. That means that also in real space, the shape of the wave packet changes, since the real space and reciprocal space wave packet are directly related by a Fourier transform. In the cases where $A(k) \simeq A(k_0)$ for most of the wave packet, i.e. when the approximations for Eq. (3.37) are valid, this is only a very small effect and the shape does not change qualitatively. However, there are cases where these requirements are not met, e.g. if $\mu\sqrt{1+\kappa_0^2} = n\pi$ with $n \in \mathbb{Z}$ or if the wavepacket

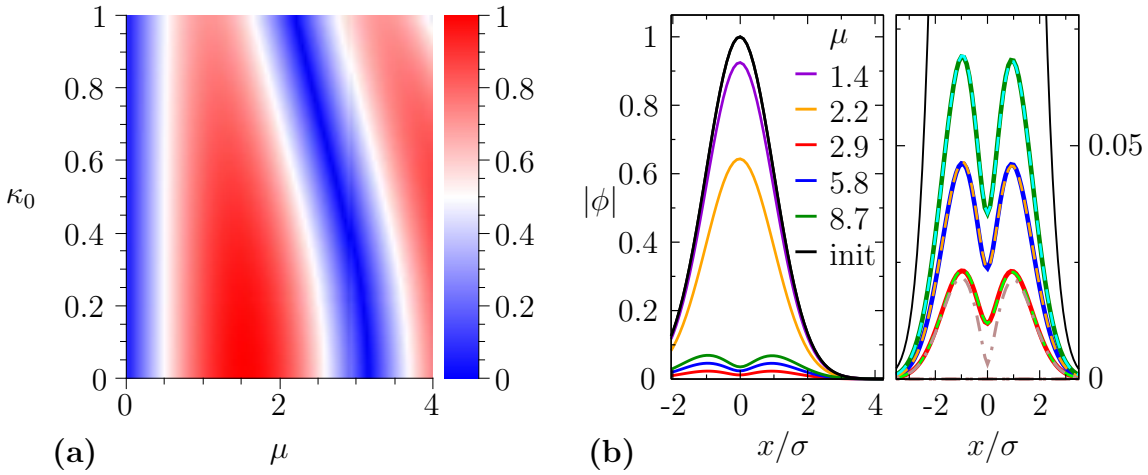

Figure 3.5: (a) The echo strength $\mathcal{C}(t_{\text{echo}})$ is plotted both, as a function of μ and $\kappa_0 = \hbar v_F k_0/M$. Due to the good accordance between the analytical approximation in Eq. (3.37) and the simulations, only the analytical results are shown (see text). (b) Change of the echo wave functions in real space for various μ and $\kappa_0 = 0.4$. Only for roots of the transition amplitude at κ_0, i.e. for μ equals integer multiples of ~ 2.9 the wave packet shape changes qualitatively. On the left hand side, a closeup of the changed wave functions is shown. The dashed curves are the expected shapes with the full transition amplitude, whereas the brown, dotted-dashed line shows the linear approximation in Eq. (3.40) for $\mu = 2.9$. The wave functions are normalized by the amplitude of the initial wave packet.

consists of a wide range of k-modes (e.g. $\Delta k \gtrsim k_0$). Let us consider the case that $\mu\sqrt{1+\kappa_0^2} = n\pi$ and approximate the transition amplitude in linear order of $\tilde{\kappa} = \kappa - \kappa_0$:

$$A(k) = \frac{-i}{\sqrt{1+(\kappa_0+\tilde{\kappa})^2}} \sin\left(\mu\sqrt{1+(\kappa_0+\tilde{\kappa})^2}\right) = (-1)^{n+1}\frac{i\,\tilde{\kappa}\kappa_0}{\sqrt{1+\kappa_0^2}^3} + \mathcal{O}(\tilde{\kappa}^2) \tag{3.40}$$

For a 1d initial Gaussian wave packet ϕ_0, this yields for the echo wave packet

$$\begin{aligned}
|\phi_{\text{echo}}(x)| &= \left|\int \frac{\mathrm{d}k_x}{\sqrt{2\pi}}\, \mathrm{e}^{ik_x x} A(k_x)\phi_0(k_x)\right| \approx \frac{\kappa_0}{\sqrt{1+\kappa_0^2}^3}\left|\int \frac{\mathrm{d}k_x}{\sqrt{2\pi}}\, \mathrm{e}^{ik_x x}\frac{k_x-k_0}{M/(\hbar v_F)}\phi_0(k_x)\right| \\
&= \frac{\hbar v_F\,\kappa_0}{M\sqrt{1+\kappa_0^2}^3}\left|\int \frac{\mathrm{d}\tilde{k}_x}{\sqrt{2\pi}}\, \mathrm{e}^{i\tilde{k}_x x}\,\tilde{k}_x \mathrm{e}^{-\frac{\tilde{k}_x^2}{2\sigma^2}}\right| \\
&= \frac{\hbar v_F\,\kappa_0}{M\sqrt{1+\kappa_0^2}^3}\left|-i\frac{\partial}{\partial x}\int \frac{\mathrm{d}\tilde{k}_x}{\sqrt{2\pi}}\, \mathrm{e}^{i\tilde{k}_x x}\mathrm{e}^{-\frac{\tilde{k}_x^2}{2\sigma^2}}\right| = \frac{\hbar v_F\,\kappa_0}{M\sqrt{1+\kappa_0^2}^3}\left|\frac{\partial}{\partial x}\phi_0(x)\right| \\
&= \frac{\hbar v_F\,\kappa_0}{M\sqrt{1+\kappa_0^2}^3}\frac{x}{\sigma^2}\,|\phi_0(x)| = \frac{\hbar v_F}{M\sigma}\frac{\kappa_0}{\sqrt{1+\kappa_0^2}^3}\left|\frac{x}{\sigma}\phi_0(x)\right| \propto |x|\,\mathrm{e}^{-\frac{x^2}{2\sigma^2}},
\end{aligned} \tag{3.41}$$

which means that the shape of the Gaussian is qualitatively changed by inducing a node at $x = 0$.

In Fig. 3.5(b), the line cuts at $y = 0$ of the echo wave packets in 2D are compared to the initial wave packet for various μ at fixed $\kappa_0 = 0.4$ corresponding to Fig. 3.3(b).

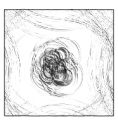

The wave packets are scaled such that the amplitude of the initial wave packet is one. It can be seen that only at the root of the sine in the transition amplitude, i.e $\mu\sqrt{1+\kappa_0^2} = n\pi$ or $\mu \simeq 2.9\,n$, with $n \in \mathbb{N}$, the shape of the wave changes qualitatively. Note that already for $\mu = 2.8$ and also $\mu = 3.0$, the shape resembles again a Gaussian, meaning that the shape-changing features of the QTM are quite limited.

In the right panel of Fig. 3.5(b), a closeup of the left hand side is shown for the wave packets which change their shape. The dashed lines are the analytically expected wave packets given by Fourier transformation of the initial wave packet times the transition amplitude in **k**-space and they match nearly perfectly the simulated (solid lines) wave packets. For the brown dashed line, only the linear approximation of Eq. (3.40) for the transition amplitude is used.

Although there is not a node at $x = 0$ for those wave packets as expected from the 1D linear approximation of Eq. (3.41), the probability of presence is greatly reduced at $x = 0$. There is not a true node, most importantly because $2.9\,n\sqrt{1+0.4^2} = 0.99\,n\pi$. Therefore the expansion of the sine has also a constant contribution which gives an offset of $\simeq 0.03\,n|\phi_0|$, which leads to $|\phi_{\text{echo}}(x=0) \simeq 0.017|\phi_0(x=0)|$. This is in reasonable agreement with the numerical value of $\simeq 0.013|\phi_0(x=0)|$. The deviation of $0.99\,n\pi$ is due to the discretized timeline, in this case by a timestep of $0.1\hbar/M_0$. In principle, we could adjust the timeline to get closer to the root of the sine, but we only wanted to emphasize the shape changing effect on the wave packet in real space by our QTM, which is already clearly visible.

In this subsection, we have seen that in principle, it is possible to change the qualitative shape of the wave function, but in most cases, this is a negligible effect.

In principle one could try to make use of the k-dependence of $A(\mathbf{k})$, e.g. as a **k**-filter as demonstrated above. Possible suggestions would be to manipulate the *echo* wave packet by only reflecting certain k-modes, or to change the *ongoing* wave packet by adjusting its **k**-mode structure using subsequent pulses. However, this task seems to be doomed from the start, since one cannot adjust the transition amplitude for every k-mode separately. Once the two pulse parameters M and Δt (implying μ and κ) are chosen, the transition amplitude is fixed for all modes. Thus, there is probably not enough tunability in the system to get the desired outcome.

3.4 Long pulse durations

Up to now, only rather short pulse durations Δt, resp. $\mu < 20$ (compare Fig. 3.3(b)) have been considered, where the wave packet does not move substantially during the pulse. So, the question arises what happens for much longer Δt?

The intuitively expected picture is quite clear (compare Fig. 3.6): We start with an initial eigenstate, which therefore moves in one direction away from the initial position. During the (very long) pulse, it becomes a superposition of the new eigenstates $|\chi_\pm\rangle$, which have opposed velocities $\mathbf{v}_\pm = \nabla_{\mathbf{k}}\varepsilon_{\pm,\mathbf{k}} = \pm\nabla_{\mathbf{k}}\varepsilon_{+,\mathbf{k}}$. Thus, the two partial wave packets composed positive and negative components will move away from each other. Then, the pulse ends and each partial wave packet splits again, leading to two distinct echoes.

Indeed, this can be seen below in the simulation data of Fig. 3.7(a), where a

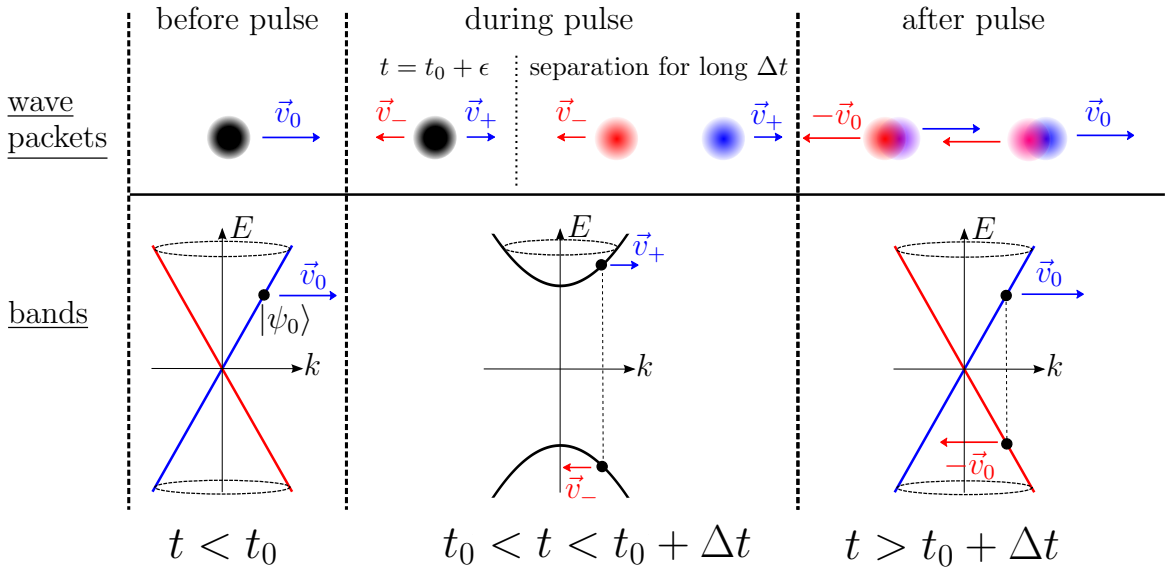

Figure 3.6: Separation of the wave packet for long pulse durations Δt. The upper row shows the wave packet in real space at different times, whereas the lower row depicts the band structure in the according time intervals, which is the Dirac cone before and after the pulse, and a gapped spectrum during the pulse. Initially, the wave packet lives only in the blue branch and moves to the right. During the pulse, it splits into two sub-wave packets which move in opposite directions and, thus, separates for long enough Δt. After the pulse, each sub-wave packet splits again and two distinct echoes will become visible.

Gaussian wave packet with $\kappa_0 = 0.4$ is simulated also for longer pulse durations. As expected already in Sec. 3.1, the echo happens later and later for larger Δt (because there $t_{\text{echo}} = 2t_0 + \Delta t$). The new feature is that for $\mu \gtrsim 90$, the echo peak splits into two distinct peaks due to the separation of the sub-wave packets during the pulse, such there are now two echo times $t^{\pm}_{\text{echo}}$ with additional terms.

Let us consider now more analytically the time evolution to be able to quantitatively predict the echo strength. For that purpose, we want to remind of the translation operator in real space, which will become important in this derivation

$$\exp\left(-i\mathbf{k}\cdot\mathbf{r}_0\right)\psi(\mathbf{r}) = \psi(\mathbf{r}-\mathbf{r}_0), \tag{3.42}$$

due to properties of the Fourier transform. As a side remark, Eq. (3.42) is the reason for a velocity constant of linear band structures ($E_s(\mathbf{k}) = \hbar v_F \mathbf{k}\cdot\mathbf{e}_r$, where the radial unit vector is $\mathbf{e}_r = \mathbf{k}/|\mathbf{k}|$):

$$\langle \mathbf{r} \mid \varphi_{\mathbf{k},s}\rangle \quad \xrightarrow{t>0} \quad \exp\Big(-i\,\mathbf{k}\cdot\underbrace{(\mathbf{e}_r v_F t)}_{\mathbf{r}_0(t)}\Big)\langle \mathbf{r} \mid \varphi_{\mathbf{k},s}\rangle = \langle \mathbf{r} - \mathbf{e}_\mathbf{r} v_F t \mid \varphi_{\mathbf{k},s}\rangle. \tag{3.43}$$

Now, let us consider what happens during and after the pulse with a wave packet peaked around $\mathbf{k}_0$ living initially only in band s

$$\langle \mathbf{k}|\psi_0\rangle = \psi_0(\mathbf{k})\,|\varphi_{\mathbf{k},s}\rangle \tag{3.44}$$

where $\psi_0(\mathbf{k}) \in \mathbb{C}$ gives the shape of the wave function in reciprocal space, e.g. Gaussian.

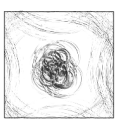

From Subsec. 3.1, Eq. (3.27), we know that the "reflected" part $\langle \mathbf{k}|\psi_{\text{refl}}\rangle$, i.e. the part of the wave packet that changed to the other band, becomes after the pulse at $t = t_0 + \Delta t + t_1$:

$$\langle \mathbf{k}|\psi_{\text{refl}}(t)\rangle = \psi_0(\mathbf{k}) A(k)\, \mathrm{e}^{-\frac{i}{\hbar}\left(E_{\mathbf{k}_0,s} t_0 + E_{\mathbf{k}_0,-s} t_1\right)} \langle \mathbf{k}|\varphi_{\mathbf{k},-s}\rangle, \tag{3.45}$$

where t_1 is the time after the pulse and $A(k)$ is the transition amplitude of Eq. (3.21):

$$A(k) = \frac{-i}{\sqrt{1+\kappa^2}} \sin\left(\frac{M\,\Delta t}{\hbar}\sqrt{1+\kappa^2}\right). \tag{3.46}$$

The movement of the sub-wave packet during the pulse shown in Fig. 3.6 is hidden in the sine of the transition amplitude, which can be expanded to

$$\sin\left(\frac{M\,\Delta t}{\hbar}\sqrt{1+\kappa^2}\right) = \frac{1}{2i}\sum_{l=\pm} l \exp\left(il\frac{M\,\Delta t}{\hbar}\sqrt{1+\kappa^2}\right), \tag{3.47}$$

where the two summands in Eq. (3.47) correspond to the two sub-wave packets living in the two bands. Due to different signs in the exponent, whose terms linear in $\mathbf{k}$ are responsible for translation, the two sub-wave packets move away from each other.

To be able to see the translation according to Eq. (3.42), we linearize the exponent of Eq. (3.47) in k around k_0, where the wave packet is peaked,

$$\sqrt{1+\kappa^2} \approx \sqrt{1+\kappa_0^2} + \frac{\kappa_0}{\sqrt{1+\kappa_0^2}} \frac{\hbar v_F (k-k_0)}{M}, \tag{3.48}$$

with $\kappa_0 = \hbar v_F k_0 / M$. Note that higher-order terms of $(k - k_0)$ lead to distortion and spreading of the wave packet (e.g. in the free Schrödinger case), which lead in general to a decrease of the echo. However for small wave packets in reciprocal space, these effects play a minor role, because they are by definition of higher order in $(k - k_0)$.

With Eq. (3.48), the reflected part of the wave packet from Eq. (3.45) becomes

$$\begin{aligned}\langle \mathbf{k}|\psi_{\text{refl}}(t)\rangle \approx &-\frac{1}{2\sqrt{1+\kappa^2}}\,\psi_0(\mathbf{k})\langle \mathbf{k}|\varphi_{\mathbf{k},-s}\rangle \sum_{l=\pm} l\, \mathrm{e}^{il\frac{M\,\Delta t}{\hbar}\left(\sqrt{1+\kappa_0^2}-\kappa_0^2/\sqrt{1+\kappa_0^2}\right)} \\ &\times \exp\left\{-isv_F k\left(t_0 - t_1 - l\frac{\kappa_0}{\sqrt{1+\kappa_0^2}}\Delta t\right)\right\},\end{aligned} \tag{3.49}$$

where the important part for the translation of the sub-wave packets is the exponent in the last line, which is linear in k. In real space, this term leads to a translation as seen by a Fourier transform:

$$\begin{aligned}\langle \mathbf{r}|\psi_{\text{refl}}(t)\rangle &= \int \frac{\mathrm{d}^2 k}{2\pi} \mathrm{e}^{i\mathbf{k}\cdot\mathbf{r}} \langle \mathbf{k} \mid \psi_{\text{refl}}(t)\rangle \\ &\approx -\frac{1}{2\sqrt{1+\kappa_0^2}}\,\langle \mathbf{k}_0|\varphi_{\mathbf{k}_0,-s}\rangle \sum_{l=\pm} l\, \mathrm{e}^{il\frac{M\,\Delta t}{\hbar}\left(\sqrt{1+\kappa_0^2}-\kappa_0^2/\sqrt{1+\kappa_0^2}\right)} \\ &\quad \times \int \frac{\mathrm{d}^2 k}{2\pi} \mathrm{e}^{i\mathbf{k}\cdot\mathbf{r}} \psi_0(\mathbf{k}) \exp\left\{-isv_F k\left(t_0 - t_1 - l\frac{\kappa_0}{\sqrt{1+\kappa_0^2}}\Delta t\right)\right\}\end{aligned}$$

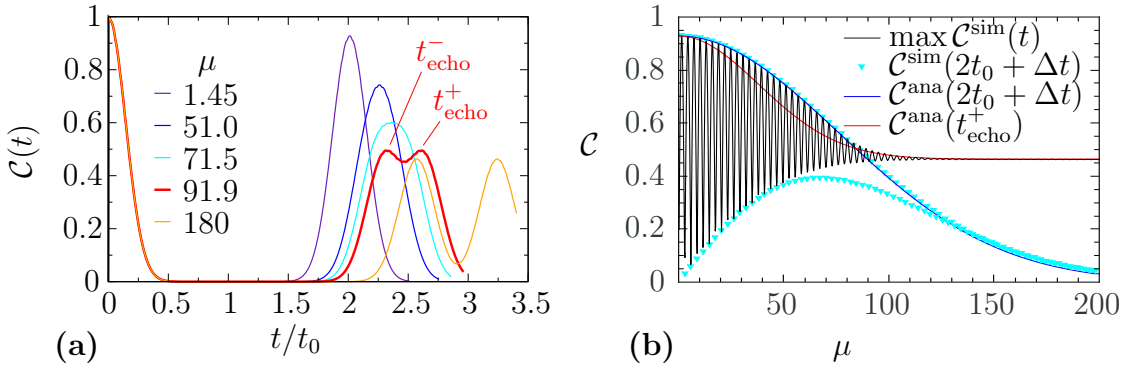

Figure 3.7: The QTM for long pulse durations Δt. (a) The correlations $\mathcal{C}(t)$ is shown for different pulse durations μ, resp. Δt. While for smaller $\mu \lesssim 80$ a single echo peak is visible, the peak splits for larger μ into two echoes at different times $t^{\pm}_{\text{echo}}$, due to the separation of the sub-wave packets during the pulse (see also Fig. 3.6). (b) μ-dependence of the echo strength with different measures. While the black curve shows the maximal values of $\mathcal{C}(t)$ in time obtained by simulation, the other curves show $\mathcal{C}$ at fixed times. The cyan triangles show the local maxima and minima of $\mathcal{C}(2t_0+\Delta t)$, i.e. at the initially expected echo time from Sec. 3.1, and the blue line depicts the according analytical values of Eq. (3.64). The red curve shows $\mathcal{C}(t^+_{\text{echo}})$ from Eq. (3.63), i.e. the correlation at the time when one of the splitted peaks comes back to the initial position, explaining well the saturation for long Δt (see also Eq. (3.57)).

$$= -\frac{1}{2\sqrt{1+\kappa_0^2}} \langle \mathbf{k}_0 | \varphi_{\mathbf{k}_0,-s} \rangle \sum_{l=\pm} l\, \mathrm{e}^{il\frac{M\Delta t}{\hbar}\left(\sqrt{1+\kappa_0^2}-\kappa_0^2/\sqrt{1+\kappa_0^2}\right)} \times \psi_0\left(\mathbf{r} - \mathbf{e}_r s v_F \left[t_0 - t_1 - l\frac{\kappa_0}{\sqrt{1+\kappa_0^2}}\Delta t\right]\right). \tag{3.50}$$

Here, we used in the second step that the initial wave function in reciprocal space is highly peaked at $\mathbf{k}_0$ to get rid of most $\mathbf{k}$-dependent terms in the integral, except for $\psi_0(\mathbf{k})$ and the $\mathbf{k}$-dependent phases. Thus, the modulus of the wave function, which is important for the echo becomes

$$|\langle \mathbf{r}|\psi_{\text{refl}}(t)\rangle| = \frac{1}{2\sqrt{1+\kappa_0^2}} \left| \sum_{l=\pm} l\, \mathrm{e}^{il\mu\left(\sqrt{1+\kappa_0^2}-\kappa_0^2/\sqrt{1+\kappa_0^2}\right)} \psi_0\left(\mathbf{r} - \mathbf{r}_l(t)\right) \right| \tag{3.51}$$

with the translation vector $\mathbf{r}_l(t) = \mathbf{e}_r s v_F \left(t_0 - t_1 - l\frac{\kappa_0}{\sqrt{1+\kappa_0^2}}\Delta t\right)$.

In general, an echo happens when the translation is zero $\mathbf{r}_l(t) = 0$, which means that the wave packet moves back to its initial position for

$$t_1 = t_0 \pm \frac{\kappa_0}{\sqrt{1+\kappa_0^2}}\Delta t, \tag{3.52}$$

corresponding to two (partial) echoes due to the different signs as we see in Fig. 3.7(a) for $\mu \gtrsim 90$.

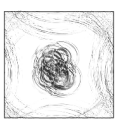

For a quantitative analysis of the echo strength, let us investigate first the limit of such long pulses that the wave packet splits completely,

$$\frac{\kappa_0}{\sqrt{1+\kappa_0^2}}\Delta t \gg \sigma_x, \tag{3.53}$$

since the other limit has been already investigated in Sec. 3.1. Here, σ_x is the real space width of the wave packet. In this limit, the modulus becomes

$$|\langle \mathbf{r}|\psi_{\text{refl}}(t)\rangle| = \frac{1}{2\sqrt{1+\kappa_0^2}} \sum_{l=\pm} |\psi_0\left(\mathbf{r}-\mathbf{r}_l(t)\right)|, \tag{3.54}$$

since there is effectively no overlap of the sub-wave packets for $l = +$ and $l = -$, and thus the mixed terms in the sum over l vanish:

$$\psi_0^*\left(\mathbf{r}-\mathbf{r}_+(t)\right)\psi_0\left(\mathbf{r}-\mathbf{r}_-(t)\right) \approx 0. \tag{3.55}$$

Therefore, the correlation defined in Eq. (3.32) is peaked at the two echo times

$$t_{\text{echo}}^{\pm} = 2t_0 + \Delta t\left(1 \pm \frac{\kappa_0}{\sqrt{1+\kappa_0^2}}\right). \tag{3.56}$$

Since also the initial state effectively overlaps only with (at most) one of the sub-wave packets at a time and because the sub-wave packets did not change their (relative) shape in our approximation, the echo strength yields

$$\begin{aligned} \mathcal{C}(t_{\text{echo}}^{\pm}) &= \int \mathrm{d}^2\mathbf{r}\,|\psi_0(\mathbf{r})|\,|\psi_{\text{refl}}(\mathbf{r}, t_{\text{echo}}^{\pm})| = \frac{1}{2\sqrt{1+\kappa_0^2}}\int \mathrm{d}^2\mathbf{r}\,|\psi_0(\mathbf{r})|^2 \\ \Rightarrow \mathcal{C}(t_{\text{echo}}^{\pm}) &= \frac{1}{2\sqrt{1+\kappa_0^2}}, \end{aligned} \tag{3.57}$$

independent of Δt (as long as its large enough), as verified in Fig. 3.7(b) by simulation. Note that the analysis from Sec. 3.2 to evaluate the correlation strength at $t = 2t_0 + \Delta t$ in Eq. (3.33) is still applicable, but the problem is that the echo does not take place at that time anymore.

Since, we know the echo strength in the cases of small Δt (Sec. 3.2), where the sub-wave packets have not moved at all during the pulse and for very long pulse durations Δt, such that the wave packet do not overlap anymore at all, we now want to get an analytical approximation for the echo strength also in the intermediate Δt-regime.

More precisely, we only want to estimate the envelope function, i.e. local maxima, of the correlation $\mathcal{C}(t)$ as a function of μ for a Gaussian wave packet. Therefore, we use as simplification the estimate $|\sum_i \beta_i| \leq \sum_i |\beta_i|$ for the modulus of the wave function in Eq. (3.51)

$$|\langle \mathbf{r}|\psi_{\text{refl}}(t)\rangle| \leq \frac{1}{2\sqrt{1+\kappa_0^2}} \sum_{l=\pm} |\psi_0\left(\mathbf{r}-\mathbf{r}_0(t)\right)|. \tag{3.58}$$

This estimate corresponds to perfect constructive interference of the two reflected sub-wave packets. In Subsec. 3.1, this is the case for

$$\mu\left(\sqrt{1+\kappa_0^2}-\kappa_0^2/\sqrt{1+\kappa_0^2}\right)\approx\mu\sqrt{1+\kappa_0^2}=\pi/2. \tag{3.59}$$

Indeed, in this case Eq. (3.58) is a good estimate, because then

$$l\,\mathrm{e}^{il\pi/2}=i, \tag{3.60}$$

i.e. it becomes *independent* of $l=\pm$ and the modulus in Eq. (3.51) becomes redundant for a real and positive ψ_0.

Consider now a Gaussian wave packet

$$|\psi_0(\mathbf{r})|=\frac{1}{\sqrt{2\pi}\sigma}\exp\left(-\frac{\mathbf{r}^2}{2\sigma^2}\right), \tag{3.61}$$

such that the correlation defined in Eq. (3.32) can be calculated analytically, because the product of two Gaussians is again a Gaussian. Using

$$\frac{1}{2\pi\sigma^2}\int \mathrm{d}x\,\mathrm{e}^{-\frac{(x-x_1)^2}{2\sigma^2}}\mathrm{e}^{-\frac{(x-x_2)^2}{2\sigma^2}}=\mathrm{e}^{-\frac{(x_1-x_2)^2}{4\sigma^2}}, \tag{3.62}$$

the correlation becomes

$$\mathcal{C}(t)=\frac{1}{2\sqrt{1+\kappa_0^2}}\sum_{l=\pm}\mathrm{e}^{-\frac{\mathbf{r}_l(t)^2}{4\sigma^2}} \tag{3.63}$$

under the assumption of Eq. (3.58), i.e. a perfectly constructive interference of the sub-wave packets. For spatially separated wave packets, i.e. no overlap, Eq. (3.57) is recovered, since the exponential in one summand of Eq. (3.63) becomes 1 ($\mathbf{r}_l=0$), whereas in the other summand, the exponential is very close to 0 ($\mathbf{r}_{-l}\gg\sigma$), thus negligible.

In Fig. 3.7(b), we compare the analytical approximations of this section with simulation data obtained by TQT, where a Gaussian wave packet with mean relative energy $\kappa=0.4$ and $\Delta k=k_0/8=1/\sigma$ is evolved in time. The maximal value of the correlation $\max_t\mathcal{C}(t)$ of each simulation are shown as function of Δt, resp. μ (black). The cyan triangles correspond to $\mathcal{C}(2t_0+\Delta t)$ obtained also by simulation, where μ was chosen such that only local minima and maxima are shown to prevent too crowded figures. Thus the difference between the black and cyan data is that in the prior case, the actual best echo is shown, whereas in the other case (cyan), the correlation at the initially expected (but in general wrong) echo time $t_{\mathrm{echo}}=2t_0+\Delta t$ is plotted, such that it undervalues the actual echo strength more and more, the larger μ.

Furthermore, the blue curve shows the analytically expected (upper) envelope of $\mathcal{C}(2t_0+\Delta t)$ from Eq. (3.63), which reduces to

$$\mathcal{C}(2t_0+\Delta t)=\frac{1}{\sqrt{1+\kappa_0^2}}\exp\left(-\frac{1}{4}\frac{\kappa_0^2}{1+\kappa_0^2}\mu^2\Delta\kappa^2\right), \tag{3.64}$$

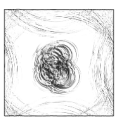

with $\Delta\kappa = \hbar v_F \Delta k/M$. The simulation data for $\mathcal{C}(2t_0 + \Delta t)$ is matched (as well as from semi analytics from Eq. (3.33), although not shown). However the best achievable echo does not happen anymore at that time $t = 2t_0 + \Delta t$ for large enough $\mu \gtrsim 90$, but at $t^{\pm}_{\text{echo}}$ from Eq. (3.56), which is why the actual echo is undervaluated.

Last but not least, the red curve shows the correlation $\mathcal{C}(t^{\pm}_{\text{echo}})$ at the time when one of the sub-wave packets comes back which is given analytically in Eq. (3.57). For small $\mu \lesssim 90$ deviations to the black curve appear, because the wave packet has not splitted far enough, such that the maximal echo still appears at $t = 2t_0 + \Delta t$ due to the overlap of both reflected sub-wave packets. However, the long Δt limit, where the wave packets have separated and the echo strength saturates to $1/2\sqrt{1+\kappa_0^2}$ is recovered.

Experimentally, the main result of this section, which is the saturation of the echo strength for long pulses, might be of interest. Depending on the experimental setup, it might be easier to have rather long pulses (e.g. order of picoseconds) than very short ones (e.g. order of femtoseconds). For long pulses, we have seen that not only the echo is still possible, but also that the exact echo strength becomes independent of Δt (as long as it is large enough). However, there are also two downsides: One is that the echo strength is considerably smaller (factor of 1/2 or even 1/4 for the probability density related to $|\psi|^2$), as compared to the best achievable echoes for small Δt, because no constructive interference of the back propagating modes can happen, which can in principle yield an echo close to 100%. The other downside is the potential spreading and deforming of the wave packet during the pulse, which was neglected here due to $\Delta k/k_0 \ll 1$. Although spreading and deforming, which happens before the pulse is perfectly inverted in the reflected wave packet after the pulse, this is not possible when these distortions happen during the pulse. Nevertheless, in a real setup, one has to ponder the advantages of one or the other possibility, as well as the feasibilities and then decide, which way is better suited.

As a last comment, we note that these results of long pulse durations are in principle applicable also in all other system, below, if not otherwise stated. However, from now on we will only consider pulses short enough such that the wave packet does not move considerably during the pulse in order not to intermix too many different effects.

3.5 Wave packets with more complicated shapes

Above, we always used a Gaussian wave packet to verify the QTM principle. Now, we want to see what happens to more complicated wave packets. To show the power of this method of time-reversal and to see its very good spatial resolution, a complicated $\hbar$-shaped wave packet is propagated (see Fig. 3.8). In momentum space, the distribution of the wave packet is on average isotropic such that the wave packet spreads uniformly in all directions, as can be seen in the second and third panel and the original shape is soon not identifiable anymore.

In the simulation, three pulses are applied subsequently to show that the resolution of the initial wave packet is not affected by several kicks, even though the echo strength decreases with every echo. The pulses take place at $t = t_0$, and the

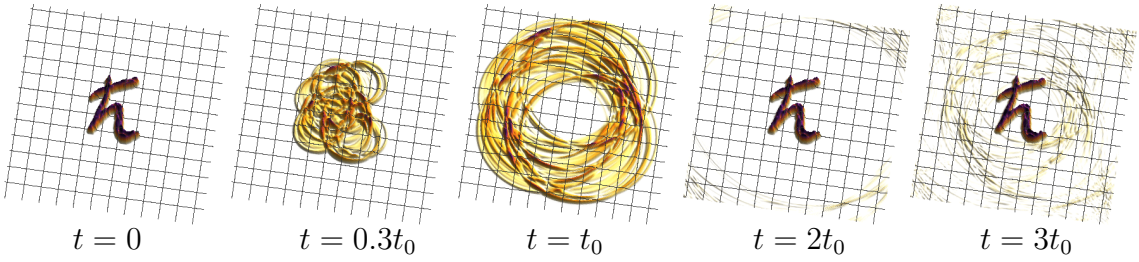

Figure 3.8: Snapshots for the propagation of the $\hbar$-wave packet in real space. Due to the isotropic distribution of $\mathbf{k}$-modes in the wave packet, the initial $\hbar$-shape spreads radially until $t = t_0$, where the first pulse takes place. At this point in time, the spatial overlap compared to the initial wave packet is almost zero. At $t = 2t_0$ and, due to a pulse at $t = 2.5t_0$, also at $t = 3t_0$, the initial structure is recovered with a very high spatial resolution. See also the pictures in the footer, which can be used as a flicker book, to see the full propagation related to the snapshots shown here.

arbitrarily chosen times $t = 2.5t_0$ and $t = 3.125t_0$, such that echo of the previous pulse is not influenced.

As discussed above, a necessary condition for a good echo is that the pulse strength M is strong compared to the initial energy of the wave packet. Here, we chose $M = 8\langle E_k \rangle$, where $\langle E_k \rangle$ is the mean energy of the initial wave packet. Moreover, to get a strong echo, the pulse duration is adjusted to $\mu = M\Delta t/\hbar = \pi/2$ such that the sine in Eq. (3.37) is close to one.

Additionally, the wave packets at the first echo ($t = 2t_0$) and second echo ($t = 3t_0$) are shown in Fig. 3.8. The spatial structure is well conserved, although the echo strength decreases slightly with each new pulse. This can be seen in Fig. 3.9(a), where the black line shows the correlation defined in Eq. (3.32) for the propagation of the $\hbar$-wave packet. The five black dots indicate the time of the snapshots in Fig. 3.8.

One can see that the correlation goes up quite symmetrically after a pulse compared to the decline before. However, since a perfect echo is only possible for $E_k/M = 0$, parts of the wave packet are not reflected and the echo strength is smaller than 1. The two subsequent echoes lose a similar amount of strength, but the spacial resolution stays almost perfectly the same.

The last feature of the QTM discussed in this chapter of the basic properties of the Dirac QTM, is the echo behaviour of a highly random wave packet to show with the help of simulations that the echo mechanism itself is completely independent of the structure of the initial wave packet. The wave packet propagated in TQT is random to the effect that any $\mathbf{k}$-mode up to a maximal absolute value $k_{\max}$ gets a uniformly distributed weight between 0 and 1. Since this is done for both bands independently, the initial wave packet is now also a mixture of the two bands. As we have seen in Eq. (3.21), $A(k)$ does not depend on the band index and we expect this mixture not to be important which is verified in Fig. 3.9(b). There, the theoretical echo strength $\mathcal{C}^{\text{ana}}$ of Eq. (3.21) of the given wave packet is compared to the simulated echo strength $\mathcal{C}^{\text{sim}}$. We use this direct comparison of expected and simulated echo strength because the echo strength depends on the random choice of

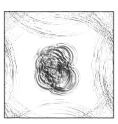

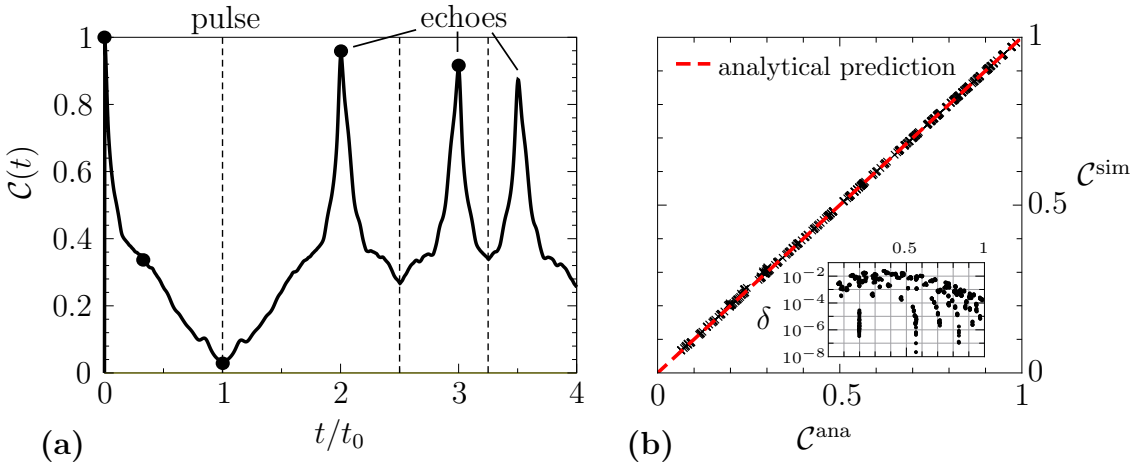

Figure 3.9: QTM for more complex wave packets. (a) The correlation $\mathcal{C}$ for the propagation of a $\hbar$-shaped wave packet is shown as function of time. The three distinct echoes are generated by pulses at $t = t_0$, $t = 2.5t_0$ and $t = 3.25t_0$. The black dots mark the time spots of the snapshots in Fig. 3.8. (b) The simulated echo strength $\mathcal{C}^{\mathrm{sim}}$ for a randomly generated wave packet is plotted against the analytical strength $\mathcal{C}^{\mathrm{ana}}$ predicted by Eq. (3.33). The data is expected to lie on the indicated red diagonal. Indeed, for every randomly generated wave packet, the difference $\delta = |\mathcal{C}^{\mathrm{sim}} - \mathcal{C}^{\mathrm{ana}}|$ shown in the inlet is at most 10^{-2}.

the wave packet. Thus only after choosing the wave packet, the echo strength can be calculated using Eq. (3.21).

We see also in this example of a highly non-smooth wave packet that the analytical calculation of Eq. (3.33) yields the correct result and that also here high echoes can be achieved if the right parameters are used.

3.6 Discussion of the experimental realization and outlook

In this chapter, the basic properties of the QTM have been studied which result from the Dirac Hamiltonian of Eq. (3.1) and a mass pulse described in Eq. (3.6). Due to this new approach to QTMs the according publication [80] aroused some interest in the internet with articles on the two popular-science webpages “ars technica” [81] and “inside science” [82].

In more detail, the investigated features in this chapter are the parameter dependence of the transition amplitude and thus the echo strength, the change of the spatial shape of the reflected amplitude, the behavior for long pulse durations, as well as more complicated (even arbitrary) wave packets. The next chapter will deal with the effects of perturbation, i.e. of changing the Hamiltonian, e.g. by incorporating disorder or switching on external fields.

But before we come to that, we want to discuss the experimental realizability of the proposed population inversion Dirac QTM. Thereto, we first mention again that not only graphene possesses the Dirac cone band structure, but also other system in

which an experimental realization might be easier. A few examples of other Dirac systems are artificial graphene [83] using ultracold atoms that are trapped in a periodic potential generated interfering laser beams, surface states of 3d topological insulators [78], Dirac plasmons in metallic nanoparticle lattices [84] and polaritons in a honeycomb lattice [85].

To start with, let us consider the electron wave packet generation, that will be certainly not "$\hbar$"-shaped, which was only used in this thesis to illustrate the spatial resolution of the echo wave function. Experimentally, there are several ways to inject electron wave packets in graphene, like quantum dots as single electron sources [86] or short voltage ("Leviton") pulses [87], so the generation of the wave packet seems to be no obstacle.

A larger problem for experimental realizations is the used single particle picture. Pristine graphene is half-filled, i.e. the Fermi energy coincides with the intersection point of the Dirac cone, which prevents a switching from positive to negative energies of the considered wave packet since the state it is supposed to transition to is occupied. Moreover, not only the wave packet will be affected by the pulses, but also the whole Fermi sea, leading to additional problems. However, the Fermi energy of graphene can be influenced by a substrate and, more importantly, tuned by external gates. To be as close as possible to the single particle setup described in this thesis, one should use a negative Fermi energy E_F far away from the Dirac cone, such that the Fermi sea is hardly affected by the pulse ($|M| \ll |E_F|$). In that case, a generated wave packet with energy close to the Dirac point will find empty states in the other band it can transition to such that the echo is possible. In a bosonic system like the above mentioned Dirac plasmons, at least the question of empty states is not of importance.

Moreover, the energy relaxation of the wave packet due to inelastic scattering has to be considered, i.e. the propagation has to be faster than the related time scale. Otherwise, the injected and excited state will decay to equilibrium according to the Fermi-Dirac statistics. The dominating mechanism of inelastic scattering is the electron-phonon scattering with an estimated relaxation time in the range of 1 ps in highly doped layers and up to 11 ps in undoped layers [88]. An additional time scale on which the echo decays, which is the elastic scattering time due to static disorder, will be discussed in the next chapter.

Let us come to the heart of the QTM mechanism, the time-inversion pulse, which we assumed to be a mass pulse proportional to σ_z. As discussed above, the used box-shape of the time-dependent pulse is only used for analytical reasons and is not essential. Any other pulse shape might do the trick as long as the time-dependence is fast enough not to be in the adiabatic regime, where no transition will happen.

Although a gap in graphene can be generated in multiple ways, e.g. by substrates like Cu(111) [89] or transition-metal dichalcogenides [90], most of them are not suited for fast switching. However, gaps can be dynamically opened and closed by THz radiation [91–93], and recently even by light fields [94]. Whether or not theses dynamical, fast oscillating, potentials mimic the mass pulses in the desired way is currently under investigation. On the other hand, in topological insulators, gaps can be easily generated by applying magnetic fields.

Finally the detection of the echo probability seems to be achievable, e.g. by using

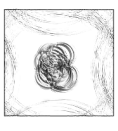

pump-probe spectroscopy combining [95] subcycle terahertz, field-resolved detection (time resolution: $\sim 10\,\mathrm{fs}$) with scattering-type near-field scanning optical microscopy (spatial resolution: $\sim 10\,\mathrm{nm}$).

Having discussed the experimental realizability of the QTM, the justified question arises why the QTM is or could be of interest. From an academical point of view, our proposal serves to solve the long standing question of effectively time-inverting the wave function (orbital degrees of freedom) in a quantum system. Its classical (time-inversion mirror) as well as quantum mechanically discrete (spin echo) analogy, are a overwhelming success with uncountable technical applications, as discussed in the introduction, Chap. 1. Thus, also from the QTM, applications can be anticipated.

A major point of the high fidelity echo is its utility for further basic research. For instance, by applying multiple pulses and thus generating a kind of time-lattice, analogies to effects occurring due to spatial lattices are expected to appear in time. Examples are Bloch oscillations in time or Fabry Pérot in time, where the interference of phase coherent over and over "reflected" and "transmitted" states controlled by the QTM can be investigated.

Another possibility which comes to mind by looking at the snapshots of Fig. 3.8 is cryptography. The idea is still in its infancy but is based on the simple observation that in the aforementioned figure, the information "$\hbar$" is initially visible. During the propagation this information is destroyed for the eye, i.e. the "$\hbar$" cannot be recognized anymore. By using the right "key" (e.g. pulse or Hamiltonian), the initial message becomes visible again. More involved, one could think of an array of Gaussian wave packets, each representing a bit. The wave packets have different mean energies, such that a time-reversal pulse will reflect some wave packets more, some less. The key used to extract the information are the pulse parameters, i.e. its strength M and length Δt, such that only the wave packets intended by the sender yield an echo above a certain threshold, e.g. 50%. The bit pattern of the echo wave function above the threshold then contains the information. Problems for this type of cryptography lie at hand, e.g. how to send (thus copy) the initial quantum system. Nevertheless, better devised cryptography protocols might circumvent these problems.

Furthermore, the QTM can be used to fabricate a discrete quantum walk (in a continuous system) using many time-reversal pulses. Discrete quantum walks can be used in quantum computing (Grover algorithm) [96], e.g. for searching faster through an unsorted database [97,98] than using classical random walks, because in the quantum random walk, the space is transmigrated faster. The discrete walk is possible in the continuous system due to the discrete times of the pulses and echoes, which are directly related. The discrete quantum walk in a continuous system is currently investigated by the Master student Vanessa Junk, who showed that our QTM system is indeed quantitatively the same as the theoretically well-studied truly discrete quantum walks.

Chapter 4

Dirac quantum time mirrors under perturbations

4.1 Disorder

4.1.1 Implementation of the disorder potential

In an experimental setup, the sample will never be perfectly clean. Among others, there might be lattice distortions, vacancies and adatoms. But not only the sample, also the fields generating the pulse will not be perfectly homogeneous. Therefore, we want to test the robustness of the echo mechanism to two kinds of disorder, a spatial disorder and a spatial inhomogeneity of the pulse. Both types of disorder are simulated by a random potential. To make sure that the particular configuration does not play a role, the results are averages of many realizations of the disorder.

In order to generate the random, inhomogeneous disorder potential V_{imp}, every grid point is assigned a normally distributed random number β_i. To avoid a highly fluctuating potential, an average over neighboring points weighted by a Gaussian profile with a range l_0 is taken at each site, which gives

$$V_{\text{imp}}(\mathbf{r}) = \frac{u_0}{\mathcal{N}} \sum_{i=1}^{N} \beta_i \mathrm{e}^{-\frac{(\mathbf{r}-\mathbf{r}_i)^2}{l_0^2}}. \tag{4.1}$$

Here, the sum runs over grid points of count N. u_0 is related to the mean impurity strength and $\mathcal{N}$ is a normalization factor to assimilate different realizations with the same parameters u_0 and l_0,

$$\mathcal{N} = \left[\frac{1}{A} \int_A \mathrm{d}^2 r \left(\sum_{i=1}^{N} \beta_i \mathrm{e}^{-\frac{(\mathbf{r}-\mathbf{r}_i)^2}{l_0^2}} \right)^2 \right]^{\frac{1}{2}}, \tag{4.2}$$

where A is the finite area of the grid. $\mathcal{N}$ can be thought of the mean deviation of the potential strength over the whole area.

Of course, technically, the integral in Eq. (4.2) is actually a sum over all grid points times the area per point $dA = dx \cdot dy$ with dx, dy being the distance of two lattice points. However, this notation is consistent with the rest of this thesis, because in principle, also $V_{\text{imp}}(\mathbf{r})$ or the spinor $\phi(\mathbf{r})$ are known numerically only on a

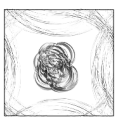

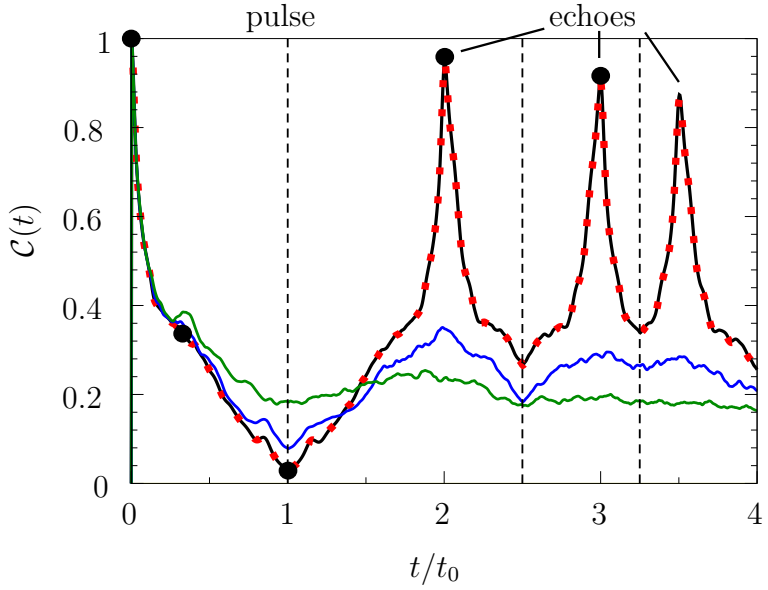

Figure 4.1: Effect of disorder to the QTM mechanism. The correlation $\mathcal{C}$ for the propagation of the same $\hbar$-shaped wave packet as in Fig. 3.8 is shown as a function of time, again with three distinct echoes generated by pulses at $t = t_0$, $t = 2.5t_0$ and $t = 3.25t_0$. The black solid line belongs to the simulation of a clean system (same as Fig. 3.9(a)) and the black dots mark again the time spots of the snapshots in Fig. 3.8. The blue and green curve show the correlation for a system with rather strong spatial disorder ($\tau_0 \approx 0.8t_0$ (blue) and $\tau_0 \approx 0.2t_0$ (green)) showing strong deviations from the clean system. The red dotted curve belongs to a system with gap disorder of similar strength. Nevertheless, the gap disorder shows no deviations at all.

finite grid. The approximation which enters this notation is justified for fine enough grids and large lattices.

In App. C, we show that due to self-averaging effects, the normalization factor – for a lattice with infinite points – simplifies to

$$\mathcal{N} = \sqrt{\frac{\pi}{2}} \frac{l_0}{\sqrt{dx \cdot dy}} \tag{4.3}$$

and is therefore independent on the actual realization of the disorder potential.

As mentioned above, we investigate two different kinds of disorder: Pseudospin-independent spatial disorder and inhomogeneities during the pulse, referred to as gap disorder. The additional potentials to the Hamiltonian in Eq. (3.10) are

$$\begin{aligned} V_r(\mathbf{r}) &= V_{\text{imp}}(\mathbf{r})\sigma_0, \\ V_{\text{gap}}(\mathbf{r}) &= V_{\text{imp}}(\mathbf{r})f(t)\sigma_z, \end{aligned} \tag{4.4}$$

respectively, with $f(t)$ as in Eq. (3.10), i.e. $f(t) = 1$ during the pulse and $f(t) = 0$ else.

A first glimpse of the effect of disorder can be seen in Fig. 4.1, where the correlation $\mathcal{C}(t)$ is shown. The different curves correspond to simulation of a clean system

(black), medium (blue) and strong (green) disorder strength with $u_0 = 0.025M$ and $u_0 = 0.055M$, respectively, and gap disorder (red dotted) with $u_0 = 0.055M$. There, the results of one typical disorder realization is plotted. While the gap disorder does not affect the correlation at all, spatial disorder has a clearly visible effect, leading to large randomization of the wave packet in the whole simulation area and the distinct echo peaks are blurred. The reason for this will be explained below.

4.1.2 Scattering time

We want to describe the random potential by a single quantity to simplify the analysis. Suitable candidates are among others the mean free path and the elastic scattering time, which are related via the velocity. Due to its relevance in the theory of Loschmidt echoes in the subsequent Subsec. 4.1.3, we stick to the elastic scattering time τ.

Starting from Fermi's golden rule, the elastic scattering time for a potential can be derived (see e.g. [99]) to yield

$$\frac{\hbar}{\tau_k} = \int \frac{\mathrm{d}^2\mathbf{k}'\,\mathrm{d}^2\mathbf{r}}{2\pi}\,\delta(E_k - E_{k'})\langle V_{\mathrm{imp}}(0)V_{\mathrm{imp}}(\mathbf{r})\rangle e^{i(\mathbf{k}-\mathbf{k}')\cdot\mathbf{r}}, \tag{4.5}$$

where $\langle\cdot\rangle$ is the disorder average and $\langle V_{\mathrm{imp}}(\mathbf{r})V_{\mathrm{imp}}(\mathbf{r}')\rangle$ is the correlator of the impurity potential between the two points $\mathbf{r}$ and $\mathbf{r}'$. The disorder average can be calculated by taking a large number m of realizations and averaging the object of interest over all of them

$$\langle f\rangle = \lim_{m\to\infty}\frac{1}{m}\sum_{l=1}^{m} f^{(l)}, \tag{4.6}$$

where l is the index of one particular realization of the impurity potential V_{imp}.

To calculate $\langle V_{\mathrm{imp}}(\mathbf{r})V_{\mathrm{imp}}(\mathbf{r}')\rangle$, we make use of the averaging properties of the normally distributed variable β, namely the expectation value $\overline{\beta}$ and the variance $\mathrm{Var}(\beta)$:

$$\overline{\beta} = \frac{1}{n}\sum_{i=1}^{n}\beta_i \xrightarrow{n\to\infty} 0, \tag{4.7}$$

$$\mathrm{Var}(\beta) = \overline{(\beta_i - \overline{\beta})^2} = \overline{\beta_i^2} = \frac{1}{n}\sum_{i=1}^{n}\beta_i^2 \xrightarrow{n\to\infty} 1. \tag{4.8}$$

The result does not depend on whether i in Eqs. (4.7) and (4.8) runs over the lattice points in the grid or the different realization of V_{imp}, because in both cases, the corresponding β_i are independent. For more details see also App. C.

A useful relation, which directly derives from Eqs. (4.7) and (4.8) is the following:

$$\sum_{l,k=1}^{n}\beta_l\beta_k = \sum_{l=1}^{n}\beta_l^2 + \underbrace{\sum_{l=1}^{n}\beta_l}_{\approx 0}\sum_{\substack{k=1\\k\neq l}}^{n}\beta_k \approx n\,\underbrace{\frac{1}{n}\sum_{l=1}^{n}\beta_l^2}_{\approx 1} + 0 \approx n, \tag{4.9}$$

which is a good approximation for a large number n. Here the sum runs over different realizations whereas in a similar calculation in App. C, the index i denotes different

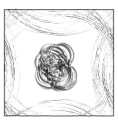

lattice sites. To distinguish between these two random components, we will use the following notation: $\beta_i^{(l)}$, where the subscript i stands for the lattice site and the superscript (l) for the realization of V_{imp}, similar to the notation beforehand.

For the disorder correlator $\langle V_{\text{imp}}(\mathbf{r})V_{\text{imp}}(\mathbf{r}')\rangle$, we make use of the fact that the normalization factor $\mathcal{N}^{(l)} \approx \mathcal{N}$ for a large lattice is independent of the disorder realization (see Eq. (4.3)).

$$\begin{aligned}
\langle V_{\text{imp}}(\mathbf{r})V_{\text{imp}}(\mathbf{r}')\rangle &= \lim_{m\to\infty}\frac{1}{m}\sum_{l=1}^{m} V_{\text{imp}}^{(l)}(\mathbf{r})V_{\text{imp}}^{(l)}(\mathbf{r}') \\
&= \lim_{m\to\infty}\frac{1}{m}\sum_{l=1}^{m}\left(\frac{u_0}{\mathcal{N}^{(l)}}\right)^2\sum_{i,j=1}^{N}\beta_i^{(l)}\beta_j^{(l)}\mathrm{e}^{-\frac{(\mathbf{r}-\mathbf{r}_i)^2+(\mathbf{r}'-\mathbf{r}_j)^2}{l_0^2}} \\
&\approx \frac{u_0^2}{\mathcal{N}^2}\sum_{i,j=1}^{N}\mathrm{e}^{-\frac{(\mathbf{r}-\mathbf{r}_i)^2+(\mathbf{r}'-\mathbf{r}_j)^2}{l_0^2}}\underbrace{\lim_{m\to\infty}\frac{1}{m}\sum_{l=1}^{m}\beta_i^{(l)}\beta_j^{(l)}}_{\delta_{ij},\text{ see Eq. (4.9)}} \\
&= \frac{2u_0^2}{\pi l_0^2}dx\,dy\sum_{i=1}^{N}\mathrm{e}^{-\frac{(\mathbf{r}-\mathbf{r}_i)^2+(\mathbf{r}'-\mathbf{r}_i)^2}{l_0^2}} \qquad (4.10)
\end{aligned}$$

To proceed, we use the fineness of the grid to convert the sum over all lattice points into an integral over the simulation area A. It comes in handy, that the necessary factor for the area element $dA = dx \cdot dy$ are already included in $\mathcal{N}^2$ (see Eq. (4.3)).

$$\langle V_{\text{imp}}(\mathbf{r})V_{\text{imp}}(\mathbf{r}')\rangle = \frac{2u_0^2}{\pi l_0^2}\int_A \mathrm{d}^2\mathbf{r}_i\mathrm{e}^{-\frac{(\mathbf{r}-\mathbf{r}_i)^2+(\mathbf{r}'-\mathbf{r}_i)^2}{l_0^2}}. \qquad (4.11)$$

Completing the square in the exponential to get a Gaussian integral is analogous to the calculation in App. C and yields

$$\begin{aligned}
\langle V_{\text{imp}}(\mathbf{r})V_{\text{imp}}(\mathbf{r}')\rangle &= \frac{2u_0^2}{\pi l_0^2}\int_A \mathrm{d}^2\mathbf{r}_i\exp\left(-\frac{2(\mathbf{r}_i-\frac{\mathbf{r}+\mathbf{r}'}{2})^2}{l_0^2}-\frac{(\mathbf{r}-\mathbf{r}')^2}{2l_0^2}\right) \\
&= \frac{2u_0^2}{\pi l_0^2}\exp\left(-\frac{(\mathbf{r}-\mathbf{r}')^2}{2l_0^2}\right)\underbrace{\int_A \mathrm{d}^2\mathbf{r}_i\exp\left(-\frac{2(\mathbf{r}_i-\frac{\mathbf{r}+\mathbf{r}'}{2})^2}{l_0^2}\right)}_{l_0^2\pi/2} \\
&= u_0^2\,\exp\left(-\frac{(\mathbf{r}-\mathbf{r}')^2}{2l_0^2}\right). \qquad (4.12)
\end{aligned}$$

This expression seems reasonable, because the impurity potential at two lattice points is correlated via the Gaussian smoothing in Eq. (4.1) which has a similar form.

Now, the elastic scattering time $\tau_{\mathbf{k}}$ can be calculated using Eq. (4.5), where the space integral becomes a Fourier transform of a Gaussian.

$$\frac{\hbar}{\tau_k} = u_0^2\int\frac{\mathrm{d}^2\mathbf{k}'\,\mathrm{d}^2\mathbf{r}}{2\pi}\delta(E_k-E_{k'})\exp\left(-\frac{\mathbf{r}^2}{2l_0^2}+i(\mathbf{k}-\mathbf{k}')\cdot\mathbf{r}\right)$$

$$
\begin{aligned}
&= \frac{u_0^2}{v_F\hbar}\int \mathrm{d}^2\mathbf{k}'\,\delta(k-k')\underbrace{\int\frac{\mathrm{d}^2\mathbf{r}}{2\pi}\exp\left(-\frac{\mathbf{r}^2}{2l_0^2}+i(\mathbf{k}-\mathbf{k}')\cdot\mathbf{r}\right)}_{\text{Fourier of Gaussian}}\\
&= \frac{u_0^2}{v_F\hbar}\int_0^\infty \mathrm{d}k'\,k'\int_0^{2\pi}\mathrm{d}\varphi\,\delta(k-k')l_0^2\exp\left(-\frac{(\mathbf{k}-\mathbf{k}')^2l_0^2}{2}\right)\\
&= \frac{u_0^2l_0^2}{v_F\hbar}k\exp\left(-k^2l_0^2\right)\int_0^{2\pi}\mathrm{d}\varphi\exp\left(k^2l_0^2\cos\varphi\right)\\
&= \frac{u_0^2l_0^2}{v_F\hbar}k\exp\left(-k^2l_0^2\right)2\pi I_0\left(k^2l_0^2\right)\\
\Rightarrow \frac{\hbar}{\tau_k} &= \frac{2\pi}{v_F\hbar}k\,u_0^2l_0^2\exp\left(-k^2l_0^2\right)I_0\left(k^2l_0^2\right). \qquad (4.13)
\end{aligned}
$$

The elastic scattering times in a Gaussian correlated disorder potential is in agreement with previous reports (e.g. [100,101]). Here, I_ν is the modified Bessel function of ν-th kind, with

$$I_0(0) = 1, \qquad (4.14)$$

$$I_0(x) \xrightarrow{x\to\infty} \frac{\mathrm{e}^x}{\sqrt{2\pi x}}. \qquad (4.15)$$

Thus, for $l_0k \gg 1$, i.e. smooth potential such that the wave length is small compared to the variation of the disorder, the elastic scattering time τ_k becomes independent on k, whereas for $l_0k \ll 1$ the scattering rate $1/\tau_k \propto k$ is linear in the momentum.

In the subsequent simulations, we will choose Gaussian wave packets as in the beginning of Subsec. 3.2 with $\Delta k \ll k_0$ and thus the scattering time will not change substantially over the width of the wave packet. Therefore, we assign to the whole Gaussian wave packet an elastic scattering time $\tau_0 \equiv \tau_{k_0}$.

4.1.3 Loschmidt Echoes

Theory and Fidelity

So far, we have used the correlation $\mathcal{C}$ defined in Eq. (3.32) to quantify the echo, where only the magnitudes of the wave function play a role which are the experimentally relevant quantities, as opposed to the phases. In the case of disorder however, a different quantity might be better suited where the role of disorder has been already studied (see e.g. [102]) extensively and thoroughly: the Loschmidt echo or fidelity, respectively. The corresponding theory was developed to quantify the accuracy of a non-perfect time reversal of a quantum system with two Hamiltonians H_1 and H_2.

The fidelity is defined by

$$\tilde{m}(t) = |\langle\psi \mid \mathrm{e}^{+\frac{i}{\hbar}H_2t}\mathrm{e}^{-\frac{i}{\hbar}H_1t} \mid \psi\rangle|^2, \qquad (4.16)$$

which can be interpreted in two ways. The first one is that the initial state $|\psi\rangle$ is propagated by the Hamiltonian H_1 for time t, then it is propagated by "$-H_2$" for the same time t – which is equivalent to a propagation backwards in time by H_2 –

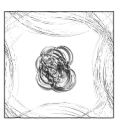

and the overlap with the initial state is taken. The other way to look at it is that the initial state is propagated twice, once by H_1 and once by H_2, and then the overlap of the two propagated states is taken.

Clearly, if $H_1 = H_2$, the fidelity in Eq. (4.16) becomes 1 and the larger the deviation between the two Hamiltonians, the smaller is $\tilde{m}$. Moreover, it is intuitive that for $H_1 \neq H_2$, $\tilde{m}$ decays with time since the longer the perturbation can act, the more the states in the two system deviate.

Depending on the perturbation strength between H_1 and H_2 and also the time of propagation t, different regimes of decay can be found [102, 103]. For small times, $\tilde{m}$ decays parabolically, for intermediate times, the decay is either exponential or Gaussian. For long times, a saturation sets in which is related to the size of the Hilbert space, that is finite in our simulations given by the number of grid points times additional degrees of freedom, here 2 for the pseudospin.

Whether there is an exponential or Gaussian decay for intermediate times depends on perturbation strength – which can be identified in our case with the disorder strength u_0 – compared to the level spacing Δ of the unperturbed Hamiltonian, in our case $\Delta = \hbar v_F dk \lesssim 0.001 M_0$ for typically used lattice sizes and pulse strengths $M_0 \gg E_{k_0}$. If $u_0 \ll \Delta$, the Gaussian regime is valid and for $u_0 \gtrsim \Delta$, the exponential decay regime, also called golden rule decay, is entered.

For our simulations with typical parameters ($u_0 \gtrsim 0.001 M_0$), we are always in the golden rule decay, or already in saturation regime for large disorder or long times. The parabolic regime, i.e. small propagation times, is not of importance because in that situation, the initial wave packet has not moved enough away from the initial position, such that time-inverted and proceeding parts of the wave packet still largely overlap during the echo.

It has been shown (e.g. [104]) that the timescale of the exponential decay in the golden rule regime is the elastic scattering time. Thus, the fidelity decays over time as

$$\tilde{m}(t) \sim \mathrm{e}^{-t/\tau_0}. \tag{4.17}$$

From this, it is already clear why gap disorder plays almost no role, as compared to space disorder for similar disorder strengths. The timescale on which gap disorder acts is the pulse length Δt whereas spatial disorder acts on time scales of the echo time $2t_0 \gg \Delta t$. Due to the exponential decay, the effect of the gap disorder is negligible compared to space disorder which is why we only consider space disorder hereinafter.

To single out the effect of disorder from the echo, we consider the Loschmidt echo of the full propagations until the echo, i.e. with the time reversal pulse $M(t)$, for both the clean system $H_1 = H$ and the disordered system $H_2 = H_{\mathrm{imp}} = H + V_r$ for the same, initial Gaussian wave packet. This will not tell us anything about the change of the echo strength due to disorder, which is the ultimate goal of this subsection, but it will confirm the theory such that we can proceed with confidence.

In Fig. 4.2(a), the fidelity is plotted as function of the time of the pulse t_0 for different impurity strengths u_0 ranging between $0.002M$ and $0.022M$. The initial wave packet is again a Gaussian with $\Delta k \ll k_0$. Every data point is the average of 50 realizations of the impurity potential and the error bars show the standard error of the mean. The red lines are exponential fits to the data of equal u_0, since we

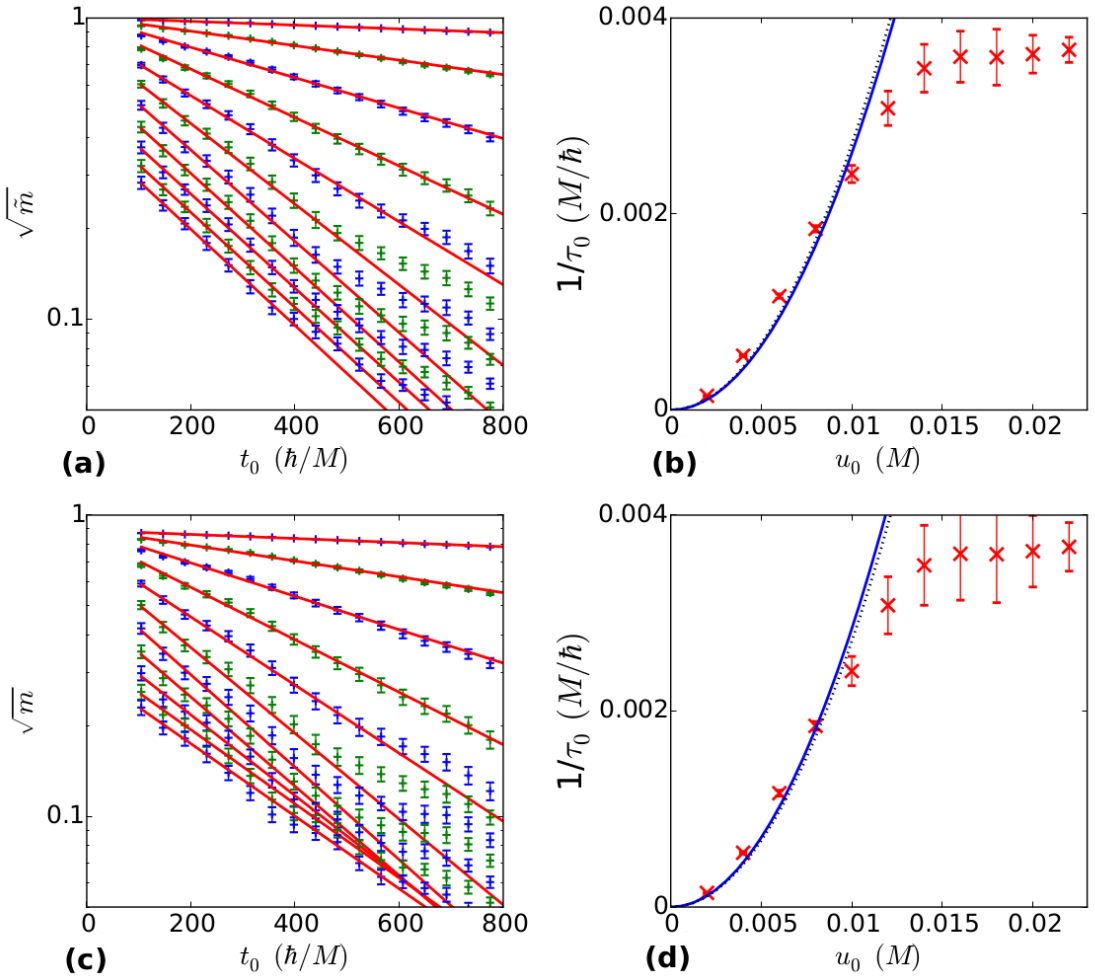

Figure 4.2: Loschmidt echo for disordered system. (a) The fidelity (actually its square root $\sqrt{\tilde{m}}$) is plotted as a function of the pulse time t_0 – which means that the full propagation time is until the echo is $t \simeq 2t_0$ – for varying disorder strengths between $u_0 = 0.002M$ and $0.022M$. The data points are averages over 50 realizations of the disorder potential and the error bars are the standard errors of the mean. The alternation between blue and green data points is supposed to help better distinguish between different u_0 and has no further meaning. The red lines are exponential fits to extract the decay rate $1/\tau_0^{(\mathrm{fit})}$. (b) The extracted decay rates $1/\tau_0^{(\mathrm{fit})}$ of (a) are plotted as a function of u_0 (red crosses). The error bars show the uncertainty of the exponential fit. The blue line is the fitted parabolic curve for $u_0 \leq 0.01M$ and the black dotted line is the analytically expected value of Eq. (4.13). Thus, theory and simulation match very well. (c) and (d) is the same as (a) and (b), respectively, but for the echo fidelity $\sqrt{m}$, which includes the in general non-perfect occupation-inversion of the QTM.

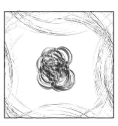

expect in the golden rule regime a decay according to Eq. (4.17). For small u_0 or for not so large times t_0, the exponential decay fits the data very well. For high u_0 and/or large t_0, the data deviates more and more from the exponential fit, which is probably due to entering the aforementioned expected saturation regime.

Since the total propagation time is $t = t_{\text{echo}} \simeq 2t_0$, one expects an exponential decay for $\sqrt{\tilde{m}(t_{\text{echo}})}$ in Fig. 4.2(a) of the form

$$\sqrt{\tilde{m}(t_{\text{echo}})} \sim \mathrm{e}^{-\frac{t_{\text{echo}}}{2\tau_0}} \simeq \mathrm{e}^{-\frac{t_0}{\tau_0}}, \tag{4.18}$$

meaning that the decay rate is supposed to be the scattering time τ_0.

There is a intuitive way to heuristically motivate this formula: The scattering time tells us the time span until a certain fraction $(1/e)$ of a quantum system is scattered on average. Every part of the wave packet, which is scattered, deviates from the wave packet in the clean system and therefore does not contribute to the fidelity. As a consequence, the fidelity should have a similar time-dependence as the fraction of the wave packet, which is scattered, and that is the exponential decay of Eq. (4.18).

In Fig. 4.2(b), the decay rate $1/\tau_0^{\text{fit)}}$ (red crosses) of the fitted exponential decay from Fig. 4.2(a) is plotted as a function of u_0. For $u_0 \gtrsim 0.014M$, the fitted scattering rate $1/\tau_0^{\text{fit)]}}$ seems to run again into a saturation, which is expected in [103] and therefore the expected parabolic behavior $1/\tau_0 \sim u_0^2$ of Eq. (4.13) is only valid up to some $u_0^{\max}$, which seems to be in our setup $u_0^{\max} \sim 0.01M_0$. The blue line is a fit to the expected parabolic behavior of the decay rate as a function of u_0 and the black dotted line is the purely analytically expected $1/\tau_0$ of Eq. (4.13), which show a good agreement between theory and simulation.

Echo Fidelity

So far, we have shown that the theory of Loschmidt echoes is in agreement with the simulations for the full propagations of a clean system and a disordered system. However, the echo strength is yet unregarded, because in both propagations, the time reversal pulse was present.

We want to investigate now the impact of disorder to the echo strength. Unfortunately, we cannot hope to apply the theory of Loschmidt echoes to the correlator $\mathcal{C}$, which was the measure for the echo strength above, because it has a different structure than the fidelity defined in Eq. (4.16). However, in Sec. 3.1, we mentioned a quantity which looks similar to the fidelity and which we will call in analogy "echo fidelity" m:

$$m(t_{\text{echo}}) = |\langle \sigma_z \phi_0 \mid U(0, t_{\text{echo}}) \mid \phi_0 \rangle|^2 = |\langle \phi_0 \mid \sigma_z \mathrm{e}^{-\frac{i}{\hbar} H_0' t_0} \mathrm{e}^{-\frac{i}{\hbar} H' \Delta t} \mathrm{e}^{-\frac{i}{\hbar} H_0' t_0} \mid \phi_0 \rangle|^2 \tag{4.19}$$

Here we introduced the Hamiltonians $H_0' = H_0 + V_r$ and $H' = H + V_r = H_0 + M + V_r$, where the prime indicates that spatial disorder is present, whereas the subscript 0 indicates that the pulse is not present. The σ_z is needed as in the derivation of the transition amplitude, because the pulse is supposed to switch the bands of the initial wave packet. The fidelity between initial and propagated wave packet would be 0 even for a perfect echo, because the eigenstates of H_0 are orthogonal. Since σ_z

is the operator which maps the eigenstate of one band to the eigenstate of the other band, the overlap in Eq. (4.19) becomes 1 for a perfect echo.

Comparing the echo fidelity of Eq. (4.19) and the fidelity of Eq. (4.16), the only accordance is that the overlap between an initial state and its time propagated state is taken. The important feature of the Loschmidt echo, which is the propagation back in time by H_2 seems to be completely absent in the echo fidelity. However, we can rewrite the echo fidelity of Eq. (4.19) such that this important property is effectively recovered. To this ind, we assume that during the short pulse duration $\Delta t \ll \tau_0$, the effect of disorder is not of importance, i.e. $H' \approx H$.

For the clean system, we know from Subsec. 3.1 that the action of the pulse can be written in terms of the transition amplitude $A(k)$ and the ongoing wave packet (see Eq. (3.19)), which is lost for the echo and therefore does not contribute in the overlap with the initial wave function. Then, the echo fidelity becomes

$$\begin{aligned} m(t_0) &\approx |\langle\phi_0 \mid \sigma_z \mathrm{e}^{-\frac{i}{\hbar}H_0' t_0} \sigma_z A(k) \mathrm{e}^{-\frac{i}{\hbar}H_0' t_0} \mid \phi_0\rangle|^2 \\ &= |\langle\phi_0 \mid \mathrm{e}^{-\frac{i}{\hbar}\sigma_z H_0' \sigma_z t_0} A(k) \mathrm{e}^{-\frac{i}{\hbar}H_0' t_0} \mid \phi_0\rangle|^2 \\ &= |\langle\phi_0 \mid \mathrm{e}^{-\frac{i}{\hbar}(-H_0+V_r)t_0} A(k) \mathrm{e}^{-\frac{i}{\hbar}(H_0+V_r)t_0} \mid \phi_0\rangle|^2 \\ &= |\langle\phi_0 \mid \mathrm{e}^{+\frac{i}{\hbar}(H_0-V_r)t_0} A(k) \mathrm{e}^{-\frac{i}{\hbar}(H_0+V_r)t_0} \mid \phi_0\rangle|^2. \end{aligned} \tag{4.20}$$

Here we made use of special features of the Pauli matrices, first that they are unitary $\sigma_i^2 = \mathbb{1}$ to transfer σ_z to the exponential. Secondly, the anti-commutation relation $\{\sigma_i, \sigma_j\} = 2\delta_{ij}$ implies $\sigma_z \sigma_i \sigma_z = -\sigma_i$ for $i = x, y$ and therefore, H_0 effectively changes sign ($\sigma_z H_0 \sigma_z = -H_0$) whereas the disorder potential remains unchanged ($\sigma_z V_r \sigma_z = V_r$) because of pseudospin independence. This is a very important observation: the pulse only effectively inverts the propagation due to the clean Hamiltonian H_0, but the effect of V_r cannot be reverted. In the discussion part below, this property will be recapitulated to get a more qualitative understanding of what happens.

If we further assume that the transition amplitude is nearly constant over the (already scattered) wave packet $A(k) \approx A_0$, the echo fidelity is

$$m(t_0) \approx |A_0|^2 \, |\langle\phi_0 \mid \mathrm{e}^{+\frac{i}{\hbar}(H_0-V_r)t_0} \mathrm{e}^{-\frac{i}{\hbar}(H_0+V_r)t_0} \mid \phi_0\rangle|^2, \tag{4.21}$$

which is up to the constant prefactor the same as the fidelity with $H_1 = H_0 + V_r$ and $H_2 = H_0 - V_r$, which is why it is reasonable to assume the same decaying behavior. Since the effect of the disorder potential cannot be reverted by the pulse, the disorder potential acts over the whole propagation time $2t_0$, which is why we expect the echo fidelity to decay as

$$m(t_0) \sim \mathrm{e}^{-\frac{2t_0}{\tau_0}}, \tag{4.22}$$

which is exactly the same behavior as for the fidelity. The difference is that there is the additional factor $|A_0|^2$, which makes the echo fidelity smaller in amplitude. Note that the assumption $A(k) \approx A_0$ is not necessary but simplifies the notation, because otherwise every **k**-mode would have to be treated individually, which is of course possible.

For the simulations, the same wave packet is used as in the calculation for the fidelity in the subsection above. Similar to the case of the fidelity, $\sqrt{m}$ is plotted

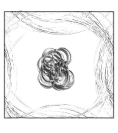

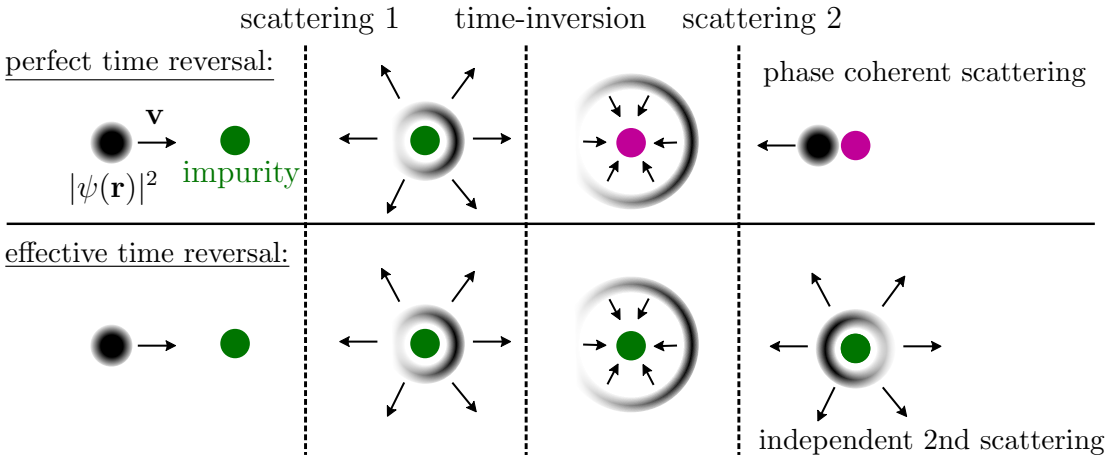

Figure 4.3: Difference between a perfect (real) time-reversal and our effective time-reversal due to the QTM. The wave packet is scattered by an impurity and the time-inversion is applied after the scattering. In the case of perfect time-reversal (upper panels), i.e. $H \to -H$ and especially $V_r \to -V_r$ as indicated by the change of color of the impurity, the second scattering refocuses the wave packet perfectly. In the case of our QTM (effective time reversal), i.e. $H_{\text{kin}} + V_r \to -H_{\text{kin}} + V_r$, the second scattering at the same impurity is independent of the first one, because the sign of V_r is not inverted (compare Eq. (4.20) and the discussion in Subsec. 4.1.4). Thus, the wave packet does not refocus but is scattered in different directions.

in Fig. 4.2(c) as a function of t_0 for varying u_0 and the exponential decay rate, which is extracted via an exponential fit, is plotted in Fig. 4.2(d) in dependence on u_0. There a parabolic function is again fitted and compared to the black dotted analytical expectation of Eq. (4.13). The same saturation regimes appear and in the golden rule regime, theory and simulation match quite well.

Moreover, Eq. (4.21) compares the echo fidelity with the fidelity which should be approximately proportional with the factor $|A(k_0)|^2$, respectively $|A(k_0)|$ for their square roots which are actually plotted in Fig. 4.2. Using the data shown in (a) and (c), the proportionality factor is on average $\sqrt{m/\tilde{m}} = 0.86 \pm 0.06$ which is in accordance with the analytical prediction of $|A(k_0)| = 0.87$.

4.1.4 Discussion

In this part, we want to interpret and explain the results of the calculation for the echo fidelity in a more qualitative way and we want to emphasize the key arguments why our "time-reversal" pulse is not perfect, i.e. why it is sensitive to static spatial disorder as opposed to the Hahn spin echo, for instance.

The difference between perfect time reversal and our effective time reversal mechanism is shown in Fig. 4.3. By a *perfect* time-reversal pulse, we do not mean that necessarily 100% of the wave packet has to come back. Instead, for the part of the wave packet which is reflected, the propagation after the pulse has to look exactly like the propagation until the pulse, just backwards in time.

First, let us consider the situation described in the upper half of Fig. 4.3, namely what happens if the pulse would lead to a perfect time inversion. For simplicity, we

consider only one $\mathbf{k}$-mode and only one scattering process at one impurity. After the scattering process, the pulse is applied and the wave packet comes back to the same impurity again. At the first scattering process, the initial mode is scattered with a given amplitude a to a wide range of new modes:

$$|\psi_{\mathbf{k}}\rangle \xrightarrow{1^{\text{st}}\text{ scattering}} \sum_{\mathbf{k}'} a(\mathbf{k},\mathbf{k}')\,|\psi_{\mathbf{k}'}\rangle, \tag{4.23}$$

which is why the wave packet spreads, i.e. it moves in different directions.

After the time-reversal pulse each of the new $\mathbf{k}'$-modes comes back to the impurity and is in principle scattered again in wide range of modes:

$$|\psi_{\mathbf{k}'}\rangle \xrightarrow{2^{\text{nd}}\text{ scattering}} \sum_{\mathbf{k}''} a(\mathbf{k}',\mathbf{k}'')\,|\psi_{\mathbf{k}''}\rangle, \tag{4.24}$$

In a perfect time-reversal setup, only the mode $\mathbf{k}'' = -\mathbf{k}$ is allowed to survive after the full scattering event, such that the motion of the wave packet is time reversed as compared to the initial incoming one. At first sight, it might be not so clear, why in this second scattering process all the $\mathbf{k}'$-modes interfere such that only $-\mathbf{k}$ survives and every other mode is canceled by destructive interference. This can be easiest explained by the single particle interference in the Feynman path approach.

In general, the propagation of a quantum system can be explained by the single particle interference of all possible paths in phase-space, weighted with a phase determined by the action S of the given path e^{iS}. Similar to classical mechanics, only the paths near an extremum of the action contribute, because for the others, fast changing phases of neighboring paths interfere destructively and their physical weight is suppressed. Considering one particular path of the scattering problem above, we see that until the time reversal, a certain phase is acquired due to e^{iS}. If exactly the same path, but time-reversed ($H \to -H$) is chosen on the way back, the additional cumulated phase is the same, but with a negative sign. Thus, the phase at the initial position is 0, if the path before and after the pulse are the same. This is true for any of the paths before the pulse and they all interfere constructively.

On the other hand, if a different path is chosen after the pulse as compared to the original one, e.g. by scattering into a different mode $\mathbf{k}'' \neq -\mathbf{k}$, an arbitrary phase is collected. Moreover, every other initial path which is scattered into the same $\mathbf{k}'' \neq -\mathbf{k}$ also collected an arbitrary phase which is (nearly) unrelated for every initial path. Thus on average, the sum of all these phases vanishes, or in other words, all these paths interfere destructively such that in total, only the mode $\mathbf{k}'' = -\mathbf{k}$ survives. (Note that this is not a strict proof why all the other modes vanish but a mere intuitive explanation why the constructive interference of the initial mode $-\mathbf{k}$ should dominate.)

So far, we were talking about an theoretical, perfect time-reversal pulse. How is this related to our "effective time-reversal" pulse and where do they differ? The deviations are visualized in the lower half of Fig. 4.3.

The important step can be seen both in the calculation in Eq. (4.20) and in the comments underneath Eq. (4.20). There, we saw that for the reflected wave packet, due to the sandwiching between σ_z-matrices, the sign of the Hamiltonian for the propagation after the pulse changes, which means effectively a propagation

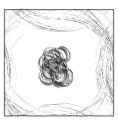

backwards in time. However, this is only true for the parts of the Hamiltonian which are proportional to σ_x and σ_y, i.e. H_0, whereas the pseudospin-independent disorder V_r (as well as gap disorder $\propto \sigma_z$) is not affected. Therefore, an *independent* second scattering after the pulse at the same impurity occurs and thus, no constructive interference happens to $-\mathbf{k}$. Thus, the actual echo is strongly dependent on spatial (static) disorder V_r.

In contrast, the effective time-reversal pulse for the spin echo is insensitive to static disorder of whatever kind as discussed in the introduction in Chap. 1. Disorder – or let's say different environments of the spins – leads to a different local magnetic field and therefore a different Larmor frequency, i.e. a different precession speed, which is why the spins dephase over time. The π-pulse at $t = t_0$ inverts the population of all the spins inplane, which means that faster precessing spins find themselves "behind" the slow ones, catching up more and more until at $t = 2t_0$, all the spins are in phase, again (at least if they started in phase). Here, to destroy the echo, a time-dependent change of the Larmor frequency, i.e. between initiation and rephasing, is needed such that fast rotating spins before the pulse are not necessarily fast spins after the pulse. The decay time due to this *in*elastic mechanism is called T_2, which is the analogue to the *elastic* scattering time τ in our QTM.

However, a major difference to our case is that for the Hahn echo, the spins are typically assumed not to move significantly during the process. If the spins moved through a disordered medium as the wave function does in our QTM setup, their environment, and thus the Larmor frequency, would change in time also for static disorder and therefore, the Hahn echo would be equally sensitive to static disorder.

Indeed, the sensitivity of the Hahn echo to static disorder for spins of moving protons is used in NMR to distinguish the environment of the spins [105] which is the reason why noninvasive pictures of biological, for instance, can be made. Depending on whether the protons are in a liquid or solid, the dephasing time T_2 strongly varies and thus, measuring T_2 with spatial resolution allows to distinguish between different kinds of tissue.

Similarly, the QTM could be used to measure the cleanness of a system, provided the echo strength can be measured, but for this, experimental realizations of the Quantum time mirror are needed, first.

4.2 General discussion of perturbations

In the previous section, we have seen that perturbations can affect the QTM using the example of disorder. For short enough pulse durations Δt, i.e. that the orbital degrees of freedom of the wave function (e.g. $\mathbf{k}$) are not considerably altered, the action of the additional potential is important only during the free propagation before and after the pulse. The analysis for long Δt as done in Sec. 3.4 is in this general setup more difficult, because not only the position but also $\mathbf{k}$ changes during the pulse due to $V(\mathbf{r})$, and will not be considered in this thesis.

In this section, we want to qualitatively investigate whether an additional potential in the Hamiltonian will destroy the effective time reversal. In other words, does a transition to the other band induced by the pulse lead to an effective time-reversal, if there is additionally some (static) potential V? Note that we do not want to give

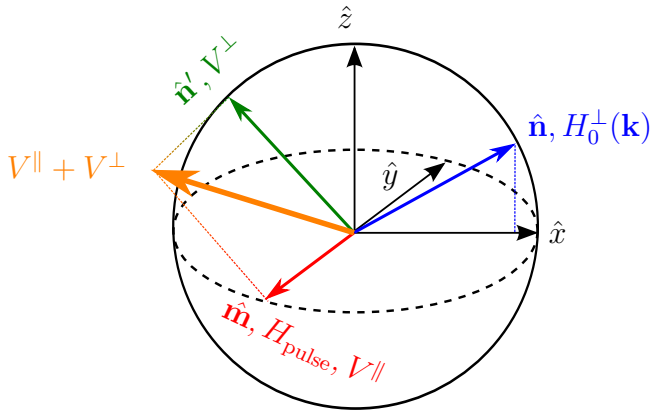

Figure 4.4: Visualization of the directions of the Hamiltonian in the Bloch sphere. $\hat{\mathbf{n}}$ (blue) is the direction of the unperturbed Hamiltonian $h_0^\perp(\mathbf{k})$ and $\hat{\mathbf{m}}$ (red) the direction of the homogeneous and $\mathbf{k}$-independent pulse. The perturbation potential splits into parts parallel to the pulse $V^\parallel$ and perpendicular (green) $V^\perp$ in direction $\hat{\mathbf{n}}'$. By definition, $\hat{\mathbf{n}} \perp \hat{\mathbf{m}} \perp \hat{\mathbf{n}}'$, but $\hat{\mathbf{n}}$ and $\hat{\mathbf{n}}'$ are neither necessarily parallel nor perpendicular. Additionally, both V and H_0 might have pseudospin-independent parts, which cannot be visualized in the Bloch sphere. The pulse can only effectively time-invert the parts of the Hamiltonians, which are perpendicular to it, as seen in Eq. (4.37).

a rigorous proof but merely a heuristic motivation of why certain perturbations can be effectively time-reversed, and why others cannot.

Note that although we call it perturbation, the additional potential is not meant to be small, here. Thus, we do not want to use perturbation theory, but instead "perturbation" is used to indicate that there are deviations from the initial (Dirac) Hamiltonian, e.g. via external fields or disorder as seen above.

In this general section, it is not mandatory to use the Dirac Hamiltonian, but any homogeneous initial (two-band) Hamiltonian is suitable that is of the general form

$$H_0(\mathbf{k}) = H_0^{\mathbb{1}}(\mathbf{k}) + H_0^\perp(\mathbf{k}) = h_0^{\mathbb{1}}(\mathbf{k})\mathbb{1} + h_0^\perp(\mathbf{k})\sigma_n, \tag{4.25}$$

and for which a population inversion leads to an effective time inversion (compare Chap. 5). Here, we denote $H_0^\perp(\mathbf{k}) = h_0^\perp(\mathbf{k})\hat{\mathbf{n}} \cdot \boldsymbol{\sigma}$ with some unit vector $\hat{\mathbf{n}}$ and $\sigma_n = \hat{\mathbf{n}} \cdot \boldsymbol{\sigma}$ and we will omit the explicit $\mathbf{k}$-dependence henceforth.

The general eigenenergies of H_0 are denoted by $E_{\mathbf{k},s}$ and the eigenstates by $|\varphi_{\mathbf{k},s}\rangle$ (see also Fig. 4.4).

The notation is chosen such that capital letters in the Hamiltonian are matrices in pseudospin space, i.e. the Pauli matrices are included, whereas lowercase letters are scalars in pseudospin space (but are in general functions of position and/or momentum operator). The superscript $\perp$ denotes that the related direction in pseudospin space (here $\hat{\mathbf{n}}$) is *perpendicular* relative to the corresponding direction of the pulse Hamiltonian (see below), which is chosen because of reasons that will become clear later in the end of the section.

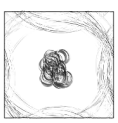

The potential related to the most general perturbation considered here is

$$V = V^{\mathbb{1}} + V^{\parallel} + V^{\perp} = v^{\mathbb{1}}\mathbb{1} + v^{\parallel}\sigma_m + v^{\perp}\sigma_{n'}, \tag{4.26}$$

where $\sigma_{n'} = \hat{\mathbf{n}}' \cdot \boldsymbol{\sigma}$, with $\hat{\mathbf{n}}' \perp \hat{\mathbf{m}}$, but not necessarily $\hat{\mathbf{n}}' \parallel \hat{\mathbf{n}}$ (see also Fig. 4.4). Thus, we consider a time-independent potential which is arbitrary function of position and momentum operator ($\mathbf{k}$ and $\mathbf{r}$) and simultaneously an operator in pseudospin space.

The time-dependent pulse Hamiltonian on the other hand is assumed to be homogeneous

$$H_{\text{pulse}}(t) = \Lambda \hat{\mathbf{m}} \cdot \boldsymbol{\sigma} f(t) = \Lambda \sigma_m f(t), \tag{4.27}$$

with $\hat{\mathbf{m}} \perp \hat{\mathbf{n}}$, such that σ_m maps an eigenstate of one band to the eigenstate of the other band (without changing the other good quantum numbers, e.g. possibly $\mathbf{k}$):

$$\sigma_m |\varphi_{\mathbf{k},s}\rangle = \mathrm{e}^{i\alpha} |\varphi_{\mathbf{k},-s}\rangle, . \tag{4.28}$$

Here, the phase α depends on the exact choice of the eigenstates $|\varphi_{\mathbf{k},s}\rangle$ – which are given only up to a phase – and is therefore physically irrelevant. Note that in general, the pulse need not be perpendicular, but for simplicity only the perpendicular part is considered because it is the only one which will lead to a transition (see e.g. Sec. 3.1 and 5.1.1).

The time-dependence of the pulse is chosen as in Sec. 3.1 to be

$$f(t) = \begin{cases} 1, & t_0 < t < t_0 + \Delta t, \\ 0, & \text{otherwise.} \end{cases} . \tag{4.29}$$

Let us consider the time evolution of an initial eigenstate to see whether its motion is effectively time-inverted after the pulse. The time-evolution operator can be split in three step-wise time-independent parts – before, during and after the pulse. Remember that for time-independent systems, can be written as

$$U(t_A, t_B) = \mathrm{e}^{-\frac{i}{\hbar} H (t_B - t_A)}. \tag{4.30}$$

Since we are interested in the echo, we consider again the overlap with the band inverted eigenstate, similar to the echo fidelity in the disorder Sec. 4.1, Eq. (4.20):

$$\langle \varphi_{\mathbf{k},-s} \mid U(t_0 + \Delta t, t_0 + \Delta t + t_1) U(t_0, t_0 + \Delta t) U(0, t_0) \mid \varphi_{\mathbf{k},s} \rangle. \tag{4.31}$$

In the derivation of Eq. (4.20), we used

$$\mathrm{e}^{-i\boldsymbol{\beta}\cdot\boldsymbol{\sigma}} = \mathbb{1} \cos|\boldsymbol{\beta}| - i \frac{\boldsymbol{\beta}\cdot\boldsymbol{\sigma}}{|\boldsymbol{\beta}|} \sin|\boldsymbol{\beta}|, \tag{4.32}$$

but since $\mathbb{1}$ will not lead to a transition in pseudospin space, it is omitted there and in the calculations below.

In general, Eq. (4.32) is only true for commuting components of $\boldsymbol{\beta}$. Nevertheless, we use this expansion during the pulse, because we assume that it is short enough such that the orbital degrees of freedom (momentum and position) are not changed considerably. This implies that the operator-character of position and momentum operator during the pulse can be approximately neglected, which we motivate by

considering the momentum-translation operator acting for a short Δt on the momentum eigenstate:

$$\mathrm{e}^{-i\mathbf{r}\cdot\boldsymbol{\nu}\Delta t}|\mathbf{k}_0\rangle = |\mathbf{k}_0 - \boldsymbol{\nu}\Delta t\rangle \approx |\mathbf{k}_0\rangle. \tag{4.33}$$

The "$\approx$" is due to the approximation that the pulse duration Δt should be short enough that the orbital degrees of freedom (here momentum) do not change during the pulse. Thus, we see in Eq. (4.33) that in the time-evolution operator, terms containing the position operator $\mathbf{r}$ have no effect, when acting in momentum space. Vice versa, one could show that the momentum operator has no effect in position space. In that sense, a short pulse duration means that we can neglect all terms of the Hamiltonian that depend on the position operator.

However, we do not have to be as strict to derive the qualitative result of why the propagation after the pulse is for some potential equivalent to a time-reversal and for others not. To this end, we only have to neglect the (anti)commutators of momentum and position operator during the pulse. Since these terms would not contribute in case of neglecting all terms containing the position operator as motivated above, this is a valid choice for small enough Δt.

To summarize, in this approximation the Pauli matrices are the only objects which we treat as operators during the pulse, i.e. quantities that do not commute, such that the expansion of Eq. (4.32) is justified. Thus, Eq. (4.31) becomes

$$\langle\varphi_{\mathbf{k},-s} \mid \mathrm{e}^{-\frac{i}{\hbar}(H_0+V)t_1}\left(\Lambda\sigma_m + H_0 + V\right) g(\mathbf{h}_0, \mathbf{v}, \Lambda)\mathrm{e}^{-\frac{i}{\hbar}(H_0+V)t_0} \mid \varphi_{\mathbf{k},s}\rangle, \tag{4.34}$$

where the function $g(\mathbf{h}_0, \mathbf{v}, \Lambda) = g(h_0^{\mathbb{1}}, h_0^{\perp}, v^{\mathbb{1}}, v^{\perp}, v^{\parallel}, \Lambda)$ corresponds to the term $\sin(|\boldsymbol{\beta}|)/|\boldsymbol{\beta}|$ of Eq. (4.32), but it is not important in the further qualitative derivation. The only relevant feature is that it is a scalar in pseudospin-space.

By splitting Eq. (4.34) into pulse part and everything else,

$$\begin{aligned}&\langle\varphi_{\mathbf{k},-s} \mid \mathrm{e}^{-\frac{i}{\hbar}(H_0+V)t_1}\sigma_m\Lambda g(\mathbf{h}_0, \mathbf{v}, \Lambda)\mathrm{e}^{-\frac{i}{\hbar}(H_0+V)t_0} \mid \varphi_{\mathbf{k},s}\rangle \\ +&\langle\varphi_{\mathbf{k},-s} \mid \mathrm{e}^{-\frac{i}{\hbar}(H_0+V)t_1}\left(H_0 + V\right) g(\mathbf{h}_0, \mathbf{v}, \Lambda)\mathrm{e}^{-\frac{i}{\hbar}(H_0+V)t_0} \mid \varphi_{\mathbf{k},s}\rangle,\end{aligned} \tag{4.35}$$

we see that the second line in Eq. (4.35) cannot lead to a time reversal, because everything commutes there such that the exponentials before and after the pulse can be added:

$$\langle\varphi_{\mathbf{k},-s} \mid \left(H_0 + V\right) g(\mathbf{h}_0, \mathbf{v}, \Lambda)\mathrm{e}^{-\frac{i}{\hbar}(H_0+V)(t_1+t_0)} \mid \varphi_{\mathbf{k},s}\rangle. \tag{4.36}$$

No time-reversal after the pulse as compared to before the pulse is to be expected from this term, since the signs of the Hamiltonians in the exponentials are unchanged. This is why we keep only the first line in Eq. (4.35). Due to Eq. (4.28), we can rewrite this term to

$$\begin{aligned}&\langle\varphi_{\mathbf{k},s} \mid \sigma_m\mathrm{e}^{-\frac{i}{\hbar}(H_0+V)t_1}\sigma_m\ \Lambda g(\mathbf{h}_0, \mathbf{v}, \Lambda)\ \mathrm{e}^{-\frac{i}{\hbar}(H_0+V)t_0} \mid \varphi_{\mathbf{k},s}\rangle \\ =&\langle\varphi_{\mathbf{k},s} \mid \mathrm{e}^{-\frac{i}{\hbar}\sigma_m(H_0+V)\sigma_m t_1}\ \Lambda g(\mathbf{h}_0, \mathbf{v}, \Lambda)\ \mathrm{e}^{-\frac{i}{\hbar}(H_0+V)t_0} \mid \varphi_{\mathbf{k},s}\rangle \\ =&\langle\varphi_{\mathbf{k},s} \mid \mathrm{e}^{-\frac{i}{\hbar}(H_0^{\mathbb{1}}+V^{\mathbb{1}}+V^{\parallel}-H_0^{\perp}-V^{\perp})t_1}\ \Lambda g(\mathbf{h}_0, \mathbf{v}, \Lambda)\ \mathrm{e}^{-\frac{i}{\hbar}(H_0^{\mathbb{1}}+V^{\mathbb{1}}+V^{\parallel}+H_0^{\perp}+V^{\perp})t_0} \mid \varphi_{\mathbf{k},s}\rangle,\end{aligned} \tag{4.37}$$

where we used $\sigma_m^2 = \mathbb{1}$ to get σ_m into the exponential function and $\sigma_m\sigma_{n^{(\prime)}}\sigma_m = -\sigma_{n^{(\prime)}}$, because $\hat{\mathbf{n}}^{(\prime)} \perp \hat{\mathbf{m}}$ by definition.

The important observation of Eq. (4.37) is that only terms of the Hamiltonian *perpendicular* to the pulse change their sign, which means that only those parts can be effectively time-reversed. Thus, pseudospin-independent terms in the Hamiltonian can never be effectively time-inverted by our mechanism, as we have seen in the case of disorder. However, problems can also arise if H_0 itself has a $\mathbf{k}$-dependent $H_0^{\mathbb{1}}$-term (asymmetric bands), as will be discussed in Chap. 5. Note that even if only one part of the Hamiltonian (including the potential) does not switch its sign, the full system cannot not be effectively time-inverted.

Of course, if the perturbation is small enough, it might not make a difference, as we have seen in the case of disorder. The echo will continuously decrease, the stronger the non-reversible term gets. On the other hand, if every present term in the Hamiltonian switches sign in Eq. (4.37), the system is partially perfectly[1] time-inverted, no matter how strong the potential is.

To conclude this section, we want to comment again on the derivation of the qualitative result in Eq. (4.37). Note that this discussion was only meant to figure out whether a perturbation in the Hamiltonian destroys the echo mechanism, but not to get quantitative results like the echo strength. In order to achieve this, we need to define the system at hand more precisely, as done in the preceding sections for external, static fields. Moreover, the choice of taking the eigenstates $|\varphi_{\mathbf{k},s}\rangle$ in Eq. (4.31) is not necessarily the best. Instead, an eigenstate of $H_0 + V$ would be better for the general analysis, but is usually not known. Here, only the general approach was to be made clear that yields the main message: pseudospin-independent potentials can never be effectively time-reversed, whereas pseudospin-dependent potentials might be, depending on the pulse.

4.3 Static magnetic field

In this and the next section, we want to verify the qualitative general findings above, using external, static fields. The first example is a homogeneous magnetic field perpendicular to the graphene plane, where we only consider the orbital effects, but not the spin splitting by the Zeeman term, since it does not affect the propagation of a wave packet (neglecting spin orbit coupling, which is small in graphene). Note that the cyclotron motion of wave packets in graphene with a magnetic field has been studied before [106, 107]. We want to go one step further and invert the cyclotron motion by the QTM pulse. However, magnetic fields are known to break time-reversal symmetry, as opposed to electric fields. So, the valid question arises whether an effective time-reversal by our population inversion QTM is still possible.

As before in Chap. 3, the population inversion is induced by a mass pulse ($\sigma_m = \sigma_z$), i.e.

$$H_{\text{pulse}}(t) = M\sigma_z f(t), \tag{4.38}$$

with the usual, step-like time-dependence $f(t)$ of Eq. (4.29).

[1] "Partially" because only parts of the wave packet undergo a transition (compare e.g. Sec. 3.1). "Perfectly" because these parts behave perfectly as if the were time-inverted, so they move exactly back to their initial position and also anything else what changed until the pulse is recovered.

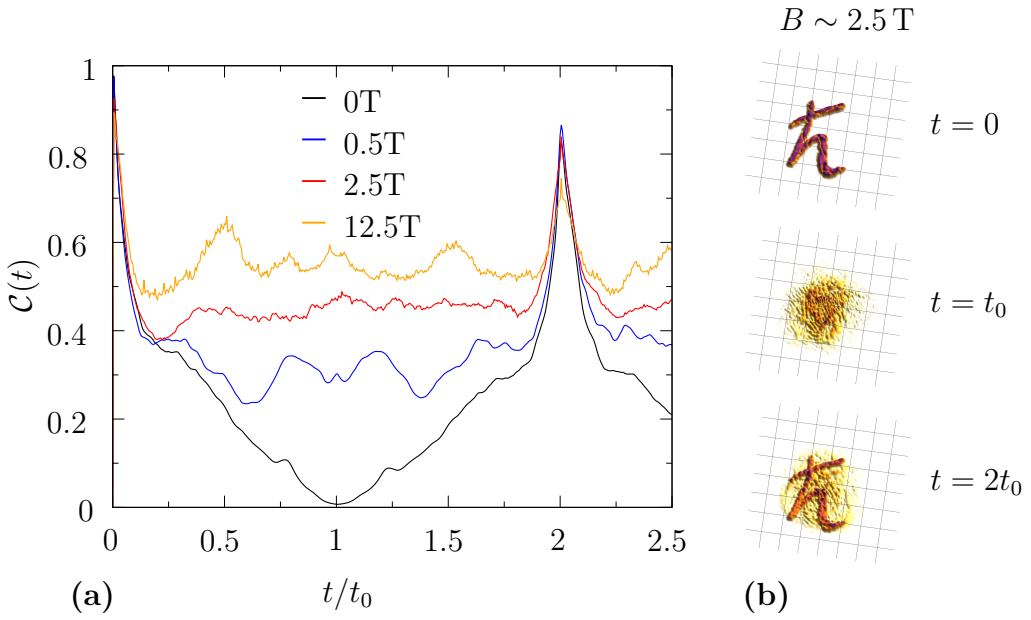

Figure 4.5: Magnetic field dependence of the Dirac QTM. (a) The correlation $\mathcal{C}(t)$ defined in Eq. (3.32) is shown as a function of time for different magnetic field strengths. Although it differs for most of the time, the echo strength $\mathcal{C}(2t_0)$ is quite independent of the magnetic field and thus, our effective time-reversal is not destroyed by breaking time-reversal symmetry by a magnetic field. (b) The snapshots correspond to the simulation of the red curve in (a), at the beginning ($t = 0$), the time of the pulse ($t = t_0$) and the echo ($t = 2t_0$). Indeed, the initial $\hbar$-shape, which is lost in the meantime, recovers nicely at the echo time. The noisy background is due to the parts of the wave packet, which have not undergone a transition by the pulse, and is not of major importance.

We use the symmetric gauge $\mathbf{A} = \frac{B}{2}(-y, x, 0)$ for the magnetic field $\mathbf{B} = (0, 0, B)$, and the Hamiltonian becomes via minimal coupling

$$H = \hbar v_F \left(\mathbf{k} + \frac{e}{\hbar}\mathbf{A}\right) \cdot \boldsymbol{\sigma} = H_0^{\perp} + V^{\perp}. \tag{4.39}$$

According to Eq. (4.37) in the general section, the parts of the Hamiltonian perpendicular to the pulse (in pseudospin) can be effectively time-reverted. Since both $H_0^{\perp}$ and $V^{\perp}$ are by definition perpendicular to the pulse, we expect the effective time-reversal to work, although time-reversal symmetry is broken, which is indeed verified in Fig. 4.5(a). There, the correlation $\mathcal{C}$ defined in Eq. (3.32) is plotted as a function of time, obtained by simulating with TQT the time-evolution of the $\hbar$-wave packet of Sec. 3.3 for different magnetic fields. The stated magnetic field strength correspond to mean wave packet energies of $\sim 100\,\mathrm{meV}$.

The correlation differs most of the time for different magnetic fields, because the stronger the magnetic field, the more localized is the propagation of the wave packet (classically: cyclotron orbits), therefore the spatial overlap is all the time larger (see also snapshots in 4.5(b). However, we are interested in the effective time reversal of a propagation, thus we want to see whether the initial state be recovered. Therefore, the relevant quantity is the echo strength, i.e. $\mathcal{C}(2t_0)$, which is largely independent of the magnetic field strength, as expected.

The snapshots for $B \sim 2.5T$ further verify the expectation. The initial wave packet stays locally in the same area and looses its shape over time (compare $t = t_0$), but at the echo time $t_{\text{echo}} \simeq 2t_0$, the initial shape is nicely recovered, where the noisy background is due to the modes which did not undergo the transition during the pulse.

The qualitative explanation for the recovery of the "$\hbar$"-shape of the wave packet is that Landau levels of positive energy, from which the initial wave packet is built up, tend to rotate in one direction, say counterclockwise. After the pulse, the parts of the wave packet which transitioned to negative Landau levels, rotate exactly opposite, i.e. clockwise, such that the "reflected" wave packet recovers its shape.

So far, we have verified the results of the general Sec. 4.2, but since the system in this section is clearly specified, we can investigate is more quantitatively. Thereto, let us consider the eigenenergies and -states of the initial system, the Landau levels in graphene, which are derived in Sec. 2.1.2:

$$E_{n,s} = s\frac{\hbar v_F}{l_B}\sqrt{2n} =: s\, E_n \tag{4.40}$$

$$|\varphi_{n,s}\rangle = \frac{1}{\sqrt{2}}\begin{pmatrix} |n-1\rangle \\ s\,|n\rangle \end{pmatrix}, \tag{4.41}$$

with $l_B = \sqrt{\hbar/eB}$ and the harmonic oscillator eigenstates $|n\rangle$. Since the sign of the energy s appears only in the lower component of Eq. (4.41), the chosen mass pulse perfectly maps Landau levels of a given energy to the negative energy:

$$\sigma_z|\varphi_{n,s}\rangle = |\varphi_{n,-s}\rangle. \tag{4.42}$$

In a similar way (compare again Sec. 2.1.2), the eigensystem during the pulse can be derived to yield

$$\varepsilon_{n,s} = s\sqrt{M^2 + E_n^2} =: s\,\varepsilon_n \tag{4.43}$$

$$|\chi_{n,s}\rangle = \frac{1}{\sqrt{2}\sqrt{\varepsilon_{n,s}^2 - \varepsilon_{n,s}M}}\begin{pmatrix} E_n|n-1\rangle \\ (\varepsilon_{n,s} - M)\,|n\rangle \end{pmatrix}. \tag{4.44}$$

The transition amplitude A_n from a Landau level $|\varphi_{n,s}\rangle$ to its energy inverted equivalent $|\varphi_{n,-s}\rangle$ is easiest obtained in analogue to unperturbed graphene as shown in the end of Sec. 3.1:

$$\begin{aligned} A_n(\Delta t) &= \langle\varphi_{n,-s} \mid U(t_0, t_0+\Delta t) \mid \varphi_{n,s}\rangle \\ &= \langle\varphi_{n,-s} \mid \frac{-i(H + M\sigma_z)}{\varepsilon_n}\sin\left(\frac{\varepsilon_n \Delta t}{\hbar}\right) \mid \varphi_{n,s}\rangle \\ &= \frac{-iM}{\varepsilon_n}\sin\left(\frac{\varepsilon_n\Delta t}{\hbar}\right)\langle\varphi_{n,-s} \mid \sigma_z \mid \varphi_{n,s}\rangle \\ &= \frac{-i}{\sqrt{1+\frac{E_n^2}{M^2}}}\sin\left(\mu\sqrt{1+\frac{E_n^2}{M^2}}\right), \end{aligned} \tag{4.45}$$

where $\langle\varphi_{n,-s} \mid H \mid \varphi_{n,s}\rangle = 0$ due to perpendicular eigenstates and the familiar $\mu = M\Delta t/\hbar$ from Chap. 3. The expansion of $U(t_0, t_0+\Delta t)$ as in Eq. (4.32) is allowed,

because $M \in \mathbb{R}$ commutes with H. Note that an explicit expansion of the initial Landau levels into the modified Landau levels during the pulse and recombination into initial Landau levels after the pulse, as done in Sec. 3.1 and visualized by Fig. 3.2, is in principle possible and yields the same result as it needs to, but due to its tediousness it is not shown here.

The first feature to notice from Eq. (4.45) is that the transition amplitude $A_n(\Delta t)$ is the same as the transition amplitude without magnetic field by replacing $E_n \leftrightarrow E_k$. Moreover, we see from calculation of Eq. (4.45) that transitions happen only between Landau level with same n but different signs s. The reason for this is the homogeneous pulse which does not change the orbital degrees of freedom and thus the harmonic oscillator eigenstates $|n\rangle$ are unaffected.

Again in analogy to Sec. 3.1, the transition amplitude for each Landau level is used to obtain the state after the pulse, which is used for instance to calculate the real space wave function after the pulse to get the echo strength, i.e. the correlation at the echo time $t_{\text{echo}} = 2t_0 + \Delta t$ (when all kinetic phases have canceled):

$$\begin{aligned}\mathcal{C}(t_{\text{echo}}) &= \int \mathrm{d}^2\mathbf{r}\, |\phi_0(\mathbf{r})|\, |\phi(\mathbf{r}, t_{\text{echo}})| \\ &= \int \mathrm{d}^2\mathbf{r} \left|\phi_0(\mathbf{r})\right| \left| \sum_{n,s} \varphi_{n,s}(\mathbf{r}) A_n(\Delta t) \langle \varphi_{n,s} \mid \phi_0 \rangle \right|, \end{aligned} \tag{4.46}$$

with $\varphi_{n,s}(\mathbf{r}) = \langle \mathbf{r} \mid \varphi_{n,s} \rangle$.

Again, the echo strength of Eq. (4.46) is similar to the case without magnetic field from Eq. (3.33), which yielded

$$\mathcal{C}(t_{\text{echo}}) = \int \mathrm{d}^2\mathbf{r} \left|\phi_0(\mathbf{r})\right| \left| \int \frac{\mathrm{d}^2\mathbf{k}}{2\pi} A(k) \phi_0(\mathbf{k}) e^{i\mathbf{k}\cdot\mathbf{r}} \right|, \tag{4.47}$$

with the difference that a discrete sum over the Landau levels instead of the integral over all $\mathbf{k}$ is to be evaluated. However, as long as the spacing between Landau levels is small as compared to the energy (width) of the wave packet, no difference is to be expected between no magnetic and small enough magnetic fields, as verified in Fig. 4.5(a). As mentioned above, small differences of the echo strength are seen there only for large magnetic fields $B \gtrsim 10\,T$, when the level spacing becomes large enough such that the deviations between sum and integral $\int \mathrm{d}\mathbf{k} \to \sum_n$ start to make a difference. Indeed, the separation of zeroth and first Landau level for $B \simeq 10\,T$ is according to Eq. (2.30): $E_1 - E_0 \simeq 100\,\text{meV}$, which is here the mean energy of our wave packet.

To conclude this section, we emphasize again that in systems where time-reversal symmetry is broken, our effective time-reversal by the population inversion QTM can work and surely does work in the specific case of graphene in a magnetic fide. The reason is that our QTM setup with a homogeneous pulse does not make use of the time-reversal symmetry, but instead the velocity has to be inverted, which is related to a chiral symmetry, i.e. $E_- = -E_+$. For more details, see also Sec. 5.1.2.

4.4 Static, in-plane electric field

The very first comment is related to the action of an electric field in graphene (or other systems with linear band structure), since it contradicts the intuition from classical physics and quantum physics in a parabolic band structure and is therefore a common source of misconceptions. Independent of the band structure, an electric field changes the momentum of a charged particle (see below), as intuitively expected. The non-intuitive part is that the velocity in the linear band structure is *not* proportional the momentum, but instead it is constant in magnitude of v_F and parallel to $\mathbf{k}$. Thus, an electric field does not lead to an acceleration ($d|\langle v\rangle|/dt = 0$) of the electrons the way it would be in parabolic bands, but only the direction of movement might change. That being said, let us define the system and investigate with regard to the QTM setup.

The Dirac Hamiltonian including a homogeneous electric field reads

$$H = \hbar v_F \mathbf{k}\cdot\boldsymbol{\sigma} + e\mathbf{E}_0\cdot\mathbf{r}\,\mathbb{1}. \tag{4.48}$$

The reason for the above mentioned change of the momentum is that the time-evolution operator related to the electric field is the translation operator in momentum space

$$\mathrm{e}^{-\frac{i}{\hbar}e\mathbf{E}_0\cdot\mathbf{r}t}\,\psi(\mathbf{k}) = \psi\left(\mathbf{k} + \frac{e\mathbf{E}_0}{\hbar}t\right). \tag{4.49}$$

Thus, in the analytical calculations, we treat the electric field as a linear shift of the momentum in time

$$\mathbf{k}(t) = \mathbf{k}(0) + \frac{e\mathbf{E}_0}{\hbar}t, \tag{4.50}$$

independent of the band, due to pseudospin independence. Note that in principle, this momentum change could lead to band transitions, because after changing $\mathbf{k}$, the eigenstate might not be the same anymore:

$$|\varphi_{\mathbf{k}(0),s}\rangle \neq |\varphi_{\mathbf{k}(t),s}\rangle, \tag{4.51}$$

or more precisely:

$$|\varphi_{\mathbf{k}(0),s}\rangle = \alpha_{\mathbf{k}}(t)|\varphi_{\mathbf{k}(t),s}\rangle + \beta_{\mathbf{k}}(t)|\varphi_{\mathbf{k}(t),-s}\rangle, \tag{4.52}$$

but we consider the adiabatic case, i.e. small electric field compared to the energy separation at a given $\mathbf{k}$.

Coming back to the QTM, the time-reversal pulse is again a mass gap

$$H_{\mathrm{pulse}}(t) = M\sigma_z f(t) \tag{4.53}$$

with the usual step-like time-dependence $f(t)$ of Eq. (4.29). In comparison with the general Sec. 4.2, we can write the Hamiltonian including an electric field of Eq. (4.48) as

$$H = H_0^{\perp} + V^{\mathbb{1}}. \tag{4.54}$$

Thus we do not expect an effective time reversal, because there is the pseudospin-independent part $V^{\mathbb{1}}$ in the Hamiltonian.

To verify the expectation, we simulate the time propagation of initially Gaussian wave packets $|\phi_0\rangle$ in an electric field in x-direction $\mathbf{E}_0 = (E_0, 0, 0)$. To be able to better compare the obtained data, we want the wave packets for different electric field to have the same mean momentum $\mathbf{k}_0(t_0)$ at the pulse time, such that the transition amplitude is independent of the electric field strength. Thus, the wave packet is initially peaked in reciprocal space around

$$\mathbf{k}_0(t = 0) = \mathbf{k}_0(t_0) - \frac{eE_0}{\hbar}\hat{\mathbf{e}}_x t_0. \tag{4.55}$$

The $\mathbf{k}$-space width of the wave packet Δk is chosen in the simulations to be $\Delta k = |\mathbf{k}_0(t_0)|/8$.

In Fig. 4.6, the echo strength as function of electric field for certain simulations is evaluated by both the correlation $\mathcal{C}$ defined in Eq. (3.32) as otherwise used in this thesis, and the echo fidelity m defined in Eq. (4.19), which are qualitative different, as explained below. We choose a negative $k_{0,x}$ such that electric field first decreases the magnitude of the momentum and brings it closer to the **K**-point, where exceptions are expected (see also below). The normalization of the electric field strength E_{ref} is the strength at which the change of $\mathbf{k}$ due to the electric field is the same as the momentum at the time of the pulse $\mathbf{k}_0(t_0)$:

$$E_{\text{ref}} = \frac{\hbar|\mathbf{k}_0(t_0)|}{et_0}. \tag{4.56}$$

For typical wave vectors such that the energy is $\hbar v_F|\mathbf{k}_0(t_0)| = 100\,\text{meV}$ and propagation times $t_0 \simeq 1\,\text{ps}$, the reference electric field corresponds to $E_{\text{ref}} \simeq 10^5\,\text{V/m}$.

Analytically, the echo fidelity of Eq. (4.19) at the usual echo time $t_{\text{echo}} = 2t_0 + \Delta t$ becomes the overlap of Gaussians that have moved away from each other in $\mathbf{k}$-space due to the change of $\mathbf{k}$ over time in Eq. (4.50) (for calculation, compare also Eqs. (C.4) and (C.5)):

$$m(2t_0 + \Delta t) = |\langle \sigma_z \phi_0 \mid U(0, t_{\text{echo}}) \mid \phi_0 \rangle| = \exp\left(-\frac{e^2 E_0^2 t_{\text{echo}}^2}{4\Delta k^2}\right). \tag{4.57}$$

Compared to the simulation (green squares) in Fig. 4.6, the expected echo fidelity (red line) of Eq. (4.57) indeed matches the data well.

Thus, the expected result of the general section namely that no time-reversal is possible seems to be true, or can we somehow circumvent the inevitable destruction of the echo for larger and larger electric fields?

In that regard, the special velocity structure of graphene[2] might help:

$$\langle \varphi_{\mathbf{k}(t),s} \mid \hat{\mathbf{v}} \mid \varphi_{\mathbf{k}(t),s} \rangle = s \begin{pmatrix} \cos\gamma_{\mathbf{k}}(t) \\ \sin\gamma_{\mathbf{k}}(t) \end{pmatrix} \tag{4.58}$$

If $\gamma_{\mathbf{k}}(t)$ changes, there is no hope, at least for strong enough electric fields, because then, the direction of propagation changes, which is not inverted by the pulse. On the other hand, for $\mathbf{k}_0(t = 0) \parallel \mathbf{E}_0$ and a very narrow angular width Δk of the wave packet in $\mathbf{k}$-space, the angle $\gamma_{\mathbf{k}}(t) = \gamma_{\mathbf{k}}(0)$ is a constant over time. Thus, the mean

[2] possibly also in other systems, see the discussion in the end of this section

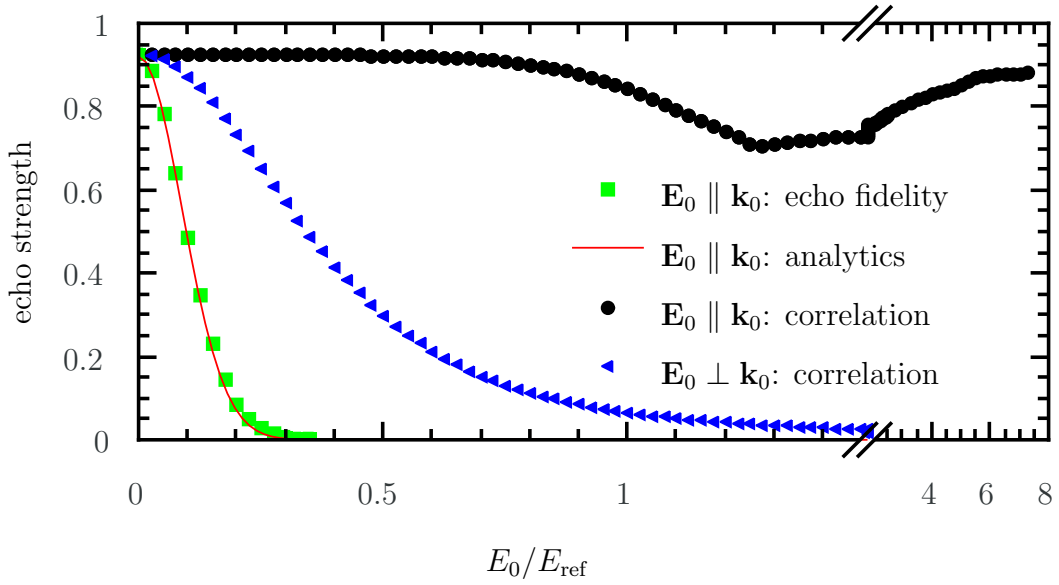

Figure 4.6: Effect of an electric field to the Dirac QTM. Although the system is not effectively time-reversed, as shown by the echo strength measured by the echo fidelity (green squares) and the analytical prediction of Eq. (4.57) as well as the case of $\mathbf{E}_0 \perp \mathbf{k}_0$ (blue triangles), a high quality echo can still be achieved in the case of a propagation direction parallel to the electric field. This is due to the special velocity of a linear band structure, which is independent of $|\mathbf{k}|$ but depends only on its direction. Therefore, the mean velocity of the wave packet can be mapped to $\langle\hat{\mathbf{v}}\rangle \to -\langle\hat{\mathbf{v}}\rangle$. The only problem arises when the electric field is strong enough to bring the mean momentum to $\mathbf{k} \simeq 0$, i.e. $E_0 \simeq E_{\mathrm{ref}}$, because there, the modes in the wave packet with $\mathbf{k} \nparallel \mathbf{E}_0$ move away from the wave packet for any finite width Δk.

velocity of the wave packet is $\langle v_x\rangle = sv_F$ before the transition and $\langle v_x\rangle = -sv_F$ in the opposite direction after the transition. Therefore, the wave packet is expected to come back to the initial at $t_{\mathrm{echo}} = 2t_0 + \Delta t$ resulting in an echo.

Indeed this $\mathbf{k}$-direction dependence of the echo can seen in Fig. 4.6. For $\mathbf{E}_0 \perp \mathbf{k}_0(t_0)$ the echo decays as a function of the electric field E_0 (blue triangles), whereas for $\mathbf{E}_0 \parallel \mathbf{k}_0(t_0)$ (black dots), the echo is for $E_0 < E_{\mathrm{ref}}$ independent of the electric field. The only problem and reason, why the echo strength decreases in the parallel, is when the electric field is strong enough ($E_0 \simeq 1$) such that $\mathbf{k} = 0$ is crossed. In that case, the "narrow" angular width ($\Delta k \ll |\mathbf{k}_0(t)|$) cannot be achieved for any finite width Δk.[3] Otherwise said, the wave packet does not only consist of $\mathbf{k}$-modes parallel to the electric field. This becomes more important, the closer we get to $\mathbf{k} = 0$ due to the electrical field, because then, the different modes start to move in different directions, which cannot be reversed by our QTM. However, if the passage through $\mathbf{k} = 0$ is fast enough ($E_0 \gtrsim 2$), such that the wave packet does not have enough time to change its shape distinctively during the transition of $\mathbf{k} = 0$, the echo gets again larger and even close to its value without electric field.

To conclude this section, we want to stress again the major feature of the QTM

[3] the adiabaticity is also not necessarily given

in an electric field. As generally expected, the pseudospin-independent term in the Hamiltonian due to the electric field causes the wave packet not to be effectively time-inverted after switching bands. Nevertheless there are observables, like the correlation $\mathcal{C}$, where an echo can be seen. This is similar to the Hahn echo, where the system is not effectively time-inverted (the spins do not precess in the opposite direction after the π-pulse), but still the initial spin configuration is (partly) recovered in the sense that the spins rephase, such that an signal can be measured.

As a final comment and preview to the next chapter, where the QTM in arbitrary two-band systems is considered, we want to mention that the echo of the wave function in presence of an electric field despite the fact that the system is not effectively time reversible, is not necessarily related to the linear band structure. The important feature is that the electric field is (essentially) parallel to the propagation direction of the wave packet and that after the pulse, all reflected modes come back at the same time, although they change their momentum. Although we do not show it here, preliminary calculations suggest that this could be possible in a band structure consisting of two parabolic bands with curvature $a > 0$ and $b < 0$.

4.5 Conclusion and outlook

In this chapter, we studied the effects of perturbation to our Dirac-QTM. First, we considered the consequences of static disorder in Sec. 4.1. As opposed to the spin echo, the wave packet cannot be effectively time-reversed in presence of static disorder, because of the inherent motion of the wave packet through the disturbed system. Thus, this is not in contradiction with the spin echo, which would also be affected by static disorder (of the local magnetic field), if the spins moved through the system.

Although not discussed, we assume that intervalley scattering due to short-range potentials, i.e. scattering in the Brillouin zone from $\mathbf{K}$ to $\mathbf{K}'$, is supposed to affect the QTM in the same way as the considered intravalley scattering: the pulse will also flip the propagation direction but the scattering events on the way back are independent from the scattering events before the pulse. Therefore, the scattered parts of the wave function are lost for the echo.

In Sec. 4.2, we studied qualitatively the effects of a general perturbation to a general two-band system, to be able to predict whether some perturbation affect the effective time-reversal of our QTM setup, or not. The used time-reversal pulse is assumed to be homogeneous and $\mathbf{k}$-independent, i.e. only the pseudospin degree of freedom is changed. The result is that while pseudospin-*in*dependent parts in the Hamiltonian (including the perturbation) cannot be effectively time-reverted, pseudospin-*dependent* parts can be, depending on the exact system and pulse.

In the remaining of the chapter, we investigated the QTM setup for static, homogeneous external fields. The magnetic field is considered in Sec. 4.3. According to the general predictions of Sec. 4.2 and despite breaking time-reversal symmetry, the magnetic field does not destroy our effective time-reversal and the echo strength is largely independent of the strength of the magnetic field.

An interesting feature is found in the case of an electric field: although an effective time-inversion is not possible, a system can behave in some parts as if it was

time-reversed, e.g. that an echo happens. The reason in this case is that the velocity is mapped from $\mathbf{v} \to -\mathbf{v}$, but other observables might not be "time-inverted". In the example of the electric field in Sec. 4.4, the change of the momentum $\mathbf{k}$ due to the pseudospin-independent electric field is not inversed. Nevertheless, for parallel propagation direction of the wave packet related to the electric field, the initial position can be still recovered, because the velocity reversed.

So far, the pulses used the pseudospin structure to initiate the transition to the other band. But in principle, also other mechanisms are possible, using for instance time-dependent external fields. An example is to apply a time-dependent electric field to make use of a Landau-Zener-Stückelberg interference. By non-adiabatic driving of the momentum through the effective gap ($k_y \neq 0$), the state splits into the two bands, each part accumulating a different phase. Changing the sign of the electric field initiates a second transition through the gap, where each part splits again. Due to the different phases, the individual parts interfere (Landau-Zener-Stückelberg interference). Depending on the used parameters, an almost perfect destructive interference can be achieved in the initial band, such that almost 100% of the wave packet switch the band. First simulations could verify the almost perfect constructive interference for band switching. For large enough electric fields and thus short enough pulses, the spreading of the wave packet due to the change of the propagation direction (since $\mathbf{k}$ is changed) are negligible and a nice echo is visible. The only problem, as always for in-plane electric fields, is that it works well only for certain initial propagation directions of the wave packet. Thus, the echo of a radial spreading wave packet like the "$\hbar$" in Fig. 3.8 is not assumed to be very good.

Another idea is to use a time-dependent magnetic field as time-reversal pulse to switch the propagation direction. The idea is the following: we always used a pulse proportional to σ_z to open a gap and make the state switch bands. Instead one could in principle use a magnetic field to open gaps by the Landau quantization. The magnetic field has to be appropriately large such that the splitting of the Landau levels is at least in the range of the energy width of the wave packet. First simulation verified the this is in principle possible. The mechanism is that during the pulse, any $\mathbf{k}$-mode splits into many Landau levels (also with negative energy) and after the pulse, modes with negative energies are occupied. Analytical calculation could verify the action of the pulse and are in agreement with the simulations. Although the procedure is clear from a theoretical point of view, the remaining challenge is to find a suitable physical configuration of the fields, since a time-dependent magnetic field will always be accompanied by a (strong) electric field. Again, it is important that the wave packet does not considerably move during the pulse because else, its propagation direction will change due to the change of momentum in the magnetic field.

In the next chapter, we want to further generalize the QTM. Although the general Sec. 4.2 did not explicitly deal with a linear band structures, the underlying system in the examples has always been graphene (or any other system described by the Dirac cone band structure) so far. Below, we will study homogeneous (clean) two-band systems in general with regard to our population inversion QTM, where in principle, the results of perturbations of Sec. 4.2 can be applied analogously.

Chapter 5

Quantum time mirror for general two-band systems

In the previous chapters, we investigated the population inversion time mirror for graphene, i.e a two level system with linear, chiral symmetric bands. The nice feature is the constant absolute velocity of the **k**-modes, but opposite propagation directions in the two bands. In this chapter, we want to generalize the results to a broader range of two-band Hamiltonians. Indeed, we will see that neither the linear bands, nor perfect chiral symmetry are necessary conditions for the echo.

First, we will consider the QTM in general two-band systems and derive the general transition amplitude and derive general requirements to the band structure related to the corresponding velocity of the two bands (Sec. 5.1). Then, we will check the general results for three examples. The first one is a toy Hamiltonian with linear bands but different slopes for positive and negative energies (Sec. 5.2), i.e. without chiral symmetry. Then we investigate the echo mechanism for an initial hyperbolic band structure in Sec. 5.3 showing that the linear band structure is not important. Finally, in Subsec. 5.4, we combine the two setups, meaning a nonlinear band structure without chiral symmetry, i.e. parabolic bands with different curvatures.

5.1 General theory of the QTM for two-band systems

5.1.1 Transition amplitude

We first investigate the general case of homogeneous two-band systems

$$H_0(\mathbf{k}) = \sum_{i=0}^{3} h_0^i(\mathbf{k})\sigma_i = h_0^0(\mathbf{k})\mathbb{1} + h_0^{\mathrm{ps}}(\mathbf{k})\hat{\mathbf{n}}_{\mathbf{k}} \cdot \boldsymbol{\sigma} = H_0^0 + H_0^{\mathrm{ps}}, \tag{5.1}$$

where $h_0^{\mathrm{ps}} = \sqrt{(h_0^x)^2 + (h_0^y)^2 + (h_0^z)^2}$ is the modulus of the pseudospin-dependent part of the initial Hamiltonian. In general, the Pauli matrices σ_i appearing in the Hamiltonian need not be a pseudospin operator in the sense of the pseudospin in graphene, but anything that generates two bands in the Hamiltonian, e.g. the spin

in a 2d topological insulator. However, for consistency, we will continue to denote it by pseudospin.

Concerning the notation in Eq. (5.1) and in the rest of this chapter, capital H means that the Pauli matrices in pseudospin space are included, whereas lowercase letters h are scalars in pseudospin space, but can still depend on the momentum operator $\mathbf{k}$. Note that the general Hamiltonian is defined differently to Sec. 4.2, because different features are to be stressed here.

The direction of the Hamiltonian in pseudospin space $\hat{\mathbf{n}}_\mathbf{k}$ (see also Fig. 5.1) is given in usual spherical coordinates

$$\hat{\mathbf{n}}_\mathbf{k} = \begin{pmatrix} \cos\gamma_\mathbf{k} \sin\vartheta_\mathbf{k} \\ \sin\gamma_\mathbf{k} \sin\vartheta_\mathbf{k} \\ \cos\vartheta_\mathbf{k} \end{pmatrix}. \tag{5.2}$$

The $\mathbf{k}$-dependence of the terms in the Hamiltonians is omitted henceforth. The corresponding eigenstates and energies are denoted by

$$E_{\mathbf{k},\pm} = h_0^0 \pm h_0^\mathrm{ps} = h_0^0 \pm \sqrt{(h_0^x)^2 + (h_0^y)^2 + (h_0^z)^2}, \tag{5.3}$$

$$|\varphi_{\mathbf{k},+}\rangle = \begin{pmatrix} \cos\frac{\vartheta_\mathbf{k}}{2} \\ \sin\frac{\vartheta_\mathbf{k}}{2}\, \mathrm{e}^{i\gamma_\mathbf{k}} \end{pmatrix}, \tag{5.4}$$

$$|\varphi_{\mathbf{k},-}\rangle = \begin{pmatrix} \sin\frac{\vartheta_\mathbf{k}}{2} \\ -\cos\frac{\vartheta_\mathbf{k}}{2}\, \mathrm{e}^{i\gamma_\mathbf{k}} \end{pmatrix}. \tag{5.5}$$

We assume a homogeneous and $\mathbf{k}$-independent pulse of the form

$$H_\mathrm{pulse} = \sum_{i=1}^{3} \Lambda^i \sigma_i, \tag{5.6}$$

such that the full Hamiltonian reads

$$H = H_0 + f(t) H_\mathrm{pulse}. \tag{5.7}$$

Note that there is no pseudospin-independent term in the homogeneous pulse Hamiltonian, since it would only lead to a (constant) shift of the energy but no transitions and thus, it would have physically no impact.

For simplicity, the time-dependence is chosen as in the chapters before

$$f(t) = \begin{cases} 1, & t_0 < t < t_0 + \Delta t, \\ 0, & \text{otherwise}, \end{cases}, \tag{5.8}$$

to enable analytical calculations.

Let us rewrite the pulse Hamiltonian to better relate it to the initial Hamiltonian H_0:

$$H_\mathrm{pulse} = \left(\Lambda^\parallel \hat{\mathbf{n}}_\mathbf{k} \cdot \boldsymbol{\sigma} + \Lambda^\perp \hat{\mathbf{m}}_\mathbf{k} \cdot \boldsymbol{\sigma}\right) = \Lambda^\parallel \sigma_\mathbf{n} + \Lambda^\perp \sigma_\mathbf{m} \tag{5.9}$$

with $\hat{\mathbf{m}}_\mathbf{k} \perp \hat{\mathbf{n}}_\mathbf{k}$, such that $\Lambda^\parallel$ and $\Lambda^\perp$ belong to the part of the pulse parallel or perpendicular to H_0 in pseudospin space, respectively. For brevity, we have introduced the notation $\sigma_\mathbf{n} = \hat{\mathbf{n}}_\mathbf{k} \cdot \boldsymbol{\sigma}$ and $\sigma_\mathbf{m} = \hat{\mathbf{m}}_\mathbf{k} \cdot \boldsymbol{\sigma}$.

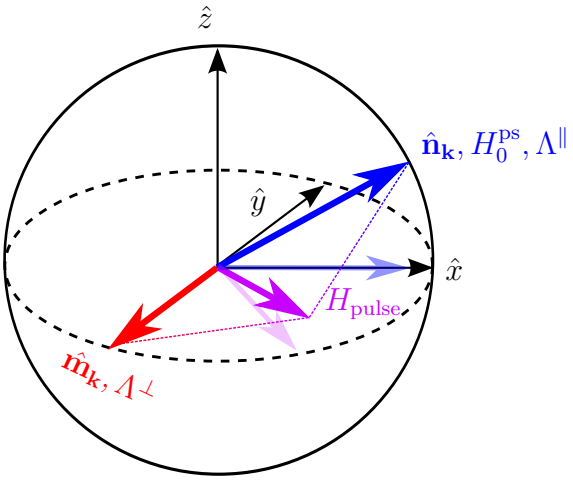

Figure 5.1: The directions of the initial Hamiltonian H_0 of Eq. (5.1) and the pulse Hamiltonian H_{pulse} of Eq. (5.9) for a general two-band system in the Bloch sphere. $\hat{\mathbf{n}}_\mathbf{k}$ (blue) is the direction of the pseudospin-dependent part of the initial Hamiltonian H_0^{ps}. The pulse Hamiltonian H_{pulse} (purple arrow) is in general a linear combination of parts parallel to $\hat{\mathbf{n}}_\mathbf{k}$ ($\Lambda^{\parallel}$) and in some direction $\hat{\mathbf{m}}_\mathbf{k} \perp \hat{\mathbf{n}}_\mathbf{k}$ (red arrow) with magnitude $\Lambda^{\perp}$. Only the perpendicular parts of the pulse $\Lambda^{\perp}$ lead to a transition (compare Eq. (5.16)), because they lead to a rotation of the initial eigenstates on the Bloch sphere. The transparent arrows are the projections to the x-y-plane, for better spatial awareness.

During the pulse, the eigenenergies become

$$\varepsilon_{\mathbf{k},\pm} = h_0^0 \pm \hbar\Omega_\mathbf{k}, \tag{5.10}$$

where we have defined a new frequency,

$$\hbar\Omega_\mathbf{k} = \sqrt{\sum_{i=1}^{3} \left(h_0^i + \Lambda^i\right)^2} = \sqrt{\left(h_0^{\mathrm{ps}} + \Lambda^{\parallel}\right)^2 + \left(\Lambda^{\perp}\right)^2}, \tag{5.11}$$

which will become important for the transition amplitude below.

Now let us study the QTM mechanism, more precisely the transition of one band to the other. This calculation is analogous to the graphene case at the end of Sec. 3.1, but for a general band structure. We want to know the quantum mechanical amplitude for a transition during the pulse ($t_0 \to t_0 + \Delta t$) from a given eigenstate $|\varphi_{\mathbf{k},s}\rangle$ to the other band $|\varphi_{\mathbf{k},-s}\rangle$, which is

$$A_s(\mathbf{k}) = \langle \varphi_{\mathbf{k},-s} \mid \exp\left\{-\frac{i}{\hbar}\left(H_0 + H_{\mathrm{pulse}}\right)\Delta t\right\} \mid \varphi_{\mathbf{k},s}\rangle. \tag{5.12}$$

Note that the propagations before and after the pulse are trivial since we consider eigenstates of H_0.

To simplify the expression, the identity of Eq. (3.28) for exponentials of Pauli matrices of Sec. 3.1 can be applied, because all prefactors of the Pauli matrices are functions only of the momentum operator, but not of the position operator, such

that they commute. The transition amplitude then becomes

$$A_s(\mathbf{k}) = \mathrm{e}^{-\frac{i}{\hbar}h_0^0\Delta t}\langle\varphi_{\mathbf{k},-s} \mid \cos(\Omega_{\mathbf{k}}\Delta t)\,\mathbb{1} - \frac{i\sin(\Omega_{\mathbf{k}}\Delta t)}{\hbar\Omega_{\mathbf{k}}}\left[(h_0^{\mathrm{ps}} + \Lambda^{\parallel})\boldsymbol{\sigma}_{\mathbf{n}} + \Lambda^{\perp}\boldsymbol{\sigma}_{\mathbf{m}}\right] \mid \varphi_{\mathbf{k},s}\rangle. \tag{5.13}$$

Since by definition

$$\boldsymbol{\sigma}_{\mathbf{n}}\,|\varphi_{\mathbf{k},s}\rangle = s|\varphi_{\mathbf{k},s}\rangle = s\mathbb{1}|\varphi_{\mathbf{k},s}\rangle \tag{5.14}$$

and due to the orthogonality in pseudospin space of the eigenstates $|\varphi_{\mathbf{k},s}\rangle$ for every $\mathbf{k}$,

$$\langle\varphi_{\mathbf{k},s'} \mid \varphi_{\mathbf{k},s}\rangle = \delta_{ss'}, \tag{5.15}$$

only the $\Lambda^{\perp}$-term in Eq. (5.13) survives. Moreover, since $\hat{\mathbf{m}}_{\mathbf{k}} \perp \hat{\mathbf{n}}_{\mathbf{k}}$, $\boldsymbol{\sigma}_{\mathbf{m}}$ is the transition operator which maps an eigenstate to the other band

$$\boldsymbol{\sigma}_{\mathbf{m}}\,|\varphi_{\mathbf{k},s}\rangle = \mathrm{e}^{i\alpha}|\varphi_{\mathbf{k},-s}\rangle. \tag{5.16}$$

This can be seen geometrically in the Bloch sphere (compare Fig. 5.1), where the operator $\boldsymbol{\sigma}_{\mathbf{m}}$ is a rotation of π around the direction $\hat{\mathbf{m}}$. The phase $\mathrm{e}^{i\alpha}$ in Eq. (5.16) depends on the exact definition of the eigenstates, which is again arbitrary up to some phase, such that with the right choice of the eigenstates, we get $\mathrm{e}^{i\alpha} = 1$.

Therefore, the transition amplitude becomes

$$A_s(\mathbf{k}) = \frac{-i\Lambda^{\perp}}{\hbar\Omega_{\mathbf{k}}}\mathrm{e}^{-\frac{i}{\hbar}h_0^0\Delta t}\sin(\Omega_{\mathbf{k}}\Delta t)\,. \tag{5.17}$$

So, let us discuss the individual terms of the transition amplitude in more detail with regard to their effect on a possible QTM echo. The oscillations as function of Δt in the sin-term are due to interference of the two possible paths (positive eigenstate or negative eigenstate of the pulse Hamiltonian, see also Sec. 3.1 and Fig. 3.2). Tuning the pulse length Δt during a certain setup, it can be always brought close to 1 and thus, it is in principle not the limiting factor for the echo. Similarly, the phase factor $\mathrm{e}^{-\frac{i}{\hbar}h_0^0\Delta t}$ of magnitude 1 is not of important for the transition strength for a given $\mathbf{k}$, but it influences the time of the (possible) echo t_{echo} in linear order of Δt, which is supposed to be small. It will be discussed below in more detail for the examples with non-chiral band structure, i.e. $E_-(\mathbf{k}) \neq -E_+(\mathbf{k})$.

The prefactor $\frac{\Lambda^{\perp}}{\hbar\Omega_{\mathbf{k}}}$ on the other hand strongly affects the transition strength for a given setup. Rearranging this prefactor by substituting $\Omega_{\mathbf{k}}$ from Eq. (5.11) to better see its dependences on the individual terms, it yields

$$\frac{|\Lambda^{\perp}|}{\hbar\Omega_{\mathbf{k}}} = \frac{1}{\sqrt{1 + \dfrac{(h_0^{\mathrm{ps}} + \Lambda^{\parallel})^2}{(\Lambda^{\perp})^2}}} \leq 1. \tag{5.18}$$

Note that it is smaller (or equal) to one, such that the normalization of the wave function is not violated. Moreover, for a good transition, this prefactor has to be close to one, which happens if both conditions

$$|\Lambda^{\perp}| \gg |\Lambda^{\parallel}| \quad \text{and} \quad |\Lambda^{\perp}| \gg |h_0^{\mathrm{ps}}| \tag{5.19}$$

are met. Hence, the part of the pulse perpendicular to the initial Hamiltonian has to be the dominant energy term during the pulse (not considering the $\mathbb{1}$-term). Alternatively, one could try to cancel h_0^{ps} by $\Lambda^{\parallel}$, i.e. $\Lambda^{\parallel} = -h_0^{\mathrm{ps}}(\mathbf{k})$, because in that case, Eq. (5.18) yields one. However, since we are assuming a $\mathbf{k}$-independent pulse, the cancellation will happen only for certain $\mathbf{k}$. Even for $\mathbf{k}$-dependent pulses, it is in most cases rather unlikely that they can cancel. Therefore, this case is not further investigated.

For the transition amplitude in Eq. (5.17), geometrical considerations are necessary in order to obtain $\Lambda^{\perp}$. Although it is in principle possible, it might be tedious in some cases. Therefore, we state an alternative version of Eq. (5.17),

$$A_s(\mathbf{k}) = \frac{-i}{\hbar\Omega_{\mathbf{k}}} \mathrm{e}^{-\frac{i}{\hbar}h_0^0\Delta t} \sin\left(\Omega_{\mathbf{k}}\Delta t\right) \, \langle \varphi_{\mathbf{k},-s} \mid H_{\mathrm{pulse}} \mid \varphi_{\mathbf{k},-s} \rangle, \tag{5.20}$$

where instead the tedious part is to calculate the matrix elements of H_{pulse}. However, it might be more convenient in some cases than the geometrical considerations, as we will see below in the examples.

Thus, the transition from one to the other band by a time-dependent, homogeneous pulse is known for any initial wave packet in a general two-band system. However, a transition does not necessarily mean that the propagation after the pulse is effectively time-inverted. Therefore, we investigate in the next subsection under which conditions of the initial system, echoes of the wave function are possible.

5.1.2 Effective time reversal and wave packet echo

The effective time-reversal in a more general case has already been discussed in Sec. 4.2, but for homogeneous Hamiltonians, we can go into more details. Let us consider the propagation of the part of an eigenstate $|\varphi_{\mathbf{k},s}\rangle$ which switches band until some time after the pulse $t' = t_0 + \Delta t + t_1$:

$$\langle \varphi_{\mathbf{k},-s} \mid U(0,t') \mid \varphi_{\mathbf{k},s} \rangle = \langle \varphi_{\mathbf{k},-s} \mid \mathrm{e}^{-\frac{i}{\hbar}H_0 t_1} \mathrm{e}^{-\frac{i}{\hbar}(H_0+H_{\mathrm{pulse}})\Delta t} \mathrm{e}^{-\frac{i}{\hbar}H_0 t_0} \mid \varphi_{\mathbf{k},s} \rangle \tag{5.21}$$

Since $|\varphi_{\mathbf{k},s}\rangle$ is an eigenstate of H_0 and thus only acquires some phase until the pulse and remains otherwise unchanged, the time evolution during the pulse reduces to the transition amplitude times $\sigma_{\mathbf{m}} = \hat{\mathbf{m}}_{\mathbf{k}} \cdot \boldsymbol{\sigma}$:

$$\begin{aligned}
\langle \varphi_{\mathbf{k},-s} \mid U(0,t') \mid \varphi_{\mathbf{k},s} \rangle &= A_s(\mathbf{k}) \langle \varphi_{\mathbf{k},s} \mid \sigma_{\mathbf{m}} \mathrm{e}^{-\frac{i}{\hbar}(H_0^0+H_0^{\mathrm{ps}})t_1} \sigma_{\mathbf{m}} \mathrm{e}^{-\frac{i}{\hbar}(H_0^0+H_0^{\mathrm{ps}})t_0} \mid \varphi_{\mathbf{k},s} \rangle \\
&= A_s(\mathbf{k}) \langle \varphi_{\mathbf{k},s} \mid \mathrm{e}^{-\frac{i}{\hbar}\sigma_{\mathbf{m}}(H_0^0+H_0^{\mathrm{ps}})\sigma_{\mathbf{m}} t_1} \mathrm{e}^{-\frac{i}{\hbar}(H_0^0+H_0^{\mathrm{ps}})t_0} \mid \varphi_{\mathbf{k},s} \rangle \\
&= A_s(\mathbf{k}) \langle \varphi_{\mathbf{k},s} \mid \mathrm{e}^{-\frac{i}{\hbar}(H_0^0-H_0^{\mathrm{ps}})t_1} \mathrm{e}^{-\frac{i}{\hbar}(H_0^0+H_0^{\mathrm{ps}})t_0} \mid \varphi_{\mathbf{k},s} \rangle.
\end{aligned} \tag{5.22}$$

As expected from Sec. 4.2, the pseudospin-*dependent* term of the initial Hamiltonian H_0^{ps} changes its sign in the exponential, which means that it is effectively time-reversed, as opposed to the pseudospin-*in*dependent part H_0^0. At first sight, this seems to imply that only for $H_0^0 = 0$ (or constant) and thus chiral symmetric band structures ($E_{\mathbf{k},-} = -E_{\mathbf{k},+}$), the QTM is expected to work. However, already in the case of an electric field in Sec. 4.4, we have seen that although the system could not be (effectively) time-reversed, an echo can be possible. The important quantity to look at is the velocity, respectively its expectation value for the two

energy eigenstates at a given $\mathbf{k}$. Let us assume a wave packet living in one band, say $s = +$. The translation vector $\mathbf{d_k}$ of a (reflected) plane wave at time $t' = t_0 + \Delta t + t_1$ is given by

$$\mathbf{d_k}(t') = \langle \hat{\mathbf{v}} \rangle_{\mathbf{k},+} t_0 + \langle \hat{\mathbf{v}} \rangle_{\mathbf{k},-} t_1, \tag{5.23}$$

where the subscript $\mathbf{k}, \pm$ means that the expectation value is taken with the eigenstates with $\mathbf{k}$ of the corresponding band. Note that we assume a short pulse, such that a considered wave packet does not move considerably during the pulse, which is why Δt is omitted here. An echo will happen, if all modes of this wave packet come back at the same time:

$$\mathbf{d_k}(t_{\text{echo}}) \stackrel{!}{=} 0, \;\; \forall \mathbf{k} \quad \Leftrightarrow \quad \langle \hat{\mathbf{v}} \rangle_{\mathbf{k},-} = -\frac{t_0}{t_{\text{echo}} - t_0} \langle \hat{\mathbf{v}} \rangle_{\mathbf{k},+}, \;\; \forall \mathbf{k} \tag{5.24}$$

which means that the velocities in the two bands have to be related by a $\mathbf{k}$-*in*dependent constant $\xi_v > 0$:

$$\langle \hat{\mathbf{v}} \rangle_{\mathbf{k},-} = -\xi_v \langle \hat{\mathbf{v}} \rangle_{\mathbf{k},+} \tag{5.25}$$

Thus, let us find out what the requirements are for the Hamiltonian H_0 of Eq. (5.1) to fulfill Eq. (5.25). For that, recall that the velocity operator is defined as

$$\hat{\mathbf{v}} = \nabla_{\mathbf{k}} H, \tag{5.26}$$

and thus the requirement of Eq. (5.25) becomes

$$\begin{aligned}
\langle \varphi_{\mathbf{k},-} \mid \nabla_{\mathbf{k}} H_0 \mid \varphi_{\mathbf{k},-} \rangle &= -\xi_v \langle \varphi_{\mathbf{k},+} \mid \nabla_{\mathbf{k}} H_0 \mid \varphi_{\mathbf{k},+} \rangle \\
\langle \varphi_{\mathbf{k},+} \mid \sigma_{\mathbf{m}} \nabla_{\mathbf{k}} H_0 \sigma_{\mathbf{m}} \mid \varphi_{\mathbf{k},+} \rangle &= -\xi_v \langle \varphi_{\mathbf{k},+} \mid \nabla_{\mathbf{k}} H_0 \mid \varphi_{\mathbf{k},+} \rangle \\
\langle \varphi_{\mathbf{k},+} \mid \nabla_{\mathbf{k}} (H_0^0 - H_0^{\text{ps}}) \mid \varphi_{\mathbf{k},+} \rangle &= -\xi_v \langle \varphi_{\mathbf{k},+} \mid \nabla_{\mathbf{k}} (H_0^0 + H_0^{\text{ps}}) \mid \varphi_{\mathbf{k},+} \rangle \\
\Rightarrow (1 + \xi_v) \nabla_{\mathbf{k}} H_0^0 + (\xi_v - 1) \nabla_{\mathbf{k}} H_0^{\text{ps}} &= 0
\end{aligned} \tag{5.27}$$

which is fulfilled only if

$$\nabla_{\mathbf{k}} H_0^0 = \frac{1 - \xi_v}{1 + \xi_v} \nabla_{\mathbf{k}} H_0^{\text{ps}}, \quad \forall \mathbf{k}. \tag{5.28}$$

Therefore, even if a perfect time-reversal is not possible ($H_0^0 \neq$const), there still can be an echo, if the requirement of Eq. (5.25), and thus Eq. (5.28) are met. This can happen in bands with different velocities. In this situation, the propagation after switching the band is different (slower/faster) to before the pulse, but still an echo can happen as long as all modes come back at the same time, as we will show in the examples of Secs. 5.2 and 5.4.

Note that the requirement of "all modes come back at the same time" is not very strict. Even if this is not perfectly met, there will be an echo to some extent, but the stronger the deviations, the more blurred the echo becomes, since different $\mathbf{k}$-modes come back at different times. In real materials, Eq. (5.28) will never be completely true, but as long as it holds well enough, e.g. over the width of the wave packet, the QTM mechanism in principle works.

For completeness, the echo time becomes in general for a transition from positive to negative energy

$$t_{\text{echo}}^{+} = \left(1 + \xi_v^{-1}\right) t_0 + \frac{1 + \xi_v^{-1}}{2} \Delta t, \tag{5.29}$$

and for transitions from the negative to the positive band:

$$t_{\text{echo}}^{+} = (1+\xi_v)\, t_0 + \frac{1+\xi_v}{2}\Delta t. \tag{5.30}$$

The graphene Hamiltonian of Sec. 3.1 is obtained by substituting

$$h_0^{\text{ps}} = \hbar v_F k, \tag{5.31}$$
$$h_0^{0} = 0, \tag{5.32}$$
$$\Lambda^{\parallel} = 0, \tag{5.33}$$
$$\Lambda^{\perp} = M. \tag{5.34}$$

The general formulas for the transition amplitude then yield

$$A^{\text{graphene}}(k) = \frac{-i}{\sqrt{1+\hbar^2 v_F^2 k^2/M^2}} \sin\left(\frac{M\Delta t}{\hbar}\sqrt{1+\hbar^2 v_F^2 k^2/M^2}\right) \tag{5.35}$$

and the echo time becomes

$$t_{\text{echo}}^{\text{graphene}} = 2t_0 + \Delta t, \tag{5.36}$$

which match the expected results (compare e.g. Eq. (3.21)).

One last comment is that **k**-dependent pulses, e.g. by switching on and off spin-orbit coupling, are in general no problem and can be treated in the same way as shown in this section. The only problem might be a possible pseudospin-independent term $\Lambda^{\mathbb{1}}(vk)\mathbb{1}$, which leads to a noninvertable motion during the pulse. For short pulses however, i.e. when the wave packet does not have enough time to considerably move during the pulse, this effect is negligible. For long pulses, one can derive the following requirement that this term does not affect the echo but only shifts the echo time, similarly to Eq. (5.28):

$$\nabla_{\mathbf{k}}\Lambda^{\mathbb{1}}(vk) = \xi_h \nabla_{\mathbf{k}} H_0^{\text{ps}}, \quad \forall \mathbf{k}, \tag{5.37}$$

where ξ_h is again a **k**-*in*dependent constant.

To conclude this section, we have derived the transition amplitude for general two-band systems from Eq. (5.17) and discussed the requirements of the two bands regarding velocity, such that an echo can happen. Note that the implications of the basic Chap. 3 for the QTM apply also in the general case. For instance, the echo strength $\mathcal{C}(t_{\text{echo}})$ in the correlation defined in Eq. (3.32) can be approximated for a narrow wave packet in **k**-space (peaked at $\mathbf{k}_0$) by the transition amplitude $A(\mathbf{k}_0)$. For a general wave packet, the echo strength is given by Eq. (3.33), where all **k**-modes are taken into account.

In the following sections, the general findings above are investigated for three example systems, some toy models, some resembling physical systems like direct gap semi-conductors or bilayer graphene. We will also discuss and stress additional features, which went short in the general discussion.

5.2 Linear band structure with different slopes

As an example for a system without chiral symmetry, we use in this subsection a toy model Hamiltonian which has still linear bands, but different slopes for positive energy as compared to negative energies: $E_{\mathbf{k},\pm} = \pm a_\pm |\mathbf{k}|$, with $a_\pm > 0$ (compare Fig. 5.2(a)). Since the slope is directly related to the velocity, we see that the velocities in the two bands are multiples of each other. Thus the requirement for an echo of Eq. (5.25) is met with the $\mathbf{k}$-independent constant $\xi_v = \frac{a_-}{a_+}$.

The pseudospin basis is rather arbitrary in this system, but to be in analogy to the graphene case, we use a basis where the energy-eigenstates are the same as in graphene $|\varphi_{\mathbf{k},s}\rangle$ in the sublattice basis:

$$H_0 = \frac{a_+ - a_-}{2}|\mathbf{k}|\mathbb{1} + \frac{a_+ + a_-}{2}\mathbf{k}\cdot\boldsymbol{\sigma} = \begin{pmatrix} \frac{a_+ - a_-}{2}|\mathbf{k}| & \frac{a_+ + a_-}{2}(k_x - ik_y) \\ \frac{a_+ + a_-}{2}(k_x + ik_y) & \frac{a_+ - a_-}{2}|\mathbf{k}|. \end{pmatrix} \tag{5.38}$$

The pulse is again $M\sigma_z$, switched on at t_0 for the duration of Δt. In comparison to the general case of Sec. 5.1, we have the following quantities

$$h_0^0(\mathbf{k}) = \frac{a_+ - a_-}{2}|\mathbf{k}|, \tag{5.39}$$

$$h_0^{\mathrm{ps}}(\mathbf{k}) = \frac{a_+ + a_-}{2}|\mathbf{k}|, \tag{5.40}$$

$$\Lambda^\perp = M, \tag{5.41}$$

$$\Lambda^\parallel = 0. \tag{5.42}$$

Thus, the transition amplitude becomes according to Eq. (5.17)

$$\begin{aligned} \langle \varphi_{\mathbf{k},-s} \mid U \mid \varphi_{\mathbf{k},s}\rangle &= \langle \varphi_{\mathbf{k},-s} \mid \mathrm{e}^{-\frac{i\Delta t}{\hbar}(H_0 + M\sigma_z)} \mid \varphi_{\mathbf{k},s}\rangle \\ &= \langle \varphi_{\mathbf{k},-s} \mid \mathrm{e}^{-\frac{i}{\hbar}\tilde{a}k\Delta t}\frac{-i\sigma_z}{\sqrt{1+\tilde{\kappa}^2}}\sin\left(\mu\sqrt{1+\tilde{\kappa}^2}\right) \mid \varphi_{\mathbf{k},s}\rangle \\ &= \mathrm{e}^{-\frac{i}{\hbar}\tilde{a}k\Delta t}\frac{-i}{\sqrt{1+\tilde{\kappa}^2}}\sin\left(\mu\sqrt{1+\tilde{\kappa}^2}\right). \end{aligned} \tag{5.43}$$

Here, we have introduced new variables

$$\tilde{\kappa} = \frac{a_+ + a_-}{2}\frac{|\mathbf{k}|}{M}, \tag{5.44}$$

$$\tilde{a} = \frac{a_+ - a_-}{2}, \tag{5.45}$$

and $\mu = \frac{M\Delta t}{\hbar}$, which is already familiar from the previous chapters. We see that the transition amplitude of Eq. (5.43) is quite similar to the case of graphene in Eq. (3.21). One difference is that we have to use the average $\tilde{\kappa}$, as compared to the constant $\kappa = \hbar v_F k/M$ in graphene, but this does not affect the possibility of an echo.

The second difference is the k-dependent phase $\mathrm{e}^{-\frac{i}{\hbar}\tilde{a}k\Delta t}$, which leads to a movement of the wave packet also during the pulse, since a phase in momentum space linear in $\mathbf{k}$ leads to a translation of the wave packet in real space, because of

$$\mathrm{FT}\{f(\mathbf{k})\}(\mathbf{r}) = \hat{f}(\mathbf{r}) \quad \Rightarrow \quad \mathrm{FT}\{f(\mathbf{k})\mathrm{e}^{i\mathbf{k}\cdot\mathbf{r}_0}\}(\mathbf{r}) = \hat{f}(\mathbf{r}-\mathbf{r}_0). \tag{5.46}$$

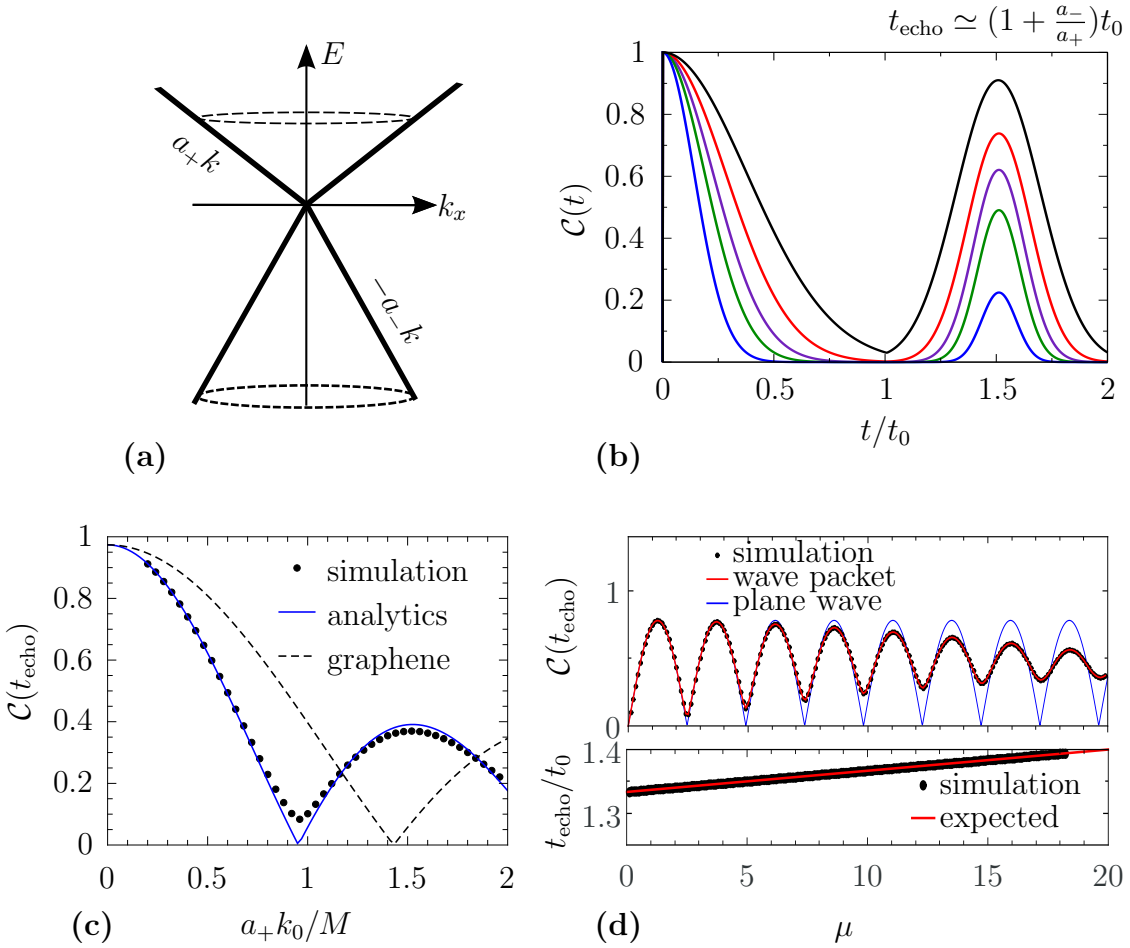

Figure 5.2: (a) Example of the band structure of the toy Hamiltonian of Eq. (5.38) for $a_+ < a_-$. (b) The correlation defined in Eq. (3.32) is shown for different wave packet energies starting in the positive energy branch. The Hamiltonian parameters are $a_- = 2a_+$, which is why the velocity after the pulse is twice as large and thus the echo takes place already at $t = 1.5t_0$. The different (but unimportant) decay rates of the correlation are due to different wave packet widths given by the relation $\Delta k = k_0/8$, where Δk is the width of wave packet in reciprocal space. (c) The echo strength $\mathcal{C}(t_{\text{echo}})$ is plotted as a function of the initial energy a_+k_0 relative to the pulse strength M. The simulation (black dots) is compared to the modulus of the transition amplitude of Eq. (5.43) (blue), which approximates the wave packet as plane wave. The deviations are due to the finite width of the wave packet as in the graphene case above. The black dashed line shows analytically the case of symmetric bands (graphene), i.e. $a_- = a_+$. (d) Dependence of echo time t_{echo} (below) and echo strength $\mathcal{C}(t_{\text{echo}})$ (above) on the pulse duration, or equivalently μ, for fixed M and $a_- = 3a_+$, both matching very well the expectation.

In the end, this phase leads only to a slight change of the scattering time, which can be seen by looking at all the phases which are accumulated during the time evolution of the part of the wave packet which is important for the echo. For simplicity, we consider a wave packet with initially positive energy. The corresponding phases are

$$\text{before pulse:} \quad \mathrm{e}^{-\frac{i}{\hbar}a_+ k t_0}, \tag{5.47}$$

$$\text{during pulse:} \quad \mathrm{e}^{-\frac{i}{\hbar}\tilde{a} k\, \Delta t}, \tag{5.48}$$

$$\text{after pulse:} \quad \mathrm{e}^{-\frac{i}{\hbar}(-a_-)k t_1}, \tag{5.49}$$

$$\text{total phase:} \quad \mathrm{e}^{-\frac{i}{\hbar}k(a_+ t_0 + \tilde{a}\,\Delta t - a_- t_1)}. \tag{5.50}$$

Here, $t_1 = t_{\text{echo}} - (t_0 + \Delta t)$ is the time duration between end of the pulse and echo.

The echo takes place, when the wave packet is back at the origin, i.e. when the translation in real space is 0, which leads to the condition

$$a_+ t_0 + \tilde{a}\,\Delta t - a_- t_1 = 0 \Rightarrow t_1 = \frac{a_+}{a_-} t_0 + \frac{\Delta t}{2}\left(\frac{a_+}{a_-} - 1\right), \tag{5.51}$$

which means, that here ,also the pulse duration Δt influences the time duration t_1, even for small Δt, as opposed to the graphene case, where we had exactly $t_1 = t_0$. The echo time thus changes from $t_{\text{echo}} = 2t_0 + \Delta t$ in the graphene case to

$$t_{\text{echo}} = t_0 + \Delta t + t_1 = \left(\frac{a_+}{a_-} + 1\right) t_0 + \frac{\Delta t}{2}\left(\frac{a_+}{a_-} + 1\right), \tag{5.52}$$

as can be nicely seen in Fig. 5.2(b) and (d). This result corresponds to the general echo time of Eq. (5.29). For very long Δt, the separation of the sub-wave packet has to be taken into account, analogue to Sec. 3.4. Note that in bands with a general slope, the graphene case is recovered by inserting $a_+ = a_-$, as it should be.

In Fig. 5.2, we see (a) an exemplary band structure, (b) the correlations of simulations for certain parameters and (c) and (d) the echo strength of the simulations which matches quite well the analytical expectations from Eq. (5.43). The only deviations are due to the extended wave packet width Δk in reciprocal space. Although not shown here, by taking the full width of the wave packet into account using Eq. (3.33) with the new transition amplitude, analytical expectations and simulation agree perfectly (mean deviation of $\sim 10^{-6}$).

Qualitatively, the results are similar to the case of graphene. The most significant difference can be seen in Fig. 5.2(b): due to the different velocities before and after the pulse, the time of the echo changes from $t_{\text{echo}} \approx 2t_0$ to $t_{\text{echo}} \approx t_0 + \frac{a_+}{a_-} t_0$, where we assumed that the wave packet has initially only positive energies (and $\Delta t \ll t_0$). However, because of this feature, it becomes obvious that the wave packet in this asymmetric band structure needs to be initially composed only of either positive or negative energy states. Otherwise, there will be two separate echo peaks in the correlation at $t_+ \approx t_0 + \frac{a_+}{a_-} t_0$ and $t_- \approx t_0 + \frac{a_-}{a_+} t_0$, whose strength depends on the particular composition of the wave packet.

In this subsection, we have seen that the perfect chiral symmetry is not important for the echo, since also in this asymmetric, linear toy model, it does not fundamentally change the echo properties, but only certain features, like the time of the echo.

5.3 Hyperbolic bands

5.3.1 Mass gap

So far, we only considered linear band structures to verify the working principle of the QTM. However, why should not any other chiral symmetric band structure be just as good? The main point is that the transition from $E_{\mathbf{k},s}$ to $E_{\mathbf{k},-s} = -E_{\mathbf{k},s}$ is automatically a reversion of the velocity, as discussed in Sec. 5.1.2, which holds for any chiral symmetric band structure.

To investigate this situation, we use an initially gapped, hyperbolic band structure, and a pulse with the same time dependence $f(t)$ as before, which has the strength M_1,

$$H = H_0 + H_{\text{pulse}}(t) = \hbar v_F \mathbf{k} \cdot \boldsymbol{\sigma} + M_0 \sigma_z + f(t)\, M_1 \sigma_z, \tag{5.53}$$

such that it further widens the gap to $M = M_0 + M_1$ (see Fig. 5.3(a)). The eigenenergy and eigenstates of the initial Hamiltonian H_0 are given by Eqs. (3.11) and (3.12), respectively, where we have to substitute M by M_0 and κ by $\eta = \hbar v_F k / M_0$:

$$E_{\mathbf{k},\pm} = \pm\sqrt{M_0^2 + \hbar^2 v_F^2 k^2} = \pm M_0 \sqrt{1+\eta^2}, \tag{5.54}$$

$$\begin{aligned} \langle \mathbf{k} \mid \varphi_{\mathbf{k},\pm} \rangle &= \frac{1}{\sqrt{(M_0 + E_{\mathbf{k},\pm})^2 + \hbar^2 v_F^2 k^2}} \begin{pmatrix} M_0 + E_{\mathbf{k},\pm} \\ \hbar v_F k\, \mathrm{e}^{i\gamma_{\mathbf{k}}} \end{pmatrix} \\ &= \frac{1}{\sqrt{2}\sqrt{1+\eta^2 \pm \sqrt{1+\eta^2}}} \begin{pmatrix} 1 \pm \sqrt{1+\eta^2} \\ \eta\, \mathrm{e}^{i\gamma_{\mathbf{k}}} \end{pmatrix}. \end{aligned} \tag{5.55}$$

We choose a notation in this section (e.g. $M = M_0 + M_1$, $\kappa = \hbar v_F k / M$) such that the eigensystem during the pulse stays the same as in Eqs. (3.11) and (3.12). Compared to the general Sec. 5.1, we have

$$h_0^0 = 0, \tag{5.56}$$

$$h_0^{\text{ps}} = M_0 \sqrt{1+\eta^2}, \tag{5.57}$$

$$\Lambda^{\perp} = M_1 \frac{\eta}{\sqrt{1+\eta^2}} = M_1 \frac{\kappa}{\sqrt{\frac{M_0^2}{M^2} + \kappa^2}}, \tag{5.58}$$

$$\Lambda^{\parallel} = M_1 \frac{1}{\sqrt{1+\eta^2}}. \tag{5.59}$$

The fact that $\Lambda^{\parallel} \neq 0$ is the main difference here compared to the linear band structures studied before, as visualized in Fig. 5.3(b). It is due to the fact that the transition operator which maps $|\varphi_{\mathbf{k},s}\rangle$ to $|\varphi_{\mathbf{k},-s}\rangle$ is σ_z in the linear case and therefore k-independent. In the hyperbolic case however, it is *k-dependent* (compare Eq. (5.55)). Only in the limit $\kappa \to \infty$, i.e. $\hbar v_F k \gg M_0$, σ_z is the transition operator. Otherwise, only a fraction of the σ_z-pulse leads to a transition and for $k = 0$ there is even no transition at all, because the eigenvectors become $(1,0)$ and $(0,1)$ and thus they are eigenstates of σ_z. This will be reflected in the transition amplitude by an additional factor decreasing the echo strength.

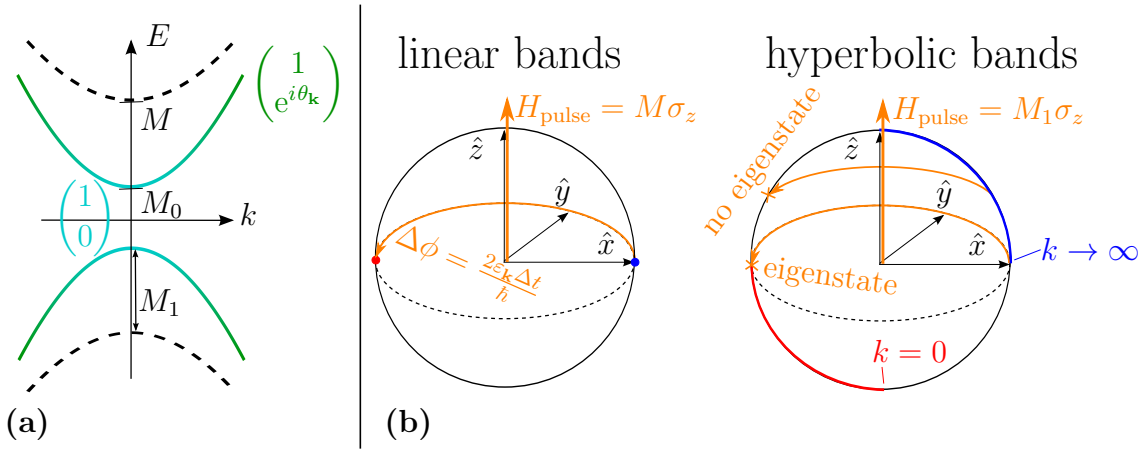

Figure 5.3: (a) Hyperbolic band structure of the Hamiltonian in Eq. (5.53) with the corresponding pseudospin structure indicated by the color. (b) The transition during the pulse is shown in the Bloch sphere for linear and hyperbolic band structures. For simplicity, we choose $\mathbf{k} = (k, 0)$. For initially linear bands, an eigenstates (blue dot) can be mapped (orange curved arrow) to the other band (red dot) for any k, because the pulse "direction" $\sim \sigma_z$ (orange vertical arrow) is always perpendicular to the eigenstates. For hyperbolic bands, the direction of the initial eigenstates depends on k (blue and red quarter circle), such that σ_z is not perpendicular anymore for finite k. Thus, eigenstates are not mapped to eigenstates in the other band (upper orange curved arrow).

According to Eq. (5.17), the transition amplitude becomes

$$A_s(\mathbf{k}) = \underbrace{\frac{M_1}{M}}_{<1} \underbrace{\frac{\kappa}{\sqrt{\frac{M_0^2}{M^2} + \kappa^2}}}_{<1} \underbrace{\frac{i}{\sqrt{1+\kappa^2}} \sin\left(\mu\sqrt{1+\kappa^2}\right)}_{\text{graphene case}} . \tag{5.60}$$

The magnitude of the transition amplitude for the hyperbolic band structure is independent of s and the direction of $\mathbf{k}$ ($A_s(\mathbf{k}) = A(k)$). Moreover, it is always smaller than in graphene (see Eq. (3.21)) and even goes to zero for $k \to 0$, because σ_z does not lead to a transition of the energy eigenfunctions there, as discussed above.

In the limit $M_0 \to 0$, we have to obtain the same amplitude as in the graphene case, which is indeed fulfilled since then $M = M_1$ and the first factors in Eq. (5.60) yield 1. The only difference is the minus sign, which is just due to the choice of the eigenstates, because changing the sign of $|\varphi_{\mathbf{k},-}\rangle$, for example, will not change the physics, but will result in an additional minus sign in the transition amplitude.

The analytical result of Eq. (5.60) is compared to the simulations in Fig. 5.4(a) and shows the expected agreement. Again, by taking the width of the wavepacket into account, the average deviation is negligible (8×10^{-4}). As mentioned above, due to the coupling of the linear bands via σ_z in H_0 and the consequent avoided band crossing at $k = 0$, the transition amplitude yields zero at $\kappa = 0$.On the other hand, it also vanishes for $\kappa \to \infty$, as in the graphene case, because in this limit, the pulse is negligibly small compared to the energy of the wave packet, which is why no transition is driven. Due to the continuity of $A(\mathbf{k})$, there is a value of $\kappa > 0$

for which the transition amplitude is maximal, which can be found by looking for a horizontal tangent of the transition amplitude in Eq. (5.60).

$$0 \stackrel{!}{=} \frac{\partial}{\partial \kappa} A(k) \tag{5.61}$$

In general, this will lead to a transcendental equation, which can be solved numerically.

One special case, which is worth to consider, is the maximally achievable echo for a given pulse strength M_1 and initial band gap M_0 in the hyperbolic case. In that case, we choose Δt such that $\mu\sqrt{1+\kappa^2} = \pi/2$, i.e. the sine becomes one and the only limiting factor for the echo is the prefactor in the transition amplitude.

$$\begin{aligned}
0 &\stackrel{!}{=} \frac{\partial}{\partial \kappa}\left(\frac{M_1}{M}\frac{\kappa}{\sqrt{\frac{M_0^2}{M^2}+\kappa^2}}\frac{i}{\sqrt{1+\kappa^2}}\right) \\
&= \frac{iM_1}{M}\frac{\partial}{\partial \kappa}\frac{\kappa}{\sqrt{\kappa^4 + (1+\frac{M_0^2}{M^2})\kappa^2 + \frac{M_0^2}{M^2}}} \\
&= \frac{iM_1}{M}\frac{\partial}{\partial \kappa}\frac{1}{\sqrt{\kappa^2 + (1+\frac{M_0^2}{M^2}) + \frac{M_0^2}{M^2}\frac{1}{\kappa^2}}} \\
&= -\frac{1}{2}\frac{iM_1}{M}\frac{1}{\sqrt{\kappa^2 + (1+\frac{M_0^2}{M^2}) + \frac{M_0^2}{M^2}\frac{1}{\kappa^2}}^3}\left(2\kappa - \frac{2}{\kappa^3}\frac{M_0^2}{M^2}\right) \\
\Rightarrow \kappa_{\max} &= \sqrt{\frac{M_0}{M}}
\end{aligned} \tag{5.62}$$

Thus, the best echo can be approximately achieved for $\kappa_{\max}$ (and $\mu = \pi/2/\sqrt{1+\frac{M_0}{M}}$) and yields

$$\begin{aligned}
|A(\kappa_{\max})| &= \frac{M_1}{M}\frac{1}{\sqrt{\kappa_{\max}^2 + (1+\frac{M_0^2}{M^2}) + \frac{M_0^2}{M^2}\frac{1}{\kappa_{\max}^2}}} \\
&= \frac{M_1}{M}\frac{1}{\sqrt{\frac{M_0}{M} + (1+\frac{M_0^2}{M^2}) + \frac{M_0}{M}}} \\
&= \frac{M_1}{M}\frac{1}{\sqrt{\left(1+\frac{M_0}{M}\right)^2}} = \frac{M-M_0}{M}\frac{1}{1+\kappa_{\max}^2} \\
\Rightarrow |A(\kappa_{\max})| &= \frac{1-\kappa_{\max}^2}{1+\kappa_{\max}^2} = \frac{M-M_0}{M+M_0}.
\end{aligned} \tag{5.63}$$

It is not surprising that both $\kappa_{\max}$ and the value of the best echo depend on the gaps of the initial system and the gap during the pulse.

To verify Eq. (5.63), corresponding simulations are shown in Fig. 5.4(b), i.e. the pulse duration Δt is adjusted for every simulation such that the sine in the transition amplitude of Eq. (5.60) becomes 1. The echo strength is plotted as a function of κ for different ratios $\frac{M_0}{M_1}$ ranging from 0.2 to 0.9 in steps of 0.1. The first thing

to notice is that the smaller $\frac{M_0}{M_1}$, i.e. the smaller the initial gap M_0, the better the echo. Furthermore, the black dashed line gives the position $\kappa_{\max}$ and value of the expected maxima of the curves with $\frac{M_0}{M_1} = \text{const}$ according to Eqs. (5.62) and (5.63). It coincides very well with both the position and the value of the maxima of the simulated echo strengths for a given ratio of gaps $\frac{M_0}{M_1}$.

To conclude this section, we want to stress again that we do not have to consider that the different modes have different velocity in the hyperbolic band structure. This is simply due to the fact that the homogeneous pulse, $\mathbf{k}$ is conserved and that because of the chirally symmetric band structure, the positive energy branch modes have the same magnitude of velocity as the negative energy modes at the same $\mathbf{k}$, but with opposed direction. Thus, a wave packet will spread until the pulse due to the different velocities over the time t_0. After the pulse, the slow, mirrored modes find themselves closer to the initial position than the fast, mirrored modes and indeed they come back at the initial position at the same time t_0.

This is similar to the spin Hahn echo, where the spins in the ensemble dephase due to different environments (T_2^*-time) and therefore (slightly) different Larmor frequencies. After the π-pulse the phase of the fast precessing spins finds itself "behind" the slow precessing ones. For a static environment, the frequencies before and after the pulse are the same and thus, they rephase at the same amount of time which is equal to the time between the exciting $\pi/2$-pulse and the "rephasing" π-pulse. The difference here is that instead of the dephasing of an ensemble of spins, the different $\mathbf{k}$-modes of a wave packet dephase and are made to yield an echo.

5.3.2 Other homogeneous pulses

In the linear band case (which means a direct band crossing due to uncoupled bands), we have the special case that the transition operator from one band to the other is $\mathbf{k}$-independent, namely σ_z. For hyperbolic bands, we have seen that instead, the operator mapping the eigenstates from one band to the other depends on $\mathbf{k}$. Only far away from the initial gap, σ_z leads to a good transition whereas directly at the gap ($k = 0$), the transition becomes 0 (see also Fig. 5.3(a) and (b)).

However, for any $\mathbf{k}$ there exists an operator which corresponds to the transition from one band to the other of an eigenstate. In the Bloch sphere, the direction of this operator is perpendicular to the direction of the given eigenstate. For $k = 0$, the according spinor part of the eigenstates of the Hamiltonian are $(1, 0)$ and $(0, 1)$, thus σ_x and σ_y are both leading to a band "flip" for these eigenstates.

Note that it is not surprising that there are two independent operators doing the trick. Actually, also in the linear band case, there are two operators for the energy change, but only σ_z is independent of k. One can think of it geometrically, by considering the eigenstates in the Bloch sphere. Since $\sigma_j = i(\mathbb{1} \cos\frac{\pi}{2} - i\sigma_j \sin\frac{\pi}{2}) = i \exp\left(-i\frac{\pi}{2}\sigma_j\right)$, the action of σ_j on a given state describes a rotation in the Bloch sphere of this state around the j-axis with an angle of π and thus to its orthogonal state. In three dimensions, a rotation by 180° can be done around any direction which is perpendicular to the direction of the object to be rotated. So we can always choose two directions, which are orthogonal among each other and orthogonal to the initial state in the Bloch sphere. In graphene, the eigenstates are always in the x-y-plane of the Bloch sphere and thus, σ_z flips the energy of any of them, but in principle

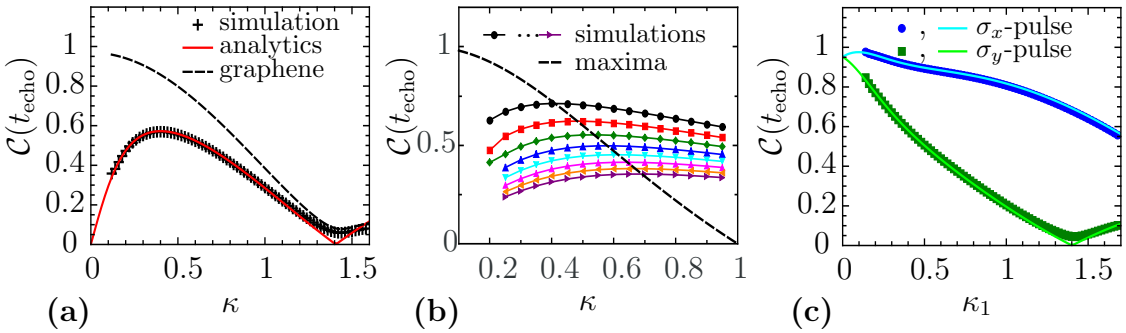

Figure 5.4: (a) The echo strength $\mathcal{C}(t_{\text{echo}})$ is shown as a function of the initial energy relative to the total gap, $\kappa = \hbar v_F k_0/M$, and with a pulse duration that yields $\mu = M\Delta t/\hbar = 1.8$. The simulation (black crosses) is compared to the modulus of the transition amplitude of Eq. (5.60) (red). The deviations are again due to the finite width of the wave packet. The black dashed line shows the corresponding results of the simulation for the graphene case, i.e. symmetric linear bands. (b) Δt is adjusted for each simulation such that the sine becomes 1 in the transition amplitude of Eq. (5.60). Each data point corresponds to one simulation, where the ratio M_0/M_1 ranges from 0.2 (black dots) to 0.9 (violet triangles) in steps of 0.1. The black dashed line corresponds to the expected maximal values for a given ratio M_0/M_1, according to Eq. (5.63) and matches the maxima obtained by simulation well. (c) Using σ_x- and σ_y-pulses, we compare the simulated echo strength $\mathcal{C}(t_{\text{echo}})$ of a wave packet around $\mathbf{k}_0 = k_0/\sqrt{2}\,(-1,1)$ with the analytically expected values (for a plane wave) given by the transition amplitudes of Eqs. (5.72) and (5.73) as a function of $\kappa_1 = \hbar v_F k_0/M_1$, which shows a good agreement.

there is always another one inplane. In this subsection, we want to consider other pulses, which might be better suited for a given system to do the energy transition, e.g. near $k = 0$. As an example, we consider σ_x and σ_y-pulses. The general case can be in principle obtained by using the combination of the results of σ_x-, σ_y- and σ_z-pulses, but is not expected to yield further insight.

The initial Hamiltonian is the hyperbolic Hamiltonian of Eq. (5.53), but the pulse-Hamiltonian changes:

$$H = H_0 + H_{\text{pulse}}(t) = \hbar v_F \mathbf{k}\cdot\boldsymbol{\sigma} + M_0\sigma_z + f(t)\,M_1\sigma_j, \quad j \in \{x,y\} \tag{5.64}$$

The initial energy $E_{\mathbf{k},s}$ and the corresponding eigenstates $|\varphi_{\mathbf{k},s}\rangle$ are thus still the same as in Eqs. (5.54) and (5.55). During the pulse, instead of opening a gap, the origin in $\mathbf{k}$-space is effectively shifted by M_1 in direction j, because the term proportional to σ_j in the Hamiltonian is $\hbar v_F k_j + M_1$. Nevertheless, we keep the notation (M_1), which initially indicated as mass gap. The energy for the quasi-static Hamiltonian during the pulse yields

$$\begin{aligned}\varepsilon_{k,\pm} = \pm\varepsilon_k &= \pm\sqrt{M_0^2 + \hbar^2 v_F^2 k^2 + 2\hbar v_F k_j M_1 + M_1^2} \\ &= \pm M_1\sqrt{1 + \kappa_1^2 + \frac{M_0^2}{M_1^2} + 2\kappa_{1,j}}.\end{aligned} \tag{5.65}$$

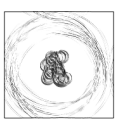

Here, we introduced $\kappa_1 = \hbar v_F k/M_1$ and $\kappa_{1,j} = \hbar v_F k_j/M_1$. Moreover, we will use below the abbreviation

$$\xi(\kappa_1) = 1 + \kappa_1^2 + \frac{M_0^2}{M_1^2} \tag{5.66}$$

To have some diversion, we use Eq. (5.20) in this example for calculating the transition amplitude, where instead of doing geometry, we have to calculate a scalar product. The transition amplitude becomes accordingly

$$A_j(\mathbf{k}) = \frac{-i \sin\left(\mu_1 \sqrt{\xi(\kappa_1) + 2\kappa_{1,j}}\right)}{\sqrt{\xi(\kappa_1) + 2\kappa_{1,j}}} \langle \varphi_{\mathbf{k},-s} \mid \sigma_j \mid \varphi_{\mathbf{k},s} \rangle. \tag{5.67}$$

So, we need the scalar product of the different energy eigenstates with the Pauli matrices σ_x and σ_y, given in App. B. To remind the reader, we use the notation $\eta = \hbar v_F k/M_0$ as opposed to $\kappa_1 = \hbar v_F k/M_1$ (and $\kappa = \hbar v_F k/(M_0 + M_1)$, which we do not need here). Thus, we get

$$\langle \varphi_{\mathbf{k},-s} \mid \sigma_x \mid \varphi_{\mathbf{k},s} \rangle = \frac{1}{\sqrt{1+\eta^2}} \cos\gamma_{\mathbf{k}} + is \sin\gamma_{\mathbf{k}}, \tag{5.68}$$

and

$$\langle \varphi_{\mathbf{k},-s} \mid \sigma_y \mid \varphi_{\mathbf{k},s} \rangle = -\frac{1}{\sqrt{1+\eta^2}} \sin\gamma_{\mathbf{k}} + is \cos\gamma_{\mathbf{k}}, \tag{5.69}$$

where $\gamma_{\mathbf{k}}$ is the polar angle of $\mathbf{k}$ in the x-y-plane. Therefore, the transition amplitudes for potentials in either x- or y-direction become

$$A_x(\mathbf{k}) = \frac{-i \sin\left(\mu_1 \sqrt{\xi(\kappa_1) + 2\kappa_{1,x}}\right)}{\sqrt{\xi(\kappa_1) + 2\kappa_{1,x}}} \left(\frac{1}{\sqrt{1+\eta^2}} \cos\gamma_{\mathbf{k}} + is \sin\gamma_{\mathbf{k}} \right), \tag{5.70}$$

$$A_y(\mathbf{k}) = \frac{-i \sin\left(\mu_1 \sqrt{\xi(\kappa_1) + 2\kappa_{1,y}}\right)}{\sqrt{\xi(\kappa_1) + 2\kappa_{1,y}}} \left(\frac{-1}{\sqrt{1+\eta^2}} \sin\gamma_{\mathbf{k}} + is \cos\gamma_{\mathbf{k}} \right). \tag{5.71}$$

Their moduli are

$$|A_x(\mathbf{k})| = \sqrt{\frac{\frac{1}{1+\eta^2}\cos^2\gamma_{\mathbf{k}} + \sin^2\gamma_{\mathbf{k}}}{\xi(\kappa_1) + 2\kappa_{1,x}}} \left| \sin\left(\mu_1 \sqrt{\xi(\kappa_1) + 2\kappa_{1,x}}\right) \right|, \tag{5.72}$$

$$|A_y(\mathbf{k})| = \sqrt{\frac{\frac{1}{1+\eta^2}\sin^2\gamma_{\mathbf{k}} + \cos^2\gamma_{\mathbf{k}}}{\xi(\kappa_1) + 2\kappa_{1,y}}} \left| \sin\left(\mu_1 \sqrt{\xi(\kappa_1) + 2\kappa_{1,y}}\right) \right|. \tag{5.73}$$

In Fig. 5.4(c), we compare the transition amplitude calculated in Eqs. (5.70) and (5.71) of a plane wave, with the simulated time propagations with TQT of a Gaussian wave packet for fixed $\mu_1 = 1.4$. In both cases, we use the same wave packet with mean wave vector $\mathbf{k}_0 = k_0/\sqrt{2}\,(-1, 1)$ and a width of $\Delta k = k_0/8$. The two corresponding pulse-Hamiltonians are $M_1\sigma_x$ and in the other simulations $M_1\sigma_y$.

First, we can see indeed that there is a strong enhancement for initial energies close to the band gap ($\kappa_1 \ll 1$), as compared to the σ_z-pulse from Fig. 5.4(a), as

explained above. Furthermore, as we can see from the transition amplitudes, not only the absolute value but also the direction of the wave vector $\mathbf{k}_0$ is important for the probability of the energy change, which is why the simulations for a σ_x-pulse differ from the σ_y-pulse. In the first case, the pulse moves the gap minimum in $\mathbf{k}$-space effectively closer to $\mathbf{k}_0$ which leads to a lower energy during the pulse and therefore to a higher transition (the energy during the transition is in the denominator), whereas in the latter case (σ_y) the band gap minimum is moved away from $\mathbf{k}_0$ leading similarly to a smaller transition (and higher frequency).

To conclude, we have shown in this section, that the QTM works in the case of non-linear bands, but still with chiral symmetry. The broadening of a wave packet due to different velocities of the individual modes is perfectly reverted, such the part of the wave packet which is "reflected" by the QTM pulse looks exactly as if it moved backwards in time. Moreover, we considered different types of pulses, which might be better suited for high echoes, depending on the ratio of initial energy of the wave packet and initial gap size M_0. The analytically expected echo strengths from Sec. 5.1 are confirmed by simulations in all cases.

5.4 Asymmetric parabolic bands

For the last example of different band gaps, we want to combine both changes compared to a graphene band structure discussed in this section: no strict chiral symmetry as in the case of linear bands with different slopes (Sec. 5.2), and no linear bands as in the hyperbolic case (Sec. 5.3), where the magnitude of the velocity becomes $\mathbf{k}$-dependent.

In the general Sec. 5.1.2, we have seen that the velocity in the two bands needs to fulfill the following requirement to get an echo

$$\langle \hat{\mathbf{v}} \rangle_{\mathbf{k},-} = -\xi_v \langle \hat{\mathbf{v}} \rangle_{\mathbf{k},+} \quad \text{and} \quad \xi_v \in \mathbb{R}^+ \tag{5.74}$$

$$\Rightarrow \nabla_{\mathbf{k}} E_{\mathbf{k},-} = -\xi_v \nabla_{\mathbf{k}} E_{\mathbf{k},+}. \tag{5.75}$$

Assuming that the initial band structure is isotropic, i.e. it does not depend on the direction of $\mathbf{k}$ but only on its modulus k, the condition becomes

$$\Rightarrow \frac{\partial E_{k,-}}{\partial k} = -\xi_v \frac{\partial E_{k,+}}{\partial k}. \tag{5.76}$$

For linear bands, this is always fulfilled, since the velocity does not depend on k.

Let us consider the case of a parabolic band structure $E_\pm = a_\pm (k - b_\pm)^2 + c_\pm$. There, we get the following requirement:

$$2a_-(k - b_-) = -\xi_v \, 2a_+(k - b_+), \quad \forall k \tag{5.77}$$

$$\Rightarrow \xi_v = -\frac{a_-}{a_+} \quad \text{and} \quad b_+ = b_-. \tag{5.78}$$

Thus, the extrema of the parabolas have to be at the same $\mathbf{k}$, but the curvature of the two parabolas does not matter as long as one is positive and the other is negative. Examples of physical system with such a band structure are bilayer graphene and direct gap semi-conductor in the vicinity of the gap minimum, since we can expand

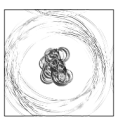

the band structure there and obtain approximately parabolic bands as described above.

We will investigate the parabolic bands with the requirement of Eq. (5.78), i.e. different curvature but same vertex position as an example of generalized chiral symmetry. By generalized chiral symmetry, we mean that instead of $E_-(\mathbf{k}) = -E_+(\mathbf{k})$, the requirement of Eq. (5.75) has to be fulfilled, i.e. that the group velocity in the two bands differs only by a $\mathbf{k}$-*in*dependent factor. The initial Hamiltonian is

$$H_0 = \begin{pmatrix} a_+k^2 + c_+ & 0 \\ 0 & -a_-k^2 - c_- \end{pmatrix}, \tag{5.79}$$

where we set without loss of generality the position of the direct gap in the origin of the reciprocal space. Furthermore, we can shift the energy scale to the center of the gap between the two bands, which yields $c_+ = c_- \equiv c_0$.

The initial Hamiltonian can be written in terms of Pauli matrices as

$$H_0 = \frac{a_+ - a_-}{2}k^2\mathbb{1} + \left(\frac{a_+ + a_-}{2}k^2 + c_0\right)\sigma_z = \alpha k^2\mathbb{1} + \left(\zeta k^2 + c_0\right)\sigma_z, \tag{5.80}$$

with $\alpha = \frac{a_+ - a_-}{2}$ and $\zeta = \frac{a_+ + a_-}{2}$, visualized in Fig. 5.5(a). Since the Hamiltonian H_0 is diagonal, the eigenvectors are $(1, 0)$ and $(0, 1)$, which are in this basis independent of $\mathbf{k}$.

Note that in this subsection, we use a 2-band model in the basis of its eigenstates. Thus, the pseudospinors are not related to the pseudospinors of graphene, where the basis states are the localized wave functions around the two atoms of the unit cell. Depending on the actual system, the Hamiltonian will look different, using a physically relevant basis. In that basis, the transition operator, which maps the eigenstates from one band to the other, can in general depend on $\mathbf{k}$. Nevertheless, with our choice of the system, any linear combination of the operators σ_x and σ_y leads to a perfect transition between the two bands. Without loss of generality, we use σ_x and the same time-dependence as always:

$$H_{\text{pulse}} = f(t)\Lambda_x\sigma_x. \tag{5.81}$$

To distinguish from the graphene case, where the chosen perturbation leads to a mass gap, we denote here the pulse strength Λ_x instead of M, although theoretically it is similar because both induce the transition between the bands. Compared to the general section, the parameters become here

$$h_0^0(\mathbf{k}) = \alpha k^2, \tag{5.82}$$
$$h_0^{\text{ps}}(\mathbf{k}) = (\zeta k^2 + c_0), \tag{5.83}$$
$$\Lambda^\perp = \Lambda_x, \tag{5.84}$$
$$\Lambda^\parallel = 0, \tag{5.85}$$

and the transition amplitude in this example yields, according to Eq. (5.17),

$$A_s(\mathbf{k}) = \mathrm{e}^{-\frac{i}{\hbar}\alpha k^2 t}\frac{-i\sin\left(\mu_x\sqrt{1 + \frac{(\zeta k^2 + c_0)^2}{\Lambda_x^2}}\right)}{\sqrt{1 + \frac{(\zeta k^2 + c_0)^2}{\Lambda_x^2}}}, \tag{5.86}$$

where we have introduced $\mu_x = \Delta t \Lambda_x/\hbar$. We see that the transition is independent of the band index s. Still, a wave packet living in both bands will not lead to a single echo but to two echoes at $t_0(1+\frac{a_+}{a_-})$ for the upper band and $t_0(1+\frac{a_-}{a_+})$ for the lower band, compare Eq. (5.29). The reason is that the mode which switches from the faster band to the slower band comes back later than modes switching from the slow to the fast band.

Moreover, we see the amplitude in Eq. (5.17), i.e. omitting the sin-term, is higher the smaller k and the smaller ζ. The reason is equivalent to the one given in the general Sec. 5.1, that the energy related to h_0^{ps}, which is in this case related to the average energy of the two bands at a given $\mathbf{k}$ (ζk^2), should be much smaller than the energy of the pulse for a strong echo.

Without loss of generality, we let the energy of the wave packet be positive. Similar to the asymmetric linear bands, there is an additional k-dependent phase in the transition amplitude of Eq. (5.86). As discussed in the general Sec. 5.1.1, this phase leads to an additional shift of the echo time by $a_+/(2a_-)\Delta t$. This can be seen again by examining the phases accumulated before and after the pulse.

$$\text{before pulse:} \quad \mathrm{e}^{-\frac{i}{\hbar}(a_+k^2+c_0)t_0}, \tag{5.87}$$

$$\text{during pulse:} \quad \mathrm{e}^{-\frac{i}{\hbar}\alpha k^2\,\Delta t}, \tag{5.88}$$

$$\text{after pulse:} \quad \mathrm{e}^{-\frac{i}{\hbar}(-a_-k^2-c_0)t_1}, \tag{5.89}$$

$$\text{total phase:} \quad \mathrm{e}^{-\frac{i}{\hbar}k^2(a_+t_0+\alpha\,\Delta t-a_-t_1)-\frac{i}{\hbar}c_0(t_0-t_1)}. \tag{5.90}$$

The last term in the total phase is unimportant, since it would only yield a constant phase shift of the echo wave packet compared to the initial wave packet. The term proportional to k^2 on the other hand implies a k-dependent shift of the wave packet in real space. This means that the wave-packet as a whole moves away from the initial position and additionally spreads, which is well-known from the free Schrödinger equation. For the echo, this phase shift needs to be 0, which yields the condition:

$$a_+t_0 + \alpha\,\Delta t - a_-t_1 = 0 \quad \Rightarrow \quad t_1 = \frac{a_+}{a_-}t_0 + \frac{1}{2}(\frac{a_+}{a_-}-1)\Delta t, \tag{5.91}$$

leading to an echo time of

$$t_{\mathrm{echo}} = t_0 + \Delta t + t_1 = (1+\frac{a_+}{a_-})t_0 + \frac{\Delta t}{2}(1+\frac{a_+}{a_-}), \tag{5.92}$$

exactly as in the linear band case with different slopes in Eq. (5.52).

Let us come back to the strength of the echo. We have seen in Eq. (5.86) that it is independent of the band index s, which means that only the k-dependence of the wave packet plays a role, or in otherwise said, for a given k, the transition amplitude does not change in the different bands. This implies that if we consider the (modulus of the) energy E_k instead the wave vector, the transition amplitude becomes s-dependent due to the asymmetric bands. Since in the subsections above, the transition amplitude is given in terms of the ratio of initial mean wave packet energy and pulse strength in the section above, we will do the same here.

To obtain the transition amplitude in terms of the initial mean energy of a wavepacket $E_0^{\pm} = \pm E_0$, we insert in the transition amplitude of Eq. (5.86) either

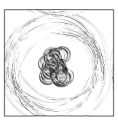

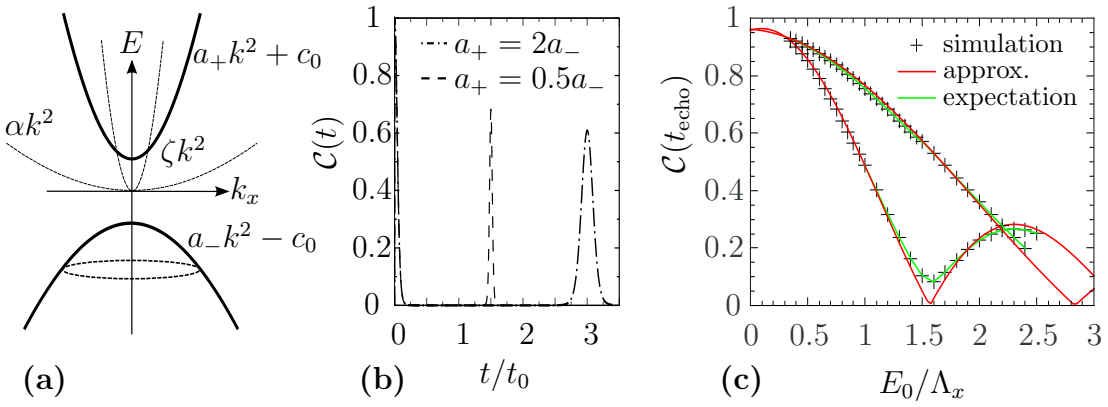

Figure 5.5: QTM for parabolic bands. (a) The band structure (solid) of the Hamiltonian in Eq. (5.79) is shown as well as the individual terms (dashed) of the equivalent Hamiltonian in Eq. (5.80). (b) Correlation $\mathcal{C}(t)$, showing that the echo time changes for going from "fast" to "slow" band compared to vice versa, according to Eq. (5.98). (c) Echo strength $\mathcal{C}(t_{\mathrm{echo}})$ as a function of the average energy of the wave packet, obtained by simulation (black crosses), as well as using the transition amplitude of Eq. (5.93) for plane waves (red) and for the whole wave packet (green). The data set with (mostly) smaller values corresponds to $a_+ = 0.5a_-$ and the data set with the higher echoes to $a_+ = 2a_-$.

$k^2 = \frac{E_0 - c_0}{a_+}$ or $k^2 = \frac{E_0 - c_0}{a_-}$, depending on the initial band. For the rest of the discussion, we will consider a wave packet with initially positive energy - the only change for an initially negative energy is to substitute a_+ by a_- everywhere. Thus, the energy-dependent transition amplitude yields

$$\begin{aligned} A(E_0^+) &= \mathrm{e}^{-\frac{i}{\hbar}\alpha k^2 t} \frac{-i \sin\left(\mu_x \sqrt{1 + \frac{1}{\Lambda_x^2}(\zeta \frac{E_0 - c_0}{a_+} + c_0)^2}\right)}{\sqrt{1 + \frac{1}{\Lambda_x^2}(\zeta \frac{E_0 - c_0}{a_+} + c_0)^2}} \\ &= \mathrm{e}^{-\frac{i}{\hbar}\alpha k^2 t} \frac{-i \sin\left(\mu_x \sqrt{1 + \frac{1}{4}\left((1 + \frac{a_-}{a_+})\frac{E_0}{\Lambda_x} + (1 - \frac{a_-}{a_+})\frac{c_0}{\Lambda_x}\right)^2}\right)}{\sqrt{1 + \frac{1}{4}\left((1 + \frac{a_-}{a_+})\frac{E_0}{\Lambda_x} + (1 - \frac{a_-}{a_+})\frac{c_0}{\Lambda_x}\right)^2}}. \end{aligned} \tag{5.93}$$

Its absolute value is limited by

$$A(E_0^s) \leq \frac{1}{\sqrt{1 + \frac{1}{4}\left((1 + \frac{a_-}{a_+})\frac{E_0}{\Lambda_x} + (1 - \frac{a_-}{a_+})\frac{c_0}{\Lambda_x}\right)^2}}. \tag{5.94}$$

We see that the transition amplitude depends on many parameter: most of all the ratios of initial energy and pulse strength E_0/Λ_x and between initial gap and pulse strength c_0/Λ_x and also the ratio of curvatures of the bands a_-/a_+. If the first two are small (strong pulse), there will be a good echo. Note that the seeming asymmetry of a_+ and a_- is only due to our choice of a wave packet in the positive branch, and it would be the other way round for a wave packet of negative energy.

Due to the minus sign in the bracket in the root, one would hope for cancellation of terms and therefore also strong echo even for smaller pulse strength Λ_x. The best value would be achieved, if the bracket under the root becomes zero. The condition for this case is

$$E_0 \left(1 + \frac{a_-}{a_+}\right) = -c_0 \left(1 - \frac{a_-}{a_+}\right), \tag{5.95}$$

which yields a mean energy of the wavepacket E_0 for given band structure of

$$E_0 = c_0 \frac{-1 + \frac{a_-}{a_+}}{1 + \frac{a_-}{a_+}}. \tag{5.96}$$

Unfortunately, since a_+ and a_- are both positive real numbers, this would yield

$$|E_0| \leq c_0, \tag{5.97}$$

and thus a wave packet energy inside the gap, which is not allowed.

Nevertheless, we can see that the smaller the ratio of a_-/a_+, the higher the transition amplitude. This implies that the echo is higher for a transition from higher group velocity to lower group velocity for the same magnitude of the initial energy $|E_0|$. The reason for this is that here, the transition amplitude is given as a function of the energy, instead of momentum, and the above discussed ζk^2-dependence of the transition amplitude in Eq. (5.86). Since ζ is the average of the curvatures of the parabolas and smaller ζ equals larger amplitude, the energy-dependent transition amplitude is larger when transitioning to a band with an as flat as possible curvature (ζ becomes smaller).

In Fig. 5.5(b), the correlation $\mathcal{C}(t)$ is shown for two different in two different band structures: first $a_+ = 2a_-$ i.e. transition from high to low group velocity and second $a_+ = 0.5a_-$. The initial (mean) energy relative to the gap is $E_0/\Lambda_x = 0.75$ and $\mu = 1.4$. The main difference to graphene is that the time of the echo changes according to Eq. (5.29) to

$$t_{\text{echo}} \approx t_0(1 + a_+/a_-), \tag{5.98}$$

where we used $\Delta t \ll t_0$.

As in the sections above, we compare in Fig. 5.5(c) the echo strength obtained via simulation, $\mathcal{C}(t_{\text{echo}})$, with the analytical expectations. A Gaussian wave packet is considered with the initial energy $E_0 = a_+ k_0^2 + c_0$, where $\mathbf{k}_0$ is the mean wave vector of the wave packet, in two different band structures: first $a_+ = 2a_-$ i.e. transition from high to low group velocity and second $a_+ = 0.5a_-$. For the chosen parameters ($c_0 = 0.3\Lambda_x$, $\mu_x = 1.3$) the denominator in the transition amplitude of Eq. (5.93) yields

$$a_+ = 0.5a_- : \quad \sqrt{1 + \left(1.5\frac{E_0}{\Lambda_x} - 0.15\right)^2}, \tag{5.99}$$

$$a_+ = 2a_- : \quad \sqrt{1 + \left(0.75\frac{E_0}{\Lambda_x} + 0.075\right)^2}. \tag{5.100}$$

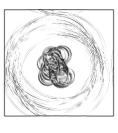

On the whole, the analytical expectations are confirmed by simulations. Thus, the population inversion QTM works also in the case of non-linear bands and an extended chiral symmetry (i.e. the matching velocity relation in the two bands), where the propagation after the pulse does not exactly look like the time-inverted propagation before the pulse. Instead, the "reflected" wave packet is faster or slower than initially depending on the setup, but still, it is possible to recover nicely the initial wave packet.

5.5 Conclusion for the two-band QTM

To summarize this chapter, we calculated the transition amplitude for a general two-band structures (see Eq. (5.17)) in Sec. 5.1 and derive requirements of the velocity in the two bands for a generalized chiral symmetry (see Eq. (5.25)) that allows us to obtain echoes of the wave function. These general results indicate whether any band structure with a given pulse is suited for our proposed population inversion QTM or not. The general results have then been tested in several examples: linear bands (Sec. 5.2), hyperbolic bands (Sec. 5.3) and parabolic bands (Sec. 5.4). In all systems, strong echoes are possible, depending on parameters and chosen pulses and the simulations confirm the analytical expectations very well.

Since this is the last chapter discussing the population inversion QTM, let us give an overall outlook. In Chaps. 3 to 5, the population inversion QTM for two-band systems has been treated thoroughly and the experimental realizability is discussed for graphene in Sec. 3.6. We do not want to discuss the experimental realizability for all proposed systems here, like bilayer graphene or direct gap semi-conductors, since considering all possibilities is beyond the scope of this thesis. Instead, we want to stress again Secs. 4.2 and 5.1, where the general results and requirements for the population inversion QTM are presented. With the help of the results derived in these sections, any two-band system at hand can be tested on suitability. In case some system turns out to be experimentally not suited for the QTM, e.g. because of non-realizable pulses needed or too short (in)elastic scattering times, there are still uncountable system out there, in which the requirements might better qualify for implementing the QTM. Thus, we are convinced that sooner or later, a population inversion QTM will be verified experimentally.

Chapter 6

Effective time-inversion for Bose-Einstein condensates

6.1 Introduction to Bose-Einstein condensates and the nonlinear Schrödinger equation

The experimental realization in 1995 of BECs using alkali atoms at very low temperatures of a few hundred nanokelvins [108–110] created a huge interest in this topic (e.g. [111]), which culminated in the Nobel prize in 2001 awarded to Cornell, Wieman and Ketterle for its realization and early fundamental studies of the properties of the condensates.

In this chapter, we want to study the QTM for the quantum-mechanical, spatially extended wave function of a Bose-Einstein condensate (BEC) cloud propagating in free space. Our QTM strategy utilizes well-established experimental techniques to tune the interaction strength among the cloud atoms [112,113] the so-called Feshbach resonance. However, not only the propagation, but also the broadening of the wave function in a parabolic band structure can be inverted, using a slightly adjusted protocol, which we will call quantum time lens (QTL). Applying a the QTL pulse several times, in the right limits, even soliton-like solutions can be obtained, i.e. that the shape of the wave packet does not change (considerably) over a long time.

Note that in this chapter, we do not go as much into detail as in the rest of the thesis, since most calculations and results have been obtained by others: All the analytical work has been done by Arseni Goussev [114,115] and most of the simulation data has been produced by Bachelor students under my supervision. More precisely, Thomas Buchner has studied the quantum time lens for single pulses of Sec. 6.3.1 with varying parameters and pulses [116]. Andreas Hauke then considered multiple pulses (see Sec. 6.3.2) and the parameter space in which a refocus of the wave packet is still possible [117]. And finally, Florian Moser investigated numerically the solitonic solutions proposed, again, by Arseni Goussev (see Sec. 6.4), showing that a certain wave packet keeps its shape for a few thousand pulses and more (depending on the parameters) [118]. For more details on the subject we refer the reader to their Bachelor theses.

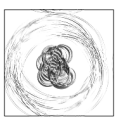

6.2 Towards quantum time mirrors for BEC

6.2.1 Action of the nonlinear kick

We want to consider the propagation of the ground state of a Bose-Einstein condensate (BEC). The differential equation describing the motion of the ground state is the Gross-Pitaevskii equation (GPE), also called nonlinear Schrödinger equation(NLSE), which can be obtained as mean field solutions in Hartree-Fock for a bosonic many-particle system with δ-function like contact interactions, under the constraint of particle number conservation [119]

$$i\hbar\frac{\partial}{\partial t}\psi(\mathbf{r},t) = \left(-\frac{\hbar^2}{2m}\nabla^2 + V(\mathbf{r}) + g|\psi|^2\right)\psi(\mathbf{r},t). \tag{6.1}$$

It looks similar to the Schrödinger equation, but it has an additional nonlinear term controlled by the parameter g, which is related to the strength of the repulsion ($g > 0$) or attraction ($g < 0$) among the bosons.

Our goal is to revert the motion of the BEC using time-dependent pulses, to get a QTM for BECs. We want to consider the case $V(\mathbf{r}) = 0$ and a time-dependent nonlinearity, i.e. $g = g(t)$ which serves as the QTM pulse. Thus, the system first moves according to the free Schrödinger equation, then the short nonlinear pulse acts and afterwards, hopefully, some part of the system comes back to its initial position, again obeying the free Schrödinger equation.

But first we want to remind the reader how a Gaussian wave packet of the form

$$\psi_0(x) = \frac{1}{\sqrt{\sqrt{\pi}\sigma}}\mathrm{e}^{-\frac{x^2}{2\sigma^2}+ik_0x} \tag{6.2}$$

evolves in time according to the free Schrödinger equation. For simplicity, we consider the 1d-case, but it is analogous for higher dimensions. The according calculation can be found in most standard text books about quantum mechanics, e.g. [120–122]. The procedure is to go to reciprocal space, since $\mathbf{k}$ is a good quantum number, make the time-evolution and go back to real space. Although it is straightforward since only Gaussian integrals are involved, we skip the calculation and state the result

$$\psi(x,t) = \frac{1}{\sqrt{\sqrt{\pi}\sigma(1+i\,\varrho t)}}\exp\left(-\frac{(x-v_0t)^2}{2\sigma^2(1+i\,\varrho t)} + i(k_0x-\omega_0t)\right) \tag{6.3}$$

with

$$v_0 = \frac{\hbar k_0}{2m}, \qquad \omega_0 = \frac{\hbar k_0^2}{2m}, \qquad \varrho = \frac{\hbar}{m\sigma^2}. \tag{6.4}$$

The main features are that the wave packet moves away from its initial position, which is what we want to invert in this section, and that the wave packet spreads, i.e. it gets broader over time, according to its standard deviation of the position expectation value

$$\Delta x_t = \frac{\sigma}{2}\sqrt{1+(\varrho t)^2}. \tag{6.5}$$

Reverting this spreading will then be the focus of the quantum time lens in Sec. 6.3, but let us focus first on the fundamental mechanism of the proposed QTM.

The NLSE of our setup is

$$i\hbar\frac{\partial}{\partial t}\psi(\mathbf{r},t) = \left(-\frac{\hbar^2}{2m}\nabla^2 + g(t)|\psi|^2\right)\psi(\mathbf{r},t), \tag{6.6}$$

where we choose for analytical reasons the time-dependence of the pulse as

$$g(t) = \lambda\delta(t-t_0), \tag{6.7}$$

with t_0 being the time of the pulse and we refer to λ in the rest of this chapter by pulse strength. Note that experimentally, a stronger coupling does not necessarily mean a larger magnetic field using the Feshbach resonance discussed below. Thus, we want to stress that we are always talking about the strength λ when mentioning stronger pulses.

But why should the given setup lead to an echo of the initial wave packet, i.e. why should the pulse make parts of the wave packet move back to its initial position? The mechanism is explained qualitatively in Fig. 6.1. There, snapshots of the simulated time-evolution of an initially Gaussian wave packet $|\psi|^2$ are shown. The initial state is indicated by the black dashed line, whereas the $|\psi(t)|^2$ is plotted in red. At the time of the pulse t_0, the wave packet has moved away from its initial position. Then, for a short time, the nonlinearity is switched on. In the NLSE of Eq. (6.6), this is equivalent to a potential which is proportional to the wave function itself $V \sim |\psi(t)|^2$ (blue line). Classically, a particle is accelerated according to $-\partial V/\partial x$, thus the left part of the wave packet is expected to be accelerated to the left, whereas the right part is accelerated to the right. If this acceleration is strong enough to overcome the initial velocity $\sim k_0$, (at most) half of the wave packet moves right again. Indeed, this is what we can see at $t = t_{\text{echo}}$.

A few comments can be made already from the qualitative picture. Compared to the two-band QTM discussed in Chaps. 3-5, the quality of the echo in this setup is not even close. As already mentioned, at most half of the wave packet can move back in this example, whereas in the Dirac case, almost 100% can be achieved in principle. Moreover, the shape of the wave packet changes here quite significantly (e.g. many sub-peaks in figure 6.1), whereas in the two-band QTM, a real effective time-reversal can be achieved, where indeed the time-evolution after the pulse looks exactly as compared to before the pulse but time-inversed, at least for certain setups (compare Secs. 4.2 and 5.1). Nevertheless, this QTM for a BEC is more close to the instantaneous time mirror for water waves [45]. There, the water wave structure also changes and has several side peaks, but still, what comes back is enough to recreate the structure of what was induces initially (e.g. Eiffel tower or a smiley). In that sense, our proposed setup might be good enough to get an echo.

Before investigating the echo mechanism in more detail, we want to rescale the Schrödinger equation, using $t \to \tau t$, $\mathbf{r} \to \xi\mathbf{r}$, $\psi \to \xi^{-D/2}\psi$ and $\lambda \to \hbar\xi^D\lambda$, where D is the (spatial) dimension of the system. We can write the nonlinear Schrödinger equation in a dimensionless form as

$$i\frac{\partial}{\partial t}\psi(\mathbf{r},t) = \left(-\frac{\hbar\tau}{2m\xi^2}\nabla^2 + \lambda\delta(t-t_0/\tau)|\psi|^2\right)\psi(\mathbf{r},t). \tag{6.8}$$

Depending on the exact problem, different choices of τ and ξ will be better suited. In this case, it makes sense to use $\tau = t_0$, $\xi = \sqrt{\frac{\hbar\tau}{2m}}$, such that the unit of time is

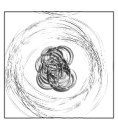

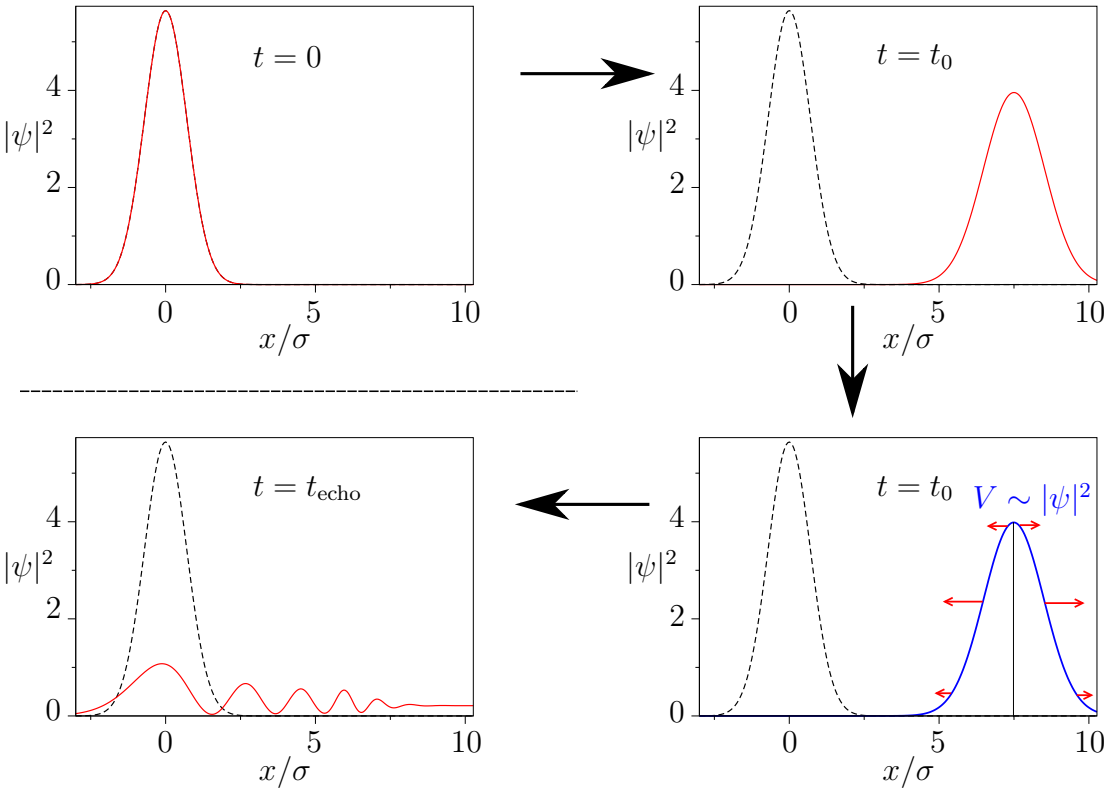

Figure 6.1: Qualitative explanation of the echo mechanism of our proposed QTM for BECs. The initial state (black dashed, in arbitrary units) propagates according to the free Schrödinger equation for $t < t_0$, moving away from its initial position and increasing its width (red). At $t = t_0$, the nonlinear term is switched on for a short time and acts effectively like a potential $V \sim |\psi|^2$ (blue). Classically, particles are accelerated according to $-\partial V/\partial x$, which would mean in this case that the left hand side of the wave packet is accelerated to the left, whereas the right part to the right, according to the red arrows. Indeed, parts of the wave move back to its initial position, with the highest overlap with the initial state at t_{echo}.

the time of the pulse and Eq. (6.8) becomes

$$i\frac{\partial}{\partial t}\psi(\mathbf{r},t) = \left(-\nabla^2 + \lambda\delta(t-1)|\psi|^2\right)\psi(\mathbf{r},t), \tag{6.9}$$

where everything is dimensionless.

Having defined the setup, let us study now the action of the pulse. Since it is $\sim \delta(t-1)$, we assume that the nonlinearity is the most important term during the pulse and we neglect the rest, meaning that the shape of the wave packet does not change during the pulse. Therefore, the propagation is governed by

$$i\frac{\partial\psi(\mathbf{r},t)}{\partial t} = \lambda\delta(t-1)|\psi_-|^2\psi(\mathbf{r},t), \tag{6.10}$$

where $\psi_-(x) = \psi(x, t_0^-)$ is the wave function directly before the pulse at $t_0^- = 1-\varepsilon$, with a small $\varepsilon > 0$. Rewriting Eq. (6.10) by dividing by ψ, we get

$$i\frac{\partial(\ln\psi(\mathbf{r},t))}{\partial t} = \lambda\delta(t-1)|\psi_-|^2$$
$$\ln\frac{\psi(\mathbf{r},t_0^+)}{\psi(\mathbf{r},t_0^-)} = -i\lambda|\psi_-|^2, \tag{6.11}$$

where in the last step, we integrated over time just around the pulse from t_0^- to $t_0^+ = 1+\varepsilon$ in dimensionless units. Therefore, the wave function $\psi_+(\mathbf{r}) = \psi(\mathbf{r},t_0^+)$ directly after the pulse reads

$$\psi_+(\mathbf{r}) = \psi_-(\mathbf{r})\mathrm{e}^{-i\lambda|\psi_-|^2}, \tag{6.12}$$

thus, we only changed the phase of the wave function. As said before, we assume that the pulse is short enough such that the probability density of the wave function does not change over the duration of the pulse such that

$$\rho = |\psi_-(\mathbf{r})|^2 = |\psi_+(\mathbf{r})|^2. \tag{6.13}$$

To see whether the phase change enables to revert the motion of the wave function, we consider the current density, which is given in dimensionless units as

$$j(\mathbf{r},t) = \mathrm{Im}\left[\psi(\mathbf{r},t)^*\,\nabla\,\psi(\mathbf{r},t)\right]. \tag{6.14}$$

After the pulse, the current $j_+(\mathbf{r}) = j(\mathbf{r},t_0^+)$ becomes

$$j_+(\mathbf{r}) = j_-(\mathbf{r}) - \rho\lambda\nabla\rho, \tag{6.15}$$

which indeed corresponds to an acceleration proportional to the gradient of the shortly acting potential ($\sim -\nabla\rho$) as expected classically (see Fig. 6.1). $j_-(\mathbf{r}) = j(\mathbf{r},t_0^-)$ is the current directly before the pulse. So indeed, if at some positions $\mathbf{r}$ the requirement that $|\rho\lambda\nabla\rho| > |j_-|$ (and that both terms have the same sign) is fulfilled, parts of the wave change their propagation direction because the sign of the current density changes.

As an example, consider the initial 1d Gaussian wave packet of Eq. (6.2). Until the pulse, it has changed its shape according to Eq. (6.3) to (up to space-independent phases)

$$\psi_-(x) = \left(\pi(\sigma^2-\sigma^{-2})\right)^{-\frac{1}{4}}\exp\left(-\frac{\tilde{x}^2}{2\sigma^2(1+i\varrho t)} + ik_0\tilde{x}\right), \tag{6.16}$$

with $\tilde{x} = x - k_0$ (in dimensionless units). Thus,

$$\rho = |\psi_-(x)|^2 = \frac{\exp\left(-\tilde{x}^2/\sigma_1^2\right)}{\sqrt{\pi}\sigma_1}, \tag{6.17}$$
$$\sigma_1 = \sqrt{\sigma^2-\sigma^{-2}} \tag{6.18}$$

and the currents before and after the pulse are according to Eqs. (6.14) and (6.15)

$$j_-(x) = \left(k_0 + \frac{\tilde{x}}{\sigma^2\sigma_1^2}\right)\rho, \tag{6.19}$$
$$j_+(x) = j_-(x) - \frac{2\lambda\tilde{x}}{\sigma_1^2}\rho^2. \tag{6.20}$$

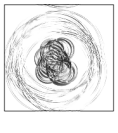

We can estimate the minimally required kicking strength $\lambda_{\min}$ by demanding that at $\tilde{x} = \sigma_1$, the current density is just about to reverse its sign

$$\begin{aligned} & j_+(k_0 - \sigma_1) \stackrel{!}{=} 0 \\ \Rightarrow \quad & \lambda_{\min} \simeq \frac{e\sqrt{\pi}}{2} k(\sigma^2 + \sigma^{-2}), \end{aligned} \tag{6.21}$$

under the assumption $k \gg 1/(\sigma^2\sigma_1)$, i.e. a wave packet that moves much faster than it spreads.

As an example for a 2d wave packet, we use a Gaussian ring

$$\psi_0(\mathbf{r}) = \sqrt{\frac{1}{2\pi^{3/2}R\sigma}} \exp\left(-\frac{(r-R)^2}{2\sigma^2} + ik_0 r\right), \tag{6.22}$$

with $r = |\mathbf{r}|$ and $k > 0$, which spreads radially with average velocity k. Similar to the 1d case, but way more tedious [114], in the regime $kR \gg 1$ and $1 \ll \sigma \ll R$, the current after the pulse yields

$$\mathbf{j}_+(\mathbf{r}) = \left(k_0\rho + \frac{2\lambda(r-R_1)}{\sigma^2\rho^2}\right)\frac{\mathbf{r}}{r}, \tag{6.23}$$

where $R_1 = R + k$ is the radius at the time of the pulse and the minimally required pulse strength can be estimated as

$$\lambda_{\min} \simeq e\sqrt{\pi}^3 (R+k)k\sigma^2. \tag{6.24}$$

To conclude the analytical section, we want to comment on the well-known technique of phase imprinting and the connection to our proposal. The phase-imprinting technique (e.g. [123]) was proposed to change the motion of a wave packet by applying a position-dependent potential for a short time. The additional position-dependent phase factor coming from the time-evolution operator changes the current density, similar to Eq. (6.12). Thus, mathematically the current-manipulation mechanism is the same as in our case. If one knows exactly the shape and the position of the wave function, one could achieve exactly the same with external potentials as we do. But here is the important difference: in our proposal, we do *not* have to know anything about the wave function. We only propose to change *homogeneously* the interaction strength among the atoms in the BEC cloud. The inherent nonlinearity in the NLSE then takes care of manipulating the current density of the wave function, such that parts come back to the initial position. Therefore, despite the non-perfectness of the echo, our setup should be much easier to be implemented than to optimally match external fields to the position and shape of the wave function.

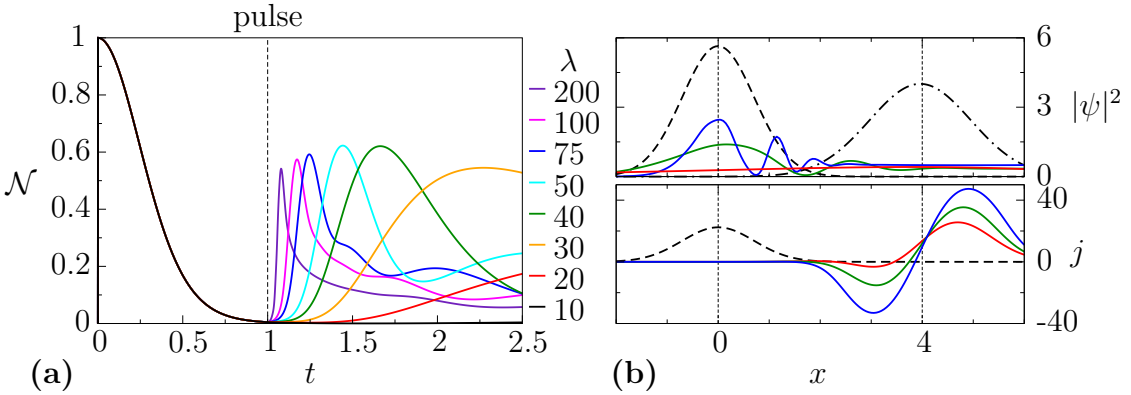

Figure 6.2: Dependence of our proposed echo mechanism on the pulse strength λ in dimensionless units. (a) The norm correlation $\mathcal{N}$ defined in Eq. (6.26) is shown as a function of time for several pulse strengths λ, with $\sigma = 1$ and $k_0 = 4$. Over a wide range, echoes can be obtained, with the general feature that the larger λ, the stronger is the effective (backwards) acceleration such that the echo happens earlier. The best echo can be achieved at around $\lambda \simeq 50$. (b) The wave function $|\psi|^2$ at the time of the echo (upper panel), as well as the current density j directly after the pulse are shown with the same color code as in (a). The initial $|\psi|^2$ and j are shown as dashed lines and the dash-dotted line in the upper panel is the wave function at the time of the pulse $t = t_0$.

6.2.2 Simulations to quantify the echo

To verify the analytically found results concerning the QTM for a BEC in the previous section, we use the TQT library to simulate the time evolution of a Gaussian wave packet $|\psi_0\rangle$ according to the nonlinear Schrödinger equation (6.6). Instead of the instantaneous δ-pulse, we use a sharp Gaussian of the form

$$g(t) = \frac{1}{\sqrt{2\pi}\Delta t} \mathrm{e}^{-\frac{(t-t_0)^2}{\Delta t^2}}, \tag{6.25}$$

with $\Delta t = 0.001 t_0$ in the 1d case and $\Delta t = 0.0025 t_0$ in 2d.

To measure the echo strength, one could use the fidelity, i.e. the overlap of initial and echo state, but taking into account that the momentum reversed its direction. However, to be closer to experiments where the quantum overlap is quite unlikely to be measured, we stick to the norm correlation $\mathcal{N}$, defines as

$$\mathcal{N}(t) = \frac{\int \mathrm{d}^D\mathbf{r} |\psi_0(\mathbf{r})|^2 \, |\psi(\mathbf{r},t)|^2}{\sqrt{\int \mathrm{d}^D\mathbf{r} |\psi_0(\mathbf{r})|^4} \sqrt{\int \mathrm{d}^D\mathbf{r} |\psi(\mathbf{r},t)|^4}}, \tag{6.26}$$

where only the probability density of initial and propagated wave packet is used. The denominator in the norm correlation serves as normalization and is the reason why also overlaps with broadened wave function yield rather high values, due to the 4th power.

In Fig. 6.2(a), the norm correlation is shown as a function of time for different values of λ. Remember that we use dimensionless variables, such that the time is

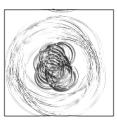

normalized to when the pulse takes place. The 1d Gaussian wave packet of Eq. (6.2) is used with width $\sigma = 1$ and the initial momentum $k_0 = 4$. As expected, the stronger the kick, the faster the acceleration such that the wave packet comes back to its initial position earlier. On the other hand, an echo can be seen over a large interval of kicking strength λ, as long as it is strong enough ($\lambda_{\text{min}} \simeq 20$, compare Eq. (6.21)) to invert the sign of the current.

The change of the current right after the pulse, as well as the echo wave function are shown for three values of λ in Fig 6.2(b), with the same color coding as in panel (a). The dashed black line shows initial current and probability density and the dash-dotted black line shows $|\psi(x, t_0)|^2$ at the time of the pulse. The current j in the lower panel of Fig. 6.2(b) right after the pulse shows nicely that indeed the sign changes for the left half of the wave packet, such that this part moves back. Moreover, in the critical case $\lambda \simeq 20$ (red), the "acceleration" due to the kick is just strong enough to make the current change its sign at some points.

Although the wave packets change their shape and are in general broader than the initial Gaussian, there is still an distinct echo visible. The side peaks of the blue curve have been present already in Fig. 6.1, with the rule of thumb: The stronger the kick, the more side peaks.

To get a better feeling for the needed parameters, the echo strength, which is the maximal value of the norm correlation after the pulse for a given simulation, is plotted as a function of λ and σ in Fig. 6.3(a) and as function of λ and k_0 in panel (b)). The missing, fixed parameter is $k_0 = 4$ and $\sigma = 1$, respectively. The black line shows the analytical approximation for the minimally required strength λ_{min} of Eq. (6.21), matching reasonably the simulation.

Furthermore, for a 2d Gaussian ring of Eq. (6.22), the same parameter plots are shown in panels (c) and (d), with fixed $k_0 = 4$ or $\sigma = 2$, respectively. The radius of the ring is $R = 6$ in all cases. Although we are not really in the valid limit used to approximate the minimally required kicking strength λ_{min} of Eq. (6.24), where we required $R \gg \sigma$, the estimate still yields reasonable results, at least to evaluate the order of magnitude of the required kicking strength.

To conclude this section, we want to comment on whether or not such a quantum time mirror in Bose-Einstein condensates is in principle realizable in atom-optics experiments. The first remark is about the time-dependence of the nonlinearity. The interaction rate of atoms in Bose-Einstein condensates can be tuned, using a magnetic field-dependent Feshbach resonance. By changing the magnetic field strength by several Gauss, the collision rate varied by a factor of 10^4 [112, 113], so even a rather fast switching on and off should be in principle possible, to make the proposed QTM possible.

Finally, let us consider realistic parameters, e.g. of a Bose-Einstein condensate of ^{7}Li atoms with mass $m = 7.016u = 1.165 \times 10^{-26}\,\text{kg}$. We assume a free propagation time until the pulse of 10 ms. Thus a typical range of wave packet width of $10 - -50\,\mu\text{m}$ corresponds in our dimensionless parameters to $1.05 < \sigma < 5.26$, and the mean velocity in the typical range of $2 - -10\,\text{mm/s}$ corresponds to $2.1 < k_0 < 10.5$. These are parameter which were considered in this section, and therefore we believe that the predicted QTM mechanism is possible in nowadays atom optics experiments.

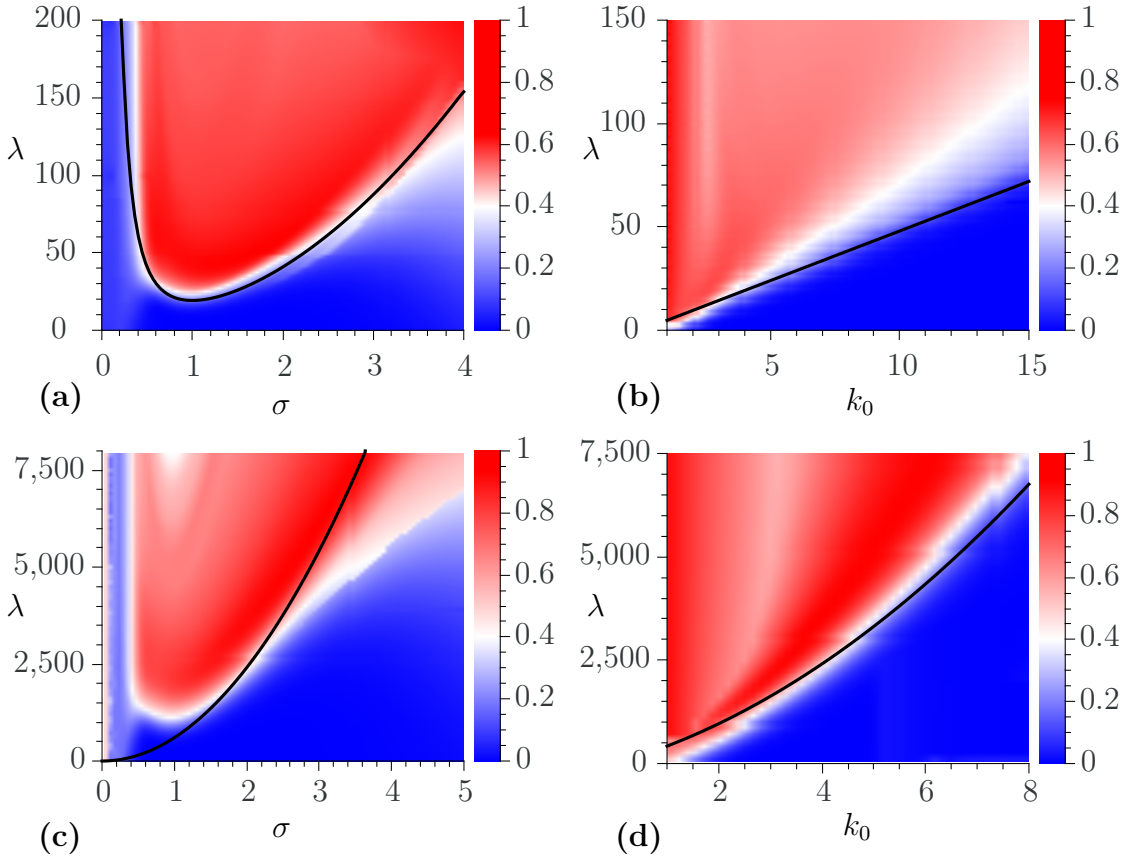

Figure 6.3: Parameter space for the BEC echo measured by the norm correlation $\mathcal{N}$ varying the pulse strength λ, the wave packet width σ and the mean velocity k_0 (dimensionless units) in 1d (a) and (b)) and 2d ((c) and (d)). The black curves are the estimated minimally required kicking strength λ_{min} of Eq. (6.21) in 1d, resp. Eq. (6.24) in 2d, below which no echo is supposed to happen. Although in the 2d case, the parameters are in a regime in which the estimation for λ_{min} is not justified (see text), the approximation yields at least the right order of magnitude of the needed value of λ.

6.3 Quantum time lens

6.3.1 Single pulse

In Sec. 6.2, we addressed the problem of inverting the motion of a BEC whose propagation is governed by the NLSE of Eq. (6.6). In this section, we are only interested in reverting the spreading, i.e. the broadening of a wave packet in the free Schrödinger equation.

The idea is simple: We manipulate the current density by the same setup, but adjust the parameters such that the desired effect happens. All we have to do is to change the sign of the nonlinear term ($\lambda < 0$), such that the effective potential during the pulse refocuses the wave packet, see Fig. 6.4(a). Moreover, since smaller velocities have to be overcome (the "spreading velocity") in this refocusing setup, the required pulse strength is supposed to be much smaller than for the time mirror.

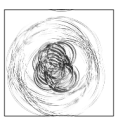

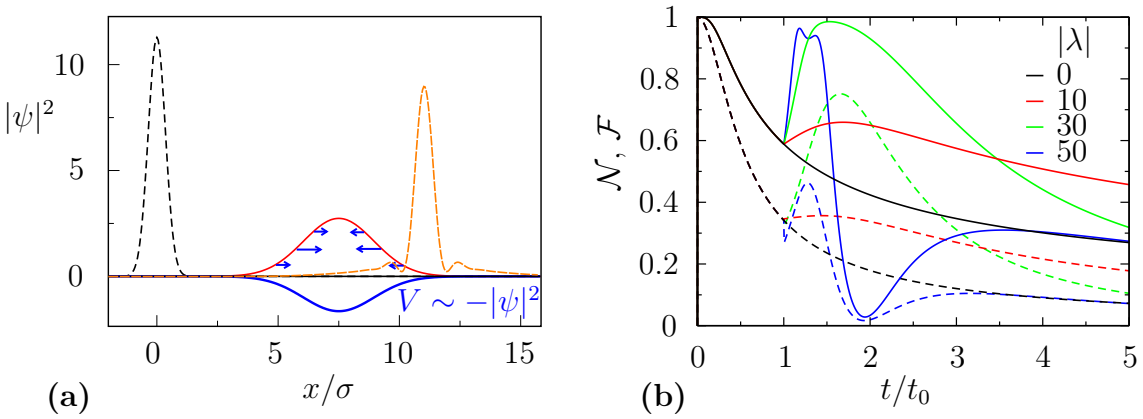

Figure 6.4: Qualitative mechanism and quantitative refocus strength of the QTL. (a) The mechanism is the same as in Sec. 6.2 (compare Fig. 6.1), with the difference that $\lambda < 0$ is used here. The initial state (black dashed) broadens until the pulse (red), where the nonlinearity acts as an effective potential (blue) which qualitatively accelerates the flanks of the wave packet towards the center (blue arrows), such that the wave function refocuses again (orange dashed). (b) The refocus strength measured by the norm correlation $\mathcal{N}$ (solid) defined in Eq. (6.26) or by the fidelity $\mathcal{F}$ (dashed) defined in Eq. (6.27) is shown as a function of time for different pulse strengths λ, with $k_0 = 0$. Though showing qualitatively similar behavior, the norm correlation overvalues the refocus strength as compared to the fidelity, because only the probability densities play a role. Another feature is that for strong pulses ($|\lambda| \gtrsim 50$), the decay after the refocus is much higher than in the case without pulse, which will become important in the self-regulation mechanism of multiple pulses in Sec. 6.3.2.

In Fig. 6.4(a), also the "refocused" wave packet (orange) is shown. For other parameters (stronger λ), the wave packet can be made to refocus to the same height, or even higher than the initial wave packet.

The analytical treatment is the same in Sec. 6.2.1, with the only difference that the outer parts of the wave packet are moving back to its center. That means that for $k_0 > 0$, the classical velocity changes from e.g. $j(x^>)/\rho > k_0$ to $j(x^>)/\rho < k_0$, where $x^> = k_0 + \varepsilon$ is a position where the spreading is faster than the mean velocity k_0. In other words, instead of demanding a negative velocity as compared to before the pulse, we require that parts faster than k_0 have a velocity smaller than k_0 after the pulse such that they move back to the center.

For the QTL, we consider as a measure for the wave packet refocus the (translated) fidelity $\mathcal{F}$

$$\mathcal{F}(t) = |\langle \tilde{\psi}_0 \mid \psi(t) \rangle|^2, \tag{6.27}$$

where $\tilde{\psi}_0$ is the initial state translated by the mean velocity $\tilde{\psi}_0(\mathbf{r}) = \psi_0(\mathbf{r} + v_0 t)$, since we want to invert only the spreading but not the over all movement of the wave packet. The reason to consider the fidelity instead of the norm correlation as in the QTM case is that, in the long run, we do not only want to do one single refocus, but many of them. Thus, not only the experimentally accessible norm correlation is of importance but rather the true "similarity" to the initial wave packet, which is better described by the fidelity since also phases are considered.

In Fig. 6.4(b), the fidelity (dashed lines) as well as the norm correlation (solid lines) are shown for a 1d Gaussian wave packet with $k_0 = 0$ and an initial width σ such that the width of the wave packet at the pulse is $\sigma_1 = 11\sigma$. The definition of these two observables of Eqs. (6.26) and (6.27) seems to be such that in the case without pulse (black), the fidelity (dashed) corresponds to the square of the norm correlation (solid): $\mathcal{F} \simeq \mathcal{N}^2$. Although the two observables are comparable qualitatively, e.g. extrema at (roughly) the same times, the norm correlation yields distinct higher refocus values, since the phases are not considered. For $\lambda = 30$, the initial and time evolved probability density of the wave packets $|\psi(\mathbf{r})|^2$ might look the same at the time of the echo in real space ($\mathcal{N} \approx 1$). However, the structure in $\mathbf{k}$-space differs, which would yield some destructive interference by evaluating $\mathcal{F}$ in real space, but this does not matter for $\mathcal{N}$ due to its dependence only on $|\psi(\mathbf{r})|^2$ and therefore $\mathcal{F} < \mathcal{N}$.

We want to draw attention to the rate of decay after the refocus has happened in Fig. 6.4(b), because this will become important later in Sec. 6.3.2. Whereas for small pulse strength, the fidelity and norm correlation decrease very slowly (see e.g. red line $\lambda = 10$), the decay rate is much higher for larger pulse strengths, see $\lambda = 50$ (blue). The reason for this is that the broadening, which decreases initially the amplitude of the wave packet is drastically accelerated, such that it even outruns the case without kick at around $t = 1.5t_0$. Therefore, due to the nonlinearity ($|\psi|^2$), the effect of a subsequent kick at $t = 2t_0$ would be effectively smaller in the case of $\lambda = 50$ than for $\lambda = 10$ or $\lambda = 30$, since the amplitude of the wave function is smaller.

In the last part of this section, we want to compare the simulations of the fidelity with analytically obtained data for a 1d Gaussian wave packet. To be able to compare with experiments, we choose physically relevant parameters for a BEC of Rubidium atoms

$$m = 86.909u = 1.44 \times 10^{-25}\,\mathrm{kg} \qquad (^{87}\mathrm{Rb\ atom}), \tag{6.28}$$

$$\sigma = 5\,\mu\mathrm{m} = 5 \times 10^{-6}\,\mathrm{m}. \tag{6.29}$$

Furthermore, instead of fixing the pulse time t_0, we set the time of the measurement (here still fidelity) to 0.2 s and vary $t_0 \in [0, 0.2\,\mathrm{s}]$ as well as the pulse strength λ.

Analytically, the initial wave packet with the shorthand notation

$$\psi^{(0)}_{\alpha_0,x_0,v_0}(x) = \left(\frac{2\mathrm{Re}(\alpha_0)}{\pi}\right)^{1/4} \mathrm{e}^{-\alpha_0(x-x_0)^2 + im\,v_0(x-x_0)/\hbar}, \tag{6.30}$$

is propagated until the pulse, using the propagator $K_0^{(t)}(x-x')$ of the free Schrödinger equation given by

$$K_0^{(t)}(\xi) = \sqrt{\frac{m}{2\pi i\hbar t}} \exp\left(i\frac{m\xi^2}{2\hbar t}\right), \tag{6.31}$$

which yields

$$\begin{aligned}\psi^{(t)}_{\alpha_0,x_0,v_0}(x) &= \int_{-\infty}^{\infty} \mathrm{d}x'\; K_0^{(t)}(x-x')\psi^{(0)}_{\alpha_0,x_0,v_0}(x') \\ &= \mathrm{e}^{i\theta_t}\psi^{(0)}_{\alpha_t,x_t,v_0}(x)\end{aligned} \tag{6.32}$$

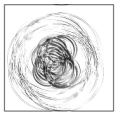

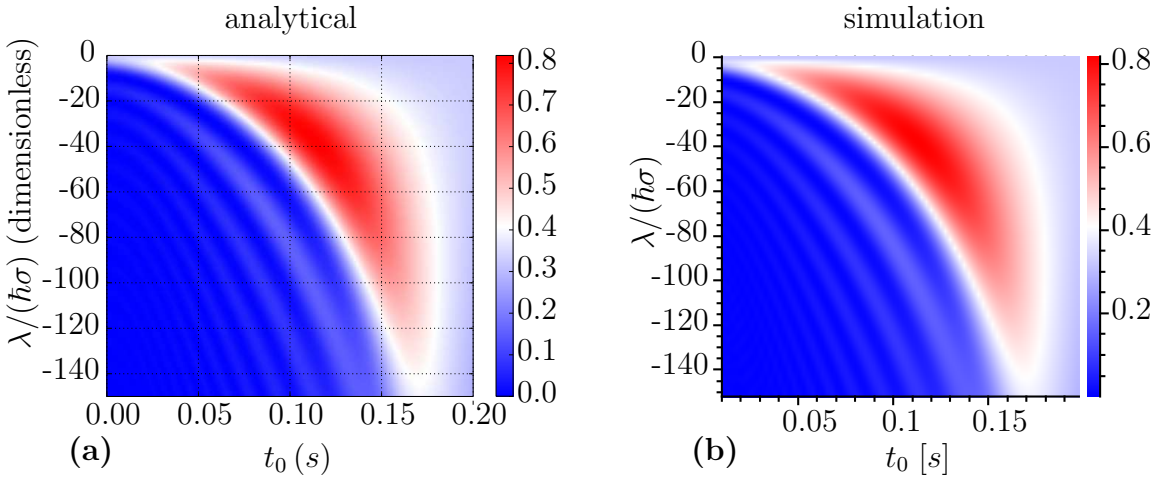

Figure 6.5: Parameter space of the refocus strength. Here, the fidelity $\mathcal{F}$ at $t = 0.2\,\mathrm{s}$ is plotted, depending on the kicking strength λ and the time of the pulse t_0, either by (a) evaluating the analytical solution of Eq. (6.38), or by (b) simulating the full propagation using TQT, which yield the same result. The other parameters are chosen to be in agreement with a BEC of Rubidium atoms, see Eqs. (6.28) and (6.29). The analytical solution of Eq. (6.38) as well as its numerical evaluation was performed by Arseni Goussev, whereas the simulation data was obtained by Thomas Buchner for his Bachelor thesis [116].

with

$$\alpha_t = \frac{\alpha_0}{1 + 2i\hbar\alpha_0 t/m}, \tag{6.33}$$

$$x_t = x_0 + v_0 t, \tag{6.34}$$

$$\theta_t = \frac{m v_0^2 t}{2\hbar} - \frac{1}{2}\tan^{-1}\left(\frac{2\hbar\alpha_0}{m}t\right), \tag{6.35}$$

in agreement with Eq. (6.3), where $\alpha_0 = 1/\sqrt{2}\sigma$. We define the pulse operator Q_λ with

$$\langle x \mid Q_\lambda \psi\rangle = \mathrm{e}^{i\phi_\lambda(x)}\psi(x) \quad \text{with} \quad \phi_\lambda(x) = -\frac{\lambda}{\hbar}|\psi(x)|^2, \tag{6.36}$$

in agreement with Eq. (6.12)

To calculate the fidelity after at $t_1 = 0.2\,\mathrm{ms}$, as a function of pulse time $t_0 < t_1$ and pulse strength λ, we let the free propagator K_0 act before and after the pulse and in between the pulse operator takes care of the right time evolution

$$\mathcal{F}(t_0, \lambda) = |\langle \psi^{(0)}_{\alpha_0, x_{t_1}, v_0} \mid K_0^{(t_1 - t_0)} Q_\lambda K_0^{(t_0)} \mid \psi^{(0)}_{\alpha_0, x_0, v_0}\rangle|^2. \tag{6.37}$$

Again, we only want to recover the initial shape of the wave function but not change the overall movement, the overlap is taken at t_1 with the bra $\langle \psi^{(0)}_{\alpha_0, x_{t_1}, v_0}|$ of the *translated* initial state. Altogether, we arrive at

$$\mathcal{F}(t_0, \lambda) = \frac{2}{\pi}\sqrt{\mathrm{Re}(\alpha_{t_0})\mathrm{Re}(\alpha_{t_1 - t_0})} \times \left| \int_{-\infty}^{\infty} \mathrm{d}x \, \exp\left\{ -(\alpha_{t_0} + \alpha_{t_1 - t_0})\, x^2 - i\frac{\lambda}{\hbar}\sqrt{\frac{2\mathrm{Re}(\alpha_{t_0})}{\pi}}\mathrm{e}^{-2\mathrm{Re}(\alpha_{t_0})x^2} \right\} \right|^2, \tag{6.38}$$

which has to be evaluated numerically and is shown in Fig. 6.5(a) for the physical parameters for mass and width in Eqs. (6.28) and (6.29) of the wave packet. A very interesting feature of Eq. (6.38) is that the refocus is independent of the velocity of the initial wave packet.

On the other hand, we can use TQT to evolve the initial wave packet of Eq. (6.30) in time with the same parameters and conditions as before, but a sharp Gaussian pulse instead of the Dirac-δ. This simulations have been done by Thomas Buchner [116]. The simulation data is shown in Fig. 6.5(b) and is in almost perfect agreement with the analytical data. The reason why it is slightly more blurred is that the calculation of the full simulation takes longer than the numerical evaluation of an integral, which is why less data points have been gathered here.

The best achievable refocus is in both cases $P_{\max} \approx 0.82$, achieved analytically at $t_0^{\max} = 0.1117\,\mathrm{s}$ and $\lambda_{\max}/\hbar\sigma = -36.25$, and by simulation at reasonable similar values of $t_0^{\max} = 0.1123\,\mathrm{s}$ and $\lambda_{\max}/\hbar\sigma = -36.99$.

6.3.2 Multiple pulses – self-regulation due to the nonlinearity

In Subsec. 6.3.1, we have seen that the initial state can be approximately refocused to its original shape by applying the nonlinear pulse. In this subsection, we want to investigate what happens if multiple pulses are applied one after the other, such that the state keeps its shape over longer time.

In his Bachelor thesis [117], Andreas Hauke investigated, among other topics, the optimal parameter sets empirically for ($\lesssim 10$) pulses, i.e. finding out the optimal time and strength of each subsequent pulse such that the refocused wave packet has again the same shape. Although quite interesting, this empirical search is quite tedious and not applicable for a lot of pulses and/or different initial wave packets and/or initial parameters.

More importantly, he found out that deviating from his perfect parameter set, e.g. by choosing a constant kicking strength Λ of each subsequent pulse and constant time intervals ΔT after the first kick, the qualitative behavior is rather independent of the exact choice of parameters. Moreover, the refocus value does not decrease monotonically, but undergoes some oscillating behavior as can be seen in Fig. 6.6(a). There, the norm correlation $\mathcal{N}$ defined in Eq. (6.26) as measure of the refocus is plotted as a function of time with physical parameters of, again, a BEC of Rubidium atoms ($m = 1.44 \times 10^{-25} kg$, $\sigma = 6 \times 10^{-6} m$) and parameters of the first pulse $\lambda/(\hbar\sigma) = 50$ and $t_0 = 0.2s$. The time between each subsequent pulse is $\Delta T = 0.7s$ and the pulse strength Λ varies from $\Lambda/(\hbar\sigma) = 35$ to $\Lambda/(\hbar\sigma) = 55$.

However, due to the nonlinear pulse, the "real pulse strength" does not only depend on Λ, but also on the wave function at the time of the pulse $|\psi(x)|^2$. Therefore, we define the "real pulse strength" as the product $\lambda|\psi(x)|^2$ at the time of the pulse. This nonlinearity leads to a self-regulation that makes the refocus strength oscillate in a range rather independent on the exact parameter.

The reason for this self-regulation is explained oversimplified in the sketch of Fig. 6.6(b). According to Sec. 6.3.1, a weak pulse leads to a slow decay after the refocus process and therefore a rather high amplitude of $|\psi(x, t_{\mathrm{pulse}})|^2$ at the time of

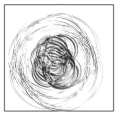

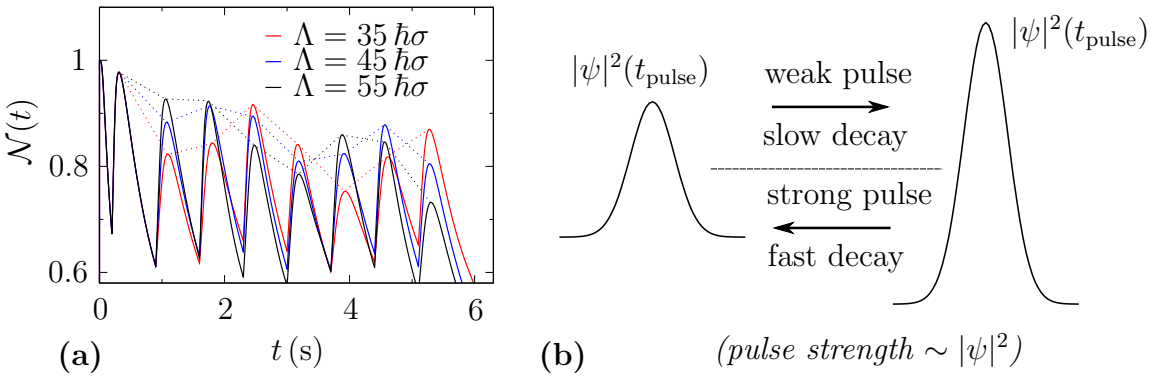

Figure 6.6: Refocusing with multiple pulses. (a) The norm correlation is shown as a function of time, with eight kicking and refocusing events, for different kicking strengths Λ for the pulses after the first one, according to Andreas Hauke [117]. The parameters are chosen to be in agreement with a BEC of Rubidium atoms (see text). Although in detail quite different, the refocus values for all three shown Λ undergo an oscillation in the same range of refocus strengths. Therefore, it does not matter, which exact pulse strength Λ is chosen. The self-regulation mechanism which is behind this oscillating behavior is (oversimplified) shown in panel (b). Due to the nonlinearity, the real pulse strength is not only governed by Λ, but also the $|\psi|^2$ itself at the time of the pulse. Thus, if after some time the amplitude of $|\psi|^2$ is rather small, the according pulse will be also rather weak. Weak pulse means (by tendency) weak refocus, but also slow decay after the refocus. Therefore, the amplitude of $|\psi|^2$ at the next pulse will be larger, such that a stronger pulse happens, with a stronger refocus. However, also the decay will be stronger and thus the amplitude of $|\psi|^2$ at the next pulse will be smaller again and the cycle begins from the top.

the next pulse. Although Λ does not change, the real pulse strength, i.e. including $|\psi(x, t_{\text{pulse}})|^2$, is still higher than before, because of the higher amplitude. Therefore, a strong pulse happens, which makes the decay again faster such that the next time, the pulse is effectively weaker, and the cycle repeats from the top. Of course, substeps of this cycle will happen in reality such that the oscillation period is not 2 pulses but rather roughly $4 - 5$ in our case, for instance. In this explanation, we assumed that the parameters are in a regime such that the refocus always happens before the next pulse. For more information, see Ref. [117].

In this section, we showed that multiple pulsing can be used to prevent the spreading of a wave packet. Moreover, due to the nonlinear pulse, a self-regulation sets in such that the exact parameters (strength Λ and time until next pulse ΔT) are not of major importance, as long as they are in the right order of magnitude. In the next section, we go one step further and look for setups where the shape of the wave function can be kept over hundred or even thousands of pulses. For that, the approach has to be more methodological, which is why we start with an analytical derivation of solitonic solutions in the pulsed nonlinear Schrödinger equation.

6.4 Solitons in the pulsed NLSE

6.4.1 1d solitons in the limit of weak pulses with high repetition rate

In Sec. 6.3.2, we considered numerically multiple ($\lesssim 10$) pulses and investigated which parameters are to be chosen. On the other hand, it is known that for the nonlinear Schrödinger equation, there exist solitonic solutions, i.e. solutions which do not change their shape. Since we are considering the free Schrödinger equation for the most time and only during the short pulse, the nonlinearity kicks in, they are not directly applicable in our case. However, in the limit of fast but weak kicks, the solutions of the static, nonlinear Schrödinger equation should be recovered. As any analytical calculations in this chapter, the following derivation has been performed by Arseni Goussev.

So let us consider the following differential equation with infinite, periodic pulses

$$i\frac{\partial\psi}{\partial t} = -\frac{\hbar}{2m}\frac{\partial^2\psi}{\partial x^2} - \lambda\sum_{n=-\infty}^{\infty}\delta(t-nt_0)|\psi|^2\psi. \tag{6.39}$$

Introducing different dimensionless parameters than in Sec. 6.2.1 of the form

$$t \to \frac{\hbar t_0^2}{m\lambda^2}t, \quad x \to \frac{\hbar t_0}{m\lambda}x, \quad \psi \to \sqrt{\frac{m\lambda}{\hbar t_0}}\psi, \tag{6.40}$$

and defining

$$\epsilon = \frac{m\lambda^2}{\hbar t_0}, \tag{6.41}$$

the differential equation (6.39) becomes

$$i\frac{\partial\psi}{\partial t} = -\frac{1}{2}\frac{\partial^2\psi}{\partial x^2} - \epsilon\sum_{n=-\infty}^{\infty}\delta(t-n\epsilon)|\psi|^2\psi. \tag{6.42}$$

Thus, the parameter ϵ is the only free parameter, which describes both, the time between two kicks and the kicking strength.

For a soliton, we require a normalizable wave function

$$\int_{-\infty}^{\infty}\mathrm{d}x\,|\psi_{\mathrm{sol}}|^2 = 1, \tag{6.43}$$

which fulfills

$$\text{if} \quad \psi(x,0^+) = \psi_{\mathrm{sol}}(x), \quad \text{then} \quad \psi(x,\epsilon^+) = \mathrm{e}^{i\phi}\psi_{\mathrm{sol}}(x-q), \tag{6.44}$$

where q and ϕ are arbitrary real numbers and the superscript " $+$ " denotes the moment just after the according time. In words, the real space shape of the soliton must not change from one pulse to the next. The only difference is that it might have acquired a kinetic phase ϕ and it is allowed to move a distance q.

As mentioned above, for weak kicks and high kicking frequency, we expect a solitonic solution to exist, as in the case of the static nonlinear Schrödinger equation.

This limit corresponds in our case to $\epsilon \ll 1$. Therefore, let us consider the time evolution from one kick to the next, as well as the action of the pulse up to linear order in ϵ. For simplicity, let us start with $\psi_0(x) = \psi(x, 0^+)$ directly after a kick until $t = \epsilon^-$, which is the (dimensionless) time right before the next kick. According to the free Schrödinger equation, we have

$$\psi_-(x) \equiv \psi(x, \epsilon^-) = \psi_0(x) + \frac{i\epsilon}{2}\psi_0''(x) + \mathcal{O}(\epsilon^2). \tag{6.45}$$

After the pulse, the wave function $\psi_+(x) = \psi(x, \epsilon^+)$ becomes due to the action of the nonlinear pulse in Eq. (6.12)

$$\begin{aligned}\psi_+(x) &= \psi_-(x)\ \exp\left(i\epsilon|\psi_-(x)|^2\right) \\ &= \psi_0(x) + i\epsilon\left(\frac{1}{2}\psi_0''(x) + \psi_0(x)|\psi_0(x)|^2\right) + \mathcal{O}(\epsilon^2).\end{aligned} \tag{6.46}$$

On the other hand, we required for a soliton Eq. (6.44), which becomes in linear order of ϵ

$$\begin{aligned}\psi_+(x) &= \mathrm{e}^{i\omega\epsilon}\psi_0(x - v_0\epsilon) + \mathcal{O}(\epsilon^2) \\ &= \psi_0(x) + i\epsilon\left(\omega\psi_0(x) + iv_0\psi_0'(x)\right) + \mathcal{O}(\epsilon^2),\end{aligned} \tag{6.47}$$

where v_0 corresponds to the velocity and ω is some energy related frequency yielding the kinetic phase. Comparing Eqs. (6.46) and (6.47), we find that $\psi_0(x)$ must fulfill

$$-\frac{1}{2}\psi_0'' + iv_0\psi_0' + (\omega - |\psi_0|^2)\psi_0 = 0. \tag{6.48}$$

Looking for solutions of the form

$$\psi(x) = f(x)\,\mathrm{e}^{iv_0\epsilon}, \tag{6.49}$$

with a real valued function $f(x)$, Eq. (6.48) demands f to satisfy

$$f'' - 2\left(\omega - \frac{v_0^2}{2} - f^2\right)f = 0. \tag{6.50}$$

With an ansatz motivated by the "static" soliton

$$f(x) = A\,\mathrm{sech}(\alpha x), \tag{6.51}$$

it can be shown that Eq. (6.50) is satisfied for all x if and only if

$$A = \alpha = \sqrt{2\omega - v_0^2}. \tag{6.52}$$

Using the normalization condition of Eq. (6.43), we find that

$$\alpha = \sqrt{2\omega - v_0^2} \tag{6.53}$$

and thus, the dispersion relation reads

$$\omega = \frac{v_0^2}{2} + \frac{1}{8}, \tag{6.54}$$

where the wave function parameters are

$$A = \frac{1}{2} = \alpha. \tag{6.55}$$

Thus finally, we arrive at the soliton solution of the wave function

$$\psi_{\mathrm{sol}}(x) = \frac{1}{2}\mathrm{sech}\left(\frac{x}{2}\right)\, \mathrm{e}^{iv_0 x}, \tag{6.56}$$

which satisfies the requirement for solitons of Eq. (6.44) with

$$q = v_0\epsilon \quad \text{and} \quad \phi = \left(\frac{v_0^2}{2} + \frac{1}{8}\right)\epsilon. \tag{6.57}$$

In the original physical parameters, i.e. not dimensionless, the soliton solution is

$$\psi_{\mathrm{sol}}(x) = \frac{1}{2}\sqrt{\frac{m\lambda}{\hbar t_0}}\mathrm{sech}\left(\frac{m\lambda}{2\hbar t_0}x\right)\, \exp\left(i\frac{m\lambda v_0}{\hbar t_0}x\right), \tag{6.58}$$

satisfying requirement of Eq. (6.44) with

$$q = v_0\lambda \quad \text{and} \quad \phi = \left(\frac{v_0^2}{2} + \frac{1}{8}\right)\frac{m\lambda^2}{\hbar t_0}. \tag{6.59}$$

The main result of this derivation is the sech-shape of the solitonic solution for weak kicks with a high frequency ($\epsilon \ll 1$) for a width of $1/2$. Note that again, the existence of the soliton is independent of the velocity in this limit, which only enters the dispersion relation in Eq. (6.54). In the next section, we will check by simulation how well these solitons survive even for finite $\epsilon \lesssim 1$ and different parameters.

6.4.2 Simulating pulsed solitons

In this section, we want to verify the analytically found solitonic solution Eq. (6.56) of the pulsed nonlinear Schrödinger equation of Eq. (6.42). Since we cannot start with pulsing at $t = -\infty$, the actual equation of motion is given by

$$i\frac{\partial\psi}{\partial t} = -\frac{1}{2}\frac{\partial t}{\partial x^2} - \epsilon\sum_{n=1}^{\infty} g(t - n\epsilon)|\psi|^2\psi, \tag{6.60}$$

with $g(t)$ being a short Gaussian as in Sec. 6.2 instead of a δ-function due to numerical reasons.

Note that there is a slight difference due to the start at finite times: Usually, after a kick, the state refocuses sometime before the next pulse and then spreads again. On the other hand, we start here at $t = 0$ with the solitonic state of Eq. (6.56), which will broaden immediately. However, it turns out that for small enough ϵ, i.e. fast enough pulses, such that there is not enough time to considerably spread between two pulses, this difference does not really matter.

In his Bachelor thesis [118], Florian Moser investigated carefully the parameter (kicking strength and time ϵ, velocity v_0, width $1/\alpha$,) dependence of the solitons numerically using TQT and found out that, in the right regime, the shape of the

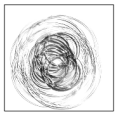

solitonic wave packet does not significantly change over 100,000 pulses. The used parameters in this case are $\epsilon = 0.1$, $v_0 = 4$ and $\alpha = 0.5$. Moreover, the exact shape, the sech, is not of major importance, but also Gaussian wave packets with the right width ($\sigma \simeq 2.3$), such that they are similar to the corresponding sech yield good results.

From a technical point of view, the most important feature that he has noticed is that numerical artifacts appear when the nonlinear pulse sets in. Depending on the velocity v_0 and the numerical time-step between two propagation steps δt, every nonlinear kick alters the velocity, resp. momentum, of the wave packet by some Δv approximately linear in theses parameters:

$$\frac{\Delta v}{v_0} \simeq -1.5 \times 10^{-4} \, \frac{\delta t}{0.01\epsilon}, \tag{6.61}$$

which means that for typical time steps of $\delta t = \epsilon/100$, i.e. hundred time-steps between two kicks, the relative change of the velocity of 0.015% is rather small. But since many pulses are applied ($> 10^3$) it adds up and leads eventually to a non-negligible effect. The reason that Δv depends on the time between two propagation steps highly suggests, that it is indeed a numerical artifact instead of a physical property of the finite time-width of the nonlinear kick, although the reason why it happens could not be identified and thus the problem has not been remedied.

The related shift in real space related to this artificial velocity can be easily nullified by calculating the effective fidelity as in Eq. (6.27), by using the displaced initial state

$$\tilde{\psi}_0(\mathbf{r}) = \psi_0(\mathbf{r} + \mathbf{r}_{\max}), \tag{6.62}$$

where $\mathbf{r}_{\max}$ is the numerically found position of the wave packet peak for any time, instead of the beforehand used $\tilde{\psi}_0(\mathbf{r}) = \psi_0(\mathbf{r}+v_0 t)$. On the other hand, the (artificial) shift in $\mathbf{k}$-space, which affects the fidelity as can be seen be evaluating the overlap in reciprocal space, cannot be circumvented as easily for a general wave packet. This difference becomes important at a later time than the real space shift, when the change of the velocity Δv is comparable to velocity width of the wave packet.

In Fig. 6.7, we show exemplarily the v_0-dependence of the soliton for fixed $\alpha = 0.5$ and $\epsilon = 0.4$, which is already not really in the limit of $\epsilon \ll 1$ anymore. In panel (a), the fidelity defined in Eq. (6.27) is plotted, as a function of time for several velocities v_0. The smooth decay for $v_0 \neq 0$ is due to the above mentioned numerical artifacts. The very rapidly oscillating changes in the cases $v_0 = 0$ at around $t = 3,000\epsilon$ and $v_0 = 2$ at around $t = 3,300\epsilon$ on the other hand cannot be explained by this numerical artifact and are very likely of physical nature, as can be seen also in panel (b).

There, the amplitude of the wave packet $\mathcal{A}(t)$ relative to the initial amplitude $\mathcal{A}(0)$ of the same simulations is shown. In the beginning, the amplitude does not change considerably in all cases, but at the same time when the fidelity wiggles for $v_0 = 0$ and $v_0 = 2$, also the amplitude changes considerably and even decreases for $v_0 = 2$. On the other hand, the amplitude is not affected at all for the higher velocities, thus the solitons seem to be more stable for higher velocities. We do not have an explanation for the velocity dependence of the solitons, which is not expected in the analytical derivation of Sec. 6.4.1. It is quite likely that higher order terms in ϵ, which are neglected in the approximation, will yield a velocity

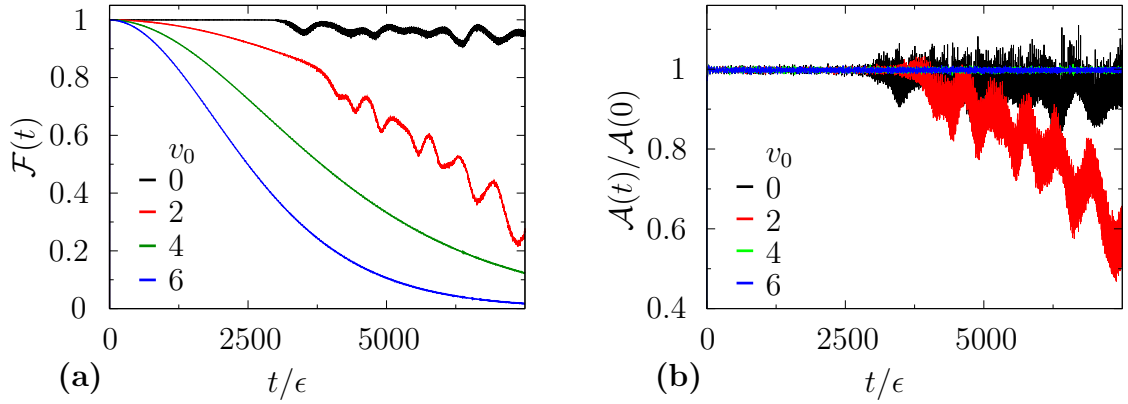

Figure 6.7: Solitons for the pulsed nonlinear Schrödinger equation, according to Florian Moser [118]. (a) The fidelity $\mathcal{F}$ is shown for different velocities v_0 as a function of time t/ϵ ($\hat{=}$ number of pulses) for the solitonic solution of Eq. (6.56) and $\epsilon = 0.4$. The smooth decay, which is stronger for higher v_0, is due to numerical artifacts coming from the nonlinear pulse (see text). Only in the parts with seemingly chaotic changes in the cases of $v_0 = 0$ (black) and $v_0 = 2$ (red) the solitonic approximation "breaks down", which happens because the solution only holds for $\epsilon \ll 1$ and small deviations accumulate over time. (b) The normalized amplitude of the same simulation as in (a) is shown, which is supposed not to change for a soliton, as in the cases $v_0 > 3$. For $v_0 = 0$ (black) and $v_0 = 2$ (red) the change of the amplitude starts at the same time as in the fidelity case, such that the soliton seems to not really hold anymore at these points in time.

dependence, but this has not been investigated in detail. Nonetheless, the solitonic wave packets, which keep their shape over a few thousand pulses, which is already quite interesting. For comparison, the relative amplitude of the wave packet without kicking decreases to 0.1 within the time of 60 pulses, i.e. $t = 60\epsilon$ in the simulations related to Fig. 6.7. For further parameter studies and more in depth investigations, we direct again the kind reader to the Bachelor thesis of Florian Moser [118].

6.5 Summary - BEC mirrors, lenses and solitons

To summarize, we have shown that using the nonlinear pulse by changing the interaction strength among the atoms of a BEC cloud, an echo of the wave function can be achieved. However, the echo is by no means as good as in the two-band systems, because in the best case, only half of the wave packet can come back to the initial position (compare Fig. 6.1), instead of up to 100% which is possible in the two-band system due to constructive interference. Moreover, the shape of the wave packet changes drastically due to the position dependent ($\sim |\psi|^2$) "acceleration" during the nonlinear pulse. Nevertheless, echoes can be achieved in wide parameter range.

Regarding applications, the quantum time lens, which inverts the broadening of the wave function, could be more important due to its higher fidelities. In future research, combinations of QTL pulses could be used to fit the individual purposes, like a first small pulse to "freeze" the wave packet width for a longer time and then

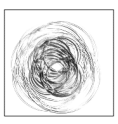

a second, stronger pulse, which "reactivates" the wave packet to first refocus and then broaden again. Moreover, one could further study the analogy to optical lenses in term of refocusing to the possible end to build combinations of lenses, which are well-known in optical systems like telescopes or microscopes.

In the last section, we showed that soliton-like solution to the kicked NLSE approximatively exist in the limit of small and high frequency pulsing. Deviations appear for stronger and not-so-frequent pulses, and the soliton quality also depends on the velocity, which is not anticipated by the linear approximation in the kicking strength. Thus, there is plenty of room for further research, also including the numerical artifacts appearing for the long-time simulations.

Finally, we want to emphasize, that since experimental possible parameters are already used in some of the simulations shown in this chapter, the suggested protocols are in reach to be verified experimentally.

Chapter 7

Zitterbewegung

7.1 From theoretical predictions of relativistic particles to experimental realizations in BEC and semiconductors

Zitterbewegung (ZB), i.e. the trembling motion of high relativistic particles described, by the Dirac equation has been found by Schrödinger already in 1930 [124, 125]. The reason for the jittery movement is the fact that velocity operator does not commute with the Hamiltonian and therefore, it is not constant of motion. Indeed, the superposition of particle- and antiparticle-like solutions of the Dirac equation leads to a harmonic oscillation, in case of electrons and positrons with a frequency of the $f = 2mc^2/h \sim 10^{20}\,\mathrm{Hz}$ and an amplitude given by the Compton wave length of $\lambda_C \sim 10^{-13}\,\mathrm{m}$, which is the reason why it has not been discovered experimentally yet [126].

On the other hand, the requirements of ZB are not unique to the relativistic Dirac equation, but can be in principle fulfilled in any two- or more band system, e.g. for solid state systems with spin-orbit coupling, as proposed for the first time by Schliemann et al. in III-V semi-conductor quantum wells [127,128], where the energy spectrum is formally similar to the Dirac Hamiltonian. Vividly, the harmonic ZB is induced in a solid state system by the periodic underlying lattice [129]. The ZB in Dirac cone systems has later been proposed for carbon nanotubes [130], graphene [107, 131] and topological insulators [132]. Also in the presence of a magnetic field, signatures of the ZB can be found in both graphene [106, 107] and III-V semiconductor quantum wells with spin-orbit coupling [133].

The first experimental realization of ZB in solid state systems has been reported in late 2016 [134]. There, the mutual motion of an ensemble of electrons in n-type InGaAs, initialized optically in the same spin state. An in-plane magnetic field of a few Tesla leads to a spin splitting of the order of a few hundred μeV and an electronically easily accessible frequency in the GHz range, measured as an change of the AC current. Vividly, the inplane magnetic fields leads to a precession of the optically generated spins. Since the velocity operator is spin-dependent, the direction of motion changes periodically, according to the spin. Note that in this setup, the motion of the ensemble of electrons is investigated as opposed to the jittery motion induced by the single particle interference of states which occupy

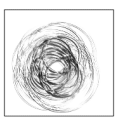

both bands (electron- and hole-like). Earlier, the first experimental realizations of ZB in general have been achieved with a single $^{40}Ca^{+}$-ion in a linear Paul trap [135] and by Bose-Einstein condensates [136, 137] with an induced spin-orbit coupling, using atom-light interactions [138].

The recent experimental realization of ZB (in a broader sense) in a solid state system [134] motivated us to investigate the trembling motion in a time-dependent setup to possibly prolongate its duration and circumvent its decay. ZB in a time-dependent driving field has not been considered extensively, yet. One of the two publications we are aware of investigated theoretically a time-dependent Rashba spin-orbit coupling in a two-dimensional electron gas [139] where the ZB indeed might be sustained indefinitely. The other one studied graphene in an external electromagnetic driving field, i.e. a time-dependent vector potential [140]. They found multimode ZB, i.e. ZB with additional emerging frequencies, which however still decay over time.

Our goal is to combine the two, i.e. to find non-decaying ZB modes in driven graphene, using a time-dependent mass gap. Moreover, we want to investigate the ZB with regard to the possibility of generating echoes, similar to the spin echo, using our QTM mechanism. But first, we give an extensive introduction about the well-known properties of ZB in static graphene. While this can be found in the literature (see e.g. the review article in Ref. [125]), we do not follow here a certain publication but show our own calculations with special focus on its decay, which is to be circumvented.

7.2 Frequency, amplitude and decay of the zitterbewegung in general two-band systems

The ZB can be described both in the Heisenberg picture, e.g. [134], and in the Schrödinger picture, e.g. [140], without significant advantages. In this thesis, we stick to the Schrödinger picture, simply because in the TQT simulations the time-dependent wave functions are calculated.

Since the ZB describes the jittery motion of particles, we are interested in the time-dependence of the expectation value of the position operator

$$\langle \hat{\mathbf{x}} \rangle(t) = \langle \psi(t) \mid \hat{\mathbf{x}} \mid \psi(t) \rangle \tag{7.1}$$

or equivalently its time-derivative: the expectation value of the velocity operator given by Ehrenfest's theorem

$$\langle \hat{\mathbf{v}} \rangle(t) := \frac{\mathrm{d}\langle \hat{\mathbf{x}} \rangle(t)}{\mathrm{d}t} = \frac{i}{\hbar} \langle \psi(t) \mid [\hat{H}, \hat{\mathbf{x}}] \mid \psi(t) \rangle. \tag{7.2}$$

Evaluating the commutator $[\hat{H}, \hat{\mathbf{x}}]$ in reciprocal space, we see that the velocity operator is given by

$$\hat{\mathbf{v}} := \frac{\mathrm{d}\hat{\mathbf{x}}}{\mathrm{d}t} = \frac{i}{\hbar}[H(\mathbf{k}), i\nabla_{\mathbf{k}}] = \frac{1}{\hbar}\nabla_{\mathbf{k}} H(\mathbf{k}) \tag{7.3}$$

In graphene close to the **K**-points, the velocity operator is $|\mathbf{k}|$-independent for instance,

$$\hat{\mathbf{v}} = v_F \boldsymbol{\sigma}. \tag{7.4}$$

In a two-band system with eigenstates $|\mathbf{k}, \pm\rangle$ and energies $\epsilon_\pm(\mathbf{k}) = \hbar\omega_{\mathbf{k},\pm}$, the time evolution of an initial $\mathbf{k}$-mode $|\psi_0^{\mathbf{k}}\rangle$ is given by

$$|\psi^{\mathbf{k}}(t)\rangle = c_{+,\mathbf{k}} \mathrm{e}^{-i\omega_{\mathbf{k},+}t} |\mathbf{k}, +\rangle + c_{-,\mathbf{k}} \mathrm{e}^{-i\omega_{\mathbf{k},-}t} |\mathbf{k}, -\rangle, \tag{7.5}$$

where $c_{+,\mathbf{k}} = \langle \mathbf{k}, + \mid \psi_0^{\mathbf{k}} \rangle$ and $c_{-,\mathbf{k}} = \langle \mathbf{k}, - \mid \psi_0^{\mathbf{k}} \rangle$ are the normalized amplitudes in the two bands, i.e

$$|c_{+,\mathbf{k}}|^2 + |c_{-,\mathbf{k}}|^2 = 1, \quad \forall \mathbf{k}. \tag{7.6}$$

We will use $\mathbf{k}$-mode and plane wave as synonyms and want to stress that they are meant to possibly live in both bands – the only requirement is that they have a single wave vector $\mathbf{k}$. We define the matrix elements of $\hat{\mathbf{v}}$ by

$$\mathbf{v}_{\mathbf{k}}^{ss'} := \langle \mathbf{k}, s \mid \hat{\mathbf{v}} \mid \mathbf{k}, s' \rangle, \tag{7.7}$$

where $s = \pm$ and $s' = \pm$. The time-dependent expectation value of the velocity operator of a plane wave in a two band setup thus yields

$$\langle \hat{\mathbf{v}}_{\mathbf{k}} \rangle(t) = |c_{+,\mathbf{k}}|^2 \, \mathbf{v}_{\mathbf{k}}^{++} + |c_{-,\mathbf{k}}|^2 \, \mathbf{v}_{\mathbf{k}}^{--} + 2\,\mathrm{Re}\{c_{+,\mathbf{k}} c_{-,\mathbf{k}}^* \, \mathrm{e}^{-i(\omega_{\mathbf{k},+} - \omega_{\mathbf{k},-})t} \, \mathbf{v}_{\mathbf{k}}^{-+}\} \tag{7.8}$$

$$=: \langle \hat{\mathbf{v}}_{\mathbf{k}}^{\mathrm{const}} \rangle + \langle \hat{\mathbf{v}}_{\mathbf{k}}^{\mathrm{ZB}} \rangle(t) \tag{7.9}$$

From Eq. (7.8), we see that only the last term is time-dependent and contributes to the ZB, whereas the first two terms describe a constant motion (of the two sub-wave packets, i.e. the wave packets in the two bands).

There are two requirements for ZB in a time-independent setup: a) the initial wave function must consist of both bands ($c_{+,\mathbf{k}} \neq 0$ and $c_{-,\mathbf{k}} \neq 0$) and b) the velocity operator must not commute with the Hamiltonian since otherwise $|\mathbf{k}, \pm\rangle$ is also an eigenstate of $\hat{\mathbf{v}}$ and the matrix element $\mathbf{v}_{\mathbf{k}}^{-+}$ vanishes because the eigenstates of the Hamiltonian are orthogonal.

Equation (7.8) can be rewritten as

$$\langle \hat{v}_{i,\mathbf{k}} \rangle(t) = \langle v_{i,\mathbf{k}}^{\mathrm{const}} \rangle + A_{i,\mathbf{k}} \cos(\Omega_{\mathbf{k}}^{\mathrm{ZB}} t + \varphi_{i,\mathbf{k}}), \tag{7.10}$$

where $i \in \{x, y\}$ and the parameters of the ZB are:

$$\text{frequency:} \quad \Omega_{\mathbf{k}}^{\mathrm{ZB}} = \omega_{\mathbf{k},+} - \omega_{\mathbf{k},-}, \tag{7.11}$$

$$\text{amplitude:} \quad A_{i,\mathbf{k}} = 2|c_{+,\mathbf{k}}| \, |c_{-,\mathbf{k}}| \, |v_{i,\mathbf{k}}^{-+}|, \tag{7.12}$$

$$\text{phase:} \quad \varphi_{i,\mathbf{k}} = -\left(\arg(c_{+,\mathbf{k}} c_{-,\mathbf{k}}^*) + \arg(v_{i,\mathbf{k}}^{-+})\right). \tag{7.13}$$

From Eq. (7.11), we can see that the frequency of the ZB is given by the difference of the two band energies, which is $\mathbf{k}$-dependent, but independent of i, which denotes the direction of the ZB. The $\mathbf{k}$-dependency will lead to dephasing and thus decay of the ZB for a wave packet, as we will explain below. Considering the amplitude, we see what we have discussed above: it is only finite, if the wave packet is a mixture of both bands and if the Hamiltonian does not commute with the velocity operator.

The phase is rather unimportant, but might diminish the amplitude of the ZB for a wave packet as it will be discussed later.

So far, the ZB does not decay, but oscillates with an amplitude and frequency given by the initial plane wave and the band structure. For a wave packet however, the ZB has a transient character [141], i.e. it vanishes. This is due to the fact that for a given initial wave packet of the general form

$$|\psi_0\rangle = \int \mathrm{d}^2k\, \psi_0(\mathbf{k})\, |\psi_0^{\mathbf{k}}\rangle, \tag{7.14}$$

where $|\psi_0^{\mathbf{k}}\rangle$ is a plane wave (living in both bands) as above, the time evolution yields

$$|\psi^{\mathbf{k}}(t)\rangle = \int \mathrm{d}^2k\, \psi_0(\mathbf{k}) \left(c_{+,\mathbf{k}} \mathrm{e}^{-i\omega_{\mathbf{k},+}t} |\mathbf{k},+\rangle + c_{-,\mathbf{k}} \mathrm{e}^{-i\omega_{\mathbf{k},-}t} |\mathbf{k},-\rangle\right) \tag{7.15}$$

(compare Eq. (7.3)). Therefore, the expectation value of the velocity related to ZB of a wave packet becomes

$$\langle \hat{\mathbf{v}}^{\mathrm{ZB}} \rangle(t) = 2 \int \mathrm{d}^2k\, \mathrm{d}^2k'\, \psi_0^*(\mathbf{k}')\psi_0(\mathbf{k})\, \mathrm{Re}\{c_{+,\mathbf{k}} c^*_{-,\mathbf{k}'}\, \mathbf{v}_{\mathbf{k}}^{-+}\, \mathrm{e}^{-i(\omega_{\mathbf{k},+} - \omega_{\mathbf{k}',-})t}\}. \tag{7.16}$$

Since for space-independent velocity operators, plane waves are eigenstates, i.e.

$$\langle \mathbf{k}', - \mid \hat{\mathbf{v}} \mid \mathbf{k}, + \rangle = \delta_{\mathbf{k},\mathbf{k}'} \langle \mathbf{k}, - \mid \hat{\mathbf{v}} \mid \mathbf{k}, + \rangle \tag{7.17}$$

the ZB of Eq. (7.16) reduces to

$$\langle \hat{\mathbf{v}}^{\mathrm{ZB}} \rangle(t) = \int \mathrm{d}^2k\, |\psi_0(\mathbf{k})|^2\, \langle \hat{\mathbf{v}}_{\mathbf{k}}^{\mathrm{ZB}} \rangle(t) \tag{7.18}$$

with the same parameters as in Eqs. (7.11)-(7.13). The $\mathbf{k}$-dependent phase given in Eq. (7.13) diminishes in general the ZB right from the start and can change the decay behavior for short times. However, we will see that for the usually chosen wave packets in a (gapped) graphene setup, the phase is almost constant over the width of the used wave packets. Moreover, it does not influence the long-term decay behavior since it is t-independent, which is the main point of this section. Therefore the phase does not play an important role for the ZB which will be considered in the next sections.

In Eq. (7.18), the vk-dependence of is $\Omega_{\mathbf{k}}^{\mathrm{ZB}}$ is of major qualitative importance, because it leads to the transient character of the ZB. From a physical point of view, due to the different frequencies of the many $\mathbf{k}$-modes in the wave packet, the ZB dephases over time and vanishes. From a mathematical point of view, this decay is described by the fact that for larger and larger t, the cosine in Eq. (7.18) oscillates stronger and stronger as function of $\mathbf{k}$. Thus, the individual terms of the integral over $\mathbf{k}$ cancel, as illustrated in Fig. 7.1. This will happen when the amplitude $|\psi_0(\mathbf{k})|^2\, A_{i,\mathbf{k}}$ is almost constant over one oscillation period of the cosine as function of $\mathbf{k}$, or more quantitatively, when the change of the argument in the cosine as function of $\mathbf{k}$ is much larger than the change of the prefactor:

$$\left|\nabla_{\mathbf{k}} \Omega_{\mathbf{k}}^{\mathrm{ZB}}\right| \frac{t}{2\pi} \gg \frac{\left|\nabla_{\mathbf{k}} \left(|\psi_0(\mathbf{k})|^2\, A_{i,\mathbf{k}}\right)\right|}{\max\limits_{\mathbf{k}} |A_{i,\mathbf{k}} |\psi_0(\mathbf{k})|^2|}, \quad \forall\, \mathbf{k} \tag{7.19}$$

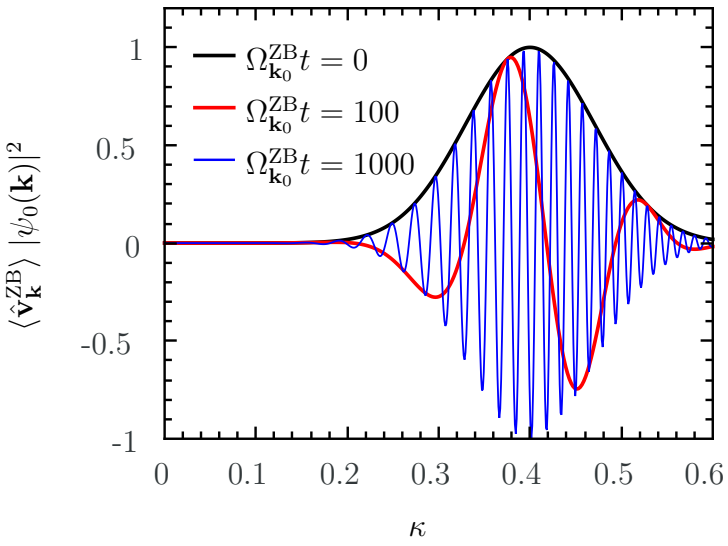

Figure 7.1: Visualization of the reason why the ZB decays. The integrand $|\psi_0(\mathbf{k})|^2 \langle \hat{\mathbf{v}}^{\mathrm{ZB}}_{\mathbf{k}} \rangle$ of the ZB of Eq. (7.18) is shown as function of $\mathbf{k}$ for different times t in arbitrary units. For simplicity, a Gaussian wave packet with equal weight in both bands is assumed ($c_{+,\mathbf{k}} = c_{-,\mathbf{k}} = 1/\sqrt{2}$) in a gapped graphene band structure (see Subsec. 7.3.2), although the exact setup does not really matter. The important statement is that while at $\Omega_{\mathbf{k}_0} t = 0$ the integral of the shown function is nonzero since the integrand is positive, it decreases over time due to the faster and faster oscillations as function of $\mathbf{k}$, which lead to cancellation of positive and negative values of the integrand. The values of the integral of the shown integrands are 0.18 (black), 8.6×10^{-3} (red) and 3.9×10^{-10} (blue).

which will be the case after long enough time, if $\Omega^{\mathrm{ZB}}_{\mathbf{k}}$ is not constant in $\mathbf{k}$. Notice that the exact structure of Eq. (7.19) is quite arbitrary, e.g. the denominator on the right hand side ($\max_{\mathbf{k}} |A_{i,\mathbf{k}} |\psi_0(\mathbf{k})|^2|$). But with this choice, we make sure that only those parts of the wave function play a role, which have a considerably large probability density $|\psi_0(\mathbf{k})|^2$.

For a constant amplitude $A_{i,\mathbf{k}} = A$, and a Gaussian wave packet of Eq. (3.39), the estimate Eq. (7.19) reduces to the more intuitive form

$$\frac{\partial \Omega^{\mathrm{ZB}}_{\mathbf{k}}}{\partial k} \Delta k \, t \overset{!}{\gg} 2\pi \frac{|(\mathbf{k} - \mathbf{k}_0)|}{\Delta k} \, \mathrm{e}^{-\frac{(\mathbf{k}-\mathbf{k}_0)^2}{\Delta k^2}} \lesssim 2\pi, \tag{7.20}$$

which states that the phase difference over the width of the wave packet Δk needs to be much larger than 2π.

Rusin and Zawadzki give an alternative explanation for the decay of the ZB by considering the movement of the two sub-wave packets in the different bands [142]. In the time-independent setup, each state stays in its band with the velocity $\mathbf{v}_{\pm} = \nabla_{\mathbf{k}} \epsilon_{\pm}(\mathbf{k})$. Thus, the two sub-packets move away from each other for different velocities in the two bands (see also Fig. 3.6 in Sec. 3.4). The overlap of the two

sub-packets is given by

$$\langle\psi_+(t)|\psi_-(t)\rangle = \int \mathrm{d}^2k\,|\psi_0(\mathbf{k}^2)|^2\left(|c_{+,\mathbf{k}}|^2+|c_{-,\mathbf{k}}|^2+2\,\mathrm{Re}\{c_{+,\mathbf{k}}c^*_{-,\mathbf{k}'}\,\mathrm{e}^{-i(\omega_{\mathbf{k},+}-\omega_{\mathbf{k}',-})t}\}\right) \tag{7.21}$$

and therefore, the time-dependent part differs from the ZB in Eq. (7.18) only by the missing velocity matrix element $\mathbf{v}^{-+}_{\mathbf{k}}$. In graphene, the magnitude of this matrix element is $\mathbf{k}$-independent, and therefore, the decay times of the ZB and the overlap of the wave packets are the same [142].

To be able to estimate the decay time in advance, we want to derive an as easy as possible formula which has more predictive power than the rather qualitative expression of Eq. (7.19). For that purpose, let us consider a Gaussian wave packet of the form

$$\psi_0(\mathbf{k}) = \frac{1}{\sqrt{\pi}\Delta k}\exp\left(-\frac{(\mathbf{k}-\mathbf{k}_0)^2}{2\Delta k^2}\right). \tag{7.22}$$

The integral in Eq. (7.18) can in principle be solved for a Gaussian wave packet and a Taylor expansion of $\langle\hat{\mathbf{v}}^{\mathrm{ZB}}_{\mathbf{k}}\rangle$ around $\mathbf{k}_0$ up to arbitrary order, using

$$\int_{-\infty}^{\infty}\mathrm{d}x\,x^{2n+1}\exp\left(-\alpha x^2\right) = 0, \tag{7.23}$$

$$\begin{aligned}\int_{-\infty}^{\infty}\mathrm{d}x\quad x^{2n}\exp\left(-\alpha x^2\right) &= (-1)^n\left(\frac{\partial}{\partial\alpha}\right)^n\int_{-\infty}^{\infty}\mathrm{d}x\,x^{2n}\exp\left(-\alpha x^2\right)\\ &= (-1)^n\frac{\partial^n}{\partial\alpha^n}\frac{\sqrt{\pi}}{\sqrt{\alpha}} = \frac{\sqrt{\pi}}{\sqrt{\alpha}^{2n+1}}\frac{\prod_{l=1}^{n}(2l-1)}{2^n}\\ &= \frac{1}{2\sqrt{\alpha}^{2n+1}}\,\Gamma\left(n+\frac{1}{2}\right).\end{aligned} \tag{7.24}$$

The general result for Eq. (7.18) is

$$\begin{aligned}\langle\hat{\mathbf{v}}^{\mathrm{ZB}}\rangle(t) = \sum_{n_x,n_y=0}^{\infty}&\frac{1}{(2n_x)!(2n_y)!}\left(\frac{\partial^{2n_x}}{\partial k_x^{2n_x}}\frac{\partial^{2n_y}}{\partial k_y^{2n_y}}\langle\hat{\mathbf{v}}^{\mathrm{ZB}}_{\mathbf{k}}\rangle(t)\right)\Big|_{\mathbf{k}=\mathbf{k}_0}\\ &\times\frac{\Delta k^{(2n_x+2n_y)}}{4\pi}\,\Gamma\left(n_x+\frac{1}{2}\right)\,\Gamma\left(n_y+\frac{1}{2}\right),\end{aligned} \tag{7.25}$$

which is still not very helpful for a quick estimation due to the infinite sum. For the approximation of the decay time, we use only the first non-vanishing correction terms, which is best suited for rather small wave packets in $\mathbf{k}$-space.

$$\langle\hat{\mathbf{v}}^{\mathrm{ZB}}\rangle(t) \approx \langle\hat{\mathbf{v}}^{\mathrm{ZB}}_{\mathbf{k}_0}\rangle(t) + \frac{1}{2}\,\frac{\Delta k^2}{2}\left(\frac{\partial^2}{\partial k_x^2}+\frac{\partial^2}{\partial k_y^2}\right)\langle\hat{\mathbf{v}}^{\mathrm{ZB}}_{\mathbf{k}}\rangle(t)\Big|_{\mathbf{k}=\mathbf{k}_0}. \tag{7.26}$$

The second derivative of $\langle\hat{\mathbf{v}}^{\mathrm{ZB}}_{\mathbf{k}}\rangle$ splits into terms of differing importance.

$$\frac{\partial^2}{\partial k_i^2}\langle \hat{v}^{\mathrm{ZB}}_{j,\mathbf{k}}\rangle = \frac{\partial^2 A_{j,\mathbf{k}}}{\partial k_i^2}\cos(\Omega^{\mathrm{ZB}}_{\mathbf{k}}t+\varphi_{j,\mathbf{k}}) - A_{j,\mathbf{k}}\cos(\Omega^{\mathrm{ZB}}_{\mathbf{k}}t+\varphi_{j,\mathbf{k}})\left(\frac{\partial\Omega^{\mathrm{ZB}}_{\mathbf{k}}}{\partial k_i}t+\frac{\partial\varphi_{j,\mathbf{k}}}{\partial k_i}\right)^2 + 2\frac{\partial A_{j,\mathbf{k}}}{\partial k_i}(-1)\sin(\Omega^{\mathrm{ZB}}_{\mathbf{k}}t+\varphi_{j,\mathbf{k}})\left(\frac{\partial\Omega^{\mathrm{ZB}}_{\mathbf{k}}}{\partial k_i}t+\frac{\partial\varphi_{j,\mathbf{k}}}{\partial k_i}\right). \tag{7.27}$$

The first term of Eq. (7.27) is in-phase to the initial ZB, but since it has no extra time-dependence, it just contributes slightly ($\mathcal{O}(\Delta k^2)$) to the initial amplitude but does not lead to a decay. The second term describes an out-of-phase change of the velocity of the ZB, which will alter the ZB but not directly lead to a decay.

The last term of Eq. (7.27) however is in phase with the initial oscillation but with opposite sign. Therefore, it is the most important contribution for the decay. Furthermore, for long enough times, the term quadratic in time will very likely be the more import one compared to $\partial\varphi_{j,\mathbf{k}}/\partial k$, due to the qualitative requirement of Eq. (7.20). For the sake of an easy first approximation formula and the reasons given above, we will only consider the in-phase term with quadratic decrease in time.

$$\frac{\partial^2}{\partial k_i^2}\langle \hat{v}^{\mathrm{ZB}}_{j,\mathbf{k}}\rangle \simeq -A_{j,\mathbf{k}}\cos(\Omega^{\mathrm{ZB}}_{\mathbf{k}}t+\varphi_{j,\mathbf{k}})\left(\frac{\partial\Omega^{\mathrm{ZB}}_{\mathbf{k}}}{\partial k_i}\right)^2 t^2 = -\langle \hat{v}^{\mathrm{ZB}}_{j,\mathbf{k}}\rangle\left(\frac{\partial\Omega^{\mathrm{ZB}}_{\mathbf{k}}}{\partial k_i}\right)^2 t^2 \tag{7.28}$$

Below, when the gapped graphene case is studied in Subsec. 7.3.2, we show in Fig. 7.3(a) at an example the importance of the different terms in Eq. (7.27), where indeed the only term which we keep here is the most important one. With Eq. (7.28), the ZB becomes:

$$\langle \hat{\mathbf{v}}^{\mathrm{ZB}}\rangle(t) \approx \langle \hat{\mathbf{v}}^{\mathrm{ZB}}_{\mathbf{k}_0}\rangle(t)\left(1-\frac{t^2}{2}\frac{\Delta k^2}{2}\sum_{i\in\{x,y\}}\left(\frac{\partial\Omega^{\mathrm{ZB}}_{\mathbf{k}}}{\partial k_i}\right)^2\Big|_{\mathbf{k}=\mathbf{k}_0}\right). \tag{7.29}$$

If the energy of the bands - and thus $\Omega^{\mathrm{ZB}}_{\mathbf{k}}$ - depends only on the magnitude of $\mathbf{k}$ and not its direction, the derivatives can be further simplified to

$$\sum_{i\in\{x,y\}}\left(\frac{\partial\Omega^{\mathrm{ZB}}_{\mathbf{k}}}{\partial k_i}\right)^2 = \sum_{i\in\{x,y\}}\left(\frac{\partial\Omega^{\mathrm{ZB}}_{\mathbf{k}}}{\partial k}\frac{\partial k}{\partial k_i}\right)^2 = \left(\frac{\partial\Omega^{\mathrm{ZB}}_{\mathbf{k}}}{\partial k}\right)^2\sum_{i\in\{x,y\}}\frac{k_i^2}{k^2} = \left(\frac{\partial\Omega^{\mathrm{ZB}}_{\mathbf{k}}}{\partial k}\right)^2 \tag{7.30}$$

and the ZB finally yields

$$\langle \hat{\mathbf{v}}^{\mathrm{ZB}}\rangle(t) \approx \langle \hat{\mathbf{v}}^{\mathrm{ZB}}_{\mathbf{k}_0}\rangle(t)\left(1-\frac{t^2}{2}\frac{\Delta k^2}{2}\left(\frac{\partial\Omega^{\mathrm{ZB}}_{\mathbf{k}}}{\partial k}\right)^2\right). \tag{7.31}$$

As an estimation for the decay time of the ZB, which we denote by T_2^* in analogy to the spin-spin dephasing time in a Hahn echo setup, we use the time when Eq. (7.31) vanishes:

$$T_2^* = \frac{2}{\Delta k\left|\frac{\partial\Omega^{\mathrm{ZB}}_{\mathbf{k}}}{\partial k}\right|} \tag{7.32}$$

So we see that the assumption for the decay in Eq. (7.20), where we demand that the time is "much larger than" is too restrict and can be reduced to "similar".

For $t > T_2^*$, our 2nd order approximation predicts rising amplitudes again. However, this is clearly just an artifact of the approximation and is cured by considering

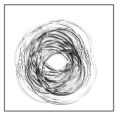

higher orders in the perturbation, which get more and more important for longer times.

Note that as already mentioned, the derivation of the decay time T_2^* is by no means meant to be very exact with all the assumptions which enter, but was designed to give an easy as possible formula to estimate the magnitude of the decay time. In the end, we arrive at a result which could have been guessed already in the beginning (up to factors of π), but is now reinforced. To anticipate the results from the simulations: We found that at the time T_2^*, the amplitude of the ZB decreases to about 30% to 40% of the initial value for the used wave packets, depending on the system.

In this section, we have seen, that the ZB of wave packets decays over time. For experiments, the decay might be an obstacle for the observation of ZB, or put in another way, the longer the ZB survives, the easier it should be to observe it. One known way is to decrease the width of the wave packet in reciprocal space, which only prolongates the lifetime but does not prevent the decay. Instead, in this thesis, we want to focus on time-dependent potentials in the Hamiltonian, that will keep the particle trembling for a long time (optimally forever) in analogy to the driven, damped classical harmonic oscillator, which will keep oscillating perpetually.

But first, in Sec. 7.3, we will start with the time-independent ZB in pristine and gapped graphene, which is already well-known, to get used to the systems. Then, we will consider a time-dependent mass term in Sec. 7.4 for these systems by using first order time-dependent perturbation theory, rotating wave approximation (RWA) and high-driving frequency approximation (HDF), where we follow the strategy of Rusin and Zawadzki [140] who considered time-dependent vector potential instead of a mass term. Moreover, they focus more on the emergent multimode ZB, whereas we are primarily interested in the long time survival of modes of the ZB to possibly facilitate the experimental observation. We will show numerical calculations verifying the analytical results in the given limits and uncovering interesting effects where we do not have analytical access.

In the last section of this chapter, we will consider a revival of ZB similar to the quantum time mirror in Chap. 3, where we will show that the ZB could be used to verify the QTM mechanism.

7.3 Time-independent zitterbewegung in graphene

7.3.1 Pristine graphene

As discussed previously, the low-energy Hamiltonian for graphene around the K-point is given by

$$H = \hbar v_F \, \mathbf{k} \cdot \boldsymbol{\sigma} = \hbar v_F \begin{pmatrix} 0 & k_x - i k_y \\ k_x + i k_y & 0 \end{pmatrix} \tag{7.33}$$

and thus, the velocity operator yields

$$\mathbf{v} = \frac{1}{\hbar} \nabla_{\mathbf{k}} H(\mathbf{k}) = v_F \boldsymbol{\sigma} = v_F \begin{pmatrix} \sigma_x \\ \sigma_y \end{pmatrix}. \tag{7.34}$$

The eigenstates are

$$|\varphi_{\mathbf{k},\pm}\rangle = \frac{1}{\sqrt{2}} \begin{pmatrix} 1 \\ \pm \mathrm{e}^{i\gamma_{\mathbf{k}}} \end{pmatrix} |\mathbf{k}\rangle \tag{7.35}$$

where $\gamma_{\mathbf{k}}$ is the polar angle in $\mathbf{k}$-space as in the rest of the thesis and the eigenenergies are

$$E_{\pm}(\mathbf{k}) = \pm \hbar v_F k =: \pm E(\mathbf{k}). \tag{7.36}$$

From Eq. (7.11), we know that the frequency of the ZB is

$$\Omega_{\mathbf{k}}^{\mathrm{ZB}} = 2 v_F k. \tag{7.37}$$

One requirement for ZB is that the velocity operator does not commute with the Hamiltonian. Calculating the commutator

$$[\hat{\mathbf{v}}, H] = \hbar v_F^2 \left[\begin{pmatrix} \sigma_x \\ \sigma_y \end{pmatrix}, k_x \sigma_x + k_y \sigma_y \right] = \hbar v_F^2 \begin{pmatrix} k_y \\ -k_x \end{pmatrix} 2i\sigma_z, \tag{7.38}$$

we see that the ZB in x-direction is only governed by the k_y part of the plane wave and in the y-direction by the $(-)k_x$ part. Thus, the ZB is perpendicular to the propagation direction of the plane wave, which is why we will refer to this type of ZB by "perpendicular ZB".

To get the amplitude of the ZB, we need to calculate the matrix element $\mathbf{v}_{\mathbf{k}}^{-+}$ with the eigenstates of Eq. (7.35), compare App. B.

$$\mathbf{v}_{\mathbf{k}}^{-+} = \langle \varphi_{\mathbf{k},-} \mid \hat{\mathbf{v}} \mid \varphi_{\mathbf{k},+} \rangle = v_F \begin{pmatrix} i \sin\gamma_{\mathbf{k}} \\ -i \cos\gamma_{\mathbf{k}} \end{pmatrix} = i \frac{v_F}{k} \begin{pmatrix} -k_y \\ k_x \end{pmatrix} \tag{7.39}$$

Thus, the ZB related part of the velocity is

$$\langle \hat{\mathbf{v}}_{\mathbf{k}}^{\mathrm{ZB}} \rangle(t) = -2 v_F \begin{pmatrix} \sin\gamma_{\mathbf{k}} \\ -\cos\gamma_{\mathbf{k}} \end{pmatrix} \mathrm{Im} \left\{ c_{+,\mathbf{k}} c_{-,\mathbf{k}}^{*} \mathrm{e}^{-i\Omega_{\mathbf{k}}^{\mathrm{ZB}} t} \right\}. \tag{7.40}$$

Without loss of generality, let us assume a plane wave with momentum $\mathbf{k} = (k_0, 0)^T$, i.e. $\gamma_{\mathbf{k}} = 0$. Furthermore, to maximize the amplitude of the ZB, let us consider a symmetric occupation of the two bands, e.g. for simplicity $c_{+,\mathbf{k}} = c_{-,\mathbf{k}} = 1/\sqrt{2}$, such that the initial state is

$$|\psi_0^{\mathbf{k}}\rangle = \begin{pmatrix} 1 \\ 0 \end{pmatrix} |\mathbf{k}\rangle. \tag{7.41}$$

In this case, the velocity related to ZB becomes

$$\langle \hat{\mathbf{v}}_{\mathbf{k}}^{\mathrm{ZB}} \rangle(t) = -v_F \begin{pmatrix} 0 \\ 1 \end{pmatrix} \sin(\Omega_{\mathbf{k}}^{\mathrm{ZB}} t), \tag{7.42}$$

which is, as expected, perpendicular to the propagation direction of the plane wave.

For a wave packet, the ZB decays over time due to the different frequencies of different $\mathbf{k}$-modes, as explained in Subsec. 7.2. From a numerical point of view, it is easy to calculate the time evolution - and the damping - of the ZB by evaluating the integral in Eq. (7.18) explicitly for a given initial wave packet. On the other hand, we can use TQT to calculate explicitly the time evolution of the wave packet and use it to get the expectation value of the velocity to see the ZB. These two

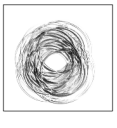

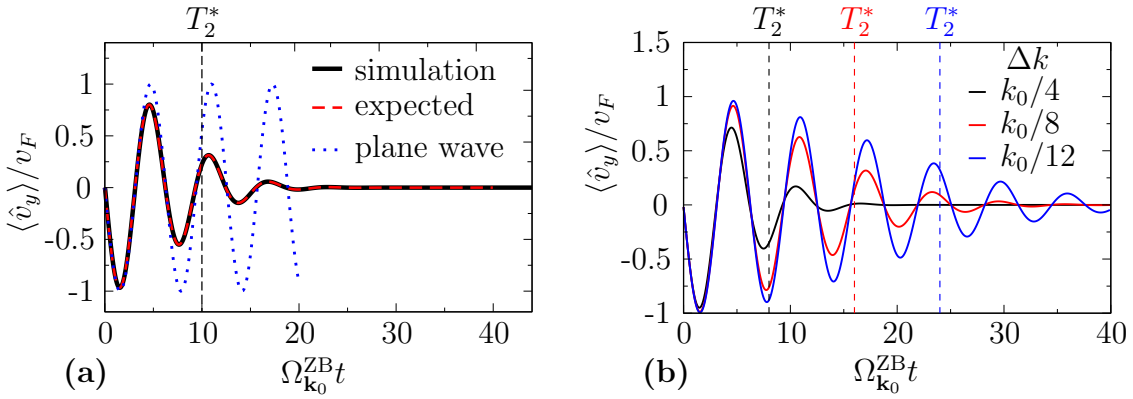

Figure 7.2: The ZB in graphene measured by the expectation value of the velocity operator perpendicular to the propagation direction as a function of time with $\Omega_{\mathbf{k}_0}^{\mathrm{ZB}} = 2v_F k_0$. (a) The result of the explicitly simulated time-evolution with TQT (black solid) is shown as well as the expected value obtained by numerically evaluating the integral in Eq. (7.18) (red dashed) for the same Gaussian wave packet with width $\Delta k = k_0/5$ and the pure analytical result of a plane wave (blue dotted) which is not damped. The results match very well showing that in our clean setup, the ZB is solely damped due to its width in $\mathbf{k}$-space, i.e. different ZB frequencies. The vertical dashed line indicates the estimated decay time T_2^* from Eq. (7.43). (b) The simulations for three different wave packets of varying width are shown (solid lines). The dashed lines indicate the estimated decay times from Eq. (7.43) in the color according to the simulation. In general, wider wave packets in $\mathbf{k}$-space decay faster because the range of the ZB frequencies is higher leading to a faster dephasing.

approaches are compared in Fig. 7.2(a). There, we can see the ZB of a wave packet obtained by both, simulation with TQT and calculated directly with Eq. (7.18). Both calculations coincide very well.

The initial wave packet is a Gaussian wave packet as in Eq. (7.22). Since the absolute values of the parameters of the system are physically not important but only their relation (which can be seen by rescaling the Schrödinger equation), we are free to choose one parameter arbitrarily and state all other parameters in its relation. Here we choose an arbitrary mean energy of the wave packet $E_0 = \hbar v_F k_0$ or equivalently k_0. The wave packet is set to propagate (mainly) in x-direction, i.e. $\mathbf{k}_0 = (k_0, 0)^T$, which does not lead to a loss of generality due to the radial symmetry of our system. The width of the chosen wave packet is rather small $\Delta k = 0.2 k_0$, but still the ZB survives only a few cycles.

The blue dotted line in Fig. 7.2(a), is the expected perpendicular ZB of a plane wave with $\mathbf{k}_0$ according to Eq. (7.42). We can see that the perpendicular ZB obtained by simulating the propagation of the wavepacket with TQT (solid black) has the same frequency but decays as expected over time Moreover, the semi-analytical result by evaluating the integral in Eq. (7.18) numerically for the given initial wave packet (dashed line), yields the same results as the pure simulation, verifying that the decay mechanism in this clean setup solely originates from the width of $\psi_0(\mathbf{k})$ in $\mathbf{k}$-space. Although not shown, there is no parallel ZB, i.e. no oscillations of $\langle v_x \rangle$.

The estimated decay time T_2^* from Eq. (7.32) yields in this gapless graphene setup

$$T_2^* = \frac{1}{\Delta k v_F} \tag{7.43}$$

which means for the chosen wave packet

$$\Omega_{\mathbf{k}_0}^{\mathrm{ZB}} T_2^* = 2 v_F k_0 T_2^* = \frac{2}{\Delta k / k_0} = 10 \tag{7.44}$$

as labeled in Fig. 7.2(a). Indeed the ZB has decreased in this example significantly at the time T_2^* to an amplitude of approximately 1/3 of the initial amplitude.

The approximation for the decay time in Eq. (7.43) states that the decay time is linear in $\frac{1}{\Delta k} = \Delta x$ with Δx being the real space width of the wave packet. In Fig. 7.2(b) the perpendicular ZB is shown for wave packets of different widths $\Delta k = k_0/4, k_0/8$ and $k_0/12$. At the estimated decay times (dashed lines) from Eq. (7.43), the amplitudes have dropped to values of roughly $33\% - 38\%$, showing that the rough estimation of Eq. (7.32) works quite well in pristine graphene as a timescale for the decay.

7.3.2 Gapped graphene - parallel and modified perpendicular zitterbewegung

In this subsection, we consider the ZB in gapped graphene with a hyperbolic band structure as discussed also at other instances in this thesis. The Hamiltonian reads

$$H = \hbar v_F \, \mathbf{k} \cdot \boldsymbol{\sigma} + M_0 \sigma_z = \hbar v_F \begin{pmatrix} \frac{M_0}{\hbar v_F} & k_x - i k_y \\ k_x + i k_y & -\frac{M_0}{\hbar v_F} \end{pmatrix}, \tag{7.45}$$

with eigenenergies

$$\varepsilon_\pm(\mathbf{k}) = \pm \sqrt{M_0^2 + \hbar^2 v_F^2 k^2} = \pm M_0 \sqrt{1 + \kappa^2} =: \pm \varepsilon(\mathbf{k}), \tag{7.46}$$

where $\kappa = \hbar v_F k_0 / M_0$, and with eigenstates

$$|\chi_{\mathbf{k},\pm}\rangle = \frac{1}{\sqrt{2}\sqrt{1 + \kappa^2 \pm \sqrt{1+\kappa^2}}} \begin{pmatrix} 1 \pm \sqrt{1+\kappa^2} \\ \kappa \, \mathrm{e}^{i\gamma_{\mathbf{k}}} \end{pmatrix} |\mathbf{k}\rangle. \tag{7.47}$$

The frequency of the ZB is given by the difference of positive and negative energies and thus yields

$$\Omega_{\mathbf{k}}^{\mathrm{ZB}} = \varepsilon_+(\mathbf{k}) - \varepsilon_-(\mathbf{k}) = 2 M_0 \sqrt{1 + \kappa^2} \tag{7.48}$$

Due to the $\mathbf{k}$-independence of the mass term, the velocity operator is the same as in the pristine graphene

$$\hat{v} = \frac{1}{\hbar} \nabla_{\mathbf{k}} H(\mathbf{k}) = v_F \boldsymbol{\sigma} = v_F \begin{pmatrix} \sigma_x \\ \sigma_y \end{pmatrix}, \tag{7.49}$$

but its commutator with the Hamiltonian changes:

$$[\hat{\mathbf{v}}, H] = \hbar v_F^2 \left[\begin{pmatrix} \sigma_x \\ \sigma_y \end{pmatrix}, k_x \sigma_x + k_y \sigma_y \right] + M_0 v_F \left[\begin{pmatrix} \sigma_x \\ \sigma_y \end{pmatrix}, \sigma_z \right]$$

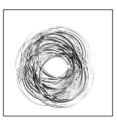

$$= \hbar v_F^2 \begin{pmatrix} k_y \\ -k_x \end{pmatrix} 2i\sigma_z + M_0 v_F 2i \begin{pmatrix} -\sigma_y \\ \sigma_x \end{pmatrix}. \tag{7.50}$$

Thus, there is an additional term, which allows also for parallel ZB.

Since we already covered the perpendicular ZB in pristine graphene in Subsec. 7.3.1, we will focus first on the parallel ZB and come back to perpendicular ZB at the end of this section. Since for the parallel ZB, the direction perpendicular to the propagation is not important, we will consider here a one-dimensional system in the x-direction, for simplicity.

For the amplitude of the ZB, we need the matrix element v_k^{-+} of the velocity operator

$$v_k^{-+} = \langle \chi_k^- \mid \hat{v} \mid \chi_k^+ \rangle = v_F \langle \chi_k^- \mid \sigma_x \mid \chi_k^+ \rangle. \tag{7.51}$$

The velocity matrix element is calculated in App. B as

$$v_k^{s,-s} = \frac{v_F}{\sqrt{1+\kappa^2}}. \tag{7.52}$$

Inserting $v_k^{s,-s}$ of the gapped graphene case in the general formula of the ZB, we get for a plane wave

$$\begin{aligned} \langle \hat{v}_k^{\mathrm{ZB}} \rangle(t) &= v_F \frac{2}{\sqrt{1+\kappa^2}} \operatorname{Re}\left\{ c_{+,k} c_{-,k}^* \mathrm{e}^{-i\Omega_{\mathbf{k}}^{\mathrm{ZB}} t} \right\} \\ &= v_F \frac{2\,|c_{+,k}|\,|c_{-,k}|}{\sqrt{1+\kappa^2}} \cos\left(\Omega_{\mathbf{k}}^{\mathrm{ZB}} t + \varphi_k\right). \end{aligned} \tag{7.53}$$

For typical wave packets, where $c_{+,k} = c_+$ and $c_{-,k} = c_-$ are k-independent, Eq. (7.53) yields

$$\langle \hat{v}_k^{\mathrm{ZB}} \rangle(t) = v_F \frac{2|c_+ c_-|}{\sqrt{1+\kappa^2}} \cos\left(\Omega_{\mathbf{k}}^{\mathrm{ZB}} t + \varphi\right), \tag{7.54}$$

where also the phase φ from Eq. (7.13) becomes k-independent.

For a wave packet, the usual dephasing process takes place, leading to a decrease of the (observable) ZB over time. The general estimation of the decay time T_2^* for a Gaussian wave packet of width Δk in Eq. (7.32), where we derive the frequency Ω_k^{ZB} of Eq. (7.48) with respect to k, yields

$$T_2^* = \frac{2}{\Delta k} \frac{1}{2v_F} \frac{\sqrt{1+\kappa^2}}{\kappa} = \frac{1}{\Delta k v_F} \underbrace{\frac{\sqrt{1+\kappa^2}}{\kappa}}_{\geq 1} \geq \frac{1}{\Delta k v_F}, \tag{7.55}$$

and is therefore larger than the decay time of the perpendicular ZB in pristine graphene (compare Eq. (7.43)).

In Fig. 7.3(a), the parallel ZB of a Gaussian wave packet is shown for gapped graphene as a function of time. Here, we state all physical quantities in relation to the gap term M_0. The used wave packet is Gaussian peaked around $k_0 = 0.4 M_0/(\hbar v_F)$, i.e. $\kappa_0 = \hbar v_F k_0 / M_0 = 0.4$ with a width $\Delta k = 0.2 k_0$. It is chosen to be an eigenstate with positive energy of the ungapped graphene Hamiltonian $|\varphi_{k,+}\rangle$ of Eq. (7.35). Thus, the occupation of positive and negative band is given by

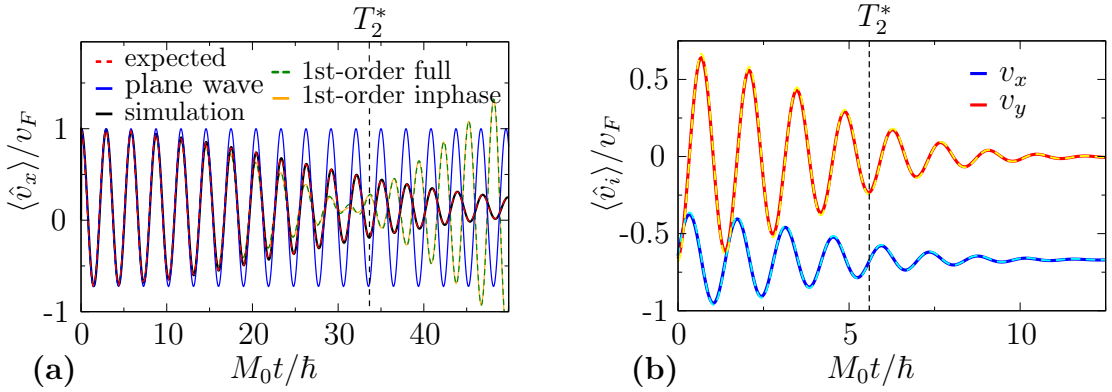

Figure 7.3: The ZB in gapped graphene. (a) The result for the parallel ZB is shown. The black solid line corresponds to the simulation (TQT), which matches perfectly the numerically evaluated integral in Eq. (7.18) (red dashed line). The nondecaying result for a plane wave with k_0 shows the same initial oscillation (blue). To compare the estimation of the decay in linear order used to derive Eq. (7.32), both the in-phase contribution (orange solid) as well as the full first non-vanishing order (green dashed) in Δk is plotted, showing almost no difference at all. The vertical dashed line indicates the estimated decay time T_2^* from Eq. (7.55), which is close to the point in time, when the amplitude of the full first non-vanishing order is zero. (b) The parallel (blueish) and perpendicular (reddish) ZB in gapped graphene is shown both with a TQT-simulation (solid lines) and numerical evaluation of Eq. (7.18) taking the width of the wave packet into account. As expected, the frequency is the same, whereas the amplitude changes from parallel to perpendicular, and they have a phase shift of π. The constant offset of $\langle v_x \rangle$ is due to the unequal occupation of the two bands.

$$c_{+,k} = \langle \chi_k^+ \mid \varphi_{k,+} \rangle, \tag{7.56}$$
$$c_{-,k} = \langle \chi_k^- \mid \varphi_{k,+} \rangle, \tag{7.57}$$

and their product yields for $k = k_0$:

$$c_{+,k_0} c_{-,k_0}^* = \frac{1}{4} \frac{1 + \kappa_0 + \sqrt{1+\kappa_0^2}}{1 + \kappa_0^2 + \sqrt{1+\kappa_0^2}} \frac{1 + \kappa_0 - \sqrt{1+\kappa_0^2}}{1 + \kappa_0^2 - \sqrt{1+\kappa_0^2}} = \frac{1}{2\sqrt{1+\kappa_0^2}}. \tag{7.58}$$

Since the product as well as the matrix element of the velocity operators are real numbers, the phase is $\varphi = 0$ and the ZB becomes

$$\langle \hat{v}_{k_0}^{\mathrm{ZB}} \rangle (t) = \frac{v_F}{1+\kappa^2} \cos\left(\frac{M_0 t}{\hbar} \sqrt{1+\kappa_0^2} \right), \tag{7.59}$$

as shown by the blue line for a plane wave with k_0 in Fig. 7.3(a). The black solid line shows the decaying ZB of the full quantum simulation by TQT. The red dashed line indicates the expected decay for the given wave packet be evaluating the integral over all k-modes in Eq. (7.18) numerically, and matches the full simulation perfectly.

Additionally, parts of the first non-vanishing order in the width Δk of the wave packet are shown, which were used to derive the formula for the decay time T_2^*

of Eq. (7.32), to show the effects of the approximations, which have entered the derivation. We see both, the full order (green dashed) as in Eq. (7.27), as well as keeping only the in-phase terms (orange). Since there is almost no difference at all, the assumption to neglect the out-of-phase terms for T_2^* is justified (at least in this example).

Furthermore, we see that it is also justified to neglect the in-phase-term which has no additional time-dependence as discussed below Eq. (7.27). The difference between keeping and neglecting this term can be seen by comparing the indicated $T_2^* = 33.67\hbar/M_0$ of Eq. (7.55) in Fig. 7.3(a) (vertical black dashed line), with the time when the amplitudes of the green and orange lines vanish, which would yield a slightly shorter decay time ($T_2^* \simeq 32\hbar/M_0$). However, this difference is not significant, especially because we are only interested in an estimation for the magnitude of T_2^*. Moreover, we see that in this order of Δk, the ZB vanishes but then reemerges. As explained in Sec. 7.2, in reality, the higher orders for larger times get more and more important, and they prevent the "revival" of the ZB, as expected only from lowest order.

Now, let us investigate the change to the perpendicular ZB. The first change is obvious: The frequency of the ZB is necessarily the difference of the energy levels as in Eq. (7.48), which has changed as compared to pristine graphene (Eq. (7.37)). For the amplitude, we need again the matrix element $\mathbf{v}_\mathbf{k}^{-+}$ of the velocity operator. Without loss of generality, let us assume again $\mathbf{k} = (k, 0)^T$. Then, the perpendicular element of $\mathbf{v}_\mathbf{k}^{-+}$ is its y-component, which yields in analogously to the parallel case Eq. (7.52)

$$\mathbf{v}_\mathbf{k}^{ss'} \cdot \hat{\mathbf{e}}_y = v_F \langle \chi_\mathbf{k}^s \mid \sigma_y \mid \chi_\mathbf{k}^{s'} \rangle = \frac{i v_F \kappa}{2} \frac{(1-1) + (-s+s')\sqrt{1+\kappa^2}}{\sqrt{(1+\kappa^2)^2 + ss'(1+\kappa^2) + (s+s')\sqrt{1+\kappa^2}^3}}, \tag{7.60}$$

which reduces for $s' = +$ and $s = -$ to

$$\mathbf{v}_\mathbf{k}^{-+} \cdot \hat{\mathbf{e}}_y = v_F \langle \chi_\mathbf{k}^- \mid \sigma_y \mid \chi_\mathbf{k}^+ \rangle = \frac{i v_F \kappa}{2} \frac{2\sqrt{1+\kappa^2}}{\kappa\sqrt{1+\kappa^2}} = i v_F, \tag{7.61}$$

as in the gapless graphene case (see also App. B).

Thus, the perpendicular ZB for gapped graphene combines the perpendicular ZB of pristine graphene (amplitude) with the parallel ZB of gapped graphene (frequency). However, this means, that the decay behavior is the same as in the parallel case, since the decay is (almost) solely due to the $\mathbf{k}$-dependence of the frequency:

$$T_2^* = \frac{1}{\Delta k v_F} \frac{\sqrt{1+\kappa^2}}{\kappa}. \tag{7.62}$$

Moreover, the phase of the ZB between x- and y-direction is shifted by $\pi/2$, since the matrix element is purely imaginary for v_y and real for v_x.

In Fig. 7.3(b), the ZB of a Gaussian wave packet centered around $\boldsymbol{\kappa}_0 = (\kappa_0, 0)^T$ with $\kappa_0 = 2$ and width $\Delta k = k_0/10$ is shown, both in x-direction (parallel) and y-direction (perpendicular) ZB. The occupation of the bands is chosen such that $c_+ = \sqrt{3}/2$ and $c_- = i/2$ at $\mathbf{k} = \mathbf{k}_0$. The imaginary c_- leads to the constant phase

shift φ of the ZB as in Eq. (7.13), which shifts the parallel ZB slightly away from the "$-\sin\Omega^{\mathrm{ZB}}t$", for instance.

As expected, the simulation and the numerical evaluation of the sum in Eq. (7.18) yield the same results. Both components of the ZB oscillate with the analytically obtained frequency with a period $T = 2\pi/\Omega^{\mathrm{ZB}}_{\mathbf{k}_0} \approx 1.4\hbar/M_0$. The initial amplitude differs in the two cases due to the different velocity matrix elements of Eqs. (7.52) and (7.61) by a factor of $\sqrt{1+\kappa_0^2} = \sqrt{5}$ ($A_x \approx 0.62$, $A_y \approx 1.38$) and the phase between parallel and perpendicular ZB is shifted by $\pi/2$ as explained above. The decay time is in both cases the same and yields for the given wave packet $T_2^* = 5.6\hbar/M_0$. At this point in time, the amplitude has decreased as in the cases before by a factor of roughly 1/3.

As already mentioned, the ZB in the static case is well-known and in this section, we have seen that our calculations match the expectations. The reason for the extensive discussion of the established transient character of the ZB is that this decay is what we want to delay or even circumvent with time-dependent potentials, here a time-dependent mass potential.

7.4 Time-dependent zitterbewegung in graphene

In this section, we want to investigate the influence of a time-dependent mass potential to the ZB. The Hamiltonian of choice is

$$H = \hbar v_F \mathbf{k}\cdot\boldsymbol{\sigma} + M_0\sigma_z + M(t)\sigma_z = H_0 + H_1(t), \tag{7.63}$$

with the time-dependent mass term

$$M(t) = \tilde{M}\sin\omega_D t, \tag{7.64}$$

where ω_D is the driving frequency. As in Subsec. 7.3.2, the frequency of the ZB for the time-independent case (e.g. $\tilde{M} = 0$) is

$$\Omega^{\mathrm{ZB}}_{\mathbf{k}} = 2\frac{M_0}{\hbar}\sqrt{1+\kappa^2}, \tag{7.65}$$

with $\kappa = \hbar v_F k/M_0$. Subsequently, we will also call $\Omega^{\mathrm{ZB}}_{\mathbf{k}}$ the frequency of the "static" ZB, although the ZB is by nature not static but what we mean is that the Hamiltonian is time-independent. Moreover, we will find that new ZB frequencies emerge in time-dependent systems. There, $\Omega^{\mathrm{ZB}}_{\mathbf{k}}$ is not to be confused with the actual frequency, but is only meant as the abbreviation defined in Eq. (7.65).

First, we want to see what happens for small time-dependent potentials in first order of time-dependent perturbation theory. Next, we use the rotating wave approximation (RWA) and the high-driving frequency (HDF) limit to determine the emerging frequencies of the driven ZB, similar to Rusin and Zawadzki [140], who considered a time-dependent vector potential instead of our mass term. After that, we will consult the simulation package TQT, first to confirm the analytic results in their valid parameter regime and then to study the multimode ZB in regimes we cannot access with our approximations. For that, we will take a Fourier transform of the numerically obtained, time-dependent velocity to find out the oscillation frequencies.

Our main goal is to find long-lived or even non-decaying modes, i.e. a long term oscillation is of interest. Therefore, we take the Fourier transform from the rest of the "signal", starting at a time when the system has settled, i.e. when the transient oscillations have decayed.

7.4.1 First order time-dependent perturbation theory

As in the time-independent case, we have to investigate the expectation value of the position or velocity operator to study the ZB. Since the time-dependent potential in the Hamiltonian in Eq. (7.63) is translational invariant, the momentum $\mathbf{k}$ is conserved. For simplicity, we will first consider a single $\mathbf{k}$-mode, which can live in both bands, before we will consider wave packets again.

We use the following general ansatz for the wave function:

$$|\psi_{\mathbf{k}}\rangle(t) = \sum_{n=\pm} c_n(t) \mathrm{e}^{-i\omega_n^{\mathbf{k}} t} |\mathbf{k}, n\rangle, \tag{7.66}$$

where $|\mathbf{k}, n\rangle := |\chi_{\mathbf{k},\pm}\rangle$ are the eigenstates of the gapped graphene Hamiltonian H_0 from Eq. (7.63), with the functional form as in Eq. (7.47), and the corresponding energy $\varepsilon_\pm(\mathbf{k}) = \hbar\omega_\pm^{\mathbf{k}}$ as in Eq. (7.46). Note that for a time-independent Hamiltonian, the coefficients c_n do not depend on time, or otherwise said, the time-dependence of $c_n(t)$ is due to the time-dependent potential $H_1(t)$.

The expectation value of the velocity then yields

$$\begin{aligned}\langle \hat{\mathbf{v}}_{\mathbf{k}} \rangle &= \sum_{m,n=\pm} c_m^*(t) c_n(t) \mathrm{e}^{-i(\omega_n^{\mathbf{k}} - \omega_m^{\mathbf{k}})t} \langle \mathbf{k}, m \mid \hat{\mathbf{v}} \mid \mathbf{k}, n \\ &= |c_+(t)|^2 \mathbf{v}_{\mathbf{k}}^{++} + |c_-(t)|^2 \mathbf{v}_{\mathbf{k}}^{--} + 2\mathrm{Re}\left\{ c_-^*(t) c_+(t) \mathrm{e}^{-i\Omega_{\mathbf{k}}^{\mathrm{ZB}} t} \mathbf{v}_{\mathbf{k}}^{-+} \right\}, \end{aligned} \tag{7.67}$$

Here we used again the definition of the velocity matrix elements as in Eq. (7.7), which is very similar to the time-*in*dependent system of Eq. (7.8), The only difference is that the coefficients c_n are now time-dependent, which means that also the diagonal terms of the velocity operator are not time-independent anymore. Thus they can additionally contribute to some kind of jiggly motion.

But also the off-diagonal terms proportional to $\mathbf{v}_{\mathbf{k}}^{-+}$ are more complicated than before due to the time-dependence of the coefficients $c_n(t)$. In general, $c_n(t)$ cannot be obtained exactly, although there are a few examples for 2 level systems, e.g. the spin-magnetic resonance (see e.g. [143]), but for the time-dependent mass potential as in our case, the exact solutions are not known, which is why we consult perturbation theory.

In App. D, the occupation coefficients $c_n(t)$ of the time-dependent perturbation are derived without going to much into detail, together with a very short reminder of the interaction picture. We are interested in the first order approximation for a 2-level system. Using the initial condition

$$|\psi_{\mathbf{k}}\rangle(0) = \sum_{n=\pm 1} c_{n,0} \, |\mathbf{k}, n\rangle, \tag{7.68}$$

where $c_{n,0} = c_n(0)$, and the formula for the first order correction from Eq. (D.18) in App. D, the occupation coefficient becomes approximatively

$$c_n(t) \approx c_n^{(0)} + c_n^{(1)}(t), \tag{7.69}$$

with

$$c_n^{(0)}(t) = c_{n,0} \tag{7.70}$$

$$c_n^{(1)}(t) = -\frac{i}{\hbar}\int_0^t \mathrm{d}t' \left(c_{n,0}\langle \mathbf{k}, n \mid H_1(t') \mid \mathbf{k}, n\rangle + c_{-n,0}\, \mathrm{e}^{in\Omega_{\mathbf{k}}^{\mathrm{ZB}}t'} \langle \mathbf{k}, n \mid H_1(t') \mid \mathbf{k}, -n\rangle \right), \tag{7.71}$$

where every quantity is known. With the chosen Hamiltonian, the first order correction becomes in our case

$$c_n^{(1)}(t) = -\frac{i}{\hbar}\tilde{M}\int_0^t \mathrm{d}t' \, \sin(\omega_D t') \left(c_{n,0}\langle \mathbf{k}, n \mid \sigma_z \mid \mathbf{k}, n\rangle + c_{-n,0}\, \mathrm{e}^{in\Omega_{\mathbf{k}}^{\mathrm{ZB}}t'} \langle \mathbf{k}, n \mid \sigma_z \mid \mathbf{k}, -n\rangle \right). \tag{7.72}$$

The integrals can be easily performed. Moreover, the matrix elements of the Pauli matrices in the basis $|\pm, \mathbf{k}\rangle$ are calculated in App. B. In total, the occupation coefficients yield in first order correction in terms of the time-dependent potential

$$\begin{aligned} c_n(t) \approx \quad & c_{n,0}\left(1 - \frac{i\tilde{M}}{\hbar\omega_D} n(1-\cos\omega_D t)\right) \\ & + c_{-n,0}\frac{i\tilde{M}}{2\hbar}\frac{\kappa}{\sqrt{1+\kappa^2}}\left(\frac{\mathrm{e}^{i(n\Omega_{\mathbf{k}}^{\mathrm{ZB}}-\omega_D)t}-1}{n\Omega_{\mathbf{k}}^{\mathrm{ZB}}-\omega_D} - \frac{\mathrm{e}^{i(n\Omega_{\mathbf{k}}^{\mathrm{ZB}}+\omega_D)t}-1}{n\Omega_{\mathbf{k}}^{\mathrm{ZB}}+\omega_D}\right). \end{aligned} \tag{7.73}$$

The first order correction to $\langle \hat{\mathbf{v}}_{\mathbf{k}} \rangle$ in $\tilde{M}$, which we call $\langle \hat{\mathbf{v}}_{\mathbf{k}}{}^{(1)} \rangle$, is obtained by inserting Eq. (7.69) into Eq. (7.67) and keeping only the terms linear in $c_n^{(1)}$:

$$\langle \hat{\mathbf{v}}_{\mathbf{k}}^{(1)} \rangle = \sum_{n=\pm 1} \left[\mathbf{v}_{\mathbf{k}}^{nn}\, 2\mathrm{Re}\left\{ c_n^{(1)^*}(t) c_n^{(0)} \right\} \right] + 2\mathrm{Re}\left\{ \mathrm{e}^{-i\Omega_{\mathbf{k}}^{\mathrm{ZB}}t} \mathbf{v}_{\mathbf{k}}^{-+} \left(c_-^{(1)^*}(t) c_+^{(0)} + c_-^{(0)^*} c_+^{(1)}(t) \right) \right\}. \tag{7.74}$$

Thus, the behavior of the mean velocity is known for every time in first order correction. For an initial wave packet

$$|\psi_0\rangle = \int \mathrm{d}^2k \, \phi_0(\mathbf{k}) \sum_{n=\pm} c_{n,0} |\mathbf{k}, n\rangle, \tag{7.75}$$

the velocity expectation value becomes in first order of $\tilde{M}$:

$$\langle \hat{\mathbf{v}} \rangle = \int \mathrm{d}^2k \, |\phi_0(\mathbf{k})|^2 \left(\langle \hat{\mathbf{v}}_{\mathbf{k}}^{(0)} \rangle + \langle \hat{\mathbf{v}}_{\mathbf{k}}^{(1)} \rangle \right). \tag{7.76}$$

In Fig. 7.4, $\langle v_x \rangle$ is shown, both from full simulation of the propagation of a Gaussian wave packet using TQT centered around $\mathbf{k}_0$, as well as from perturbation theory. For small amplitude $\tilde{M}/M_0 = 0.005$ (panel (a)) and a driving frequency $\omega_D = 1.01\Omega_{\mathbf{k}_0}^{\mathrm{ZB}}$ close to the resonance frequency of the ZB in the static case, $\Omega_{\mathbf{k}}^{\mathrm{ZB}} = 2M_0\sqrt{1+\kappa^2}$, the perturbation theory up to first order matches the simulation very well. As expected, the zeroth order (static case) decays as in Subsec. 7.3.2, the first order amplitude on the other hand increases over time until it reaches a maximum value. For large

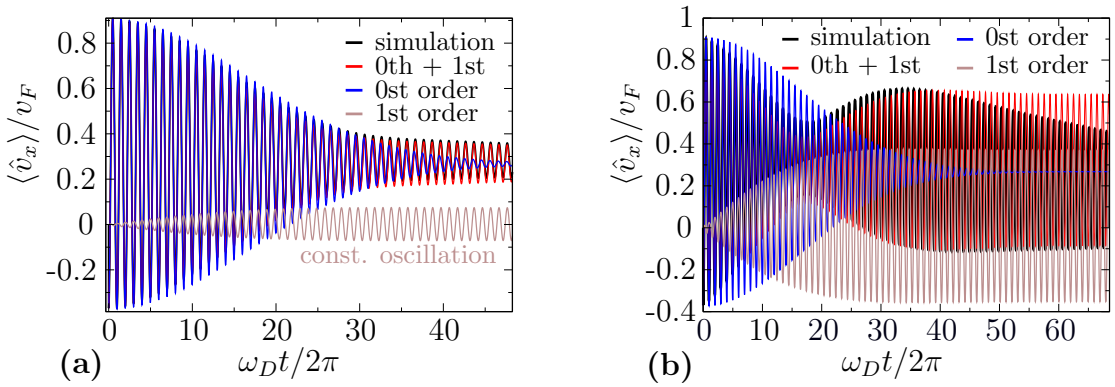

Figure 7.4: The expectation value of the velocity operator as function of time comparing full simulation (black) and time-dependent perturbation theory in $\tilde{M}$ (red, see Eq. (7.76)) for a driven mass gap for the resonant case $\omega_D \approx \Omega^{\mathrm{ZB}}_{\mathbf{k}_0}$. For small $\tilde{M}/M_0 = 0.005$, (a), the perturbation theory up to first order (red line) matches very well the simulation (black line), whereas for higher $\tilde{M}/M_0 = 0.025$, (b), deviations appear for larger times. Furthermore, only the zeroth order (blue line) is shown in both panels as well as only first order (brown line). We want to draw attention to the predicted long-time behavior of the first order time-dependent perturbation theory, which is an oscillation with constant amplitude and frequency ω_D, in agreement with the analytical approximation of Eq. (7.92).

times, the first order is a oscillation with constant amplitude and only one frequency, which is equal to the driving ω_D.

In panel (b), the same wave packet is subject to a stronger amplitude of $\tilde{M}/M_0 = 0.025$ with the same $\omega_D \approx \Omega_{\mathrm{ZB}}$ as panel (a). As expected, the agreement is worse for larger $\tilde{M}$, but still, for intermediate times, the results match quite well. Most of all, the frequency of the ZB coincides in simulation and perturbation theory, but the amplitude does not for larger times match, where the first order perturbation theory predicts a single frequency oscillations with ω_D and with constant amplitude, alike panel (a).

Since first order perturbation theory of Eq. (7.74) captures important features of the ZB, we want to understand it better on an analytical level, e.g. which terms dominate, or what is responsible for oscillation with constant amplitude and ω_D for long times. Therefore, we want to have a closer look at the first order correction of the wave function, given by $c_n^{(1)}(t)$ in Eq. (7.73):

$$\begin{aligned} c_n^{(1)}(t) = \quad & c_{n,0} \frac{i\tilde{M}}{\hbar\omega_D} n(1 - \cos\omega_D t) \\ & + c_{-n,0} \frac{i\tilde{M}}{2\hbar} \frac{\kappa}{\sqrt{1+\kappa^2}} \left(\frac{\mathrm{e}^{i(n\Omega^{\mathrm{ZB}}_{\mathbf{k}} - \omega_D)t} - 1}{n\Omega^{\mathrm{ZB}}_{\mathbf{k}} - \omega_D} - \frac{\mathrm{e}^{i(n\Omega^{\mathrm{ZB}}_{\mathbf{k}} + \omega_D)t} - 1}{n\Omega^{\mathrm{ZB}}_{\mathbf{k}} + \omega_D} \right). \end{aligned} \tag{7.77}$$

In the transition part proportional to $c_{-n,0}$, we see that there is the possibility of resonant behavior for $\Omega^{\mathrm{ZB}}_{\mathbf{k}} = \pm\omega_D$, as opposed to the part linear in $c_{n,0}$. There the case that the amplitude becomes large, i.e. $\tilde{M}/(\hbar\omega_D) \gg 1$, is not a justified limit that is reasonably covered by the perturbation theory.

Therefore, let us have a closer look at the transition part. The ratio predominates in the brackets which has a pole , since $|\Omega_{\mathbf{k}}^{\mathrm{ZB}}-\omega_D| < \Omega_{\mathbf{k}}^{\mathrm{ZB}}+\omega_D$. Thus, in the resonant regime $\omega_D \approx \Omega_{\mathbf{k}}^{\mathrm{ZB}}$, we approximate $c_n^{(1)}(t)$ by

$$c_n^{(1)}(t) \approx c_{-n,0}\frac{i\tilde{M}}{2\hbar}\frac{\kappa}{\sqrt{1+\kappa^2}}\frac{\mathrm{e}^{in(\Omega_{\mathbf{k}}^{\mathrm{ZB}}-\omega_D)t}-1}{\Omega_{\mathbf{k}}^{\mathrm{ZB}}-\omega_D}. \tag{7.78}$$

We want to study the behavior for large times $t \to \infty$. Considering only the last ratio,

$$\frac{\mathrm{e}^{i(\Omega_{\mathbf{k}}^{\mathrm{ZB}}-\omega_D)t}-1}{\Omega_{\mathbf{k}}^{\mathrm{ZB}}-\omega_D} = \frac{\cos\big((\Omega_{\mathbf{k}}^{\mathrm{ZB}}-\omega_D)t\big)-1}{(\Omega_{\mathbf{k}}^{\mathrm{ZB}}-\omega_D)} + i\frac{\sin\big((\Omega_{\mathbf{k}}^{\mathrm{ZB}}-\omega_D)t\big)}{(\Omega_{\mathbf{k}}^{\mathrm{ZB}}-\omega_D)}, \tag{7.79}$$

we see that the pole is a removable discontinuity, because both $\cos(x)-1 \approx -0.5x^2$ and $\sin(x) \approx x$ are elements of $\mathcal{O}(x)$ for $x \to 0$.

For large times $t \to \infty$, the imaginary part is known to be a representation of the Dirac-Delta in the sense of a distribution:

$$\lim_{t\to\infty}\frac{\sin(xt)}{x} = \pi\delta(x). \tag{7.80}$$

The heuristic reason for Eq. (7.80) is that for larger and larger times t, which is the "frequency" of sine in this case, the given function becomes more and more peaked around $x = 0$. While

$$\int_{\mathbb{R}} \mathrm{d}x\frac{\sin(xt)}{x} = \pi, \tag{7.81}$$

it can be shown for any $\delta > 0$ that

$$\lim_{t\to\infty}\int_{\mathbb{R}\setminus[-\delta,\delta]} \mathrm{d}x\frac{\sin(xt)}{x} = 0. \tag{7.82}$$

Therefore, all of the weight has to be inside the arbitrarily small region $[-\delta,\delta]$ and due to the high oscillations, any smooth function will cancel in the integral, except at the point $x = 0$.

Another intuitive explanation for Eq. (7.80) is the following. On the one hand, $\frac{\sin(xt)}{x}$ is (up to constant factors) the Fourier transform of the box function with width t. On the other hand, the Fourier transformation of the constant function $f(x) = 1$ is the δ-distribution. Since for $t \to \infty$, the box becomes the constant function, its Fourier transformation needs to become the δ-distribution.

There are several reasons, why the contribution to the velocity of a wave packet $\langle\hat{\mathbf{v}}\rangle$ of the real part in Eq. (7.79), i.e. the cosine term, is in most cases small compared to the imaginary part which yields the $\delta(\Omega_{\mathbf{k}}^{\mathrm{ZB}}-\omega_D)$. First of all and most important, it does not yield a contribution at the pole $\Omega_{\mathbf{k}}^{\mathrm{ZB}} = \omega_D$, because

$$\lim_{x\to 0}\frac{\cos(x)-1}{x} = 0. \tag{7.83}$$

Moreover, in the integral over $\mathbf{k}$ in Eq. (7.76), $\frac{\cos((\Omega_{\mathbf{k}}^{\mathrm{ZB}}-\omega_D)t)-1}{\Omega_{\mathbf{k}}^{\mathrm{ZB}}-\omega_D}$ is even around $\mathbf{k}_{\omega_D}$ (which is the $\mathbf{k}$-value such that $\Omega_{\mathbf{k}_{\omega_D}}^{\mathrm{ZB}} = \omega_D$). Thus, only the even parts around $\mathbf{k}_{\omega_D}$,

of the other function play a role, because else the integrand becomes odd such that the integral from $-\infty$ to ∞ vanishes. Furthermore, one can show that unlike the sine part of Eq. (7.79), the cosine part is dependent on the initial configuration of the wave packet ($\sim |c_{+,0}|^2 - |c_{-,0}|^2$,) when we want to calculate the velocity. For a symmetric wave packet, $|c_{+,0}|^2 = |c_{-,0}|^2$, this term would have no contribution.

The last reason, why we will keep only the imaginary part of Eq. (7.79) when it comes to give an estimate of $\langle \hat{\mathbf{v}} \rangle$ in Eq. (7.76), is simply convenience: The integral over $\mathbf{k}$ can always be handled by the δ-distribution, whereas the part in Eq. (7.79) with the cosine might not give an analytically solvable integral.

Due to the four reasons given above, we neglect the first term in Eq. (7.79), and approximate $c_n^{(1)}(t)$ for large times by:

$$c_n^{(1)}(t) \approx -c_{-n,0} \frac{\tilde{M}}{2\hbar} \frac{\kappa}{\sqrt{1+\kappa^2}} \pi \delta(\Omega_{\mathbf{k}}^{\mathrm{ZB}} - \omega_D). \tag{7.84}$$

Due to the δ-function, the integral in Eq. (7.76) can be performed easily. Furthermore, using that

$$\mathrm{Re}\left\{c_{-n,0}^* c_{n,0}\right\} = \frac{1}{2}\left(c_{-n,0}^* c_{n,0} + c_{n,0}^* c_{-n,0}\right) \tag{7.85}$$

is symmetric under exchange of $n \leftrightarrow -n$, and that $\mathbf{v}_{\mathbf{k}}^{nn} \propto n$, the following sum cancels.

$$\sum_{n=\pm 1} \underbrace{\mathbf{v}_{\mathbf{k}}^{nn}}_{\propto n} \mathrm{Re}\left\{c_{-n,0}^* c_{n,0}\right\} = 0 \tag{7.86}$$

Thus, the diagonal term of Eq. (7.74), i.e. the term containing $\mathbf{v}_{\mathbf{k}}^{nn}$, does not contribute in our approximation, such that the only resonant mode is due to the off-diagonal term proportional to $\mathbf{v}_{\mathbf{k}}^{-+}$.

The expectation value of the velocity $\langle \hat{\mathbf{v}} \rangle$ from Eq. (7.76) becomes

$$\langle \hat{\mathbf{v}} \rangle = \mathbf{v}_0 - \int \mathrm{d}^2 k \frac{\kappa \mathbf{v}_{\mathbf{k}}^{-+}}{\sqrt{1+\kappa^2}} \frac{\tilde{M}}{\hbar} |\phi_0(\mathbf{k})|^2 \mathrm{Re}\Big\{ \mathrm{e}^{-i\Omega_{\mathbf{k}}^{\mathrm{ZB}} t} \delta(\Omega_{\mathbf{k}}^{\mathrm{ZB}} - \omega_D) \overbrace{\left(|c_{-,0}|^2 + |c_{+,0}|^2\right)}^{1} \Big\}, \tag{7.87}$$

where $\mathbf{v}_0$ is the 0th-order result, that we know from the case of time-independent Hamiltonians in Sec. 7.3.2, which is due to the decay of the ZB a constant (or even 0) and therefore not of importance for us.

To further simplify let us consider the 1D-case, which is equivalent to a wave packet with small angular width in $\mathbf{k}$-space. Using the property

$$\delta(g(x)) = \sum_i \frac{\delta(x - x_i)}{|g'(x_i)|} \tag{7.88}$$

of the δ-distribution, where x_i are the single roots of $g(x)$, we get

$$\delta(\Omega_k^{\mathrm{ZB}} - \omega_D) = \frac{\sqrt{1+\kappa^2}}{2 v_F \kappa} \left(\delta(k - k_{\omega_D}) + \delta(k + k_{\omega_D})\right), \tag{7.89}$$

where the prefactor is due to the derivative of Ω_k^{ZB} with respect to k, which is the same for both roots, and

$$k_{\omega_D} = \frac{1}{v_F} \sqrt{\frac{\omega_D^2}{4} - \frac{M_0^2}{\hbar^2}} \tag{7.90}$$

is the positive k where $\Omega^{\mathrm{ZB}}_{k_{\omega_D}} = \omega_D$. Usually, one δ-function in Eq. (7.89) can be neglected, except if the wave packet is rather broad, and has similar weight at k_{ω_D} and $-k_{\omega_D}$. Thus, with

$$v_k^{-+} = \frac{v_F}{\sqrt{1+\kappa^2}} \operatorname{sgn}(k), \tag{7.91}$$

as in App. B, the velocity in Eq. (7.87) becomes

$$\langle \hat{v} \rangle = v_0 - \frac{\pi \tilde{M}}{2\hbar\sqrt{1+\kappa^2_{\omega_D}}} \left(|\phi_0(k_{\omega_D})|^2 - |\phi_0(-k_{\omega_D})|^2 \right) \cos(\omega_D t) \tag{7.92}$$

in first order in $\tilde{M}$, with $\kappa_{\omega_D} = \hbar v_F k_{\omega_D}/M_0$. Thus, the largest effect can be seen for small κ_{ω_D} which means for large M_0 for a given ω_D.

The important message from first order perturbation theory is, that the mass gap with the driving frequency ω_D projects out only those terms of the wave function, which oscillate naturally (in the static case) with the same frequency, whereas all other frequencies die out. Thus, if the ZB of a wave packet is off-resonant to ω_D, no contribution is expected. Indeed, according simulations with an off-resonant driving confirm this, but since the ZB looks exactly as in the static case, it is not shown explicitly. The observations from solving the integral in Eq. (7.76) are reproduced, which could be seen in Fig. 7.4, where for large times, the first order term becomes an oscillation of constant amplitude with the frequency ω_D (compare Eq. (7.92)).

In Fig. 7.5, we compare the analytically obtained first order approximation for the velocity from Eq. (7.92) with full simulation from TQT and the numerically obtained integral from Eq. (7.76). The only numerical input we need for the analytical solution is the initial wave function at k_{ω_D}, which is $\phi_0(k_{\omega_D})$. In the simulation (black solid line), the velocity expectation value of a Gaussian wave packet centered around some k_0 such that $\kappa_0 = \hbar v_F k_0/M_0 = 0.4$ with k-space width $\Delta k = 0.1k_0$ is plotted as a function of time. The parameters of the time-dependent mass potential are $\tilde{M} = 0.01M_0$ and $\omega_D = 1.01\Omega^{\mathrm{ZB}}_{k_0}$. The additional data in Fig. 7.5 are obtained from perturbation theory. The red dashed line is obtained by numerical integration of Eq. (7.76), which matches the simulation quite well, as already shown in Fig. 7.4(a).

The important statement of Fig. 7.5 is to show that despite all the approximations made during its derivation, Eq. (7.92) (purple line) is a good estimate for the actual first order correction of the velocity (brown line). The only difference is a small change is a slight phase change of the oscillation with constant frequency, and a very small change in amplitude.

To conclude this section, we want to highlight again the most important result, which is that time-dependent perturbation theory in first order predicts that there is an infinitely long lived mode of the ZB with the driving frequency ω_D, whose amplitude can be estimated by the analytical formula given in Eq. (7.92). This long lived mode is confirmed numerically for small perturbation amplitudes $\tilde{M}$.

One last comment is that the behavior from first order perturbation theory for a time-dependent mass potential is fundamentally different to a time-dependent vector potential, which was considered by [140]. First of all, their results still show a decaying ZB. Moreover, in contrast to our results, their numerical investigations match the perturbation theory only for rather short times. However, with their choice of parameters, their perturbation strength is comparable to energy of the

wave packet in the case without perturbation, such that it is not surprising that perturbation theory is not valid anymore.

In the next sections, we want to investigate a broader parameter regime, to see for instance whether a multimode ZB is appearing.

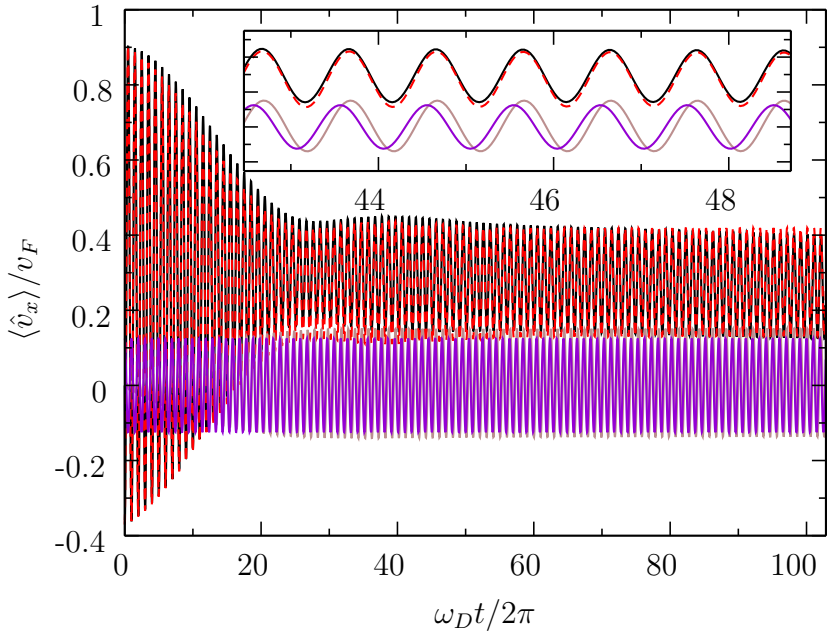

Figure 7.5: Justification of approximations that entered the derivation of the analytical formula for $\langle \hat{v} \rangle$ of Eq. (7.92) in first order time-dependent perturbation theory. The ZB of a wave packet obtained by simulation (black), 0th+1st order of perturbation theory (red), only 1st order (brown) and the analytical resonant approximation for the 1st order given by Eq. (7.92) (purple) are shown. The inlet shows a close-up, to better compare the results. The pure analytical estimation (purple) matches quite well the 1st order obtained by numerical integration (brown), up to small changes in phase and minor changes for the amplitude. The constant vertical offset compared to the simulation is just because 0th order is not incorporated to avoided a too crowded plot.

7.4.2 Rotating wave approximation

The rotating wave approximation (RWA) is well-known and often used in atomic optics to simplify the interaction between atoms, i.e. few level systems, and a laser-field. It can be applied for low intensities of the driving field, if its frequency is in resonance with one of the level spacings. In that case, all high frequency terms in the Hamiltonian average out on physical time scales and only the in-resonant terms survive [144]. In a two-level system, it is used to derive the famous Rabi oscillations for instance. Although we consider two *bands*, the system is for any arbitrary $\mathbf{k}$ effectively a two-*level* system as long as $\mathbf{k}$ is conserved, i.e. for homogeneous pulses.

In our case, the conditions for the RWA are that $\tilde{M}$ is small compared to the other energy scales in the system and that $\omega_D \approx \Omega_{\mathbf{k}}^{\mathrm{ZB}}$. In this derivation, we will

consider only a single **k**-mode, since the ZB of a wave packet is then given by a weighted superposition, according to Eq. (7.18). This subsection follows the strategy of Ref. [140], where a time-dependent vector potential is considered instead of the time-dependent mass potential.

We use a similar time-dependent Hamiltonian as before in Eq. (7.45), but rewrite it slightly

$$H = \varepsilon(\mathbf{k})\mathbf{n}_\mathbf{k} \cdot \boldsymbol{\sigma} + \tilde{M}\cos(\omega_D t), \tag{7.93}$$

where we assume a cosine-oscillation instead of the above used sine, which is not supposed to make a relevant difference. The time-independent part is

$$H_{\text{static}} := \varepsilon(\mathbf{k})\mathbf{n}_\mathbf{k} \cdot \boldsymbol{\sigma} = \begin{pmatrix} \hbar v_F k_x \\ \hbar v_F k_y \\ M_0 \end{pmatrix}. \tag{7.94}$$

Here, $\varepsilon(\mathbf{k}) = M_0\sqrt{1+\kappa^2}$ is the energy of the time-independent Hamiltonian as in Eq. (7.46). The normalized vector $\mathbf{n}_\mathbf{k}$ can be expressed in spherical coordinates by

$$\mathbf{n}_\mathbf{k} = \begin{pmatrix} \cos\gamma_\mathbf{k}\,\sin\vartheta_\mathbf{k} \\ \sin\gamma_\mathbf{k}\,\sin\vartheta_\mathbf{k} \\ \cos\vartheta_\mathbf{k} \end{pmatrix}, \tag{7.95}$$

where the azimuthal angle is denoted by $\gamma_\mathbf{k} = \arctan^{-1}\frac{k_y}{k_x}$ as in the rest of the thesis, and the polar angle is $\vartheta_\mathbf{k} = \left(\frac{\pi}{2} - \arctan^{-1}\frac{M_0}{\hbar v_F k}\right)$.

The goal is first to approximate the time evolution $|\psi(t)\rangle$ of an initial state $|\psi(0)\rangle$ and use it to calculate the ZB, i.e. $\langle\hat{\mathbf{v}}\rangle(t)$. In the preceding section, this was done in perturbation theory, but now, we want to use the rotating wave approximation (RWA).

The first step is to make the time-independent part diagonal using an unitary transformation S_{RWA}, which rotates around $\mathbf{m}_\mathbf{k} = (\sin\gamma_\mathbf{k}, -\cos\gamma_\mathbf{k}, 0)$ in pseudospin-space by $\vartheta_\mathbf{k}$:

$$S_{\text{RWA}} = \mathrm{e}^{-i\frac{\vartheta_\mathbf{k}}{2}\mathbf{m}_\mathbf{k}\cdot\boldsymbol{\sigma}}. \tag{7.96}$$

As a consequence, the time-dependent Hamiltonian ($\sim \tilde{M}\sigma_z$) is not diagonal anymore, as visualized in Fig. 7.6, where the rotations in the Bloch sphere due to the transformation S_{RWA} are shown. The important changes of the operators in pseudospin space are due to geometrical considerations

$$S_{\text{RWA}}\mathbf{n}_\mathbf{k} \cdot \boldsymbol{\sigma} S_{\text{RWA}}^\dagger = \sigma_z, \tag{7.97}$$

$$S_{\text{RWA}}\sigma_z S_{\text{RWA}}^\dagger = \begin{pmatrix} -n_x \\ -n_y \\ n_z \end{pmatrix} \cdot \boldsymbol{\sigma} =: \mathbf{n}'_\mathbf{k} \cdot \boldsymbol{\sigma}, \tag{7.98}$$

which can be verified also by calculations. Thus, the Schrödinger equation transforms to

$$i\hbar\frac{\partial}{\partial t}\psi_\mathbf{k}^{\text{RWA}}(t) = \left(\varepsilon(\mathbf{k})\sigma_z + \tilde{M}\,\mathbf{n}'_\mathbf{k} \cdot \boldsymbol{\sigma}\,\cos(\omega_D t)\right)\psi_\mathbf{k}^{\text{RWA}}(t), \tag{7.99}$$

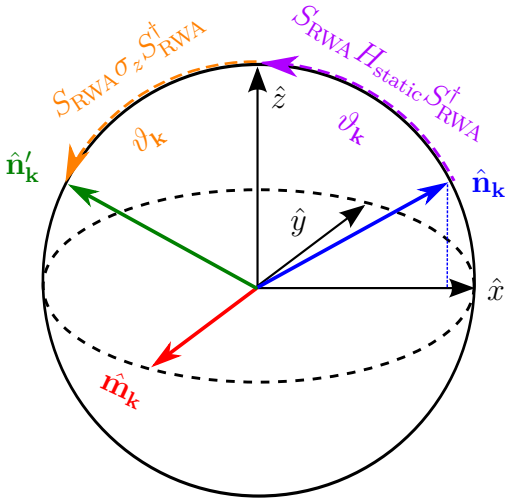

Figure 7.6: Visualization of the transformation used in RWA, S^{RWA}, to make the static part of the Hamiltonian diagonal (i.e. $\sim \sigma_z$). We choose $\mathbf{k} = (k, 0)$, i.e. $\gamma_{\mathbf{k}} = 0$, such that the direction of the stationary Hamiltonian $\hat{\mathbf{n}}_{\mathbf{k}}$ (compare Eq. (7.94)) is in the x-z-plane. The transformation S^{RWA} rotates around $\hat{\mathbf{m}}_{\mathbf{k}}$ (here $(0, -1, 0)$) by $\vartheta_{\mathbf{k}}$ as indicated by the purple dashed arrow, such that the static Hamiltonian becomes diagonal. Consequently, the initially diagonal driving with amplitude $\tilde{M}$ is rotated away from the z-axis (orange dashed arrow) to $\hat{\mathbf{n}}'_{\mathbf{k}}$, which is directly related to $\hat{\mathbf{n}}_{\mathbf{k}}$ as in Eq. (7.98).

where $\psi^{\mathrm{RWA}}_{\mathbf{k}}(t) = S_{\mathrm{RWA}}\psi_{\mathbf{k}}(t)$ is the transformed state. To cancel the time independent part in the Hamiltonian, we use the following ansatz in the transformed Schrödinger equation

$$\psi^{\mathrm{RWA}}_{\mathbf{k}}(t) = \begin{pmatrix} a_1(t)\mathrm{e}^{-\frac{i}{\hbar}\varepsilon(\mathbf{k})t} \\ a_2(t)\mathrm{e}^{+\frac{i}{\hbar}\varepsilon(\mathbf{k})t} \end{pmatrix}. \tag{7.100}$$

Note that the coefficients a_1 and a_2 depend in general on $\mathbf{k}$. However, in order not to overload the denotation, we omit all labels $\mathbf{k}$ henceforth in the derivation.

The ansatz in Eq. (7.100) leads to a set of differential equation for the coefficients a_1 and a_2

$$i\hbar\frac{\partial}{\partial t}\begin{pmatrix} a_1(t) \\ a_2(t) \end{pmatrix} = \tilde{M}\cos(\omega_D t)\left(n_z \begin{pmatrix} a_1(t) \\ -a_2(t) \end{pmatrix} + \begin{pmatrix} a_2(t)(n'_x - in'_y)\,\mathrm{e}^{+2\frac{i}{\hbar}\varepsilon(\mathbf{k})t} \\ a_1(t)(n'_x + in'_y)\,\mathrm{e}^{-2\frac{i}{\hbar}\varepsilon(\mathbf{k})t} \end{pmatrix}\right), \tag{7.101}$$

where n'_x and n'_y are the components of $\hat{\mathbf{n}}'_{\mathbf{k}}$ defined in Eq. (7.98).

Up to now, the transformations have been exact and the rotating wave approximation enters after expanding the cosine

$$\cos(\omega_D t) = 1/2(\mathrm{e}^{i\omega_D t} + \mathrm{e}^{-i\omega_D t}). \tag{7.102}$$

In the RWA, we consider the resonant case $\omega_D = 2\varepsilon(\mathbf{k})/2\hbar$ and we neglect every fast oscillating term in Eq. (7.101), which is proportional to $\mathrm{e}^{\pm i\left(2\frac{\varepsilon(\mathbf{k})}{\hbar}+\omega_D\right)t}$ or $\mathrm{e}^{\pm i\omega_D t}$, because they are supposed to cancel on physically relevant time scales. The only non-neglected, slowly oscillating terms are those which are in-resonance, i.e.

$\mathrm{e}^{\pm i\left(2\frac{\varepsilon(\mathbf{k})}{\hbar}-\omega_D\right)t}$, and thus, Eq. (7.101) simplifies to

$$i\dot{a}_1 = \frac{a_2}{2}\frac{\tilde{M}}{\hbar}(n_x' - in_y')\,\mathrm{e}^{+\frac{i}{\hbar}\Delta t}, \tag{7.103}$$

$$i\dot{a}_2 = \frac{a_1}{2}\frac{\tilde{M}}{\hbar}(n_x' + in_y')\,\mathrm{e}^{-\frac{i}{\hbar}\Delta t}, \tag{7.104}$$

with $\Delta = 2\varepsilon/\hbar - \omega_D$. Note that this approximation is in general less accurate than the one used by Rusin in Zawadzki [140], since in their considered case no terms with frequency ω_D have to be neglected but only neglect terms with frequency $(\omega_D + 2\varepsilon(\mathbf{k})/\hbar)$ which are of higher frequency than ω_D.

Next, we decouple the coupled set of differential equations in Eqs. (7.103) and (7.104), e.g. by taking the derivative of one of them a second time and insert the other one:

$$\ddot{a}_1 = +i\Delta\,\dot{a}_1 - \frac{\tilde{M}^2}{4\hbar^2}n_{xy}^2 a_1, \tag{7.105}$$

$$\ddot{a}_2 = -i\Delta\,\dot{a}_2 - \frac{\tilde{M}^2}{4\hbar^2}n_{xy}^2 a_2, \tag{7.106}$$

where we defined

$$n_{xy}^2 := n_x^2 + n_y^2 = (n_x')^2 + (n_y')^2 = \hbar^2 v_F^2 k^2/(M_0^2 + \hbar^2 v_F^2 k^2) = \kappa^2/(1+\kappa^2). \tag{7.107}$$

Since Eqs. (7.105) and (7.106) resemble the differential equation for a harmonic oscillator, we choose the ansatz

$$a_i(t) \sim \mathrm{e}^{i\Omega_i^{\pm}t} \tag{7.108}$$

to find the two linearly independent solutions of both Eq. (7.105) and Eq. (7.106). The resulting frequencies are

$$\Omega_1^{\pm} = \frac{1}{2}\left(\Delta \pm \omega_R\right), \tag{7.109}$$

$$\Omega_2^{\pm} = \frac{1}{2}\left(-\Delta \pm \omega_R\right), \tag{7.110}$$

with the Rabi-like frequency defined as

$$\omega_R = \sqrt{\Delta^2 + n_{xy}^2\tilde{M}^2/\hbar^2}. \tag{7.111}$$

Using a linear superposition of the independent solutions of $a_i(t)$ and insert them into Eq. (7.100), the time evolution of the wave function becomes

$$\psi_{\mathbf{k}}^{\mathrm{RWA}}(t) = \begin{pmatrix} A_+\mathrm{e}^{-i\frac{\omega_D+\omega_R}{2}t} + A_-\mathrm{e}^{-i\frac{\omega_D-\omega_R}{2}t} \\ B_+\mathrm{e}^{i\frac{\omega_D+\omega_R}{2}t} + B_-\mathrm{e}^{i\frac{\omega_D-\omega_R}{2}t} \end{pmatrix}. \tag{7.112}$$

Note that the amplitudes $A_\pm$ and $B_\pm$ depend on the considered $\mathbf{k}$-mode. Since the amplitudes $B_\pm$ are directly related to $A_\pm$ via the coupled differential equations (7.105) and (7.106),

$$B_\pm = A_\pm\frac{\hbar\sqrt{1+\kappa^2}}{\tilde{M}\kappa}\,\mathrm{e}^{i\gamma_{\mathbf{k}}}\,\left(\Delta \pm \omega_R\right), \tag{7.113}$$

the wave function of Eq. (7.112) becomes

$$\begin{aligned}\psi_{\mathbf{k}}^{\mathrm{RWA}}(t) &= \begin{pmatrix}\alpha_{\mathbf{k}}^{\mathrm{RWA}}(t)\\ \beta_{\mathbf{k}}^{\mathrm{RWA}}(t)\end{pmatrix}\\ &= \begin{pmatrix} A_+ \mathrm{e}^{-i\frac{\omega_D+\omega_R}{2}t} + A_- \mathrm{e}^{-i\frac{\omega_D-\omega_R}{2}t} \\ \frac{\hbar\sqrt{1+\kappa^2}}{\tilde{M}\kappa}\,\mathrm{e}^{i\theta_k}\,\left[A_+\,(\Delta+\omega_R)\,\mathrm{e}^{i\frac{\omega_D+\omega_R}{2}t} + A_-\,(\Delta-\omega_R)\,\mathrm{e}^{i\frac{\omega_D-\omega_R}{2}t}\right]\end{pmatrix},\end{aligned} \tag{7.114}$$

where the amplitudes $A_\pm$ are given by the initial condition.

Now that we know the time-evolution of a $\mathbf{k}$-mode, we can calculate the expectation value of the velocity, which will show some ZB. Let us start with the perpendicular velocity $\hat{v}_\perp = v_F\sigma_\perp$, which is by definition parallel to $\hat{\mathbf{m}}_{\mathbf{k}}$ (axis of the rotation), because it has to be in the x-y-plane and perpendicular to $\mathbf{k}$. Therefore, the $\sigma_\perp = \hat{\mathbf{m}}_{\mathbf{k}}\cdot\boldsymbol{\sigma}$ and the transformation S_{RWA} keeps $\sigma_\perp$ unchanged: $S_{\mathrm{RWA}}\sigma_\perp S_{\mathrm{RWA}}^\dagger = \sigma_\perp$ for geometrical reasons (compare Fig. 7.6), so that

$$\langle\psi \mid \sigma_\perp \mid \psi\rangle = \langle\psi_{\mathrm{RWA}} \mid \sigma_\perp \mid \psi_{\mathrm{RWA}}\rangle. \tag{7.115}$$

Without loss of generality, we can assume that $\mathbf{k} = (k,0)^T$, i.e. $\gamma_{\mathbf{k}} = 0$, and therefore $\sigma_\perp = \sigma_y$, up to a non-relevant sign factor, yielding

$$\langle\hat{v}_\perp^{\mathbf{k}}\rangle = v_F\langle\psi_{\mathbf{k}}^{\mathrm{RWA}} \mid \sigma_y \mid \psi_{\mathbf{k}}^{\mathrm{RWA}}\rangle = v_F 2\mathrm{Im}\left\{(\alpha_{\mathbf{k}}^{\mathrm{RWA}})^*\beta_{\mathbf{k}}^{\mathrm{RWA}}\right\}. \tag{7.116}$$

The result of the product $(\alpha_{\mathbf{k}}^{\mathrm{RWA}})^*\beta_{\mathbf{k}}^{\mathrm{RWA}}$ is

$$\begin{aligned}(\alpha_{\mathbf{k}}^{\mathrm{RWA}})^*\beta_{\mathbf{k}}^{\mathrm{RWA}} = \frac{\hbar\sqrt{1+\kappa^2}}{\tilde{M}\kappa}\Big\{&|A_+|^2(\Delta+\omega_R)\mathrm{e}^{i(\omega_D+\omega_R)t} + \\ &+ |A_-|^2(\Delta-\omega_R)\mathrm{e}^{i(\omega_D-\omega_R)t} + 2\Delta\,\mathrm{Re}\left(A_+^*A_-\mathrm{e}^{i\omega_D t}\right) + 2i\omega_R\,\mathrm{Im}\left(A_-^*A_+\mathrm{e}^{-i\omega_D t}\right)\Big\},\end{aligned} \tag{7.117}$$

which will be also needed later for the parallel ZB. With Eq. (7.117), the perpendicular ZB of a given $\mathbf{k}$-mode becomes

$$\begin{aligned}\langle\hat{v}_\perp^{\mathbf{k}}\rangle =& v_F\frac{\hbar\sqrt{1+\kappa^2}}{\tilde{M}\kappa}\Big\{|A_+|^2(\Delta+\omega_R)\sin\left((\omega_D+\omega_R)t\right) \\ &+ |A_-|^2(\Delta-\omega_R)\sin\left((\omega_D-\omega_R)t\right) + 2\omega_R\,\mathrm{Im}\left(A_-^*A_+\mathrm{e}^{-i\omega_D t}\right)\Big\}.\end{aligned} \tag{7.118}$$

The main result is that the perpendicular ZB oscillates with three different frequencies: ω_D, $\omega_D \pm \omega_R$, which is different to Rusin and Zawadzki [140], who obtained only the frequencies $\omega_D \pm \omega_R$ in the case of a time-dependent vector potential. We stress this point, because the mode oscillating with the driving frequency ω_D will become important in the long-time behavior of the ZB in Sec. 7.4.5. Although not shown here, the static case can be derived from Eq. (7.118), e.g. by taking the limit $\tilde{M} \to 0$.

Similarly, the parallel ZB $\langle\hat{v}_\parallel^{\mathbf{k}}\rangle$ can be obtained

$$\langle\psi_{\mathbf{k}} \mid \hat{v}_\parallel^{\mathbf{k}} \mid \psi_{\mathbf{k}}\rangle = v_F\langle\psi_{\mathbf{k}}^{\mathrm{RWA}} \mid S_{\mathrm{RWA}}\sigma_\parallel S_{\mathrm{RWA}}^\dagger \mid \psi_{\mathbf{k}}^{\mathrm{RWA}}\rangle. \tag{7.119}$$

Here, an important difference is that the according Pauli matrix in $\hat{v}_\parallel^{\mathbf{k}} = v_F \boldsymbol{\sigma} \cdot \mathbf{k}/|\mathbf{k}|$ change due to the transformation S_{RWA} and get an out-of-plane component, which yields due to geometrical considerations (compare Fig. 7.6)

$$S_{\mathrm{RWA}} \sigma_\parallel S_{\mathrm{RWA}}^\dagger = \sigma_\parallel \cos\vartheta_{\mathbf{k}} + \sigma_z \sin\vartheta_{\mathbf{k}} = \frac{\sigma_\parallel}{\sqrt{1+\kappa^2}} + \frac{\sigma_z\,\kappa}{\sqrt{1+\kappa^2}}. \tag{7.120}$$

Using again, without loss of generality, $\mathbf{k} = (k,0)^T$, i.e. $\sigma_\parallel = \sigma_x$, the individual terms are

$$\langle \psi_{\mathbf{k}}^{\mathrm{RWA}} \mid \sigma_x \mid \psi_{\mathbf{k}}^{\mathrm{RWA}} \rangle = 2\mathrm{Re}\left\{ (\alpha_{\mathbf{k}}^{\mathrm{RWA}})^* \beta_{\mathbf{k}}^{\mathrm{RWA}} \right\}, \tag{7.121}$$

$$\langle \psi_{\mathbf{k}}^{\mathrm{RWA}} \mid \sigma_z \mid \psi_{\mathbf{k}}^{\mathrm{RWA}} \rangle = |\alpha_{\mathbf{k}}^{\mathrm{RWA}}|^2 - |\beta_{\mathbf{k}}^{\mathrm{RWA}}|^2, \tag{7.122}$$

which yields after trivial calculations

$$\begin{aligned}\langle \hat{v}_\parallel^{\mathbf{k}} \rangle =& \frac{\hbar v_F}{\tilde{M}\kappa}\Big\{ |A_+|^2(\Delta+\omega_R)\cos\left((\omega_D+\omega_R)t\right) + |A_-|^2(\Delta-\omega_R)\cos\left((\omega_D-\omega_R)t\right) \\ &+ 2\Delta\,\mathrm{Re}\left(A_+^* A_- \mathrm{e}^{i\omega_D t}\right)\Big\} + 4v_F\cos(\omega_R t)\mathrm{Re}\left\{A_+^* A_-\right\} + \mathrm{const.}\end{aligned} \tag{7.123}$$

Thus, the parallel ZB oscillates even with four different frequencies: $\omega_D, \omega_D \pm \omega_R$ (from $\langle\sigma_x\rangle$) and ω_R (from $\langle\sigma_z\rangle$). Compared again to Rusin and Zawadzki [140], they only obtain a single parallel mode with frequency ω_R, which is very likely due to the fact that they only consider pristine graphene, where no parallel ZB is expected in the static case. Again, the mode with frequency ω_D found here will be important for the long-time behavior.

To conclude this subsection, let us compare the found results with the ones obtained by perturbation theory. Although they are in a similar regime (small $\tilde{M}$ and $\omega_D \simeq \Omega_{\mathbf{k}}^{\mathrm{ZB}}$, because else, there is no ZB in perturbation theory), RWA is richer in the sense that it predicts multimode ZB both perpendicular and parallel to the initial propagation direction, with three, respectively four, frequencies. The analytical results of this section will be tested by simulation in Sec. 7.4.4.

7.4.3 High driving frequency

In this subsection, we want to investigate the ZB for very high driving frequencies ω_D, i.e. $\hbar\omega_D \gg \tilde{M}, M_0$, to extend the region where we can give analytical estimates. The derivation is similar to RWA with a different initial transformation, such that the time-dependent part of the Hamiltonian is diagonal and follow again the strategy of Ref. [140]. In our case, it is already diagonal and thus, the transformation in pseudospin space is not needed. Otherwise the strategy is the same, which is why we shorten the derivation considerably. The eager reader should be still able to recover the results with the help of Subsec. 7.4.2.

We start from the same Hamiltonian of Eq. (7.93) as in the previous subsection. This time, we use an ansatz to cancel the terms proportional to σ_z in the Schrödinger equation

$$\psi_{\mathbf{k}}(t) = \begin{pmatrix} b_1(t)\mathrm{e}^{-\frac{i}{\hbar}\int_0^t \mathrm{d}t' M(t') - i\omega_0 t} \\ b_2(t)\mathrm{e}^{+\frac{i}{\hbar}\int_0^t \mathrm{d}t' M(t') + i\omega_0 t} \end{pmatrix}, \tag{7.124}$$

with $\omega_0 = M_0/\hbar$, which results again in a set of coupled differential equations for the coefficients b_i

$$i\dot{b}_1 = v_F(k_x - ik_y)\, b_2\, \mathrm{e}^{-2i\frac{\tilde{M}}{\hbar\omega_D}\sin(\omega_D t)-2i\omega_0 t}, \tag{7.125}$$

$$i\dot{b}_2 = v_F(k_x + ik_y)\, b_1\, \mathrm{e}^{+2i\frac{\tilde{M}}{\hbar\omega_D}\sin(\omega_D t)+2i\omega_0 t}. \tag{7.126}$$

The approximation of the HDF is to set $\mathrm{e}^{\pm 2i\frac{\tilde{M}}{\hbar\omega_D}\sin(\omega_D t)} \approx 1$, due to the fact that $\hbar\omega_D \gg \tilde{M}$. This estimate is applied to solve the set of differential equations analytically. Below, higher orders in $\frac{\tilde{M}}{\hbar\omega_D}$ will be used, which is a small inconsistency for the sake of getting an analytical solution at all. Decoupling Eqs. (7.125) and (7.126) the same way as for the RWA, the above mentioned approximation yields

$$\ddot{b}_1 = \quad i2\omega_0\dot{b}_1 - v_F^2 k^2 b_1, \tag{7.127}$$

$$\ddot{b}_2 = -i2\omega_0\dot{b}_2 - v_F^2 k^2 b_2, \tag{7.128}$$

which again resembles the differential equation of a harmonic oscillator. To find the linear independent solutions for both Eqs. (7.127) and (7.128), we use the ansatz $b_i(t) \sim \mathrm{e}^{i\Omega_i t}$, which yields the frequencies

$$\Omega_1^{\pm} = \omega_0\left(\quad 1 \pm \sqrt{1+\kappa^2}\right) = \quad \omega_0 \pm \frac{\Omega_{\mathbf{k}}^{\mathrm{ZB}}}{2}, \tag{7.129}$$

$$\Omega_2^{\pm} = \omega_0\left(-1 \pm \sqrt{1+\kappa^2}\right) = -\omega_0 \pm \frac{\Omega_{\mathbf{k}}^{\mathrm{ZB}}}{2}. \tag{7.130}$$

Just as in the RWA section, the amplitudes which are related to the frequencies $\Omega_1^{\pm}$ and $\Omega_2^{\pm}$, depend on each other due to the set of coupled differential equations in Eqs. (7.125) and (7.126). The time evolution of a $\mathbf{k}$-mode thus becomes

$$\begin{aligned}\psi_{\mathbf{k}}^{\mathrm{HDF}}(t) = \begin{pmatrix}\alpha_{\mathbf{k}}^{\mathrm{HDF}}\\ \beta_{\mathbf{k}}^{\mathrm{HDF}}\end{pmatrix} &= \begin{pmatrix}\left[D_+\mathrm{e}^{i\Omega_{\mathbf{k}}^{\mathrm{ZB}}t/2} + D_-\mathrm{e}^{-i\Omega_{\mathbf{k}}^{\mathrm{ZB}}t/2}\right]\mathrm{e}^{-i\frac{\tilde{M}}{\hbar\omega_D}\sin(\omega_D t)}\\ \left[F_+\mathrm{e}^{i\Omega_{\mathbf{k}}^{\mathrm{ZB}}t/2} + F_-\mathrm{e}^{-i\Omega_{\mathbf{k}}^{\mathrm{ZB}}t/2}\right]\mathrm{e}^{+i\frac{\tilde{M}}{\hbar\omega_D}\sin(\omega_D t)}\end{pmatrix}\\ &= \begin{pmatrix}\left[D_+\mathrm{e}^{i\frac{\Omega_{\mathbf{k}}^{\mathrm{ZB}}}{2}t} + D_-\mathrm{e}^{-i\frac{\Omega_{\mathbf{k}}^{\mathrm{ZB}}}{2}t}\right]\mathrm{e}^{-i\frac{\tilde{M}}{\hbar\omega_D}\sin(\omega_D t)}\\ -\frac{\mathrm{e}^{i\gamma_{\mathbf{k}}}}{2v_F k}\left[D_+\left(2\omega_0 + \Omega_{\mathbf{k}}^{\mathrm{ZB}}\right)\mathrm{e}^{i\frac{\Omega_{\mathbf{k}}^{\mathrm{ZB}}}{2}t} + D_-\left(2\omega_0 - \Omega_{\mathbf{k}}^{\mathrm{ZB}}\right)\mathrm{e}^{-i\frac{\Omega_{\mathbf{k}}^{\mathrm{ZB}}}{2}t}\right]\mathrm{e}^{+i\frac{\tilde{M}}{\hbar\omega_D}\sin(\omega_D t)}\end{pmatrix},\end{aligned} \tag{7.131}$$

where $D_\pm$ are the amplitudes of the harmonic ansatz and correspond to the $A_\pm$ in the previous subsection about RWA. Thus, they can be obtained by the initial conditions, i.e. the initial pseudospin structure of the considered mode.

To calculate explicitly the perpendicular and parallel ZB, let us assume without loss of generality that $\mathbf{k} = (k, 0)^T$, i.e. $\gamma_{\mathbf{k}} = 0$, and thus

$$\langle v_\perp^{\mathbf{k}}\rangle = v_F\langle\psi_{\mathbf{k}}^{\mathrm{HDF}} \mid \sigma_y \mid \psi_{\mathbf{k}}^{\mathrm{HDF}}\rangle = 2v_F\mathrm{Im}\left\{(\alpha_{\mathbf{k}}^{\mathrm{HDF}})^*\beta_{\mathbf{k}}^{\mathrm{HDF}}\right\}, \tag{7.132}$$

$$\langle v_\parallel^{\mathbf{k}}\rangle = v_F\langle\psi_{\mathbf{k}}^{\mathrm{HDF}} \mid \sigma_x \mid \psi_{\mathbf{k}}^{\mathrm{HDF}}\rangle = 2v_F\mathrm{Re}\left\{(\alpha_{\mathbf{k}}^{\mathrm{HDF}})^*\beta_{\mathbf{k}}^{\mathrm{HDF}}\right\}. \tag{7.133}$$

The product $(\alpha_{\mathbf{k}}^{\mathrm{HDF}})^*\beta_{\mathbf{k}}^{\mathrm{HDF}}$ yields

$$(\alpha_{\mathbf{k}}^{\mathrm{HDF}})^* \beta_{\mathbf{k}}^{\mathrm{HDF}} = -\frac{\mathrm{e}^{+i\frac{\tilde{M}}{\hbar\omega_D}\sin(\omega_D t)}}{2v_F k}\Bigg(|B_+|^2(2\omega_0 + \Omega_{\mathbf{k}}^{\mathrm{ZB}}) + |B_-|^2(2\omega_0 - \Omega_{\mathbf{k}}^{\mathrm{ZB}}) + 4\omega_0 \mathrm{Re}\left\{B_+ B_-^* \mathrm{e}^{i\Omega_{\mathbf{k}}^{\mathrm{ZB}} t}\right\} + \Omega_{\mathbf{k}}^{\mathrm{ZB}} 2i\,\mathrm{Im}\left\{B_+ B_-^* \mathrm{e}^{i\Omega_{\mathbf{k}}^{\mathrm{ZB}} t}\right\}\Bigg). \quad (7.134)$$

By expanding $\mathrm{e}^{+i\frac{\tilde{M}}{\hbar\omega_D}\sin(\omega_D t)} \approx 1 + i\frac{\tilde{M}}{\hbar\omega_D}\sin(\omega_D t)$, we get the following expectation value of the velocity operator perpendicular to the propagation direction

$$\langle v_\perp^{\mathbf{k}} \rangle = -\frac{1}{k}\left(\mathrm{const} + 2\Omega_{\mathbf{k}}^{\mathrm{ZB}} \mathrm{Im}\left\{B_+ B_-^* \mathrm{e}^{i\Omega_{\mathbf{k}}^{\mathrm{ZB}} t}\right\}\right) - \frac{4\,\tilde{M}}{k\hbar\omega_D}\omega_0\,\sin(\omega_D t)\,\mathrm{Re}\left\{B_+ B_-^* \mathrm{e}^{i\Omega_{\mathbf{k}}^{\mathrm{ZB}} t}\right\}, \quad (7.135)$$

and for the parallel direction

$$\langle v_\parallel^{\mathbf{k}} \rangle = -\frac{1}{k}\left(\mathrm{const} + 4\omega_0 \mathrm{Re}\left\{B_+ B_-^* \mathrm{e}^{i\Omega_{\mathbf{k}}^{\mathrm{ZB}} t}\right\}\right) + \frac{2\,\tilde{M}}{k\hbar\omega_D}\Omega_{\mathbf{k}}^{\mathrm{ZB}}\,\sin(\omega_D t)\,\mathrm{Im}\left\{B_+ B_-^* \mathrm{e}^{i\Omega_{\mathbf{k}}^{\mathrm{ZB}} t}\right\}. \quad (7.136)$$

In both cases, one frequency of the ZB terms is $\Omega_{\mathbf{k}}^{\mathrm{ZB}}$ as in static case. Moreover, there are suppressed oscillations of the order $\mathcal{O}(\tilde{M}/(\hbar\omega_D))$ with frequencies $\omega_D \pm \Omega_{\mathbf{k}}^{\mathrm{ZB}}$. Higher orders in the expansion of $\mathrm{e}^{+i\frac{\tilde{M}}{\hbar\omega_D}\sin(\omega_D t)}$ will lead to additional frequencies $n\omega_D \pm \Omega_{\mathbf{k}}^{\mathrm{ZB}}$, because of

$$\sin^n(x) = \sum_{l=0}^{n} \alpha_{l,n} \sin(lx), \quad (7.137)$$

with $\alpha_{n,n} \neq 0$. However, these terms are again suppressed accordingly to n-th order in $\tilde{M}/(\hbar\omega_D)$. The reason for this suppression and the survival of only the static mode ($\Omega_{\mathbf{k}}^{\mathrm{ZB}}$) is that for very fast external perturbation, the electrons cannot follow anymore and behave as if there was no extra field and only the static frequency survives.

With this subsection, we finish the analytical calculations for the driven ZB in graphene by a time-dependent mass potential. In the next subsections, we will study numerically the behavior of the driven ZB and discuss it in terms of the found analytical approximations.

7.4.4 Numerical results for the zitterbewegung frequencies

In this subsection, we want to compare the analytical results of RWA in Subsec. 7.4.2 and HDF in Subsec. 7.4.3 with the numerical data obtained by TQT. Thereto, a Gaussian wave packet with the parameters $\hbar v_F k_0 = 0.4 M_0$ and $\mathbf{k}$-space width $\Delta k = k_0/10$ is propagated in presence of the time-dependent mass potential. The expectation value of the velocity is obtained by calculating the average position of the wave packet at any discrete point in time and approximating its time-derivative by the difference quotient. The static ZB frequency for the choice of parameters yields $\Omega_{\mathbf{k}_0}^{\mathrm{ZB}} \approx 2.15 M_0/\hbar$.

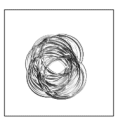

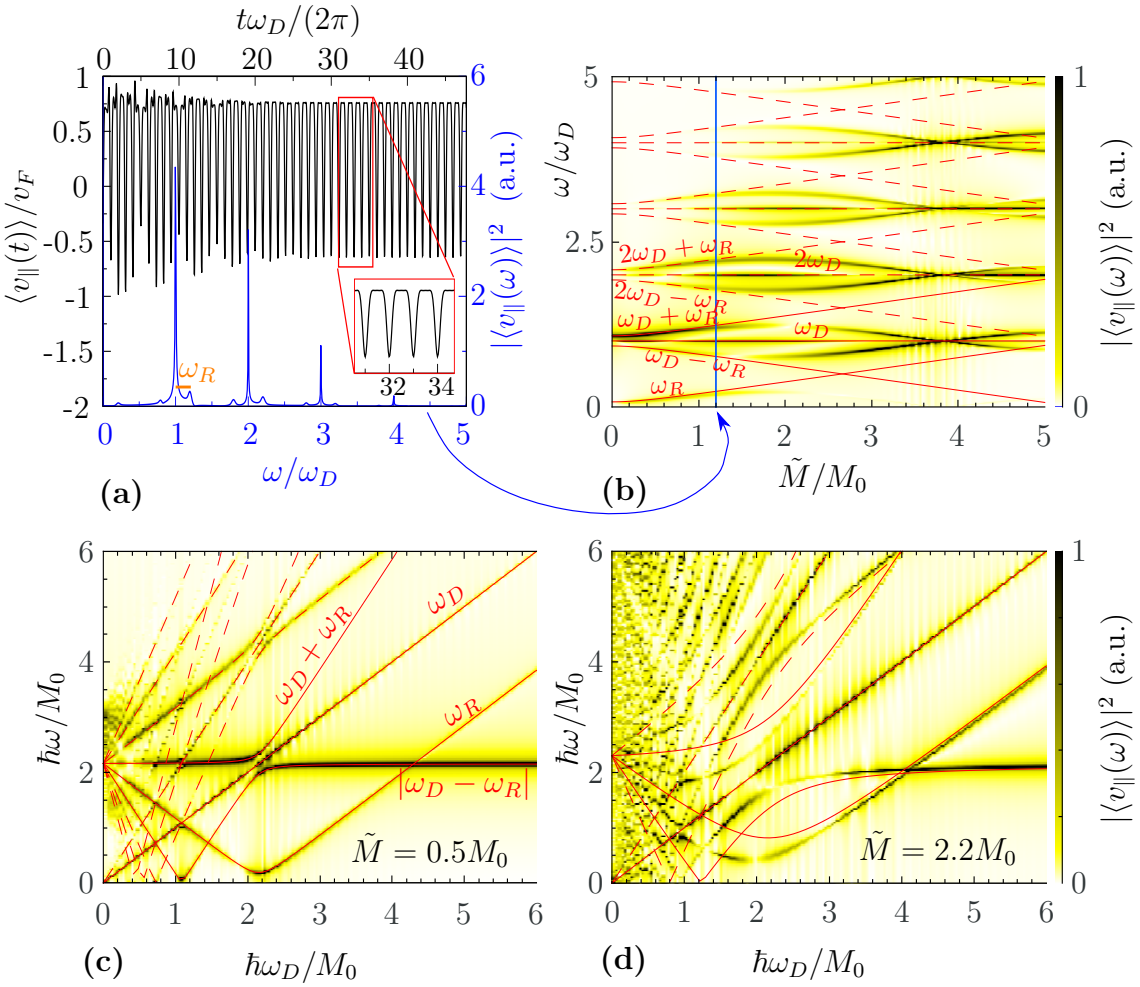

Figure 7.7: Extracting the ZB frequencies via a Fourier transformation of $\langle\hat{v}_\parallel(t)\rangle$ and comparing them to analytical results of the RWA in Eq. (7.119). (a) The parallel ZB is shown both, as a function of time (black) and its Fourier transform (blue), i.e. as function of ω, for $\omega_D = 2M_0/\hbar$ and $\tilde{M} = 1.2M_0$. The inset shows a close-up for larger times. Peaks appear in the Fourier transform at multiple integers of ω_D with satellite peaks with a distance of ω_R (orange line at the first peak) away from the major peaks. (b) The Fourier transformation of $\langle v_\parallel\rangle$ is shown as a function of the amplitude $\tilde{M}$ of the time-dependent mass term. The blue indicated line cut is the function shown in panel (a) (illustrated by the blue arrow). The expected frequencies from RWA, ω_D, $\omega_D \pm \omega_R$ and ω_R are shown (red, solid), as well as higher order terms in ω_D (red, dashed). For smaller $\tilde{M}$, up to $\tilde{M} \approx 1.5M_0$ the RWA results are recovered, but for larger $\tilde{M}$, the RWA is not justified anymore. Furthermore, the dependence of the parallel ZB on the driving frequency ω_D is shown for fixed (c) $\tilde{M} = 0.5M_0$ and (d) $\tilde{M} = 2.2M_0$. In (c) analytical results and simulations match very well, whereas in (d) deviations are visible, which vanish for $\hbar\omega_D \gg M_0$. In all plots, the mean energy of the wave packet is $E_{\mathbf{k}_0} = 0.4M_0$, such that the static ZB is $\Omega^{\mathrm{ZB}}_{\mathbf{k}_0} \approx 2.15M_0/\hbar$.

In Fig. 7.7(a), the simulation data of $\langle v_\parallel \rangle$ is shown for rather high driving amplitude $\tilde{M} = 1.2M_0$ at $\omega_D = 2M_0/\hbar$ as a function of time (black).[1] In the beginning, rather unregular behavior is visible which transitions after some time into a nicely periodic oscillation. This is similar to first order perturbation theory of Sec. 7.4.1, where initially present modes decay and only certain modes survive. The difference here is that the driving amplitude $\tilde{M}$ is here much higher, which results not in oscillation with a single frequency, but with many frequencies (as can be seen in the close-up, which is clearly not a single cosine). The reason for this behavior is explained in the next subsection.

Moreover, the Fourier transform of $\langle v_\parallel(t) \rangle$ is shown in Fig. 7.7(a) (blue) to be better able to compare the frequencies of the driven ZB. Since the timeline is discretized, we use numerically the fast Fourier transform (FFT). In panel (a), we can see that $\langle v_\parallel \rangle$ is highly peaked at integer multiples n of ω_D and smaller satellite peaks appear at $n\omega_D \pm \omega_R$, close to the major peaks. To have a better overview over the parameter dependencies, the Fourier transform of the velocity will be shown in density plots, where one vertical line corresponds to one simulation. The amplitude of the ZB is color coded and on the remaining axis, either the driving amplitude $\tilde{M}$ is varied (Fig. 7.7(b)) or the driving frequency ω_D (panels (c) and (d)).

There, the fixed parameter is $\omega_D = 2M_0/\hbar$ and the amplitude $\tilde{M}$ of the time-dependent mass term varies. the vertical blue line corresponds to the simulation shown in panel 7.7(a), as indicated by the blue arrow. The ZB frequencies expected from RWA are all present: ω_D, $\omega_D \pm \omega_R$ and ω_R (lowest four red lines). But additionally, higher frequencies emerge, which can be obtained by adding integer multiples of ω_D to the lower frequencies. Heuristically, this can be explained with the help of perturbation theory: every higher order adds another $\pm\omega_D$ to the existing frequencies, because of the factor $H_1(t) \sim \sin \omega_D t$ appears n times (compare Eq. (D.15) in App. D). The fact that higher frequencies are occupied more and more for higher $\tilde{M}$ also suggests this explanation by perturbation theory. Another hint for the emergence of frequencies that are $n\omega_D$ times higher than expected has been given in the end of the HDF section, where modes of frequency $n\omega_D + \Omega_{\mathbf{k}}^{\mathrm{ZB}}$ are more and more suppressed for higher ω_D. Also in panel 7.7(b), the modes are suppressed for higher ω_D, but the difference is that the simulated modes are not added to $\Omega_{\mathbf{k}}^{\mathrm{ZB}}$ but to the expected modes from RWA, at least for small $\tilde{M}$. However, it is not surprising that the HDF does not yield the right frequencies in a regime, where it is not valid.

For higher $\tilde{M} \gtrsim 1.5M_0$, strong deviations between RWA and simulation occur. Again, this is expected, since RWA is only valid for small $\tilde{M}$ (compared to the other energy scales in the system, e.g. M_0, $E_{\mathbf{k}_0}$). There are some qualitative observation in 7.7(b) for high $\tilde{M}$, which we cannot explain analytically. At first glance the deviations from RWA look somehow like an avoided crossing with a (more or less) periodic structure (see also Fig. 7.8(e)), since for all modes, the horizontal lines $\omega = n\omega_D$ are crossed again at $\tilde{M} \approx 3.8M_0$. However, the fact that far away from the crossings, the analytical structure is not recovered, contradicts an usual anti-crossing picture. On the other hand, the modes with frequency $n\omega_D$ are not altered themselves. Since we will find later that they are the most relevant ones for the

[1] Here, $\langle v_\parallel \rangle$ is discussed exemplarily, but similar results are obtained for $\langle v_\perp \rangle$. For simulation data of $\langle v_\perp \rangle$, see Fig. 7.8(c) and (g).

long-time behavior, this is an important result for us.

In panel (c), the parallel ZB measured by the velocity is shown as a function of ω_D and fixed $\tilde{M} = 0.5M_0$. Although $\tilde{M}$ not really small compared to M_0, the frequencies obtained by RWA (plus integer multiples of ω_D) match the numerical ZB frequencies for large enough ω_D. For $\hbar\omega_D \ll M_0$, a lot of frequencies appear such that it becomes difficult to distinguish between individual modes. In the opposed limit, the only mode which does not vanish for $\hbar\omega_D \gg M_0$ is the one with the frequency of the static ZB: $(\omega_R - \omega_D) \xrightarrow{\omega_D \to \infty} \Omega^{\mathrm{ZB}}_{\mathbf{k}_0}$, as expected by HDF in Subsec. 7.4.3.

Panel (d) shows the same as (c) but with higher $\tilde{M} = 2.2M_0$, such that the RWA is not justified anymore and deviations appear. The qualitative observation is that the frequency of the ZB modes are by tendency shifted to smaller ω_D and/or to smaller (higher) ω for left(right)-curved modes in the diagram, but we do not have an explanation for this behavior. On the other hand, for high ω_D, the ZB frequencies obtained in the HDF approximation are recovered. These are $\Omega^{\mathrm{ZB}}_{\mathbf{k}_0}$ and $\Omega^{\mathrm{ZB}}_{\mathbf{k}_0} \pm \omega_D$, where only the strength of the $\Omega^{\mathrm{ZB}}_{\mathbf{k}_0}$ does not diminish for high ω_D. Although not yet very well visible in the shown regime, the amplitude of the mode $\Omega^{\mathrm{ZB}}_{\mathbf{k}_0} \pm \omega_D$ indeed declines for larger and larger ω_D.

For the dependency of the ZB frequencies for a wider parameter regime, see the panels on the left-hand side of Fig. 7.8 (the right-hand side panels will be discussed in the next subsection). There, the panels show four additional plots of the emerging ZB frequencies, both as a function of $\tilde{M}$ and ω_D, both for the parallel and perpendicular ZB, and both for $M_0 \neq 0$ and $M_0 = 0$. The wave packet is the same as before in Fig. 7.7. The normalization factor $\tilde{\omega} = 2.5 v_F k_0$, is introduced because of the plots where $M_0 = 0$, and thus M_0 cannot be used as normalization. For comparison, $\tilde{\omega}$ is defined such that in the cases where $M_0 \neq 0$, $\tilde{\omega} = M_0/\hbar$, since $\hbar v_F k_0 / M_0 = 0.4$. Qualitatively, the results are similar to the in-depth discussed cases of Fig. 7.7: for small $\tilde{M}$ and not too small ω_D, RWA yields the correct frequencies of the multimode ZB. However, also "higher harmonics" in ω_D, i.e. $\cdots + n\omega_D$ frequency modes are present.

In general, expected modes from RWA (plus integer multiples of ω_D), which are present in the simulations are visualized by red-dashed lines. Missing modes in the simulations, regardless of whether expectedly or unexpectedly missing, are indicated by dotted violet lines. The unexpected missing modes appear in the cases of $M_0 = 0$ (panels 7.8(c) and (e)), where every second ω_D-mode is missing – for $v_\parallel$ only the even modes, for $v_\perp$ only the odd modes are present, which we cannot explain why. The only expected missing mode is the one with frequency ω_R in $\langle v_\perp \rangle$ (see 7.8(c) and (g)), which is not present in RWA (see Eq. (7.118)).

After this in-depth discussion of the emerging multimode ZB in graphene for a driving mass potential, we want to turn in the next subsection to the (for us) more important question of whether there exist modes which survive for a long time (compare Fig. 7.7(a)), similar to Ref. [139] but now in graphene instead of a two-dimensional electron gas with driven Rashba spin-orbit coupling.

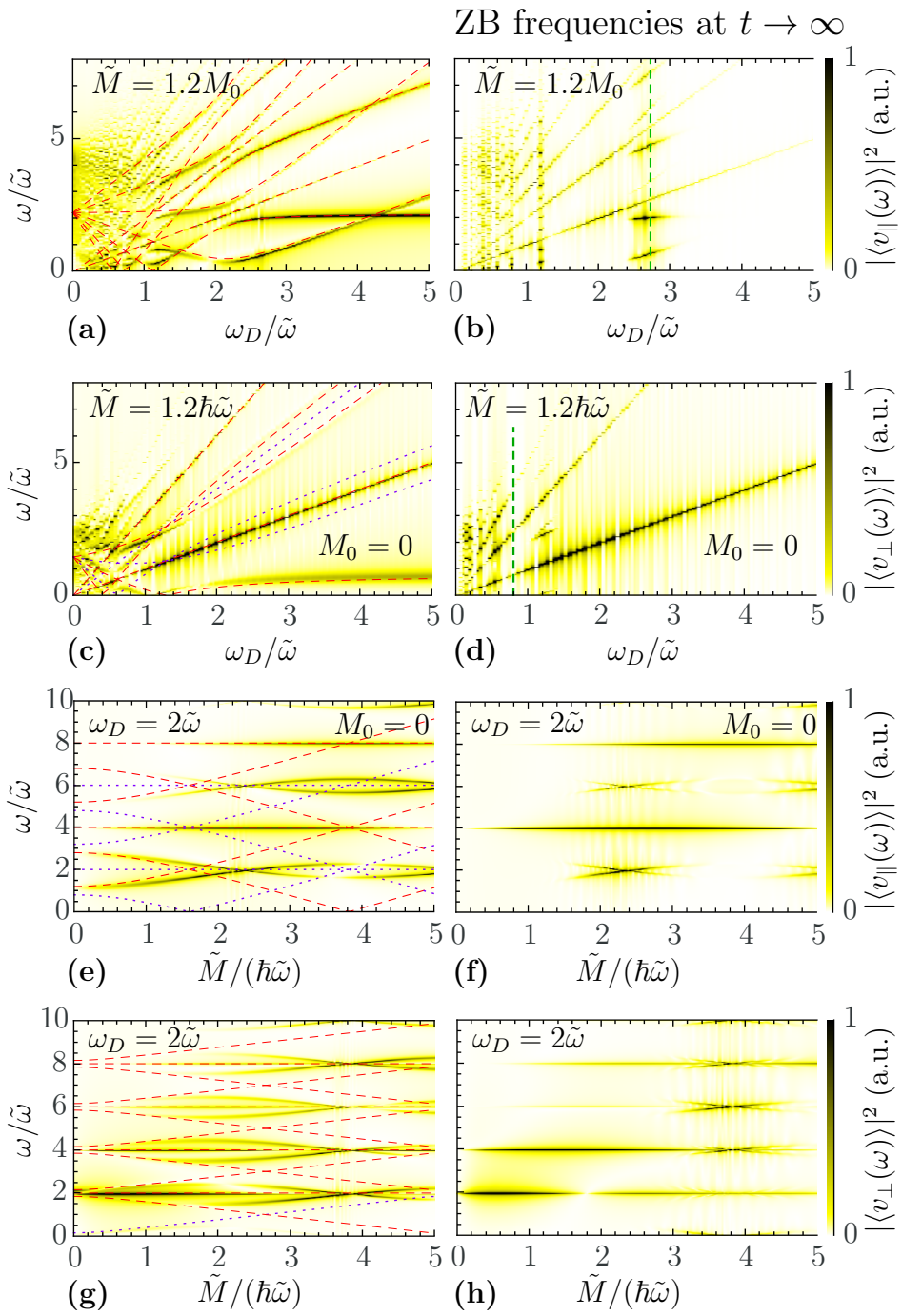

Figure 7.8: Infinitely long surviving modes of the ZB. The left column shows plots of all appearing ZB modes whereas the panels on the right side show the modes which survive a long time (as defined in the text). The emerging modes of the perpendicular and parallel ZB $\langle v_\perp(\omega)\rangle$ and $\langle v_\parallel(\omega)\rangle$ obtained by simulation are shown as a function either of the parameter ω_D or $\tilde{M}$. Furthermore, the gapless case $M_0 = 0$ is shown in panels (c), (d), (e) and (f). In the other cases, $M_0 = \hbar\tilde{\omega}$, such that $\hbar v_F k_0/M_0 = 0.4$. Analytically expected modes from RWA (red, dashed) as well as "missing" modes (dotted violet) are indicated in the left panels. In general, the surviving modes are the ones not depending on $\mathbf{k}$, e.g. multiples of ω_D or where $\partial\omega_R/\partial k = 0$ (indicated by the green dashed lines in (b) and (d)), which are thus weakly $\mathbf{k}$-dependent.

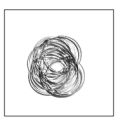

7.4.5 Long-time behavior of the zitterbewegung

In this subsection, we want to study the long-time behavior of the ZB in (gapped) graphene driven by a harmonically oscillating mass gap. We hope to find infinitely long surviving modes, since they are probably easiest to detect experimentally.First order perturbation theory of Subsec. 7.4.1 predicts one infinitely-long lived mode with frequency ω_D, however we have also seen that for larger $\tilde{M}$, deviations for the first order appear in the simulations. Thus, we want to study numerically what happens for larger perturbation $\tilde{M}$.

From the simulation data, the frequencies of the long-terms ZB can be obtained easily. Instead of starting the Fourier transformation at $t = 0$ to go from time to frequency space, we begin at a later time to avoid capturing the frequencies of the fast-decaying modes. Theoretically, we could use the analytical approximation for the static decay time T_2^* from Eq. (7.32). However, since the amplitude of the decaying modes are still around 30%-40% at T_2^*, and because we consult TQT anyway, we can use directly its simulation data for the static decay times to choose an appropriate starting time of the Fourier transformation. Here, we choose a starting time, where the relative amplitude of the ZB in the time-*in*dependent setup has decreased to less than 5% in both $\langle v_\parallel \rangle$ and $\langle v_\perp \rangle$ (if both are present) and we denote this time by $t_{0.05} > 0$. Considering the plots of the static Subsec. 7.3.1 and 7.3.2, e.g. Fig. 7.2, we expect $t_{0.05} \approx 2T_2^*$.

In Fig. 7.8, the frequency spectrum of the ZB using a Fourier transformation starting from $t = 0$ (left panels) is compared to the Fourier transformation starting at $t_{0.05}$ (right panels), i.e. the long-term ZB, for several parameter combinations. The actual simulation is the same on both sides, but only the time changes, from which on the existent frequencies are obtained. The wave packet is again the same Gaussian as in the two preceding subsections. Since we deal with the case $M_0 = 0$, we cannot use the familiar normalization relative to M_0. Instead, we introduce the normalization $\tilde{\omega} = 2.5 v_F k_0$ as in Subsec. 7.4.4, which corresponds to $\hbar\tilde{\omega} = M_0$ in the cases with $M_0 \neq 0$.

The first thing to notice on the right-hand side panels of Fig. 7.8 is that some branches drop out completely, some remain unchanged and others survive only in small parameter regime. To be able to explain this, we remind the reader of the static sections, where we showed that the decay of the ZB is due to the different frequencies of the different **k**-modes in the wave packet and the consequential dephasing (compare Fig. 7.1). Vice versa, that means that ZB modes that are **k**-independent, are supposed to survive, since no dephasing happens.

Consulting the analytical approximations of RWA and HDF, we find that the only **k**-independent ZB mode has the frequency ω_D. Indeed in all plots, modes with frequencies that are (integer multiples) of ω_D are unchanged in the long-time limit for all shown cases. Theses are the only modes, which completely survive in the long-time case.

The fact that mostly integer multiples of ω_D survive might explain the strange shape of the timeline of the long lived ZB in Fig. 7.7(a) in the previous section, which suggests long-lived modes (see close-up) but with several frequencies. The strangely regular shape of the long-term oscillation might be due to the fact that mostly modes with multiple integers of ω_D survive, which corresponds to a discrete Fourier

transformation. A discrete Fourier transformations generates a periodic structure in the timeline, in our case with frequency ω_D, that is possibly strangely regular – for a periodic box for instance, it is $f(t) \propto \sum_{k=1}^{\infty} \sin((2k-1)\omega t)/(2k-1)$.

Coming back to Fig. 7.8, we see that from other modes, only some minor parts survive. These are the parts that are locally independent of $\mathbf{k}$, i.e. changing $\mathbf{k}$ a bit does not affect the frequencies of the ZB. Thus, the corresponding frequencies of the ZB need to have horizontal tangents as a function of $\mathbf{k}$. The only $\mathbf{k}$-dependent frequency obtained in RWA is ω_R (plus integer multiples of ω_D), which is why we want to find the positions where $\partial\omega_R/\partial k \stackrel{!}{=} 0$:

$$\frac{\partial \omega_R}{\partial k} = 0 \Leftrightarrow -M_0\omega_D + \Omega_{\mathbf{k}}^{\mathrm{ZB}} M_0 + \frac{\tilde{M}^2}{2\sqrt{1+\kappa^2}^3} = 0. \tag{7.138}$$

To use it in panels (b),(d) of Fig. 7.8, where the ZB is shown as a function of ω_D, we solve Eq. (7.138) for ω_D

$$\omega_D^{\mathrm{crit}} = \Omega_{\mathbf{k}}^{\mathrm{ZB}} \left(1 + \frac{\tilde{M}^2}{4M_0^2} \frac{1}{(1+\kappa^2)^2}\right), \tag{7.139}$$

which is indicated by green dashed line for the given wave packet in the according panels. Since any $\mathbf{k}$-dependence of the frequency of every mode is because of ω_R, every mode intersecting with the green line should survive. In panel (b), this is indeed the case. Note that not only the exact ω_D^{crit} survives, but an extended region (left and right of green line). Choosing longer and longer times, these regions are supposed to shrink more and more.

In panel (d) on the other hand, the green line does not fit at all. The reason is that since here ($M_0 = 0$) and thus the expected horizontal tangent is at $\omega_D^{\mathrm{crit}} = 0.8\tilde{\omega} = 2v_F k_0$, which is much smaller than in the case of panel (b), where $\omega_D^{\mathrm{crit}} \simeq 2.75\tilde{\omega}$. However, we know that for smaller ω_D, our analytical approximation do not match anymore (see Subsec. 7.4.4), which is why the expected green line is far away from the actual surviving modes at $\omega_D^{\mathrm{crit}} = 1.25\tilde{\omega}$. A similar feature occurs in panel (b) for smaller ω_D. There, additional surviving (i.e. $\mathbf{k}$-independent modes) pop up (e.g. $\omega_D = 1.2\tilde{\omega}$), which we cannot explain in our approximations.

The only other partly surviving modes can be seen in the $\tilde{M}$-dependency plots of panels (f) and (h). There, the modes with $\omega = n\omega_D$ survive, as discussed above, but also the other modes close to the crossings with the horizontal lines $\omega = n\omega_D$ survive. Since those are not explained by our analytical approximations, as discussed in the previous subsection, we can investigate their $\mathbf{k}$-dependence only numerically. Thereto, we simulate the propagation of wave packets with different initial energies. So far, the propagated Gaussian wave packet is centered around $\mathbf{k}_0 = (0.4\tilde{\omega}/v_F, 0)^T$ with a $\mathbf{k}$-space width of $\Delta k = k_0/10 = 0.04\tilde{\omega}/v_F$. To find out the $\mathbf{k}$-dependence of the ZB modes, we simulate now two wave packets centered around $\langle\mathbf{k}\rangle = \mathbf{k}_0 \pm (\Delta k, 0)^T$ instead. If the position of the modes do not change in the diagrams, they are not $\mathbf{k}$-dependent and are supposed to survive. On the other hand, if the frequencies of the modes do change, they are $\mathbf{k}$-dependent and should therefore dephase. In Fig. 7.9, the data of these additional simulations are shown, i.e. wave packets of different initial energy are propagated, in a much smaller parameter

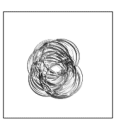

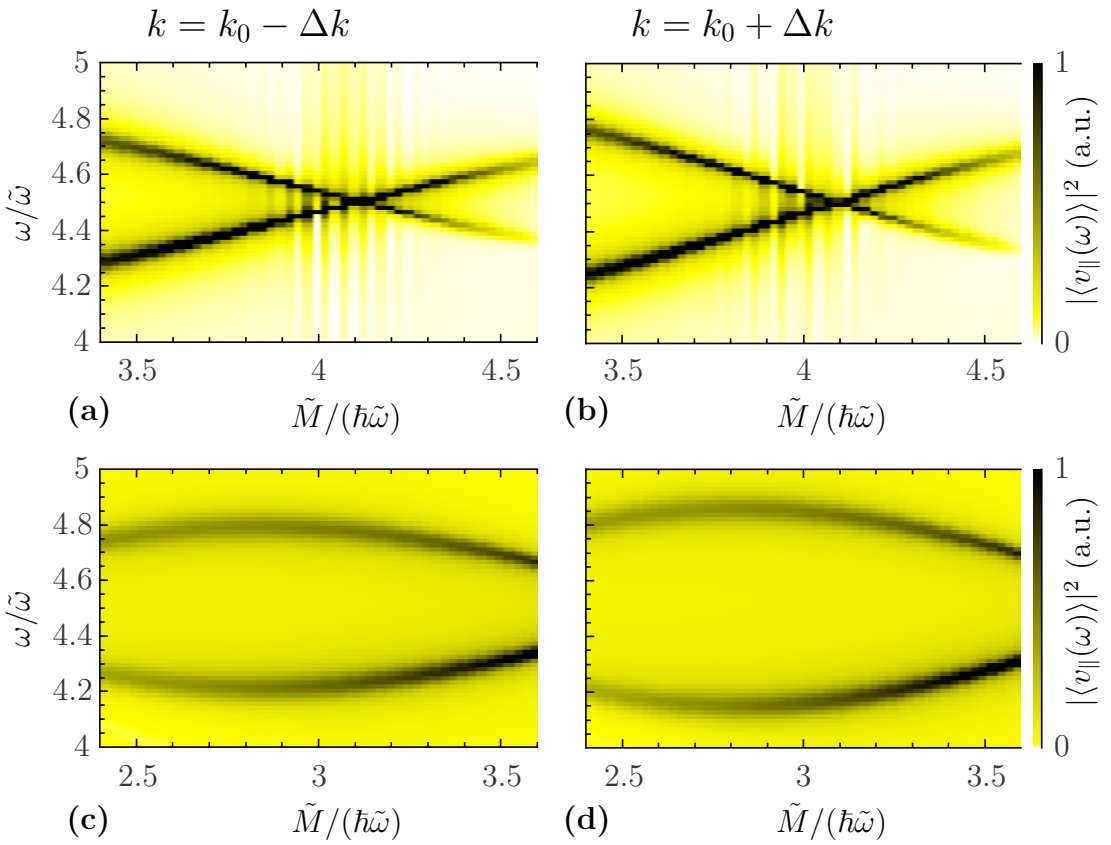

Figure 7.9: Explanation why the modes at the crossing ($\omega \approx n\omega_D$) survive in Fig. 7.8(f) and (h). The parallel velocity $|\langle v_\parallel(\omega)\rangle|^2$ is shown as a function of $\tilde{M}$ for $M_0 = 0$ and $\omega_D = 1.5\tilde{\omega}$, for two different energies with $k = 0.36\tilde{\omega}/v_F$ (in (a) and (c)) and $k = 0.44\tilde{\omega}/v_F$ (in (b) and (d)). The frequency of the ZB is quite independent at the crossings, i.e. (a) and (b) are very similar, whereas away from the crossing, it is energy dependent, i.e. (c) and (d) differ. Since only energy-independent modes survive as discussed in this section, only the crossings can be seen after a long time (Fig. 7.8(f) and (h)).

regime than before. Here, the parameters are $M_0 = 0$ and $\omega_D = 1.5\tilde{\omega}$. Panels (a) and (b), show the ZB modes at the crossing of the horizontal line $\omega = 4.5\tilde{\omega} = 3\omega_D$, for different initial energies, whereas panels (c) and (d) depict the region away from those crossings. Since the position of the crossing at $\tilde{M} \approx 4.1\hbar\tilde{\omega}$ does not considerably change, whereas away from the crossing, the position change of the modes is visible with the naked eye, the crossings are rather **k**-*in*dependent over the width of the wave packet, whereas the region away from the crossing are **k**-dependent. This is reflected in the long-time behavior, where the crossings survive and the other regions decay over time.

In conclusion, we have studied in this subsection the long-time behavior of the ZB, which shows persistent ZB modes. In all cases, the reason for the survival is the **k**-independence of these modes, such that they do not dephase as opposed to the static case discussed in previous sections.

7.4.6 Summary and discussion of the driven zitterbewegung

To finish the section of the time-dependent ZB, let us summarize the results and discuss them with respect to the literature, especially Refs. [139,140]. In this section, we investigated the effects of a harmonic driving potential ($\propto \sigma_z$) on the ZB in gapped graphene, where the case of pristine graphene can be obtained from our results using $M_0 = 0$. First, we used first order time-dependent perturbation theory, which states that the ZB of only those **k**-modes survives, which have (in the static case) the same frequency as the driving frequency, see Eq. (7.92). This is verified by simulations for small driving amplitudes $\tilde{M}$.

Furthermore, we used the strategy of Rusin and Zawadzki [140], to obtain analytical approximation in the rotating wave approximation (RWA) and in the limit of Fhigh driving frequencies (HDF), which yield a multimode ZB, and are compared to the results of simulation in Subsec. 7.4.4. Within their regime of validity, the analytical approximations yield the correct results except for the fact that higher order in ω_D appear, which can be motivated by perturbation theory.

In Subsec. 7.4.5, the long-term behavior of the ZB is studied, with the result that **k**-independent modes are persistent, i.e. that they survive for all times. Since the decay of the ZB in the static case is due to the **k**-dependence of the ZB frequency, this result is easily conceivable. These persistent modes are a significant difference to the case of a time-dependent vector potential in graphene as discussed in Ref. [140]. They find a similar multimode ZB, with the difference that no **k**-independent mode appears, which is in our case a ZB mode with the same frequency as the driving frequency ω_D. Although their ZB is prolonged by the driving, it still decays over time. Thus, we propose in our setup the (as far as we know) first persistent ZB modes in graphene with a driving potential.

Note that earlier, persistent modes driven by a time-dependent Rashba spin orbit coupling have been proposed in a two-dimensional electron gas [139]. Although they investigate their existence and features like the amplitude dependence thoroughly, they do not discuss in detail the origin of the persistent mode, which is in our case the **k**-independence.

7.5 Echoes of the zitterbewegung using the QTM-protocol

7.5.1 Analytical prediction of the echo strength

As mentioned in Sec. 7.2, the decay of the ZB of wave packets in the static case stems from the spatial separation of the two sub-wave packets in the two bands until they do not interfere anymore [142]. In the previous section a periodic modulation of mass gap is used to circumvent the decay of ZB and generate persistent modes. Vividly, the driving potential leads continuously to transitions from one band to the other such that there is always a spatial overlap of counter propagating modes and thus, the ZB can survive.

In this section, we want to use an alternative way to bring the two sub-wave packets back together, which has been used in the rest of the thesis: the quan-

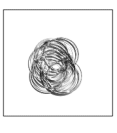

tum time mirror (QTM). Parts of both sub-wave packets are made to switch their propagation direction such that they move back to their initial position and overlap again so that they can interfere. In the physical picture of the decay due to separating wave packets, this is supposed to yield an echo of the initial ZB. Thus, let us have a closer look to the theory, e.g. to compare the echo strength $\mathcal{C}(t_{\text{echo}})$, used in Chaps. 3-5, with the relative change of the amplitude of the ZB.

To distinguish clearly from the last section, we want to stress that now, the time-dependent part of the Hamiltonian acts only very shortly, meaning that we use a pulse to induce the echo, instead of the sinusoidal modification of the previous section:

$$H = H_0 + H_{\text{pulse}}(t), \tag{7.140}$$

where we choose again a mass pulse

$$H_{\text{pulse}}(t) = M\sigma_z f(t). \tag{7.141}$$

For analytical reasons, the time-dependence $f(t)$ of the pulse is the same as in Chaps. 3, 4 and 5, i.e. it is immediately switched on at t_0 for a (short) duration Δt.

From Sec. 3.1, we know the action of the pulse on an initial eigenstate, which is

$$|\varphi_{k,s}\rangle = B_s(\mathbf{k}, \Delta t)|\varphi_{k,s}\rangle + A_s(\mathbf{k}, \Delta t)|\varphi_{k,-s}\rangle. \tag{7.142}$$

In the considered case of (gapped) graphene, the transition amplitude is independent of s and we write $A \equiv A_s$. For the echo, only the part which switches band, i.e. proportional to the transition amplitude A, is important since it propagates in the opposite direction whereas the other part ($\propto B_s$) keeps on moving in the same direction. Therefore, only the "reflected" part will be considered after the pulse.

We assume a general initial wave packet

$$|\phi_0\rangle = \sum_{\mathbf{k}} \phi_0(\mathbf{k})|\phi_0^{\mathbf{k}}\rangle = \sum_{\mathbf{k}} \phi_0(\mathbf{k}) \left(\alpha_{\mathbf{k}}^+|\varphi_{\mathbf{k},+}\rangle + \alpha_{\mathbf{k}}^-|\varphi_{\mathbf{k},-}\rangle\right), \tag{7.143}$$

with $|\alpha_{\mathbf{k}}^+|^2+|\alpha_{\mathbf{k}}^-|^2 = 1$. Let us denote the essentially reflected part of the wave packet by $|\phi_{\text{echo}}\rangle$ and neglect the ongoing part, as mentioned above. Since the propagation before and after the pulse are trivial, $|\phi_{\text{echo}}\rangle$ becomes at some time $t' = t_1 + t_0 + \Delta t$ after the pulse

$$\begin{aligned} |\phi_{\text{echo}}(t')\rangle &= \sum_{\mathbf{k}} \phi_0(\mathbf{k})\ |\phi_{\text{echo}}^{\mathbf{k}}(t')\rangle \\ &= \sum_{\mathbf{k}} \phi_0(\mathbf{k}) \sum_{s=\pm 1} \alpha_{\mathbf{k}}^s \mathrm{e}^{-i\omega_{\mathbf{k},s}t_0}\, A(\mathbf{k}, \Delta t)\, \mathrm{e}^{-i\omega_{\mathbf{k},-s}t_1}\, |\varphi_{\mathbf{k},-s}\rangle, \end{aligned} \tag{7.144}$$

because before the echo, the kinetic phase is given by its energy $E_{\mathbf{k},s} = \hbar\omega_{\mathbf{k},s}$, then the pulse acts yielding $A(\mathbf{k}, \Delta t)$ and finally after the pulse, the accumulated phase in time t_1 is governed by $E_{\mathbf{k},-s} = \hbar\omega_{\mathbf{k},-s}$ (for the echo part), since the state changed the band. Note that due to the homogeneous pulse, the momentum $\mathbf{k}$ is not changed. Thus, the amplitude in $\mathbf{k}$-space, $\phi_0(\mathbf{k})$, remains unchanged.

Now, we want to investigate the ZB. Therefore, we compare the expectation value of the velocity operator before and after the pulse. For simplicity, let us first consider only a single $\mathbf{k}$-mode. Before the pulse, it is given by Eq. (7.8) of Sec. 7.2:

$$\begin{aligned}\langle \hat{v}_{i,\mathbf{k}}^{\mathrm{ZB}} \rangle (t < t_0) &= 2\,\mathrm{Re}\{\alpha_{\mathbf{k}}^{+}(\alpha_{\mathbf{k}}^{-})^{*}\,\mathrm{e}^{-i\Omega_{\mathbf{k}}^{\mathrm{ZB}}t}\,\langle \varphi_{\mathbf{k},-} \mid \hat{v}_i \mid \varphi_{\mathbf{k},+} \rangle\} \\ &= 2|\alpha_{\mathbf{k}}^{+}|\,|\alpha_{\mathbf{k}}^{-}|\,|\langle \varphi_{\mathbf{k},-} \mid \hat{v}_i \mid \varphi_{\mathbf{k},+} \rangle| \cos\left(\Omega_{\mathbf{k}}^{\mathrm{ZB}}t + \varphi_{\mathbf{k}} + \nu_{i,\mathbf{k}}\right), \end{aligned} \tag{7.145}$$

where $i \in \{x, y\}$ denotes the direction, with the already defined static frequency of the ZB $\Omega_{\mathbf{k}}^{\mathrm{ZB}} = (E_{\mathbf{k},+} - E_{\mathbf{k},-})/\hbar$ and the phases

$$\varphi_{\mathbf{k}} = -\arg\left(\alpha_{\mathbf{k}}^{+}\,(\alpha_{\mathbf{k}}^{-})^{*}\right), \tag{7.146}$$

$$\nu_{i,\mathbf{k}} = -\arg\left(\langle \varphi_{\mathbf{k},-} \mid \hat{v}_i \mid \varphi_{\mathbf{k},+} \rangle\right). \tag{7.147}$$

After pulse, at time $t' = t_1 + t_0 + \Delta t$, and considering only the "reflected" parts of the wave packet $|\phi_{\mathrm{echo}}\rangle$, we get similarly with the help of the time evolution shown in Eq. (7.144):

$$\begin{aligned}\langle \hat{v}_{i,\mathbf{k}}^{\mathrm{ZB}} \rangle (t') &= 2|A(\mathbf{k})|^2 \mathrm{Re}\left\{\alpha_{\mathbf{k}}^{+}(\alpha_{\mathbf{k}}^{-})^{*}\,\mathrm{e}^{-i\Omega_{\mathbf{k}}^{\mathrm{ZB}}(t_0 - t_1)}\,\langle \varphi_{\mathbf{k},+} \mid \hat{\mathbf{v}} \mid \varphi_{\mathbf{k},-} \rangle\right\} \\ &= 2|A(\mathbf{k})|^2\,|\alpha_{\mathbf{k}}^{+}|\,|\alpha_{\mathbf{k}}^{-}|\,|\langle \varphi_{\mathbf{k},-} \mid \hat{v}_{i,\mathbf{k}} \mid \varphi_{\mathbf{k},+} \rangle| \cos\left(\Omega_{\mathbf{k}}^{\mathrm{ZB}}(t_0 - t_1) + \varphi_{\mathbf{k}} - \nu_{\mathbf{k}}\right), \end{aligned} \tag{7.148}$$

with the phases $\varphi_{\mathbf{k}}$ and $\nu_{\mathbf{k}}$ as in Eqs. (7.146) and (7.147). The amplitude is the same as before the pulse, except for $|A(\mathbf{k})|^2$, which is due to the fact that only the "reflected" part of the wave packet contributes to the ZB. Another difference is the sign of the phase $\nu_{i,\mathbf{k}}$ due to the fact that after the pulse $\alpha_{\mathbf{k}}^{s}$ is coupled to $|\varphi_{\mathbf{k},-s}\rangle$ as opposed to before the pulse. Thus, we have $\langle \varphi_{\mathbf{k},+}|\hat{v}_{i,\mathbf{k}}|\varphi_{\mathbf{k},-}\rangle = \langle \varphi_{\mathbf{k},-}|\hat{v}_{i,\mathbf{k}}|\varphi_{\mathbf{k},+}\rangle^{*}$, which is equivalent to changing the sign of the phase. For gapless graphene, the matrix element $\langle \varphi_{\mathbf{k},-}|\hat{\mathbf{v}}|\varphi_{\mathbf{k},+}\rangle$ is purely imaginary (see App. B) and therefore it leads to a phase jump of π, which does not affect the amplitude of the ZB.

The most important difference for the echo is the time-dependence of the cosine. The time-dependent phase, which has accumulated before the pulse in time t_0 is now continuously removed by t_1(=time after the pulse) until at $t_1 = t_0$, the initial phase is recovered. The important point is that this happens for any $\mathbf{k}$-mode in the same way, such that all modes rephase simultaneously.

Let us consider now the ZB of a wave packet instead of a plane wave. The derivation is exactly the same as in Sec. 7.2 for Eq. (7.18) leading to

$$\langle \hat{\mathbf{v}}^{\mathrm{ZB}} \rangle (t') = \int \mathrm{d}^2k\,|\phi_0(\mathbf{k})|^2\,\langle \hat{\mathbf{v}}_{\mathbf{k}}^{\mathrm{ZB}} \rangle (t'). \tag{7.149}$$

Thus, all implications of the static ZB in Sec. 7.2 also apply here. For instance, the decay of the static ZB has been due to the $\mathbf{k}$-dependence of the term $\cos(\Omega_{\mathbf{k}}^{\mathrm{ZB}}t)$ which makes the integral in Eq. (7.149) vanish at large t due to fast oscillations (compare Fig. 7.1). However, after the pulse, the according term is $\cos(\Omega_{\mathbf{k}}^{\mathrm{ZB}}(t_0 - t_1))$. As discussed above, dephasing is thus reverted after the pulse and an echo is expected at $t_1 = t_0$, which means $t_{\mathrm{echo}} = 2t_0 + \Delta t$, where all modes are in phase again and an echo is expected.

The major difference is that only parts of every $\mathbf{k}$-mode undergo the needed transition according to $A(\mathbf{k}, \Delta t)$, which appears in the integral of Eq. (7.149) due to $\langle \hat{\mathbf{v}}_{\mathbf{k}}^{\mathrm{ZB}} \rangle (t')$ of Eq. (7.148). For a highly peaked wave packet around some $\mathbf{k}_0$, such that $A(\mathbf{k}) \approx A(\mathbf{k}_0)$ over the width of the wave packet, the transition amplitude can be approximately taken out of the integral (for calculation see Sec. 3.2), and the

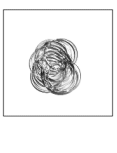

relative amplitude between initial amplitude B_{initial} and revived amplitude B_{revived} of the ZB, denoted by $\tilde{v}$, becomes

$$\tilde{v} := \frac{B_{\text{revived}}}{B_{\text{initial}}} \approx |A(\mathbf{k}_0)|^2. \tag{7.150}$$

Thus, we have shown that an echo of the ZB by the QTM mechanism is not only possible, but also derived its approximate strength in Eq. (7.150). Indeed, the setup is in some sense quite close to the spin echo. There, rotating spins whose signal is lost due to dephasing are made to rephase again, leading to an echo of the initial signal. Here, oscillating electron wave packets which dephase due to different ZB frequencies of the individual $\mathbf{k}$-modes are made to rephase by the QTM, which also leads to an echo of the ZB.

We conclude this Sec. by making a final remark of rather technical nature. As discussed above, since the complex number $\langle \varphi_{\mathbf{k},-} \mid \hat{\mathbf{v}} \mid \varphi_{\mathbf{k},+} \rangle$ is purely imaginary in graphene, i.e. its phase is $\nu_{\mathbf{k}} = \pm\pi/2$ for any $\mathbf{k}$, the pulse leads to a constant phase jump of π which does not effect the amplitude of the echo. For a general system on the other hand, the phase $\nu_{\mathbf{k}}$ becomes $\mathbf{k}$-dependent. Considering the cosine in Eq. (7.148), this leads in general at $t = 0$ and $t = t_0$ to different $\mathbf{k}$-dependent phases: $\cos(\varphi_{\mathbf{k}} \pm \nu_{\mathbf{k}})$. In principle, this influences the amplitude of the ZB of a wave packet due to the integral over $\mathbf{k}$ in Eq. (7.149). However this should in general not lead to a further reduction of the ZB compared to the initial ZB – as long as the phases $\varphi_{\mathbf{k}}$ and $\nu_{\mathbf{k}}$ are unrelated. In that case the sign in $\varphi_{\mathbf{k}} \pm \nu_{\mathbf{k}}$ does not make a qualitative difference and we assume that the different $\mathbf{k}$-dependent phases averages out.

An artificial exception would be for instance the case $\nu_{\mathbf{k}} = \varphi_{\mathbf{k}}$. This is highly unlikely, since these two quantities are independent – $\varphi_{\mathbf{k}}$ depends only on initial wave packet, whereas $\nu_{\mathbf{k}}$ only on unperturbed Hamiltonian and the velocity operator. In this unrealistic case, the ZB at $t = 0$ is diminished because $\cos(\varphi_{\mathbf{k}} + \nu_{\mathbf{k}}) \leq 1$ varies and is truly smaller than 1 in most cases of $\mathbf{k}$. On the other hand, the ZB at $t_1 = t_0$ is enhanced due to $\cos(\varphi_{\mathbf{k}} - \nu_{\mathbf{k}}) = \cos 0 = 1$ for all $\mathbf{k}$. Thus for a transition amplitude close to one ($|A(\mathbf{k})| \lesssim 1$), the amplitude of the echo ZB could be even higher than initially. However, this is a highly unlikely case, which is why we do not consider it further. Instead, we forget about the effect $\nu_{\mathbf{k}}$, which is justified for narrow wave packets in $\mathbf{k}$-space, such that the $\nu_{\mathbf{k}} \simeq \nu_{\mathbf{k}_0}$ over the width of the wave packet. In the next section, we numerically investigate the existence of the echo of the ZB.

7.5.2 Numerical confirmation of the echo of the zitterbewegung

In the previous subsection, we derived that the expected amplitude of the echo of the ZB given by the transition amplitude, more precisely by $|A(\mathbf{k}_0, \Delta t)|^2$, for a narrow wave packet reciprocal space around $\mathbf{k}_0$. Here, we want to verify this result by simulations using TQT. Since we know from Sec. 3.1 in Eq. (3.37) that for a narrow wave packet in $\mathbf{k}$-space, also the correlation $\mathcal{C}(t_{\text{echo}})$ is given by the transition amplitude

$$\mathcal{C}(t_{\text{echo}}) \approx |A(\mathbf{k}_0, \Delta t)|, \tag{7.151}$$

the relative amplitude $\tilde{v}$ is supposed to be

$$\tilde{v} = \mathcal{C}^2(t_{\text{echo}}). \tag{7.152}$$

As example of different band structures in connection with the QTM, we use pristine graphene, discussed in Chap.3, as well as gapped graphene from Sec. 5.3, where in both cases the transition amplitude is known (see Eq. (3.21) for pristine graphene and Eq. (5.60) for gapped graphene).

To get an initial ZB, we have to start with a wave packet living in both bands. For the proof of principle, we use a small width of the Gaussian wave packet in reciprocal space ($\Delta k = k_0/8$), such that we the approximation is justified made in Eq. (7.150) for the amplitude of the revived ZB. The wave packet is peaked around $\mathbf{k}_0 = (k_0, k_0)^T/\sqrt{2}$, with $\kappa_0 = \hbar v_F k_0/M = 0.4$, if not stated otherwise.

In Fig. 7.10, the data obtained by simulation is shown. In panel (a), we compare the correlation $\mathcal{C}$ defined in Eq. (3.32), to the relative amplitude of the revived ZB. Numerically, the amplitude of the echo is obtained as half of the distance between the consecutive maximum and minimum with the highest difference between them in a certain time interval $I = [t_{\text{echo}} - \delta t, t_{\text{echo}} + \delta t]$ around the expected echo time $t_{\text{echo}} = 2t_0 + \Delta t$, i.e.

$$B_{\text{revival}} = \max_{t \in I} \frac{|v_{\max}(t) - v_{\min}(t + \pi/\Omega^{\text{ZB}}_{\mathbf{k}_0})|}{2}, \tag{7.153}$$

where $v_{\max}$ is a local maximum and $v_{\min}$ a local minimum. Here, we use $\delta t = 0.5t_0$, but the exact value does not matter, as long as the revival is included in the interval I and the ZB that does not belong to the revival is excluded.

The velocities in panel (a) of Fig. 7.10 are normalized by the initial amplitude of the ZB B_{initial}. Thus, at the echo time $t_{\text{echo}} \simeq 2t_0$, the amplitude of the ZB coincides with the echo strength $\mathcal{C}^2_{\text{echo}} = \mathcal{C}^2(t_{\text{echo}}) \simeq |A(\mathbf{k}_0, \Delta t)|^2$, as expected from Eq. (7.150). In panel (b), the relative amplitude $\tilde{v} = B_{\text{revival}}/B_{\text{initial}}$ and echo strengths $\mathcal{C}^2_{\text{echo}}$ are shown as a function of the pulse length Δt, respectively $\mu = M\Delta t/\hbar$. Since no difference is visible, the expectations are met.

For gapped graphene, the velocity in panel (c) looks a bit different to the gapless case in (a). First, the chosen wave packet does not occupy both bands with the same magnitude and thus, a drift is visible in the expectation value of v_x. This drift is the reason why the velocities are no longer normalized by the initial amplitude of the ZB but by v_F, since a comparison with the naked eye as in panel (a) would be here only possible for v_y. Although not directly visible, the values $\tilde{v}$ and $\mathcal{C}^2$ indeed coincide. The third difference is the appearing ZB directly after the pulse. This is actually not surprising, because after the pulse, the wave packets splits into reflected and ongoing part which occupy different bands, which is the essential ingredient for ZB in this system and therefore, a ZB can be seen. In principle, this happens also in gapless graphene, i.e. each sub-wave packet undergoes a ZB directly after the pulse, but there, because of symmetric occupancy of both bands, the terms of the two sub-wave packets cancel exactly in the expectation value of the velocity. In panel (d), the relative amplitude of the revived ZB matches the echo strength obtained by the correlation, for varying mean wave vectors $\kappa = \hbar v_F k/M$. The agreement of the values of $\tilde{v}$ and $\mathcal{C}^2$ confirms our analytical expectations.

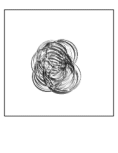

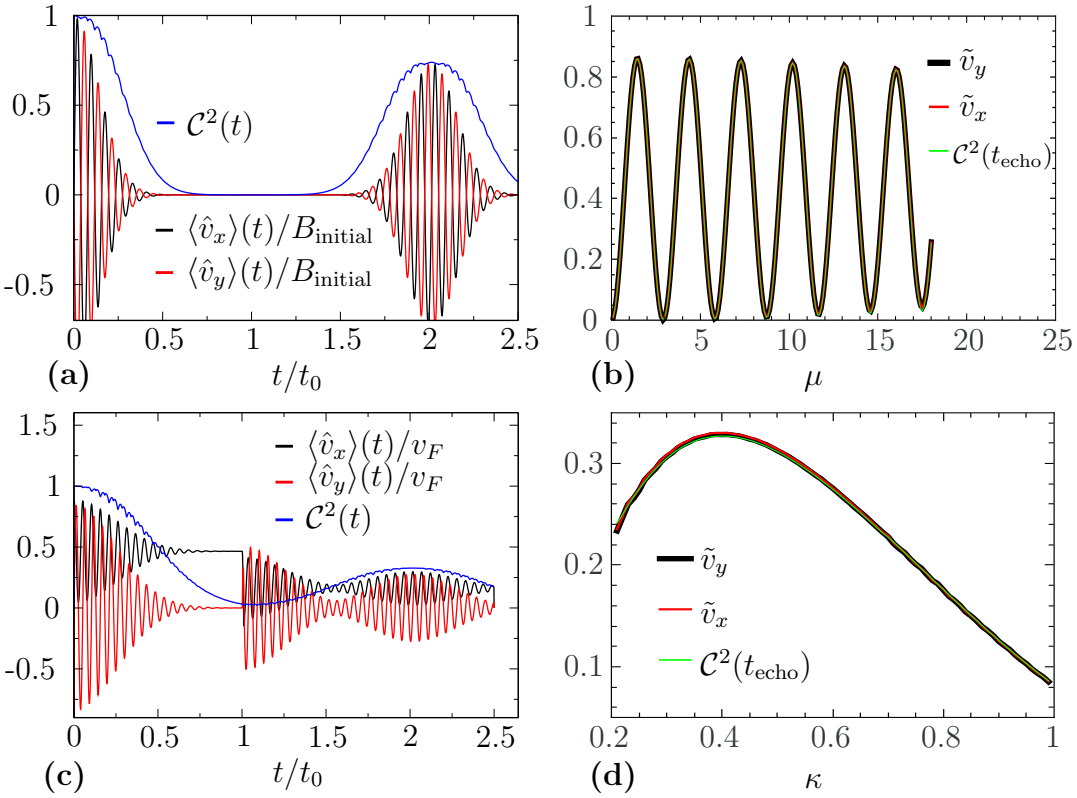

Figure 7.10: Confirmation of the proposed echo of the ZB by simulation for gapless graphene (a), (b) and gapped graphene (c), (d). In the left panels, the timeline is shown for both the expectation values of the velocity and the correlation $\mathcal{C}^2$ as defined in Eq. (3.32). In panel (a), $\mathcal{C}^2$ and the amplitude of the ZB coincides at the echo time $t_{\text{echo}} \simeq 2t_0$, as expected from Eq. (7.152). In panel (b), the echo strength $\mathcal{C}(t_{\text{echo}})$, which corresponds approximately to $|A(\mathbf{k}_0, \Delta t)|$ (see Eq. (3.37)), is compared to the relative amplitude of the revived ZB $\tilde{v}$ as function of μ and fixed $\kappa = \hbar v_F k_0/M = 0.4$. Panels (c) and (d) show the same for gapped graphene with a different velocity normalization. The good agreement in (d), with $\mu = 1.4$ and varying κ, confirms again the expected results.

7.5.3 Disorder

In the previous subsections, we showed that the echo of ZB induced by our QTM behaves as expected in pristine and gapped graphene. Now, we could continue and verify all other results obtained in the context of the QTM discussed in Chaps. 3-5. Exemplarily, we investigate the effect of disorder (compare Sec. 4.1). As a quick reminder, the disorder cannot be effectively time-inverted by the QTM and leads to an exponential decay of the echo strength (measured by the echo fidelity) as function of propagation time, which is in our case the echo time $t_{\text{echo}} \simeq 2t_0$. Due to the overlap of states with positive and negative energy in the ZB, $\tilde{v}$ is closely related to the echo fidelity and we expect a similar behavior, i.e. an exponential decay.

We use the same setup as in Sec. 4.1, i.e. pristine graphene (Hamiltonian, see e.g. Eq. (3.1)) with a pulse that opens a mass gap of strength M and an pseudospin-

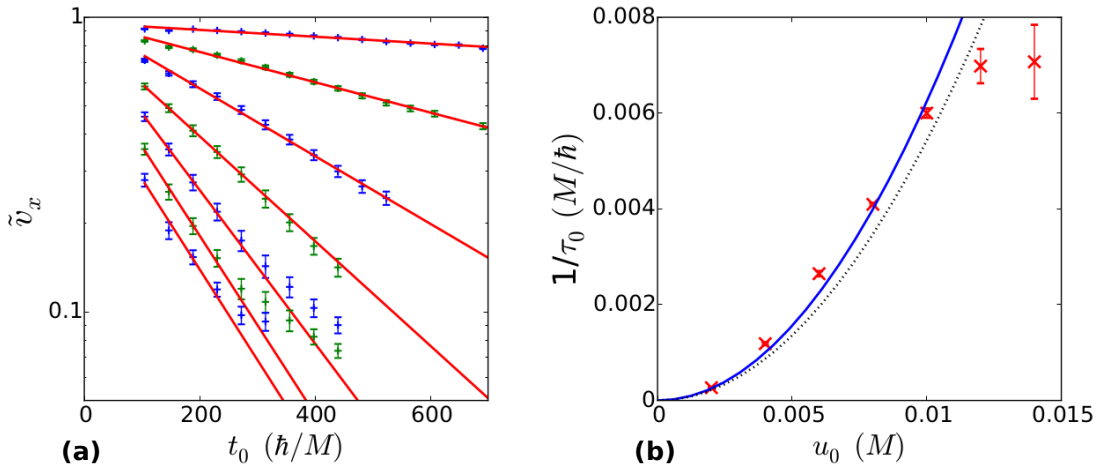

Figure 7.11: Revival of the ZB with disorder. (a) The time-dependent revival strength $\tilde{v}_x$ is shown as a function of the pulse time t_0 for different disorder strengths ranging from $u_0 = 0.002M$ to $0.014M$. An exponential decay can be seen in the small disorder regime. (b) The rate of decay $1/\tau$ is extracted by a fit (red lines in (a)) and is plotted as a function of u_0, as well as the analytically expected scattering time (black dotted) from Eq. (4.13). The quadratic fit in u_0 (blue line) to the data points, is close to the scattering time. For larger u_0 a saturation is obtained. For more details, see the discussion of disorder in Sec. 4.1 of the graphene QTM.

independent disorder potential $V_{\text{imp}}(\mathbf{r})$ as defined in Eq. (4.1). The only difference is that, in order to generate ZB, the initial wave packet lives in both bands – otherwise the simulations are the same.

As before, we measure the revival of the ZB by the relative amplitude of the echo

$$\tilde{\nu} = \frac{B_{\text{revival}}}{B_{\text{initial}}}, \tag{7.154}$$

which is plotted as a function of the pulse time t_0 in Fig. 7.11(a) for different disorder strengths u_0. Indeed, we see exponential decays of $\tilde{\nu}$ as function of the pulse time t_0, where again a saturation is achieved for high u_0 and t_0, in analogy to Sec. 4.1. The fitted decay rates $1/\tau$ of panel (a) (red lines) are plotted in panel (b) as function of the disorder strength u_0, which are expected to increase quadratically (compare Eq. (4.13)). Up to some value of $u_0 \simeq 0.012M$, the decay rate indeed increases quadratically, as can be seen by the quadratic fit (blue) and is slightly larger but close enough to the purely analytically expected decay, which was calculated in Subsec. 4.1.2 with the result given in Eq. (4.13) (black dotted line).

Thus, the disorder affects the revival of the ZB via the QTM mechanism as expected, namely in the same way as discussed earlier in the thesis. Therefore we assume that also the other features of the QTM for two-level systems discussed in Chaps. 3-5 apply for the revival of the ZB.

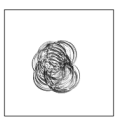

7.6 Summary, discussion and outlook

In this chapter, after giving an extensive introduction of the static ZB in graphene, we investigated the effect of a periodically driven mass term to the ZB in graphene, both analytically and by simulation and found that a multimode ZB emerges. Studying the long-time behavior, we even found persistent ZB modes which do not decay, because they are **k**-independent. Such persistent modes of the ZB might help to measure the ZB in graphene experimentally.

Moreover, we used the QTM mechanism discussed in Chaps. 3-5, to invert the aforementioned decay of the ZB. Similar to the spin echo, a revival of the ZB appears, which we studied analytically and verified by simulation. Therefore, if the ZB can be measured, it could be used to verify the QTM mechanism.

Furthermore, the effects of the QTM discussed in the rest of the thesis are highly likely to be applicable for the echo of the ZB. Explicitly, we studied the effect of disorder, which influences the echo strength in the same way as the echo fidelity of Sec. 4.1, i.e. the echo decays exponentially over time. However, in contrast to the echo fidelity, the ZB is a (in principle) measurable quantity. Thus, a measurement of the revival strength would allow to obtain the decay rate, which is given by the elastic scattering time, corresponding to the decay time T_2 in spin echo setups.

If this becomes experimentally possible, the analogy to the spin echo would come into play. For the spin echo, which is known since the 1950's, involved protocols and algorithms have been developed for a usage in technical devices. Some of those protocols – mostly T_2-weighted imaging – could be directly transferable to the echo of the ZB. An easy example would be to apply some gradients that make the frequency of the static ZB space-dependent. By investigating which frequency decays how much, one could determine locally the impurity strength. This could help in a sample, e.g. on a large graphene flake to find out where the best environment is for a particular measurement.

Unfortunately, all the experimental hurdles of the QTM discussed in Sec. 3.6 are still there and additionally, the ZB has to measured. Although the last point has been recently achieved in a solid state setup [134], it is in a different regime than what would be needed here. Nevertheless, this raises our hope that the ZB can also be measured in systems and regimes needed for the echo of the ZB.

Chapter 8

Summary

In this thesis, we address the long-standing problem of the effective time-inversion of a continuous quantum system, e.g. the wave function of a electron wave packet in a solid. Although for classical waves such time-inversion mirrors exist since the 1990's [16–24] and for discrete quantum systems even since the 1950's [7] known as the spin echo or Hahn echo, analogue implementations have failed for the quantum wave function. One major reason is the involved measuring process of the classical waves, which is not applicable in a similar way because of the projection theorem of quantum mechanics .

However, a recent development for classical time-inversion mirrors (for water waves), the instantaneous time mirror [45], circumvents the measuring of the wave completely. Instead, a short pulse is applied homogeneously to the system, which leads in their case to a partial inversion of the velocity. Therefore, parts of the waves come back to the initial position and create an echo, although the wave has lost its initial structure completely in the meantime. Due to the homogeneity of the pulse, a knowledge of the wave structure is not necessary at all, which will be helpful in quantum systems.

In this thesis, we present and investigate thoroughly two independent setups where a homogeneous, time-dependent pulse is exploited to effectively time-invert continuous quantum systems, i.e. to generate an echo of the initial wave function at the initial position. One is the population inversion quantum time mirror (QTM), that we use in two-band systems, the other one is the Bose-Einstein condensate time-mirror, which utilizes the tunability of the nonlinearity in the Gross-Pitaevskii equation. The general strategy is to first confirm the qualitative ideas by analytical calculations and further verify those by simulations of the time evolution of wave packets using the library TQT.

The basic principles of the population inversion quantum time mirror are discussed in Chap. 3 at the example of graphene. The goal is to invert the motion, i.e. change the sign of the velocity of a wave packet in the low-energy band structure of graphene, the Dirac-cone. To achieve a "reflection", a usual mirror changes the momentum of, e.g., a photon to invert its motion by breaking translational symmetry in space. In contrast, we want to use a homogeneous, time-dependent pulse that breaks translation symmetry only in *time*. Thus, the (quasi)momentum of the wave packet is conserved but its energy changes, so that parts of the wave packet can switch bands. The group velocity given by the derivative of the energy:

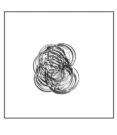

$\mathbf{v}_g = \nabla_{\mathbf{k}}\varepsilon(\mathbf{k})$, indeed has a different sign in the two bands of graphene, which is why the parts of the wave packet that switch bands indeed come back and create an echo. In graphene, a mass pulse, i.e. $\propto \sigma_z$, is considered. For an illustration of the mechanism, see Fig. 3.1 and for snapshots of the wave packet, see Fig. 3.8 or the footer, which can be used as a flicker book.

Apart from the mechanism, the echo strength is calculated analytically and confirmed numerically in Chap. 3 for short and long pulses as well as for Gaussian, "$\hbar$"-shaped and even arbitrary wave packets without showing signs of deviations from the theory. Moreover, the change of the real space structure of the wave packet, which is in principle possible, is investigated and discussed with regard to potential utilizations.

From an experimental point of view, there are many hurdles to be overcome, starting from the generation of electron wave packets, over applying a suitable pulse and measuring the "reflected" state, to integrating our single particle picture in an actual system. Promising rudiments and not yet solved problems are in-length discussed in Sec. 3.6, as well as research areas which could benefit from implementing the QTM.

The effect of imperfections in the Hamiltonian, or more generally, position dependent terms in the initial Hamiltonian, are investigated in Chap. 4. Explicitly, the low-energy Hamiltonian of graphene is studied in presence of random disorder as well as for external static electro-magnetic fields and compared to our theory for general perturbations of Sec. 4.2. Qualitatively, a system can only be effectively time-inverted by the QTM pulse if the kinetic phase of those parts that switched their energy state which is accumulated before the pulse is canceled by the kinetic phase acquired during the propagation after the pulse. Thus, a pseudospin-*in*dependent potential, like a static electric field or the considered disorder potential, destroy the echo. The reason is that the accumulated phases due to the potential do not cancel before and after the pulse but are similar because they are independent on changing the pseudospin structure (and thus occupancy of the energy levels) of the state. For disorder, this leads to an exponential decrease of the echo as a function of propagation time, where the decay rate is given by the elastic scattering time. This feature could be used experimentally to measure the disorder strength in a given sample in a similar way as the spin echo, which is discussed thoroughly in Sec. 4.1.4.

For an external electric field, a new feature appears: although the system cannot be effectively time-inverted due to the pseudospin-independent scalar potential, an echo can be still generated under certain circumstances. The reason is that as long as the velocity is inverted due to the pulse, the wave packet goes back to its initial position, despite the fact that other quantities are not inverted. In the considered case, the constant change of the momentum as consequence of the electric field cannot be inverted by the pulse. However, since the group velocity in graphene only depends on the direction of $\mathbf{k}$ but not its modulus $|\mathbf{k}|$, changing the momentum does not necessarily mean changing the velocity. In the case of a parallel electric field to the propagation direction, when the pulse "flips" the energy of the state it also flips the velocity which again remains constant after the pulse and an echo happens.

The case of a static magnetic field is at first glance contradictory. Although time-reversal symmetry is broken, the used mass gap still leads to an *effective* time-

inversion of the system. The seeming contradiction is dissolved by the fact that time-reversal symmetry is not needed for the QTM mechanism to work – instead, it is the chiral (or sub-lattice) symmetry, i.e. $E_- = -E_+ + c$, although we even show that a less strict condition suffices (see below). Indeed, the mass gap will map a Landau level n in graphene partly to its negative counterpart $-n$. Assume that a wave packet composed of Landau levels with positive energy rotates by tendency clockwise. After the pulse, the switched parts then tend to rotate counterclockwise, unwinding the propagation before the pulse and ending up at the initial position. This is in agreement with the general qualitative result of Sec. 4.2, which states that if the "direction" of the pulse Hamiltonian in pseudospin-space (here $\hat{z}$ due to σ_z) is perpendicular to the pseudospin-direction of the initial Hamiltonian (somewhere in the x-y-plane since it is a linear combination of σ_x and σ_y), the system is effectively time-inversed, in the sense that those parts of the state that change their energy behave after the pulse *exactly* as if they would move backwards in time.

Finally, the possibility of using time-dependent electro-magnetic potentials as pulse are discussed briefly, where first investigations delivered promising results.

So far, the Dirac cone has been investigated when considering an explicit system. However, its nice features, i.e. the linear band structure and the chiral symmetry, are not necessary requirements to induce an echo via the population inversion QTM. In Chap. 5, the actually needed conditions of the initial band structure – providing a homogeneous system and a homogeneous pulse – are derived. Instead of a true chiral symmetry ($E_-(\mathbf{k}) = -E_+(\mathbf{k}) + c$), a generalized version is sufficient ($\nabla_\mathbf{k} E_-(\mathbf{k}) = -\zeta \nabla_\mathbf{k} E_+(\mathbf{k})$, with $\zeta > 0$ *in*dependent of $\mathbf{k}$). It follows from the demand that the propagation distance before the pulse is canceled after the pulse at the same time for all $\mathbf{k}$-modes. Here, we do not mean that the time before and after the pulse (until the echo) should be the same, which would be the case for a true time-reversal. Instead, we allow all modes to come back faster or slower than before the pulse, but we require of them to come back at the same time. This is where the constant ζ enters.

Moreover, the quantitative echo strength (or equivalenty the transition amplitude) is derived and discussed with regard to as high as possible echoes: the pulse should be such that an initial eigenstate is mapped in the best possible way to its counterpart with negative energy. In the Bloch sphere, this requirement means that its pseudospin direction is supposed to be perpendicular to the one of the initial Hamiltonian. Moreover, during the pulse its strength needs to be the dominant energy scale. If these requirements are fulfilled, echoes close to 100% are possible.

The general findings are quantitatively confirmed in three example band structures: linear bands with different slopes for positive and negative energies, hyperbolic bands, and parabolic bands with different curvatures. Physical systems that can be described by theses examples are, among others, direct gap semi-conductors and Bernal stacked bilayer graphene.

With the general results of Sec. 4.2 and Sec. 5.1, any effective two-band system can be tested on its suitability for the QTM. With this abundance of possible systems, we are convinced that the QTM can be experimentally verified in some system or another.

In Chap. 6, we study the second and independent approach to a QTM for the

wave function, a Bose-Einstein condensate (BEC). We make use of the tunable nonlinearity of the Gross-Pitaevskii equation by a Feshbach resonance [112, 113]. A wave packet is effectively accelerated by changing the nonlinearity with a short time-dependent pulse. Depending on the choice of parameters, parts of the wave packet ($\leq 50\%$) can be made to invert their propagation direction, leading to an echo. The parameter space in which an echo is possible is investigated and in agreement with the analytically obtained critical values [114].

Qualitatively more promising than the QTM in a BEC is the quantum time lens (QTL), where the broadening of a wave packet due to the Schrödinger equation is refocused – similar to an optical lens which (re)focuses the beam of a laser, for instance. The mechanism is the same as for the echo, but here, fidelities close to 100% are in principle possible. Applying multiple QTL pulses, a wave packet can be kept in its initial width for a longer time. Even solitonic solutions can be achieved (approximately), where the initial shape is "freezed" for up to $100,000$ pulses in our simulations. Our simulations with nowadays experimentally feasible parameters show that both, QTM and QTL in a BEC are in reach, if not already possible in state of the art BEC experiments.

Finally, we investigate zitterbewegung in graphene in the presence of time-dependent potentials, with special regard to its decay for finite width wave packets. In the static case, the decay is well-known and stems from the **k**-dependence of the modes of the zitterbewegung and the related dephasing. Equivalently, the decay can be explained by the separation of sub-wave packets with positive and negative energy, whose interference is the reason for the zitterbewegung. When those sub-wave packets do not overlap anymore, they also do not interfere and thus, there is no zitterbewegung.

The time-dependent driving is hoped to have a similar effect as in a damped harmonic oscillator. Without driving, the oscillations die over time, but a sinusoidal driving can keep them alive. In a two-dimensional electron gas with driven Rashba spin-orbit coupling, such persistent modes have been proposed [139], whereas in graphene, a time-dependent electromagnetic field implemented in the Hamiltonian by a vector potential generates a multimode zitterbewegung but can only prolong its lifetime for a finite amount of time [140].

Instead, we investigate the effect of a sinusoidal mass gap ($\propto \sigma_z$) in graphene. Indeed, first order time-dependent perturbation predicts a persistent, harmonic oscillation with a single frequency – the driving frequency. Consulting the rotating wave approximation (RWA) and considering the limit of high driving frequencies (HDF), we also predict a multimode zitterbewegung. All analytically predicted frequencies of the zitterbewegung are confirmed by simulation within their respective regime of validity, including unpredicted higher orders in ω_D. Moreover, we find that some of theses modes are persistent, i.e. non-decaying, at least on the considered time-scales in the simulation. The fact that all of the surviving modes are **k**-*in*dependent suggests that they are truly persistent modes, at least in our the clean setup, where the decay only stems from the dephasing (**k**-dependence) of the modes in the wave packet. The theoretically found persistent modes of the zitterbewegung might help to facilitate the experimental evidence of zitterbewegung in graphene.

Furthermore, we propose a different setup to *revive* the initial zitterbewegung. As mentioned above, the decay of the zitterbewegung of wave packets is due to the separation of the sub-wave packets. Thus, we have to find a way to invert the motion of theses wave packets. Luckily, this is exactly what we have discussed in Chaps. 3 to 5: the QTM, where we use a time-dependent pulse to change the occupation bands leading to an inversion of the velocity. Indeed, we show analytically that the zitterbewegung is revived by a mass pulse ($\propto \sigma_z$) and derive its echo strength. The simulation of pristine and gapped graphene confirm the analytical calculations quantitatively. Moreover, we exemplarily show in the case of disorder where the zitterbewegung echo strength decays with the same rate as discussed above, that all results of Chaps. 3 to 5 are (very likely to be) directly transferable to the proposed revival of the zitterbewegung. With this, we have found a new way to experimentally verify the QTM mechanism.

To give an outlook for future research, we want to start with possible applications of the QTM. Since echoes with high fidelities are in principle possible, applying the QTM pulse several times is not a problem. With a periodic kicking, a time-lattice is generated. From a basic research point of view, this is exciting, since lattice effects known from spatially periodic structures, like Bloch oscillations, are in principle also possible in the time-domain. Moreover, periodic kicking can be used to effectively generate a discrete quantum random walk for a continuous wave packet. Such discrete quantum walks are, among others, important in quantum computing [96–98].

Another interesting point for further research is the analogy of the zitterbewegung echo with the Hahn echo, which is known since the 1950's. The well-known protocols initially developed for the spin echo are possibly directly transferable to the revival of the zitterbewegung, e.g. to apply gradients to make the frequency of the zitterbewegung position dependent. The position dependence of the frequency can in turn be used to extract locally system parameters like the elastic scattering time. With the recent first experimental evidence of zitterbewegung in a solid state system [134] – despite the fact that it deals with the jittery motion of an ensemble of electrons instead of the single particle interference due to the superposition of particle- and antiparticle-like states – a completely new field opens here with an abundance of topics to research and possible technical applications.

Appendix A

Calculating overlaps for the transition amplitude in graphene

This chapter is to outsource the details of the calculation for the transition amplitude in Sec. 3.1. Using the explicit form of the eigenenergies of Eqs. (3.2) and (3.11) and the eigenstates of Eqs. (3.3) and (3.12), the overlap between the different eigenstates at the same $\mathbf{k}$ yields:

$$\begin{aligned}\langle\varphi_{\mathbf{k},s}|\chi_{\mathbf{k},s'}\rangle &= \frac{1}{\sqrt{2}}\frac{1}{\sqrt{2}\sqrt{1+\kappa^2+s'\sqrt{1+\kappa^2}}}\begin{pmatrix}1\\ s\mathrm{e}^{i\gamma_{\mathbf{k}}}\end{pmatrix}^{\dagger}\begin{pmatrix}1+s'\sqrt{1+\kappa^2}\\ \kappa\,\mathrm{e}^{i\gamma_{\mathbf{k}}}\end{pmatrix}\\ &= \frac{1}{2}\frac{1+s'\sqrt{1+\kappa^2}+s\kappa}{\sqrt{1+\kappa^2+s'\sqrt{1+\kappa^2}}}\end{aligned} \tag{A.1}$$

Therefore, the product of scalar products in Eq. (3.15) yields:

$$\begin{aligned}P =&\langle\varphi_{\mathbf{k},s''}|\chi_{\mathbf{k},s'}\rangle\langle\chi_{\mathbf{k},s'}|\varphi_{\mathbf{k},s}\rangle\\ =&\frac{1}{4}\frac{1+s'\sqrt{1+\kappa^2}+s''\kappa}{\sqrt{1+\kappa^2+s'\sqrt{1+\kappa^2}}}\cdot\frac{1+s'\sqrt{1+\kappa^2}+s\kappa}{\sqrt{1+\kappa^2+s'\sqrt{1+\kappa^2}}}\\ =&\frac{1}{4}\frac{2+\kappa^2(1+ss'')+2s'\sqrt{1+\kappa^2}+\kappa(s+s'')\left(1+s'\sqrt{1+\kappa^2}\right)}{1+\kappa^2+s'\sqrt{1+\kappa^2}}\\ =&\frac{1}{4}\frac{2+\kappa^2(1+ss'')+2s'\sqrt{1+\kappa^2}+\kappa(s+s'')\left(1+s'\sqrt{1+\kappa^2}\right)}{s'\sqrt{1+\kappa^2}\left(s'\sqrt{1+\kappa^2}+1\right)}\\ =&\frac{1}{4}\left(\frac{(2+\kappa(s+s''))(1+s'\sqrt{1+\kappa^2})}{s'\sqrt{1+\kappa^2}\left(s'\sqrt{1+\kappa^2}+1\right)}+\frac{\kappa^2(1+ss'')}{s'\sqrt{1+\kappa^2}\left(s'\sqrt{1+\kappa^2}+1\right)}\right)\\ =&\frac{s'}{4\sqrt{1+\kappa^2}}\left(2+\kappa(s+s'')+\frac{\kappa^2(1+ss'')}{s'\sqrt{1+\kappa^2}+1}\right)\end{aligned} \tag{A.2}$$

Up to now, only arithmetic operation were performed, first expanding the product in the numerator with collecting terms of similar shape and using $(s^{(\prime)})^2=1$, then factorizing the denominator and splitting up the fraction to be able to cancel single factors. The ultimate goal is to explicitly sum over s' in Eq. (3.15) using sine and cosine functions, which is why we want to get rid of s' in the denominator. This is already achieved in the first summand in Eq. (A.2), but the second one must be

extended accordingly.

$$\begin{aligned}
P =& \frac{s'}{4\sqrt{1+\kappa^2}} \left(2 + \kappa(s + s'') + \frac{\kappa^2(1+ss'')\left(s'\sqrt{1+\kappa^2}-1\right)}{\left(s'\sqrt{1+\kappa^2}+1\right)\left(s'\sqrt{1+\kappa^2}-1\right)} \right) \\
=& \frac{s'}{4\sqrt{1+\kappa^2}} \left(2 + \kappa(s + s'') + \frac{\kappa^2(1+ss'')\left(s'\sqrt{1+\kappa^2}-1\right)}{1+\kappa^2-1} \right) \\
=& \frac{s'}{4\sqrt{1+\kappa^2}} \left(2 + \kappa(s + s'') + (1+ss'')\left(s'\sqrt{1+\kappa^2}-1\right) \right) \\
=& \frac{(s')^2(1+ss'')\sqrt{1+\kappa^2}}{4\sqrt{1+\kappa^2}} + \frac{s'}{4\sqrt{1+\kappa^2}} \left(2 + s\kappa(1+ss'') - (1+ss'')\right) \\
=& \frac{1+ss''}{4} + s' \cdot \frac{1+ss''}{4} \cdot \frac{s\kappa}{\sqrt{1+\kappa^2}} + s' \cdot \frac{2-(1+ss'')}{4\sqrt{1+\kappa^2}} \\
=& \frac{\delta_{ss''}}{2} + s' \cdot \frac{\delta_{ss''}}{2} \cdot \frac{s\kappa}{\sqrt{1+\kappa^2}} + s' \cdot \frac{1-\delta_{ss''}}{2\sqrt{1+\kappa^2}}
\end{aligned} \tag{A.3}$$

The important term for the echo is the last one, where the initial state (s) switches band ($s'' = -s$), i.e. the propagation changes direction ($\mathbf{v} \to -\mathbf{v}$).

Appendix B

Matrix elements of the Pauli matrices in the basis of (gapped) graphene eigenstates

Pristine graphene

Using the eigenstate of the graphene Hamiltonian ($H = \hbar v_F \mathbf{k} \cdot \boldsymbol{\sigma}$),

$$\langle \mathbf{k} \mid \varphi_{\mathbf{k},s} \rangle = \frac{1}{\sqrt{2}} \begin{pmatrix} 1 \\ s\, \mathrm{e}^{i\gamma_{\mathbf{k}}} \end{pmatrix}, \tag{B.1}$$

with $s = \pm 1$, we state the matrix elements of the Pauli matrices in this basis for a given $\mathbf{k}$, as needed in several instances in this thesis, e.g. for the expectation value of the velocity operator.

Diagonal terms:

$$\langle \varphi_{\mathbf{k},s} \mid \sigma_x \mid \varphi_{\mathbf{k},s} \rangle = s\frac{k_x}{k}, \tag{B.2}$$

$$\langle \varphi_{\mathbf{k},s} \mid \sigma_y \mid \varphi_{\mathbf{k},s} \rangle = s\frac{k_y}{k}, \tag{B.3}$$

$$\langle \varphi_{\mathbf{k},s} \mid \sigma_z \mid \varphi_{\mathbf{k},s} \rangle = 0. \tag{B.4}$$

Off-diagonal terms:

$$\langle \varphi_{\mathbf{k},s} \mid \sigma_x \mid \varphi_{\mathbf{k},-s} \rangle = -is\frac{k_y}{k}, \tag{B.5}$$

$$\langle \varphi_{\mathbf{k},s} \mid \sigma_y \mid \varphi_{\mathbf{k},-s} \rangle = is\frac{k_x}{k}, \tag{B.6}$$

$$\langle \varphi_{\mathbf{k},s} \mid \sigma_z \mid \varphi_{\mathbf{k},-s} \rangle = 1. \tag{B.7}$$

Gapped graphene

We state the matrix elements of the Pauli matrices for a given $\mathbf{k}$, as needed in several instances in this this, using the basis of eigenstates of the gapped graphene

Hamiltonian ($H = \hbar v_F \mathbf{k} \cdot \boldsymbol{\sigma} + M\sigma_z$),

$$\langle \mathbf{k} \mid \chi_{\mathbf{k},s} \rangle = \frac{1}{\sqrt{2}\sqrt{1+\kappa^2+s\sqrt{1+\kappa^2}}} \begin{pmatrix} 1+s\sqrt{1+\kappa^2} \\ \kappa\, \mathrm{e}^{i\gamma_{\mathbf{k}}} \end{pmatrix}, \tag{B.8}$$

with $\kappa = \hbar v_F k/M$.

Note that depending on the section of the thesis, the gapped graphene state can also be called $|\varphi_{\mathbf{k},s}\rangle$ instead of $|\chi_{\mathbf{k},s}\rangle$, e.g. if the initial Hamiltonian is already gapped.

Diagonal terms:

$$\langle \chi_{\mathbf{k},s} \mid \sigma_x \mid \chi_{\mathbf{k},s} \rangle = \frac{s\kappa}{\sqrt{1+\kappa^2}} \frac{k_x}{k}, \tag{B.9}$$

$$\langle \chi_{\mathbf{k},s} \mid \sigma_y \mid \chi_{\mathbf{k},s} \rangle = \frac{s\kappa}{\sqrt{1+\kappa^2}} \frac{k_y}{k}, \tag{B.10}$$

$$\langle \chi_{\mathbf{k},s} \mid \sigma_z \mid \chi_{\mathbf{k},s} \rangle = \frac{s}{\sqrt{1+\kappa^2}}. \tag{B.11}$$

Off-diagonal terms:

$$\langle \chi_{\mathbf{k},s} \mid \sigma_x \mid \chi_{\mathbf{k},-s} \rangle = \frac{1}{\sqrt{1+\kappa^2}} \frac{k_x}{k} + si\, \frac{k_y}{k}, \tag{B.12}$$

$$\langle \chi_{\mathbf{k},s} \mid \sigma_y \mid \chi_{\mathbf{k},-s} \rangle = -si\, \frac{k_x}{k} + \frac{1}{\sqrt{1+\kappa^2}} \frac{k_y}{k}, \tag{B.13}$$

$$\langle \chi_{\mathbf{k},s} \mid \sigma_z \mid \chi_{\mathbf{k},-s} \rangle = \frac{-\kappa}{\sqrt{1+\kappa^2}}. \tag{B.14}$$

Appendix C

Normalization factor in the disorder potential

In this appendix, we want to show that the normalization factor $\mathcal{N}$ in the disorder potential V_{imp} of Eq. (4.1) in Sec. 4.1.1 simplifies for a lattice with infinitely many points to

$$\mathcal{N} = \sqrt{\frac{\pi}{2}} \frac{l_0}{\sqrt{dx \cdot dy}}. \tag{C.1}$$

Thus, the normalization is (approximately) independent on the actual realization of V_{imp} which simplifies the calculation for the scattering time.

As stated in Sec. 4.1.1, $\mathcal{N}$ is given by

$$\mathcal{N} = \left[\frac{1}{A} \int_A \mathrm{d}^2 r \left(\sum_{i=1}^{N} \beta_i \mathrm{e}^{-\frac{(\mathbf{r}-\mathbf{r}_i)^2}{l_0^2}} \right)^2 \right]^{\frac{1}{2}}, \tag{C.2}$$

where the sum runs over all grid points. To get rid of the square root, we consider $\mathcal{N}^2$, perform the square of the integral explicitly and change order of summation and integration:

$$\mathcal{N}^2 = \frac{1}{A} \sum_{i,j=1}^{N} \beta_i \beta_j \int_A \mathrm{d}^2 r \, \mathrm{e}^{-\frac{(\mathbf{r}-\mathbf{r}_i)^2}{l_0^2}} \mathrm{e}^{-\frac{(\mathbf{r}-\mathbf{r}_j)^2}{l_0^2}}. \tag{C.3}$$

The integral is equivalent in both spatial directions which is why we only consider the x-direction:

$$\int_{-\infty}^{\infty} \mathrm{d}x \, \mathrm{e}^{-\frac{(x-x_i)^2+(x-x_j)^2}{l_0^2}} = \int_{-\infty}^{\infty} \mathrm{d}x \, \mathrm{e}^{-\frac{2x^2-2x(x_i+x_j)+x_i^2+x_j^2}{l_0^2}} = \int_{-\infty}^{\infty} \mathrm{d}x \, \mathrm{e}^{-\frac{2}{l_0^2}\left[x^2-x(x_i+x_j)+\frac{x_i^2+x_j^2}{2}\right]}. \tag{C.4}$$

By completing the square we obtain

$$
\begin{aligned}
&\int_{-\infty}^{\infty} \mathrm{d}x\, \exp\left\{-\frac{2}{l_0^2}\left[\left(x-\frac{x_i+x_j}{2}\right)^2-\frac{(x_i+x_j)^2}{4}+\frac{x_i^2+x_j^2}{2}\right]\right\}\\
&=\int_{-\infty}^{\infty} \mathrm{d}x\, \exp\left\{-\frac{2}{l_0^2}\left(x-\frac{x_i+x_j}{2}\right)^2\right\}\exp\left\{-\frac{2}{l_0^2}\left(\frac{x_i^2+x_j^2-2x_ix_j}{4}\right)\right\}\\
&=\exp\left\{-\frac{(x_i-x_j)^2}{2l_0^2}\right\}\underbrace{\int_{-\infty}^{\infty} \mathrm{d}x\, \exp\left\{-\frac{2}{l_0^2}\left(x-\frac{x_i+x_j}{2}\right)^2\right\}}_{\sqrt{\pi/2}l_0}\\
&=\sqrt{\frac{\pi}{2}}l_0\,\mathrm{e}^{-\frac{(x_i-x_j)^2}{2l_0^2}}. \qquad \text{(C.5)}
\end{aligned}
$$

Thus, Eq. (C.3) becomes

$$\mathcal{N}^2=\frac{l_0^2}{A}\frac{\pi}{2}\sum_{i,j=1}^{N}\beta_i\beta_j\mathrm{e}^{-\frac{(\mathbf{r}_i-\mathbf{r}_j)^2}{2l_0^2}}. \qquad \text{(C.6)}$$

Now, we make use of the fact that the random variable β is normally distributed, which means

$$\overline{\beta}=\lim_{n\to\infty}\frac{1}{n}\sum_{i=1}^{n}\beta_i=0, \qquad \text{(C.7)}$$

$$\mathrm{Var}(\beta)=\lim_{n\to\infty}\frac{1}{n}\sum_{i=1}^{n}(\beta_i-\overline{\beta})^2=\lim_{n\to\infty}\frac{1}{n}\sum_{i=1}^{n}\beta_i^2=1. \qquad \text{(C.8)}$$

Note that usually, one needs the probability distribution (density) p in the sum (integral) to calculate the variance and the expectation value for a discrete (continuous) random variable. In this case, p is not needed explicitly because some value of β has the appropriate probability to be chosen and is therefore implicitly hidden in the random choice of β. Due to the law of large numbers, the relative appearance of each value of β in Eqs. (C.7) and (C.8) corresponds to the probability to find this β and therefore both equations are true.

Consequently, the sum of the product of two normally distributed random variables on our lattice sites is 0 as long as they are independent, which is obviously not the case if they are at the same site $i=j$:

$$\lim_{n\to\infty}\frac{1}{n}\sum_{i,j=1}^{n}\beta_i\beta_j=\lim_{n\to\infty}\frac{1}{n}\left(\sum_{i=1}^{n}\beta_i^2+\sum_{i=1}^{n}\beta_i\sum_{\substack{j=1\\ j\neq i}}^{n}\beta_j\right)=1+0=1. \qquad \text{(C.9)}$$

To use Eq. (C.9) in Eq. (C.6), we still have to show that the exponential factor in Eq. (C.6) does not play a role for impurity potentials smoothed on a short length scale, i.e. $l_0 \ll \sqrt{A}$. For that reason, we look at all pairs of sites with a given distance R. For $R \lesssim \sqrt{A}$, and thus $R \gg l_0$, the exponential factor is negligible and the terms do not contribute.

In the other case, for $R \ll \sqrt{A}$, the number of these pairs is of the order of the number of lattice sites N, because every lattice points, which is not near the edge, has 4 neighbors with the same distance and the number of points near the edge can be neglected for $R \ll \sqrt{A}$. Since we assume a large lattice, i.e. $N \gg 1$, we can make use of the averaging effects of β for every R and we show that for $i \neq j$, i.e. $R \neq 0$, the terms are averaged out,

$$\sum_{\substack{i,j=1 \\ i \neq j}}^{n} \beta_i \beta_j \mathrm{e}^{-\frac{(\mathbf{r}_i - \mathbf{r}_j)^2}{2l_0^2}} = \sum_{R \neq 0} \mathrm{e}^{-\frac{R^2}{2l_0^2}} \sum_{\substack{i,j \\ |\mathbf{r}_i - \mathbf{r}_j| = R}} \beta_i \beta_j \approx 0, \tag{C.10}$$

where the last sum is 0 due to Eq. (C.9). Thus, only the terms $i = j$, i.e. $R = 0$, survive in Eq. (C.6) and $\mathcal{N}^2$ becomes

$$\mathcal{N}^2 = \frac{\pi}{2} \frac{l_0^2}{A} \sum_{i,j=1}^{N} \beta_i \beta_j \mathrm{e}^{-\frac{(\mathbf{r}_i - \mathbf{r}_j)^2}{2l_0^2}} = \frac{\pi}{2} \frac{l_0^2}{A} \underbrace{\sum_{i=1}^{N} \beta_i^2}_{\approx N} \approx \frac{\pi}{2} \frac{l_0^2 N}{A} = \frac{\pi}{2} \frac{l_0^2}{dx \cdot dy}, \tag{C.11}$$

which is the result which was to be proven.

To conclude, we showed in this appendix that for a lattice with many grid points, the normalization $\mathcal{N}$ becomes independent on the given realization of the impurity potential and has the form given in Eq. (4.3).

Appendix D

Time-dependent perturbation theory and the interaction picture

Interaction picture

In this subsection, we show the very basic properties of the interaction picture, most of all those which are helpful in the derivation of time-dependent perturbation theory. For simplicity, the reference time where Schrödinger and interaction picture coincide is set to $t = 0$.

Assume that for the time-dependent Hamiltonian

$$H = H_0 + V(t) = H_0 + H_1(t), \tag{D.1}$$

the eigenvalues and eigenfunctions of the time-independent part are known to be

$$H_0|n\rangle = E_n|n\rangle. \tag{D.2}$$

The transition from Schrödinger picture (state $|\psi(t)\rangle_S$ and arbitrary operator A_S) to the interaction picture (state $|\psi(t)\rangle_I$ and arbitrary operator $A_I(t)$) is done by the following operations

$$|\psi;t\rangle_I = \mathrm{e}^{iH_0t/\hbar}|\psi;t\rangle_S \tag{D.3}$$

$$A_I(t) = \mathrm{e}^{iH_0t/\hbar}A_S\mathrm{e}^{-iH_0t/\hbar}. \tag{D.4}$$

The time evolution of the states in the interaction picture is determined by V_I

$$i\hbar\frac{\partial}{\partial t}|\alpha;t\rangle_I = V_I(t)|\alpha;t\rangle_S, \tag{D.5}$$

whereas for the operators, only H_0 is important

$$\frac{dA_I}{dt} = \frac{1}{i\hbar}\left[A_I, H_0\right]. \tag{D.6}$$

Time-dependent perturbation theory

Here, we want to remind the reader of time-dependent perturbation theory and derive the transition coefficients needed in Subsec. 7.4.1 without going too much

into details. For a more in-depth explanation of time-dependent perturbation theory, we direct the kind reader to most standard textbooks about quantum mechanics, e.g. Sakurai and Napolitano [143], which was used as a guideline for creating this appendix and where we borrowed most of the notation.

The Hamiltonian is the same as in Eq. (D.1) with known eigenstates and energies of the time-independent part H_0 as in Eq. (D.2). For a given initial state at $t = 0$,

$$|\alpha\rangle = |\alpha; t = 0\rangle = \sum_n c_n(0)|n\rangle, \tag{D.7}$$

we want to find the time-evolution

$$|\alpha; t\rangle = \sum_n c_n(t)\mathrm{e}^{-iE_n t}|n\rangle, \tag{D.8}$$

where the prefactor is split as a matter of prudence in a time-dependent phase due to the time-independent Hamiltonian such that the evolution of the coefficients $c_n(t)$ is a consequence only of the time-dependent part $V(t)$.

In the interaction picture, this choice of splitting leads to (compare Eq. (D.3))

$$|\alpha; t\rangle_I = \sum_n c_n(t)|n\rangle, \tag{D.9}$$

and thus

$$c_n(t) = \langle n \mid \alpha; t\rangle_I, \tag{D.10}$$

where we use $|n\rangle$ as basis set which is possible for eigenstates of a Hermitian operator. Since $|n\rangle$ are time-independent states, the time evolution of $c_n(t)$ is similar to the one of kets in the interaction picture (see Eq. (D.5))

$$\begin{aligned} i\hbar\frac{\partial}{\partial t}c_n(t) = i\hbar\frac{\partial}{\partial t}\langle n \mid \alpha; t\rangle_I &= \langle n \mid V_I \mid \alpha; t\rangle_I \\ &= \sum_m \langle n \mid V_I \mid m\rangle\langle m \mid \alpha; t\rangle_I \\ &= \sum_m \mathrm{e}^{i(E_n - E_m)t/\hbar} V_{nm}\langle m \mid \alpha; t\rangle_I \\ &= \sum_m V_{nm}\mathrm{e}^{i(E_n - E_m)t/\hbar} c_m(t), \end{aligned} \tag{D.11}$$

where $V_{nm} = \langle n|V|m\rangle$ is the matrix element of the operator $V \equiv V_S$ in the Schrödinger picture. The coupled differential equations of Eq. (D.11) are usually not exactly solvable, which is why we turn to perturbation theory.

With the time evolution operator in the interaction picture, which is defined by

$$|\alpha; t\rangle_I = U_I(t)|\alpha; 0\rangle_I, \tag{D.12}$$

we can rewrite the coefficients $c_n(t)$ from Eq. (D.10) in terms of U_I:

$$c_n(t) = \langle n \mid U_I \mid \alpha; 0\rangle_I. \tag{D.13}$$

Using the Dyson series of U_I, which is given by an iteration of the formal solution of the Schrödinger equation

$$U_I(t) = 1 - \frac{i}{\hbar} \int_0^t V_I(t') U_I(t') \, \mathrm{d}t', \tag{D.14}$$

we obtain a series expansion of U_I in powers of the (small) time-dependent potential $V(t)$:

$$U_I(t) = 1 - \frac{i}{\hbar} \int_0^t V_I(t') \, \mathrm{d}t' + \left(-\frac{i}{\hbar} \right)^2 \int_0^t \mathrm{d}t' \int_0^{t'} \mathrm{d}t'' \, V_I(t') V_I(t'') + \ldots, \tag{D.15}$$

Inserting Eq. (D.15) in Eq. (D.12), we find an expansion of the occupation coefficients $c_n(t)$ in powers of the perturbation V:

$$\begin{aligned} c_n(t) = &\quad \langle n \mid \alpha; 0 \rangle &- &\quad \frac{i}{\hbar} \int_0^t \mathrm{d}t' \langle n \mid V_I(t') \mid \alpha; 0 \rangle &+ \ldots \\ = &\quad c_n^{(0)} &+ &\quad c_n^{(1)}(t) &+ \ldots \end{aligned} \tag{D.16}$$

Thus, for the occupation coefficient in first order perturbation theory $c_n^{(1)}(t)$, we arrive at

$$c_n^{(1)}(t) = -\frac{i}{\hbar} \sum_m c_m \int_0^t \mathrm{d}t' \mathrm{e}^{i \omega_{nm} t'} \, \langle n \mid V(t') \mid m \rangle, \tag{D.17}$$

with $\omega_{nm} = (E_n - E_m)/\hbar$. All appearing quantities of Eq. (D.17) are either given by the knowledge of the time-independent Hamiltonian H_0, the time-dependent potential in the Schrödinger picture and the initial wave function $|\alpha; 0\rangle = \sum_m c_m |m\rangle$ and therefore, it can be calculated for a given system.

For an effective two-level system ($n \in \{-1, 1\}$), Eq. (D.17) further simplifies since there are only two summands

$$c_n^{(1)}(t) = -\frac{i}{\hbar} \int_0^t \mathrm{d}t' \left(\langle n \mid V(t') \mid n \rangle + \mathrm{e}^{i \omega_{n,-n} t'} \, \langle n \mid V(t') \mid -n \rangle \right). \tag{D.18}$$

The main result of this appendix is Eq. (D.18), which will be used in Subsec. 7.4.1 to approximate the time-dependent wave function which is needed to calculate the Zitterbewegung.

Bibliography

[1] Heller H., *Gemessene Zeit - gefühlte Zeit*, LIT Verlag Münster (2006).

[2] Eddington A.S., *The nature of the physical world*, New York, The Macmillan Company; Cambridge, Eng., The University Press (1928).

[3] Boltzmann L., *Über die Beziehung eines allgemeinen mechanischen Satzes zum zweiten Hauptsatze der Wärmetheorie*, Sitzungberichte der Akademie der Wissenschaften **II**, 67 (1877).

[4] Loschmidt J., *Über den Zustand des Wärmegleichgewichts eines Systems von Körpern mit Rücksicht auf die Schwerkraft*, Sitzungberichte der Akademie der Wissenschaften **II**, 128 (1876).

[5] Baez J., *Open questions in physics*, Usenet Physics FAQ. University of California, Riverside: Department of Mathematics. "http://math.ucr.edu/home/baez/physics/General/open_questions.html". Retrieved Sept. 20 2017. (2012).

[6] Weinert F., *The Demons of Science: What They Can and Cannot Tell Us About Our World*, Springer (2016).

[7] Hahn E.L., *Spin Echoes*, Phys. Rev. **80**, 580 (1950).

[8] Bloch F., Hansen W.W., and Packard M., *Nuclear Induction*, Phys. Rev. **69**, 127 (1946).

[9] Bloch F., *Nuclear Induction*, Phys. Rev. **70**, 460 (1946).

[10] Purcell E.M., Torrey H.C., and Pound R.V., *Resonance Absorption by Nuclear Magnetic Moments in a Solid*, Phys. Rev. **69**, 37 (1946).

[11] Rooney W.D., Johnson G., Li X., Cohen E.R., Kim S.G., Ugurbil K., and Springer C.S., *Magnetic field and tissue dependencies of human brain longitudinal 1H2O relaxation in vivo*, Magnetic Resonance in Medicine **57**, 308 (2007).

[12] Lauterbur P.C., *Image Formation by Induced Local Interactions: Examples Employing Nuclear Magnetic Resonance*, Nature **242**, 190 (1973).

[13] Garroway A.N., Grannell P.K., and Mansfield P., *Image formation in NMR by a selective irradiative process*, Journal of Physics C: Solid State Physics **7**, L457 (1974).

[14] Zhang S., Olthoff A., and Frahm J., *Real-time magnetic resonance imaging of normal swallowing*, Journal of Magnetic Resonance Imaging **35**, 1372 (2012).

[15] Zoehrer F., Huellebrand M., Chitiboi T., Oechtering T., Sieren M., Frahm J., Hahn H.K., and Hennemuth A., *Real-time myocardium segmentation for the assessment of cardiac function variation*, Proc.SPIE **10137**, 10137 (2017).

[16] Fink M., *Time Reversed Acoustics*, Physics Today **50**, 34 (1997).

[17] Fink M., *Time-reversed acoustics*, Sci.Am. **281**, 91 (1999).

[18] Lerosey G., de Rosny J., Tourin A., and Fink M., *Focusing Beyond the Diffraction Limit with Far-Field Time Reversal*, Science **315**, 1120 (2007).

[19] Mosk A.P., Lagendijk A., Lerosey G., and Fink M., *Controlling waves in space and time for imaging and focusing in complex media*, Nat. Phot. **6**, 283 (2012).

[20] Fink M., *Time reversal of ultrasonic fields. I. Basic principles*, IEEE Transactions on Ultrasonics, Ferroelectrics, and Frequency Control **39**, 555 (1992).

[21] Draeger C. and Fink M., *One-Channel Time Reversal of Elastic Waves in a Chaotic 2D-Silicon Cavity*, Phys. Rev. Lett. **79**, 407 (1997).

[22] Lerosey G., de Rosny J., Tourin A., Derode A., Montaldo G., and Fink M., *Time Reversal of Electromagnetic Waves*, Phys. Rev. Lett. **92**, 193904 (2004).

[23] Przadka A., Feat S., Petitjeans P., Pagneux V., Maurel A., and Fink M., *Time Reversal of Water Waves*, Phys. Rev. Lett. **109**, 064501 (2012).

[24] Chabchoub A. and Fink M., *Time-Reversal Generation of Rogue Waves*, Phys. Rev. Lett. **112**, 124101 (2014).

[25] Pastawski H.M., Danieli E.P., Calvo H.L., and Torres L.E.F.F., *Towards a time reversal mirror for quantum systems*, EPL **77**, 40001 (2007).

[26] Calvo H.L., Jalabert R.A., and Pastawski H.M., *Semiclassical Theory of Time-Reversal Focusing*, Phys. Rev. Lett. **101**, 240403 (2008).

[27] Calvo H.L. and Pastawski H.M., *Exact time-reversal focusing of acoustic and quantum excitations in open cavities: The perfect inverse filter*, EPL **89**, 60002 (2010).

[28] Yariv A., *Four wave nonlinear optical mixing as real time holography*, Opt. Commun. **25**, 23 (1978).

[29] Miller D.A.B., *Time reversal of optical pulses by four-wave mixing*, Opt. Lett. **5**, 300 (1980).

[30] Moshinsky M., *Diffraction in time*, Phys. Rev. **88**, 625 (1952).

[31] Gerasimov A.S. and Kazarnovskii M.V., *Possibility of observing nonstationary quantum-mechanical effects by means of ultracold neutrons*, Sov. Phys. JETP **44**, 892 (1976).

[32] Č. Brukner and Zeilinger A., *Diffraction of matter waves in space and in time*, Phys. Rev. A **56**, 3804 (1997).

[33] Mendonça J.T. and Shukla P.K., *Time Refraction and Time Reflection: Two Basic Concepts*, Phys. Scripta **65**, 160 (2002).

[34] del Campo A., Garcia-Calderón G., and Muga J.G., *Quantum transients*, Phys. Rep. **476**, 1 (2009).

[35] Goussev A., *Huygens-Fresnel-Kirchhoff construction for quantum propagators with application to diffraction in space and time*, Phys. Rev. A **85**, 013626 (2012).

[36] Haslinger P., Dorre N., Geyer P., Rodewald J., Nimmrichter S., and Arndt M., *A universal matter-wave interferometer with optical ionization gratings in the time domain*, Nat. Phys. **9**, 144 (2013).

[37] Sivan Y. and Pendry J.B., *Time Reversal in Dynamically Tuned Zero-Gap Periodic Systems*, Phys. Rev. Lett. **106**, 193902 (2011).

[38] Sivan Y. and Pendry J.B., *Theory of wave-front reversal of short pulses in dynamically tuned zero-gap periodic systems*, Phys. Rev. A **84**, 033822 (2011).

[39] Sivan Y. and Pendry J.B., *Broadband time-reversal of optical pulses using a switchable photonic-crystal mirror*, Opt. Express **19**, 14502 (2011).

[40] Chumak A.V., Tiberkevich V.S., Karenowska A.D., Serga A.A., Gregg J.F., Slavin A.N., and Hillebrands B., *All-linear time reversal by a dynamic artificial crystal*, Nat. Common. **1**, 141 (2010).

[41] Karenowska A.D., Gregg J.F., Tiberkevich V.S., Slavin A.N., Chumak A.V., Serga A.A., and Hillebrands B., *Oscillatory Energy Exchange between Waves Coupled by a Dynamic Artificial Crystal*, Phys. Rev. Lett. **108**, 015505 (2012).

[42] Martin J., Georgeot B., and Shepelyansky D.L., *Cooling by Time Reversal of Atomic Matter Waves*, Phys. Rev. Lett. **100**, 044106 (2008).

[43] Martin J., Georgeot B., and Shepelyansky D.L., *Time Reversal of Bose-Einstein Condensates*, Phys. Rev. Lett. **101**, 074102 (2008).

[44] Ullah A. and Hoogerland M.D., *Experimental observation of Loschmidt time reversal of a quantum chaotic system*, Phys. Rev. E **83**, 046218 (2011).

[45] Bacot V., Labousse M., Eddi A., Fink M., and Fort E., *Time reversal and holography with spacetime transformations*, Nat. Phys. **12**, 972 (2016).

[46] Krückl V., *Wave packets in mesoscopic systems: From time-dependent dynamics to transport phenomena in graphene and topological insulators*, Ph.D. thesis, Universität Regensburg, Germany (2013), the basic version of the algorithm is available at TQT Home [http://www.krueckl.de/#en/tqt.php].

[47] Wallace P.R., *The Band Theory of Graphite*, Phys. Rev. **71**, 622 (1947).

[48] Volkov B.A. and Pankratov O.A., *Two-dimensional massless electrons in an inverted contact*, JEPT Lett. **42**, 178 (1985).

[49] Pankratov O., *Supersymmetric inhomogeneous semiconductor structures and the nature of a parity anomaly in (2+1) electrodynamics*, Physics Letters A **121**, 360 (1987).

[50] McClure J.W., *Diamagnetism of Graphite*, Phys. Rev. **104**, 666 (1956).

[51] Haldane F.D.M., *Model for a Quantum Hall Effect without Landau Levels: Condensed-Matter Realization of the "Parity Anomaly"*, Phys. Rev. Lett. **61**, 2015 (1988).

[52] Semenoff G.W., *Condensed-Matter Simulation of a Three-Dimensional Anomaly*, Phys. Rev. Lett. **53**, 2449 (1984).

[53] Peierls R., *Quelques propriétés typiques des corps solides.*, Annales de l'institut Henri Poincaré (1935).

[54] Landau L.D., *Theory of phase transformations*, Phys. Z. Sowjetunion **11** (1937).

[55] Novoselov K.S., Geim A., Morozov S.V., Jiang D., Zhang Y., Dubonos S.V., Grigorieva I.V., and Firsov A.A., *Electric Field Effect in Atomically Thin Carbon Films*, Science **306**, 666 (2004).

[56] Meyer J.C., Geim A.K., Katsnelson M.I., Novoselov K.S., Booth T.J., and Roth S., *The structure of suspended graphene sheets*, Nature **446**, 60 (2007).

[57] Bommel A.V., Crombeen J., and Tooren A.V., *LEED and Auger electron observations of the SiC(0001) surface*, Surface Science **48**, 463 (1975).

[58] Berger C. et al., *Ultrathin Epitaxial Graphite: 2D Electron Gas Properties and a Route toward Graphene-based Nanoelectronics*, The Journal of Physical Chemistry B **108**, 19912 (2004).

[59] Choucair M., Thordarson P., and Stride J.A., *Gram-scale production of graphene based on solvothermal synthesis and sonication*, Nature Nanotechnology **4**, 30 (2009).

[60] Li D., Muller M.B., Gilje S., Kaner R.B., and Wallace G.G., *Processable aqueous dispersions of graphene nanosheets*, Nature Nanotechnology **3**, 101 (2008).

[61] Dean C.R. et al., *Boron nitride substrates for high-quality graphene electronics*, Nat Nano **5**, 722 (2010).

[62] Banszerus L., Schmitz M., Engels S., Goldsche M., Watanabe K., Taniguchi T., Beschoten B., and Stampfer C., *Ballistic Transport Exceeding 28 μm in CVD Grown Graphene*, Nano Letters **16**, 1387 (2016), pMID: 26761190.

[63] Sasaki K.i. and Saito R., *Pseudospin and Deformation-Induced Gauge Field in Graphene*, Progress of Theoretical Physics Supplement **176**, 253 (2008).

[64] Schakel A.M.J., *Relativistic quantum Hall effect*, Phys. Rev. D **43**, 1428 (1991).

[65] Neto A.H.C., Guinea F., Peres N.M.R., Novoselov K.S., and Geim A.K., *The electronic properties of graphene*, Rev. Mod. Phys. **81**, 109 (2009).

[66] Katsnelson M.I., Novoselov K.S., and Geim A.K., *Chiral tunnelling and the Klein paradox in graphene*, Nature Physics **2**, 620 (2006).

[67] Beenakker C.W.J., *Colloquium: Andreev reflection and Klein tunneling in graphene*, Rev. Mod. Phys. **80**, 1337 (2008).

[68] Novoselov K.S., Geim A.K., Morozov S.V., Jiang D., Katsnelson M.I., Grigorieva I.V., Dubonos S.V., and Firsov A.A., *Two-dimensional gas of massless Dirac fermions in graphene*, Nature **438**, 197 (2005).

[69] Zhang Y., Tan Y.W., Stormer H.L., and Kim P., *Experimental observation of the quantum Hall effect and Berry's phase in graphene*, Nature **438**, 201 (2005).

[70] Novoselov K.S. et al., *Room-Temperature Quantum Hall Effect in Graphene*, Science **315**, 1379 (2007).

[71] Goerbig M.O., *Electronic properties of graphene in a strong magnetic field*, Rev. Mod. Phys. **83**, 1193 (2011).

[72] Tal-Ezer H. and Kosloff R., *An accurate and efficient scheme for propagating the time dependent Schrödinger equation*, The Journal of Chemical Physics **81**, 3967 (1984).

[73] Kosloff R., *Propagation Methods for Quantum Molecular Dynamics*, Annual Review of Physical Chemistry **45**, 145 (1994).

[74] Nauts A. and Wyatt R.E., *New Approach to Many-State Quantum Dynamics: The Recursive-Residue-Generation Method*, Phys. Rev. Lett. **51**, 2238 (1983).

[75] Park T.J. and Light J.C., *Unitary quantum time evolution by iterative Lanczos reduction*, The Journal of Chemical Physics **85**, 5870 (1986).

[76] Lanczos C., *An Iteration method for the Solution of the Eigenvalue Problem of Linear Differential and Integral Operators*, J. Res. Natl. Bur. Stand. **45**, 255 (1950).

[77] Hochbruck M. and Lubich C., *On Krylov Subspace Approximations to the Matrix Exponential Operator*, SIAM Journal on Numerical Analysis **34**, 1911 (1997).

[78] Hasan M.Z. and Kane C.L., *Colloquium : Topological insulators*, Rev. Mod. Phys. **82**, 3045 (2010).

[79] Peres A., *Stability of quantum motion in chaotic and regular systems*, Phys. Rev. A **30**, 1610 (1984).

[80] Reck P., Gorini C., Goussev A., Krueckl V., Fink M., and Richter K., *Dirac quantum time mirror*, Phys. Rev. B **95**, 165421 (2017).

[81] Lee C., *Bouncing electrons off a time mirror*, ars technica, "https://arstechnica.com/science/2017/05/undoing-ravages-of-time-by-trapping-and-releasing-an-electron-wave/". Retrieved Oct. 27 2017. (2017).

[82] Choi C.Q., *Zaps from a Laser Could 'Reverse Time' on the Quantum Scale*, inside science, "https://www.insidescience.org/news/zaps-laser-could-reverse-time-quantum-scale". Retrieved Oct. 27 2017. (2017).

[83] Tarruell L., Greif D., Uehlinger T., Jotzu G., and Esslinger T., *Creating, moving and merging Dirac points with a Fermi gas in a tunable honeycomb lattice*, Nature **483**, 302 (2012).

[84] Weick G., Woollacott C., Barnes W.L., Hess O., and Mariani E., *Dirac-like Plasmons in Honeycomb Lattices of Metallic Nanoparticles*, Phys. Rev. Lett. **110**, 106801 (2013).

[85] Jacqmin T. et al., *Direct Observation of Dirac Cones and a Flatband in a Honeycomb Lattice for Polaritons*, Phys. Rev. Lett. **112**, 116402 (2014).

[86] Bocquillon E. et al., *Electron quantum optics in ballistic chiral conductors*, Annalen der Physik **526**, 1 (2014).

[87] Jullien T., Roulleau P., Roche B., Cavanna A., Jin Y., and Glattli D.C., *Quantum tomography of an electron*, Nature **514**, 603 (2014).

[88] Sun D., Wu Z.K., Divin C., Li X., Berger C., de Heer W.A., First P.N., and Norris T.B., *Ultrafast Relaxation of Excited Dirac Fermions in Epitaxial Graphene Using Optical Differential Transmission Spectroscopy*, Phys. Rev. Lett. **101**, 157402 (2008).

[89] Frank T., Gmitra M., and Fabian J., *Theory of electronic and spin-orbit proximity effects in graphene on Cu(111)*, Phys. Rev. B **93**, 155142 (2016).

[90] Gmitra M., Kochan D., Högl P., and Fabian J., *Trivial and inverted Dirac bands and the emergence of quantum spin Hall states in graphene on transition-metal dichalcogenides*, Phys. Rev. B **93**, 155104 (2016).

[91] Fistul M.V. and Efetov K.B., *Electromagnetic-Field-Induced Suppression of Transport through $n-p$ Junctions in Graphene*, Phys. Rev. Lett. **98**, 256803 (2007).

[92] Scholz A., Lòpez A., and Schliemann J., *Interplay between spin-orbit interactions and a time-dependent electromagnetic field in monolayer graphene*, Phys. Rev. B **88**, 045118 (2013).

[93] Usaj G., Perez-Piskunow P.M., Torres L.E.F.F., and Balseiro C.A., *Irradiated graphene as a tunable Floquet topological insulator*, Phys. Rev. B **90**, 115423 (2014).

[94] Higuchi T., Heide C., Ullmann K., Weber H.B., and Hommelhoff P., *Light-field driven currents in graphene*, Nature **550**, 224 (2017).

[95] Eisele M., Cocker T.L., Huber M.A., Plankl M., Viti L., Ercolani D., Sorba L., Vitiello M.S., and Huber R., *Ultrafast multi-terahertz nano-spectroscopy with sub-cycle temporal resolution*, Nat Photon **8**, 841 (2014).

[96] Kempe J., *Quantum random walks: An introductory overview*, Contemporary Physics **44**, 307 (2003).

[97] Grover L.K., *Quantum Mechanics Helps in Searching for a Needle in a Haystack*, Phys. Rev. Lett. **79**, 325 (1997).

[98] Grover L.K. and Sengupta A.M., *Classical analog of quantum search*, Phys. Rev. A **65**, 032319 (2002).

[99] Akkermans E. and Montambaux G., *Mesoscopic Physics of Electrons and Photons*, Cambridge University Press (2007).

[100] Hartung M., *Transport and Coherent Backscattering of Bose-Einstein Condensates in Mesoscopic Systems*, Ph.D. thesis, Universität Regensburg, Germany (2009).

[101] Adam S., Brouwer P.W., and Das Sarma S., *Crossover from quantum to Boltzmann transport in graphene*, Phys. Rev. B **79**, 201404 (2009).

[102] Goussev A., Jalabert R.A., Pastawski H.M., and Wisniacki D.A., *Loschmidt Echo*, Scholarpedia **7**, 11687 (2012).

[103] Jacquod P., Silvestrov P., and Beenakker C., *Golden rule decay versus Lyapunov decay of the quantum Loschmidt echo*, Phys. Rev. E **64**, 055203 (2001).

[104] Waltner D., *Semiclassical Approach to Mesoscopic Systems*, Ph.D. thesis, Universität Regensburg, Germany (2012).

[105] Hahn E., *Spin echo technique and apparatus* (1955), US Patent 2,705,790.

[106] Schliemann J., *Cyclotron motion in graphene*, New Journal of Physics **10**, 043024 (2008).

[107] Rusin T.M. and Zawadzki W., *Zitterbewegung of electrons in graphene in a magnetic field*, Phys. Rev. B **78**, 125419 (2008).

[108] Davis K.B., Mewes M.O., Andrews M.R., van Druten N.J., Durfee D.S., Kurn D.M., and Ketterle W., *Bose-Einstein Condensation in a Gas of Sodium Atoms*, Phys. Rev. Lett. **75**, 3969 (1995).

[109] Anderson M.H., Ensher J.R., Matthews M.R., Wieman C.E., and Cornell E.A., *Observation of Bose-Einstein Condensation in a Dilute Atomic Vapor*, Science **269**, 198 (1995).

[110] Bradley C.C., Sackett C.A., Tollett J.J., and Hulet R.G., *Evidence of Bose-Einstein Condensation in an Atomic Gas with Attractive Interactions*, Phys. Rev. Lett. **75**, 1687 (1995).

[111] Andersen J.O., *Theory of the weakly interacting Bose gas*, Rev. Mod. Phys. **76**, 599 (2004).

[112] Inouye S., Andrews M.R., Stenger J., Miesner H.J., Stamper-Kurn D.M., and Ketterle W., *Observation of Feshbach resonances in a Bose-Einstein condensate*, Nature **392**, 151 (1998).

[113] Roberts J.L., Claussen N.R., Burke J.P., Greene C.H., Cornell E.A., and Wieman C.E., *Resonant Magnetic Field Control of Elastic Scattering in Cold ^{85}Rb*, Phys. Rev. Lett. **81**, 5109 (1998).

[114] Goussev A., *private communications* (2015).

[115] Reck P., Gorini C., Goussev A., Krueckl V., Fink M., and Richter K., *Quantum time mirrors*, arXiv:1603.07503 (2016).

[116] Buchner T., *Wave packet refocusing in Gross-Pitaevskii equation.* Bachelor thesis (2015).

[117] Hauke A., *Refocussing of Wave Packets through Multiple Nonlinear Pulses.* Bachelor thesis (2015).

[118] Moser F., *Beating dispersion of quantum wave packets via nonlinear stroboscopic kicking.* Bachelor thesis (2017).

[119] Pitaevskii L. and Stringari S., *Bose-Einstein Condensation*, Oxford University Press (2003).

[120] Schwabl F., *Quantenmechanik*, Springer (2002).

[121] Cohen-Tannoudji C., Diu B., and Laloë F., *Quantenmechanik*, de Gruyter (2009).

[122] Schwindt J.M., *Tutorium Quantenmechanik*, Springer Spektrum (2013).

[123] Burger S., Bongs K., Dettmer S., Ertmer W., Sengstock K., Sanpera A., Shlyapnikov G.V., and Lewenstein M., *Dark Solitons in Bose-Einstein Condensates*, Phys. Rev. Lett. **83**, 5198 (1999).

[124] Schrödinger E., *Über die kräftefreie Bewegung in der relativistischen Quantenmechanik*, Sitz. Press. Akad. Wiss. Phys.-Math. **42**, 418 (1930).

[125] Zawadzki W. and Rusin T.M., *Zitterbewegung (trembling motion) of electrons in semiconductors: a review*, Journal of Physics: Condensed Matter **23**, 143201 (2011).

[126] Huang K., *On the Zitterbewegung of the Dirac Electron*, American Journal of Physics **20**, 479 (1952).

[127] Schliemann J., Loss D., and Westervelt R.M., *Zitterbewegung*, Phys. Rev. Lett. **94**, 206801 (2005).

[128] Schliemann J., Loss D., and Westervelt R.M., *Zitterbewegung*, Phys. Rev. B **73**, 085323 (2006).

[129] Zawadzki W. and Rusin T.M., *Nature of electron Zitterbewegung in crystalline solids*, Physics Letters A **374**, 3533 (2010).

[130] Zawadzki W., *One-dimensional semirelativity for electrons in carbon nanotubes*, Phys. Rev. B **74**, 205439 (2006).

[131] Katsnelson M.I., *Zitterbewegung, chirality, and minimal conductivity in graphene*, The European Physical Journal B - Condensed Matter and Complex Systems **51**, 157 (2006).

[132] Shi L.k., Zhang S.c., and Chang K., *Anomalous electron trajectory in topological insulators*, Phys. Rev. B **87**, 161115 (2013).

[133] Schliemann J., *Cyclotron motion and magnetic focusing in semiconductor quantum wells with spin-orbit coupling*, Phys. Rev. B **77**, 125303 (2008).

[134] Stepanov I., Ersfeld M., Poshakinskiy A.V., Lepsa M., Ivchenko E.L., Tarasenko S.A., and Beschoten B., *Coherent Electron Zitterbewegung*, arXiv:1612.06190 (2016).

[135] Gerritsma R., Kirchmair G., Zahringer F., Solano E., Blatt R., and Roos C.F., *Quantum simulation of the Dirac equation*, Nature **463**, 68 (2010).

[136] Qu C., Hamner C., Gong M., Zhang C., and Engels P., *Observation of Zitterbewegung in a spin-orbit-coupled Bose-Einstein condensate*, Phys. Rev. A **88**, 021604 (2013).

[137] LeBlanc L.J., Beeler M.C., Jiménez-García K., Perry A.R., Sugawa S., Williams R.A., and Spielman I.B., *Direct observation of zitterbewegung in a Bose–Einstein condensate*, New Journal of Physics **15**, 073011 (2013).

[138] Wang C., Gao C., Jian C.M., and Zhai H., *Spin-Orbit Coupled Spinor Bose-Einstein Condensates*, Phys. Rev. Lett. **105**, 160403 (2010).

[139] Ho C.S., Jalil M.B.A., and Tan S.G., *Persistent Zitterbewegung of electron wave packet in time-dependent Rashba system*, EPL (Europhysics Letters) **108**, 27012 (2014).

[140] Rusin T.M. and Zawadzki W., *Multimode behavior of electron Zitterbewegung induced by an electromagnetic wave in graphene*, Phys. Rev. B **88**, 235404 (2013).

[141] Lock J.A., *The Zitterbewegung of a free localized Dirac particle*, American Journal of Physics **47**, 797 (1979).

[142] Rusin T.M. and Zawadzki W., *Transient Zitterbewegung of charge carriers in mono- and bilayer graphene, and carbon nanotubes*, Phys. Rev. B **76**, 195439 (2007).

[143] Sakurai J. and Napolitano J., *Modern Quantum Mechanics*, Pearson (2011).

[144] Auletta G., Fortunato M., and Parisi G., *Quantum Mechanics*, Cambridge University Press (2009).

Acknowledgements

I want to express my sincere gratitude to all people that have accompanied me during the past years.

First and foremost, I would like to thank Prof. Dr. Klaus Richter for giving me the opportunity to work in his group. His supervision is a perfect balance in close guiding through physical problems with simultaneously encouraging self-initiated ideas and leaving enough freedom to develop an independent thought process. Moreover, thanks for the trust of letting me supervise Bachelor and Master students in their work. In turn, I also want thank the students who enriched the scientific experience either by direct collaboration that found its way into the thesis, or by extending my knowledge by related projects but in other directions. These are the project students Simon Maier and Joshua Mornhinweg, the Bachelor students Thomas Buchner, Andreas Hauke and Florian Moser (see Chap. 6) and the Master students Fabian Stoeger and Vanessa Junk.

Next, I want to express my gratitude to Cosimo Gorini for many fruitful discussions and his throughout constructive and strict criticism concerning the analytical work and Arseni Goussev for the close collaboration concerning the QTM in BECs. Equally, I want to thank Viktor Krueckl for making me familiar with his library TQT and competent help with all numerical issues.

Concerning directly the thesis, I am very grateful to Susanne Irmer, Raphael Kozlovsky, Jacob Fuchs, Ming-Hao Liu, Benjamin Geiger, Petra Högl, Tobias Frank and Anna Hench for proof reading individual chapters of the thesis and for many ideas to improve. Special thanks also to Quirin Hummel for the idea of including the movie of a simulation by using the footer as a flicker book (Daumenkino) and Marei Peischl for the help of its implementation.

Over the past years, I have been sharing offices with various colleagues and want to thank Dr. Viktor Krückl, Rhonald Burgos Atencia, Fahriye Nur Gursoy and Andreas Bereczuk for a pleasant working atmosphere. Likewise, thanks to the whole group of Prof. Richter and Prof. Fabian for the overall great atmosphere and several freetime activities like movie or board game evenings and physical activities like playing soccer or basket ball.

Finally, I want to thank my wife Felizitas for her permanent support.

In this thesis, we address the long-standing question of time-reversal protocols for the quantum mechanical wave function for continuous degrees of freedom. We propose two new mechanisms - quantum time mirrors - one for two-band systems, the other one for systems described by the nonlinear Schrödinger equation like Bose-Einstein condensates. In both cases, a homogeneous pulse is applied to the system that is supposed to flip the velocity direction and thus invert the motion of the system.

In a two-band system, the pulse induces a transition from one band to the other. For bands with opposite group velocity directions, the band-transition directly leads to an inversion of the motion. By additionally investigating the effects of perturbations like disorder or electro-magnetic fields, we are able to determine for any (effective) two-band system at hand with a given pulse whether it is a suited candidate for the quantum time mirror. In the Bose-Einstein condensates, the inversion of motion is achieved by quickly varying the nonlinear term. The phases in the wave function acquired during the pulse affect the velocity and for certain parameters it switches sign.
In the last part of the thesis, we investigate zitterbewegung in two-band systems with time-dependent potentials. We find persistent modes of the zitterbewegung that would decay for a wave packet in a static environment. Moreover, using the quantum time mirror pulses described above, echoes of the zitterbewegung can be achieved that are similar to the well-known and highly exploited spin echo.

Universitätsverlag Regensburg

ISBN 978-3-86845-154-2

ISBN 978-3-86845-154-2

Alumni der physikalischen Fakultät der Universität Regensburg e.V.

Universität Regensburg